UC Santa Barbara
UC Santa Barbara Electronic Theses and Dissertations

Title

Quantum Magnetism in 2D and 3D: Theory and Material Realization

Permalink

https://escholarship.org/uc/item/6bh731nr

Author

Liu, Chunxiao

Publication Date

2021

Peer reviewed|Thesis/dissertation

UNIVERSITY of CALIFORNIA

Santa Barbara

Quantum Magnetism in 2D and 3D: Theory and Material Realization

A dissertation submitted in partial satisfaction of the

requirements for the degree of

Doctor of Philosophy

in

Physics

by

Chunxiao Liu

Committee in charge:

Leon Balents, Chair

Stephen Wilson

Cenke Xu

September 2021

The dissertation of Chunxiao Liu is approved:

_____

Professor Stephen Wilson

_____

Professor Cenke Xu

_____

Professor Leon Balents, Committee Chair

June 2021

iii

Acknowledgements

First and foremost, I want to thank my adviser, Leon Balents, for being the most influential person in my graduate career. It's been my greatest pleasure working with you as a student researcher and this fantastic journey has been indispensable to my growth as a scientist and as a person. Day one at UCSB in 2015, I aspired to work on the most theoretical, or really, mathematical, problem in condensed matter physics. Confining myself to this goal, I would have missed the most exciting and fruitful research projects that I conducted under your guidance. I came to realize that there is a philosophy of *naturalness* that underpins these research ideas: if nature has a plain solution to a problem, one should not craft a neater answer. I shall take the liberty of regarding this as a lesson I learned from you.

I feel extremely lucky to have Leon as my adviser for the vast amount of freedom he bestowed on us in determining research topics, collaborating with other people, and balancing work and life. He is incredibly supportive, open-minded, and he always reserves time to discuss with us students however busy he is. During these discussions I have quite often been amazed by the depth and breadth of his knowledge both in physics and beyond, and benefited from the insightful research ideas that he constantly shares with us. What's brilliant is Leon's ability to elucidate any complex concepts in plain language: he would discreetly avoid any unnecessary jargon and bridge any conceptual gaps left untold by seasoned experts. I would recommend the lecture notes Leon wrote for classes PHY217A&B—these are the most detailed and instructive materials I've ever had for a

many-body physics, and I enjoyed so much reading them. All these little things have huge impact on me and shape what I aim to become as a physicist.

Leon has dedicated to supporting us in every possible way. Looking back, I almost took for granted the all-time RAships (there were surely times of hardship when funding cut was common), the international travels, conferences and summer schools ("nous allons rencontrer a la Corse"!), and opportunities to collaborate with multiple groups (Leon's email would go like "I include my talented student in this project..."). I want to thank Leon for bringing many happy moments to my life: attending my piano recital, organizing group dinners, lunches, and hikes, etc. Not to mention his unreserved recommendations which played a big role in helping me secure scholarships and postdoc offers. Thank you, Leon, for your wisdom, guidance, support, patience, and for being such a wonderful adviser, mentor, collaborator, and friend to me.

I am deeply grateful to other members of my thesis defense committee, Prof. Cenke Xu and Prof. Stephen Wilson—it was among my greatest experiences talking and collaborating with you, and I couldn't have accomplished so much without your constant encouragement and support. Thank you, Cenke, for admitting me into UCSB and for guiding me in the topic of topological physics. Your advice during my advancement exam on expanding the scope of my research is of unparalleled value to me and I shall always aim to achieve this goal. Thank you Stephen—you have always been kind, thoughtful and attentive—thank you for the regular discussions with Leon and me, for always bringing exciting first-hand experimental updates of magnetic materials, and for your continued

belief in my abilities.

I would like to address my special thanks to the following scholars. To Xiao Chen, of all the people at UCSB I've known you for the longest time. Thank you for sharing your work and life experience, initiating research collaborations, and giving valuable advice whose role cannot be overestimated in deciding my future research directions. To Gábor Halász, it is my greatest pleasure to know you. Thank you for the numerous in-office discussions, Skype and Zoom meetings—you are modest, scrupulous, frank, and intelligent, and it has always been a delight and privilege to learn from, discuss and collaborate with you. To Lucile Savary—you are my role model. Thank you and Leon for writing the excellent review on quantum spin liquids (arguably the best one on the topic!), and despite having read it many times I can still learn a great deal from it. Oh and yes! Thanks for sending photos of me at the piano recital. Greatly appreciated. Last but not least, to Bill Jacobs—you encouraged and guided me throughout the course of algebra and devoted many extracurricular hours to lay down the mathematics behind my physics research. These invaluable discussions allowed me to peek through the mind of a true mathematician (an infrequent experience for many physicists!), what I deem as one of the most precious gifts as a graduate. I regret much not being able to continue our discussion as I become more and more occupied with research, but the uncompleted work still echoes in my head and I hope one day a complete understanding can be achieved.

I would like to acknowledge other professors at UCSB: Xi Dai, Matthew Fisher, Ken Goodearl, Andreas Ludwig, Chetan Nayak, Zhenghan Wang, and Andrea Young. I

learned tremendously from talking to you and/or attending your lectures, and I certainly wish I had more opportunities to do so.

There are many other local people that I feel I owe thanks to. Thank you Mengxing, for discussing physics and for the great amount of help in daily life. I want to thank my peer students and collaborators, Farzan Vafa, Kasra Hejazi, and Mitchell Bordelon, for collaborating on various projects and writing papers together—I enjoyed very much the heated arguments and debates among us, and I have learned immensely there. Thank you Yaodong for having fun chatting about quantum dynamics and quantum information. Thank you Xiao-Chuan for all the free-ranging discussions in physics—you are such a great pal, thank you for making conversation so spontaneous and enjoyable despite the time of the pandemic.

I would like to thank other members of the condensed matter community at UCSB: Mark Arildsen, Zhen Bi, Yubi Chen, Dominic Else, Tim Hsieh, Jason Iaconis, Chao-Ming Jian, Jianpeng Liu, Zhu-Xi Luo, Chaitanya Murthy, Alex Rasmussen, Kevin Slagle, Yi-Zhuang You, Haoxin Zhou, Tianci Zhou, I feel so blessed to be surrounded by people as talented and diligent as you are, for which I shall have no excuse for complacency, but only to work harder and aim higher. I also want to thank other students and friends in or outside physics, from or outside UCSB: Amber Cai, Zicao Fu, Alex Kinsella, Casey Peters, Marec Serlin, Gabriel Verastegui, Yichen Xu, Runze Zhao, you are the ones who brought joy to me and made my days memorable at UCSB. Thank you Sicheng for being a close friend, and for hosting us in Switzerland. Thank you Suoqing and Shiyi for the

Curriculum Vitæ

Chunxiao Liu

Education

2021   Ph.D. in Physics (Expected), University of California, Santa Barbara.

2018   M.A. in Physics, University of California, Santa Barbara.

2015   B.S. in Physics, Peking University.

2014   B.S. in Mathematics & Applied Mathematics (2nd Major), Peking University.

Professional Experience

2016–2021   Graduate Student Researcher, University of California, Santa Barbara.

2015–2016   Teaching Assistant, University of California, Santa Barbara.

Publications

[1] Chunxiao Liu, Gábor B Halász, and Leon Balents. Symmetric U(1) and $\mathbb{Z}_2$ spin liquids on the pyrochlore lattice. *Physical Review B*, 104(5):054401, 2021.

[2] Chunxiao Liu, Pengfei Zhang, and Xiao Chen. Non-unitary dynamics of Sachdev-Ye-Kitaev chain. *SciPost Phys.*, 10:48, 2021.

[3] Mitchell M Bordelon, Chunxiao Liu, Lorenzo Posthuma, Eric Kenney, MJ Graf, Nicholas P Butch, Arnab Banerjee, Stuart Calder, Leon Balents, and Stephen D Wilson. Frustrated heisenberg $J_1 - J_2$ model within the stretched diamond lattice of LiYbO$_2$. *Physical Review B*, 103(1):014420, 2021.

[4] Pengfei Zhang, Chunxiao Liu, and Xiao Chen. Subsystem Rényi entropy of thermal ensembles for SYK-like models. *SciPost Phys*, 8:094, 2020.

[5] Mitchell Bordelon, Chunxiao Liu, Lorenzo Posthuma, PM Sarte, NP Butch, Daniel M Pajerowski, Arnab Banerjee, Leon Balents, and Stephen D Wilson. Spin excitations in the frustrated triangular lattice antiferromagnet NaYbO$_2$. *Physical Review B*, 101(22):224427, 2020.

[6] Xiao-Tian Zhang, Yong Hao Gao, Chunxiao Liu, and Gang Chen. Topological thermal hall effect of magnetic monopoles in the pyrochlore U(1) spin liquid. *Physical Review Research*, 2(1):013066, 2020.

[7] Mitchell M. Bordelon, Eric Kenney, Chunxiao Liu, Tom Hogan, Lorenzo Posthuma, Marzieh Kavand, Yuanqi Lyu, Mark Sherwin, N. P. Butch, Craig Brown, et al. Field-tunable quantum disordered ground state in the triangular-lattice antiferromagnet $NaYbO_2$. *Nature Physics*, 15(10):1058–1064, 2019.

[8] Chunxiao Liu, Gábor B Halász, and Leon Balents. Competing orders in pyrochlore magnets from a $\mathbb{Z}_2$ spin liquid perspective. *Physical Review B*, 100(7):075125, 2019.

[9] Kasra Hejazi, Chunxiao Liu, and Leon Balents. Landau levels in twisted bilayer graphene and semiclassical orbits. *Physical Review B*, 100(3):035115, 2019.

[10] Kasra Hejazi, Chunxiao Liu, Hassan Shapourian, Xiao Chen, and Leon Balents. Multiple topological transitions in twisted bilayer graphene near the first magic angle. *Physical Review B*, 99(3):035111, 2019.

[11] Chunxiao Liu, Xiao Chen, and Leon Balents. Quantum entanglement of the Sachdev-Ye-Kitaev models. *Physical Review B*, 97(24):245126, 2018.

[12] Jason Iaconis, Chunxiao Liu, Gábor B Halász, and Leon Balents. Spin liquid versus spin orbit coupling on the triangular lattice. *SciPost Phys*, 4(003), 2018.

[13] Chunxiao Liu, Farzan Vafa, and Cenke Xu. Symmetry-protected topological hopf insulator and its generalizations. *Physical Review B*, 95(16):161116, 2017.

[14] Peng Lv, Ai-Min Guo, Huaiyu Li, Chunxiao Liu, XC Xie, and Qing-Feng Sun. Spin-flip reflection at the normal metal-spin superconductor interface. *Physical Review B*, 95(10):104516, 2017.

Abstract

Quantum Magnetism in 2D and 3D: Theory and Material Realization

by

Chunxiao Liu

The understanding and predicting of novel phenomena in magnetic materials is an important theme in condensed matter physics. The most interesting phenomena among them are the ones that exhibit intrinsic quantum behavior, where high degree of entanglement gives rise to macroscopic quantum effect not described in a traditional theory of symmetry breaking. This thesis is a collection of our efforts to combine the theoretical toolkit in analyzing exotic quantum states with recent experimental progress in realizing and finding quantum magnetic materials. We present our study in three parts:

The first part presents a study of the frustrated triangular lattice antiferromagnet $NaYbO_2$. Both spin liquid signatures in zero field and quantum-induced ordering in intermediate fields are observed, suggesting the existence of an intrinsically quantum disordered ground state. Through symmetry analysis and spin wave calculations, we determine the microscopic model relevant to $NaYbO_2$ and map out the phase diagram of magnetic orders in presence of a magnetic field. Our result indicates that $NaYbO_2$ is a promising platform for exploring spin liquid physics with full tunability of field and temperature.

The second part presents an investigation of a chemically related compound $LiYbO_2$, which has instead a stretched diamond lattice structure. Experiments reveal a rich magnetic phase diagram of $LiYbO_2$ that includes a low field incommensurate spiral order and a high field commensurate order. We first show that the former is largely captured by a $J_1 - J_2$ Heisenberg model, and then employ a phenomenological model to understand the incommensurate-to-commensurate transition at intermediate magnetic fields. Finally, several effects are addressed in order to understand a small variance between the observed and predicted phasing of Yb moments.

The last part is devoted to the classification of symmetric $\mathbb{Z}_2$ and $U(1)$ spin liquids on the three-dimensional pyrochlore lattice. We first analyze the magnetic orders linked to specific $\mathbb{Z}_2$ quantum spin liquids. We find that under certain conditions, seemingly unrelated orders are intertwined and the conventional orders detected in experiments are accompanied by hidden orders. We then turn to the study of $U(1)$ spin liquid classes and observe that, surprisingly, a large family of them is described by a $U(1)$ gauge field coupled to symmetry protected gapless multi-nodal line spinons, hence uncovering a new prototype of quantum spin liquid beyond the standard example of pyrochlore quantum spin ice. The low temperature specific heat receives a $T^{3/2}$ contribution with logarithmic corrections from the gauge–spinon coupling and the spinon bands, which serves as a simple criterion for the existence of these $U(1)$ nodal line spin liquids.

Contents

List of Figures

List of Tables

Permissions and Attributions

- Chapter 2 contains a slightly modified version of excerpts and figures reprinted with permission from Mitchell M. Bordelon, Eric Kenney, Chunxiao Liu, Tom Hogan, Lorenzo Posthuma, Marzieh Kavand, Yuanqi Lyu, Mark Sherwin, N. P. Butch, Craig Brown, M. J. Graf, Leon Balents amd Stephen D. Wilson, Field-tunable quantum disordered ground state in the triangular-lattice antiferromagnet $NaYbO_2$, Nature Physics 15(10):1058–1064 [14], published and copyrighted 2019/07/29 by Springer Nature, and Mitchell M. Bordelon, Chunxiao Liu, Lorenzo Posthuma, P. M. Sarte, N. P. Butch, Daniel M. Pajerowski, Arnab Banerjee, Leon Balents, and Stephen D. Wilson, Spin excitations in the frustrated triangular lattice antiferromagnet $NaYbO_2$, Phys. Rev. B 101, 224427 [16], published and copyrighted 2020/06/22 by the American Physical Society.

- Chapter 3 contains a slightly modified version of excerpts and figures reprinted with permission from Mitchell M. Bordelon, Chunxiao Liu, Lorenzo Posthuma, Eric Kenney, M. J. Graf, N. P. Butch, Arnab Banerjee, Stuart Calder, Leon Balents, and Stephen D. Wilson, Frustrated Heisenberg $J_1 - J_2$ model within the stretched dia-

mond lattice of LiYbO$_2$, Phys. Rev. B 103, 014420 [15], published and copyrighted 2021/01/14 by the American Physical Society.

- Chapter 4 contains a slightly modified version of excerpts and figures reprinted with permission from Chunxiao Liu, Gábor B. Halász, and Leon Balents, Competing orders in pyrochlore magnets from a $\mathbb{Z}_2$ spin liquid perspective, Phys. Rev. B 103, 014420 [94], published and copyrighted 2019/08/12 by the American Physical Society.

- Chapter 5 contains a slightly modified version of excerpts and figures reprinted with permission from Chunxiao Liu, Gábor B. Halász, and Leon Balents, Symmetric U(1) and $\mathbb{Z}_2$ spin liquids on the pyrochlore lattice, Phys. Rev. B 104, 054401 [95], published and copyrighted 2021/8/2 by the American Physical Society.

Chapter 1

Introduction

1.1 Microscopic theory of magnetism

1.1.1 Quantum chemistry: from atoms to crystals

Condensed matter physics studies the properties of almost any material that we encounter in our daily life. While there are tens of thousands of materials and the physical properties vary from one to another, the material must be made of elementary units such as atoms, ions, and electrons, and one ask whether the property of the material can be understood directly or indirectly from the property of these individual units that compose the material. This is indeed a valid viewpoint: a crystal, formed out of array of atoms, is nothing but collections of isolated individual atoms if they can be brought apart with infinite distance, and under this (idealized) circumstance any property of the crystal is simply that of the atom. It turns out that, quite often, real crystals, in which

atoms are separated with a finite distance of a few angstroms, still possess properties that can be understood from the isolated atom limit. In this case, we are justified to begin our journey from studying the quantum properties of individual atoms or ions – this is the topic of *quantum chemistry*[1].

We clarify that, by the holding of the above criterion, we do not expect the property of the crystal to be the same as that of the isolated particle. Rather, we mean the property of the former can be *inferred* from that of the latter, quite often from perturbative calculations. We also remind that we will be mostly talking about electrons in the theory of quantum magnetism. The nuclear contribution to magnetism is much weaker then the electrons.

The criterion to determine electronic states in an ion is usually summarized in the form of three Hund's rules. Within a given configuration of one-electron orbitals (assuming only one incomplete shell), the ground state of an isolated atom or ion

- has the largest value of the total spin S;

- has the largest value of the total orbital angular momentum L that is permitted by the first rule;

- has the total angular momentum is $J = |L - S|$ for less-than-half-filled shells, and $J = L + S$ for more-than-half-filled shells.

The first Hund's rule states that the spin interaction is ferromagnetic. The mechanism of direct exchange offers an explanation to this rule. To be more precise, we consider

---

[1]For an extensive review on this subject, see e.g. [41].

two electrons in the same shell, which feel each other directly through the Coulomb interactions.[2] They must form spin eigenstates, which consist of three triplets with $S = 1$ and one singlet, $S = 0$. The triplets have two parallel spins, therefore when the two electrons come closer in space, they will occupy the same quantum state, which is forbidden by the Pauli exclusion principle. Put more plainly, the orbital part of the triplet wave function vanishes when the two coordinates approach each other[3]. The singlet state, however, is not subject to Pauli exclusion principle and can have the two electrons come close to each other. However, this pushes the singlet state to higher energy due to the Coulomb repulsion felt by the electrons. Effectively, we are having ferromagnetic (FM) interactions which gives triplet ground states. We believe the same picture applies to many-electron systems in which the total spin $\boldsymbol{S} = \sum_i \boldsymbol{S}_i$ is a good quantum number. This gives the first Hund's rule.

Again assuming the electrons interact with each other only via the Coulomb interaction, the total orbital angular momentum $\boldsymbol{L} = \sum_i \boldsymbol{L}_i$ will be good quantum numbers, and the same logic in the preceding paragraph applies to orbital momentum, giving the second Hund's rule.

We emphasize that the above argument for the first and the second Hund's rule is based on direct exchange mechanism for orthogonal orbitals, and that the physical reason is fundamentally rooted in Pauli exclusion principle and Coulomb repulsion. The first and the second Hund's rules apply to almost all atoms and ions, and according to the

---

[2]In essence, what we need here is orthogonal orbitals, on top of which the Coulomb interaction is a perturbation.

[3]This is called the exchange hole effect.

viewpoint stated at the very beginning, it applies to crystals which behaves not too far from the isolated atomic limit. Other than that, there are plenty of mechanisms that restricts the validity of Hund's these rules[4].

The third Hund's rule is derived from the spin–orbit coupling. The spin–orbit coupling for a single electron writes

$$\mathcal{H}_{\text{SO},i} = \lambda \boldsymbol{S}_i \cdot \boldsymbol{L}_i, \tag{1.1}$$

where $\lambda = \frac{\hbar^2}{2m_e^2 c^2} \frac{Ze^2}{r^3} > 0$ is a constant that, importantly, is proportional to the atomic number Z.

Switching on the *total* spin–orbit coupling from each electrons lifts the degeneracy between different (L, S)[5]. The term can be written as

$$\sum_i \mathcal{H}_{\text{SO},i} \simeq \lambda(L,S)\boldsymbol{L} \cdot \boldsymbol{S} = \frac{\lambda}{2}(\boldsymbol{J}^2 - L(L+1) - S(S+1)), \quad \text{where}$$

$$\begin{cases} \lambda > 0, & \text{less-than-half-filled shell,} \\ \lambda < 0, & \text{more-than-half-filled shell.} \end{cases} \tag{1.2}$$

This gives Hund's third rule.

The above analysis holds for isolated ions. In order to apply them to crystals, the effect of crystalline environment must be additionally considered. These effects include the potential of the ion core, as well as the electrostatic potential of the surrounding ligands (oxygen ions in most cases); they are generally called the *crystal fields*. We must then examine the effect of crystal fields to the Hund's rules we introduced earlier. It turns out that, when crystal fields are strong enough compared to the exchange strength—as

---

[4]For example, the mechanism of direct exchange in non-orthogonal orbitals, the kinetic exchange and the superexchange mechanisms. As a result, Hund's rules do not generally apply to molecules.

[5]The smallness of λ justifies $\mathcal{H}_{\text{SO}}$ as a perturbation in the (L, S) subspace, even for heavy elements with large Z.

is the case of $4d$ and $5d$ transition metal compounds—the first and second Hund's rules can be invalidated, whereas they are weak enough in other cases such as $3d$ transition metals and $4f$ rare earth compounds so that the isolated ion approximation still stands to some point. we consider these two cases separately:

- Intermediate crystal field regime: in $3d$ transition metals, the spin–orbit coupling is relatively small due to the small atomic number Z, and we have

$$\text{Exchange splittings} > \text{crystal field} > \text{spin-orbit coupling}, \qquad (1.3)$$

  while Hund's first and second rules apply, the third rule ceases to apply, and J is not a good quantum number.

- Weak crystal field regime: the $4f$ orbital lies well inside the xenon core, and the core electrons outside the $4f$ orbital offers great protection to screen the fields from neighboring ions, rendering $4f$ electrons free-ion-like. Energy scales are

$$\text{Exchange splittings} > \text{spin-orbit coupling} > \text{crystal field}, \qquad (1.4)$$

  and all three Hund's rules apply. J remains a good quantum number, and crystal field effects splits states within a given J.

It turns out that, by analyzing the symmetry of the environment, we can already know—without referring to the detailed form of the Hamiltonian—how the ground state manifold further splits under the crystal field.

In this thesis we will be mostly focusing on the rare earth compounds (layered triangular, diamond-like, and pyrochlore crystals) as far as material is concerned, and we take

the element Ytterbium (Yb) as an example. It is the 14th and second last element in the lanthanide series with atomic number $Z = 70$. The electron configuration is $[\text{Xe}]4f^{14}6s^2$, where $[\text{Xe}] = 1s^2 2s^2 2p^6 3s^2 3p^6 3d^{10} 4s^2 4p^6 4d^{10} 5s^2 5p^6$ is the configuration of inner closed-shells (that of xenon). The most common ion form is Yb^{3+}, which has configuration $[\text{Xe}]4f^{13}$. Hund's first and second rules give total spin of $S = 1/2$ and total orbital angular momentum of $L = 3$; Hund's third rule asserts that the ground state manifold has total angular momentum $J = |L + S| = 7/2$, consisting of eight basis states $|J_z\rangle$ with $J_z = \pm 1/2, \pm 3/2, \pm 5/2, \pm 7/2$. The excited state manifold has $J = |L - S| = 5/2$, consisting of six basis states with $J_z = \pm 1/2, \pm 3/2, \pm 5/2$.

Now consider crystal fields. In cubic environment [75] (with cubic symmetry O_{h}), the eight ground states split to two doublets and a quadruplet.[6] The doublets cannot be further split since they are protected by time reversal symmetry; they are called the Kramers doublets.

For the compounds NaYbO_2 and LiYbO_2 studied in this thesis, the local symmetries of the Yb ion are D_{3d} and D_{2d}, respectively, both are subgroups of the cubic group. The lowering of the symmetry is an example of the Jahn–Teller effect: *if the symmetry of the crystal field is so high that the ground state of an ion is predicted to be orbitally*

---

[6]They are

$$\Gamma_6 \colon \sqrt{\frac{5}{12}}| \pm 7/2\rangle + \sqrt{\frac{7}{12}}| \mp 1/2\rangle,$$

$$\Gamma_7 \colon \frac{\sqrt{3}}{2}| \pm 5/2\rangle - \frac{1}{2}| \mp 3/2\rangle,$$

$$\Gamma_8 \colon \sqrt{\frac{7}{2}}| \pm 7/2\rangle - \sqrt{\frac{5}{12}}| \mp 1/2\rangle, \quad \frac{1}{2}| \pm 5/2\rangle + \frac{\sqrt{3}}{2}| \mp 3/2\rangle.$$

degenerate, then it will be energetically preferable for the crystal to distort in such a way that the orbital degeneracy is lifted. Indeed, either the trigonal distortion $O_h \rightarrow D_{3d}$ and the tetragonal distortion $O_h \rightarrow D_{2d}$ further splits the quadruplet into two doublets. The low energy crystal field states are therefore four Kramers doublets. At sufficiently low temperatures, only the ground state Kramers doublet is activated, which is described by an effective $J_{\text{eff}} = 1/2$ spin.

The procedures to finding the ground state effective degrees of freedom using the knowledge of Hund's rules and crystal field configurations in local environment, as exemplified in the case of Ytterbium, is quite generic—at least for rare earth compounds. In particular, it is implied that the ground state manifold of rare earth ions with an even number of electrons in $4f$ shell is a Kramers doublet, described by an effective $J_{\text{eff}} = 1/2$ spin.

1.1.2 Symmetry and model Hamiltonian

We have seen in the last subsection that quite often the effective degrees of freedom in magnetic systems behave as $S = 1/2$ spins. In the microscopic modeling of such systems, one seeks to find an exchange Hamiltonian describing the interaction among these spins. The numerical values of the exchange parameters are usually hard to determine in any means, but one can at least determine the most general form of the exchange Hamiltonian using symmetry principles. In this subsection, we outline the procedures to achieve this. While this is nothing more than an ordinary symmetry analysis, this will prepare us for

the more complicated version of *projective* symmetry analysis in the spin liquid context, to be introduced in a later subsection.

We start with a formal account of the symmetry group. A (three-dimensional crystallographic) space group G consists of all the symmetry operations that map the crystal lattice to itself. It must contain three primitive translations T_1, T_2, T_3. Denote the translation group generated by them as $T = \langle T_1, T_2, T_3 \rangle$. The point group P is a finite group that, roughly speaking, consists all the rotations, mirror reflections, inversions of the lattice symmetry lattice. It is defined by the quotient

$$\text{Point group:} \quad H \equiv G/T. \tag{1.5}$$

Underlying this definition is the fact that the translations T is a normal subgroup of G.[7]

Usually a powerful way to parse the structure of a group G is to study its generators and the relations among them[8]. While the space group G is an infinite group, its generators are finitely many, and the number of independent group relations is also finite. The idea that the generators of G is the union of translations T_1, T_2, T_3 and the generators of the point group, however, is not always correct. We have the following two cases:

- In the so-called *nonsymmorphic* space groups, some point group operations may not exist in the parent space group at all. In this case, the space group almost always[9] contains nonsymmorphic operations in the form of either a glide reflection or a screw rotation—these operations are the composition of a point group operation

---

[7]For readers enthusiastic about a mathematical description of crystallographic groups, we recommend the book [144].

[8]Mathematically, this way of characterizing a group is called the *presentation of a group*.

[9]The only exceptions to the "always" part of the claim are the No. 24 and No. 199 space groups, whose glide and screw operations are "removable"—we refer to Ref. [119] for details.

(mirror reflection or rotation) with a *fraction* of the primitive translation. We must substitute nonsymmorphic operations for some of the point group generators in order to obtain the generators of the space group.

- Otherwise, the space group is *symmorphic*, meaning all point group element are valid symmetry operations of the space group. In this case, the point group generators, combined with the translations $T_{1,2,3}$, give the generators of the space group.

Apart from the generators, it is the relations among the generators that specify the group. Apparently, the relation among translations is that they commute with each other:

$$T_i T_j = T_j T_i \quad \text{for} \quad i, j = 1, 2, 3. \tag{1.6}$$

All the point group relations must also be included; the only subtlety associated with the nonsymmorphic case is that these relations must be replaced by the corresponding relations involving the nonsymmorphic elements. Finally, one must examine the commutation relation between point group (or nonsymmorphic) generators and translations. These will give the complete relations that define the space group.

As an example, consider the symmetry group of the $NaYbO_2$. The compound family of $NaYbO_2$, called *delafossites*, have rhombohedral lattice with space group $R\bar{3}m$ (No. 166). This is a symmorphic group, with point group $R\bar{3}m/T = D_{3d}$ the dihedral group that contains 12 elements, generated by inversion P, a threefold rotation with axis perpendicular to the triangle layer C_3, and a twofold rotation with axis parallel to a nearest neighbor (NN) bond in a triangle layer, D. Therefore, the space group is generated by

9

elements

$$R\bar{3}m = \langle T_1, T_2, T_3, P, C_3, D \rangle. \tag{1.7}$$

The point group is defined by the following relations

$$P^2 = D^2 = C_3^3 = 1, \quad PD = DP, \quad PC_3 = C_3P, \quad (C_3D)^2 = 1. \tag{1.8}$$

between the translations and poin group generators, we have

$$T_1C_3 = C_3T_2, \quad T_2C_3 = C_3T_1^{-1}T_2^{-1}, \quad T_1P = PT_1^{-1}, \quad T_2P = PT_2^{-1}, \quad DT_1 = T_2D. \tag{1.9}$$

Combining relations (1.6), (1.1.2) and (1.9) gives the complete relation of $R\bar{3}m$.

As another example, consider the symmetry group of the pyrochlore lattice. The space group is $Fd\bar{3}m$ (No. 217). This is a nonsymmorphic group, with point group $O_{\mathrm{h}} = Fd\bar{3}m/T$ the cubic group. The cubic group contains 48 elements and is generated by inversion P, a threefold rotation C_3 with axis parallel to the body-diagonal of the pyrochlore unit cell, and a mirror reflection Σ that contains a pair of parallel face-diagonals. The last point group generator, Σ, is not in the space group; instead, this element is replaced by the space group generator S, which is a twofold screw operation. For the detailed definition of S, the structure of the point group and the space group relations, see Appendix A.1 and A.2.

Having familiarized ourselves with the symmetry structure, it is then straightforward to use them to obtain symmetry allowed microscopic Hamiltonians. The most general form of an $S = 1/2$ exchange Hamiltonian is

$$H = \frac{1}{2} \sum_{\boldsymbol{r}_\mu, \boldsymbol{r}'_\nu} \hat{\boldsymbol{S}}_{\boldsymbol{r}_\mu}^T \mathbf{J}_{\boldsymbol{r}_\mu, \boldsymbol{r}'_\nu} \hat{\boldsymbol{S}}_{\boldsymbol{r}'_\nu}. \tag{1.10}$$

10

where $\boldsymbol{r}$ labels unit cells and μ is a sublattice index. The exchange parameters $\mathbf{J}_{\boldsymbol{r}_\mu, \boldsymbol{r}'_\nu}$ is a 3×3 symmetric matrix.

Under a space group operation $\mathcal{O}$ the spins transform as

$$\mathcal{O}: \hat{\boldsymbol{S}}_{\boldsymbol{r}_\mu} \to U_\mathcal{O} \hat{\boldsymbol{S}}_{\mathcal{O}(\boldsymbol{r}_\mu)} U_\mathcal{O}^\dagger, \tag{1.11}$$

where $U_\mathcal{O}$ is the SU(2) rotation matrix associated with the operation $\mathcal{O}$. First, considering translations $T_{1,2,3}$. The SU(2) matrix $U_\mathcal{O}$ is just identity. The effect on the exchange parameters is translation invariance

$$\mathbf{J}_{\boldsymbol{r}_\mu, \boldsymbol{r}'_\nu} = \mathbf{J}_{(\boldsymbol{r}-\boldsymbol{r}')_\mu, 0_\nu} \equiv \mathbf{J}_{\mu,\nu}(\boldsymbol{r} - \boldsymbol{r}'). \tag{1.12}$$

Next, consider non-translation elements $\mathcal{O}$ of the space group. Suppose the point group element that corresponds to $\mathcal{O}$ defines a rotation along axis $\boldsymbol{n}$ with angle θ. The spin rotation matrix is then written as $U_\mathcal{O} = e^{-i\frac{\theta}{2}\boldsymbol{n}\cdot\boldsymbol{\sigma}}$, where $\boldsymbol{\sigma} = (\sigma^1, \sigma^2, \sigma^3)$ are the Pauli matrices. The SU(2) equation (1.11) can then be written as

$$\mathcal{O}: \hat{\boldsymbol{S}}_{\boldsymbol{r}_\mu} \to \mathbf{R}^{-1}(\boldsymbol{n}, \theta) \hat{\boldsymbol{S}}_{\mathcal{O}(\boldsymbol{r}_\mu)}, \tag{1.13}$$

In order to make Hamiltonian (1.10) invariant under $\mathcal{O}$, we need to determine what constraints Eq. (1.13) imposes on the exchange tensor (1.12). Importantly, constraints are produced only when an exchange bond is mapped back to itself under $\mathcal{O}$. Modulo translations, the problem can be formulated this way: given a finite set consisting of all the spins in a primitive cell of the lattice labeled by sublattice index $\mu = 1, 2, ...,$ examine the action of the point group elements on this set. For any unordered pair $\{\mu, \nu\}$ that represents a bond, say the $(\mu, \nu) = (1, 2)$ bond, find its *stabilizer group* $P_{\{\mu,\nu\}}$— the subgroup of P that maps $\{\mu, \nu\}$ to itself—these are the operations that produce

11

constraints on $\mathbf{J}_{\mu,\nu}$. Finally, by solving all the constraints, one obtains the symmetry allowed exchange Hamiltonian.

Following the procedures outlined above, one can systematically obtain the exchange Hamiltonian for a given lattice, up to exchanges at arbitrarily far neighbor level. This will be used in Section 2.3 to determine the symmetry allowed NN exchange Hamiltonian (both inlayer and interlayer) for the delafossites, and in Section 3.3.2 for the symmetry allowed Hamiltonian for the stretched diamond lattice up to NNN level.

1.1.3 Symmetry breaking, magnetic orders, and spin waves

Many spin systems—whose low energy degrees of freedom are spins, subject to some exchange Hamiltonians as described in the last subsection—undergo the transition into magnetically ordered phase upon cooling. In the magnetically ordered state, the spins develop nonzero expectation value, in contrast to the high temperature disordered phase in which the expectation value vanishes. The physics mentioned is an instance of spontaneous symmetry breaking, whose essential physics has been captured in Landau's theory of phase transition. In this section, we illustrate the content of this theory via simple model Hamiltonians, from which general principles will be summarized.

The model we choose is a simple NN $S = 1/2$ Heisenberg model on a cubic lattice

$$H = J \sum_{\langle i,j \rangle} \boldsymbol{S}_i \cdot \boldsymbol{S}_j \tag{1.14}$$

where i, j label sites of the cubic lattice. Here $J > 0$ and $J < 0$ correspond to an antiferromagnetic (AFM) exchange and a ferromagnetic (FM) exchange, respectively. We

choose a three dimensional lattice to avoid complications due to the Mermin–Wagner theorem[10]. We choose the cubic lattice and restricting to NN to avoid lattice frustration in the AFM case (lattice frustration will be introduced later). While the cubic lattice possesses many spatial symmetries, we will temporarily be oblivious to them in this section, but instead focus on the internal symmetries of the model (1.14): the model has global SU(2) spin rotation symmetry. We point out that, while symmetry analysis outlined in the last subsection indicates that more terms are allowed by the cubic symmetry than the Heisenberg term in (1.14), and that these additional terms necessarily break the global SU(2) spin rotation symmetry down to a lower one, in reality these terms are of spin–orbit coupling in origin, and are usually small compared to the Heisenberg term which is dominant in a *Mott insulator*.

Let us first look at the FM case, with $J < 0$. Then, it is obvious that for arbitrary size of the cubic lattice N, the state with maximally alignment along the $\hat{z}$ direction, $| + z \rangle \equiv \prod_i |S_i^z = 1/2 \rangle$, is a ground state. The ground state manifold consists of all the states that differ from $| + z \rangle$ by a global spin rotation; each of these states breaks the global SU(2) spin rotation symmetry of the model (1.14) down to a global U(1) spin rotation around the aligned direction. Adopting a formal language, we denote the original unbroken global symmetry—the SU(2) spin rotation symmetry—by G, and the residual global symmetry in a ground state—the U(1) spin rotation symmetry—by H. Then, the ground states are in one-to-one correspondence with the elements of G/H.

---

[10]The Mermin–Wagner theorem states that spontaneous symmetry breaking cannot happen in systems with spatial dimensions two or lower at any non-zero temperature. The precise statement of the theorem, as well as generalized to quantum systems at zero temperature, can be found in Ref. [9].

We then look at the AFM case, with $J > 0$. Since neighboring spins tend to anti-align with each other, our naive guess of a ground state would be the state $|\pm z\rangle \equiv \prod_{i \in A} |S^z = +1/2\rangle \prod_{j \in B} |S^z = -1/2\rangle$, where A and B consist of sites whose coordinate sum are even and odd, respectively. Such a state, however, is not the ground state of the AFM model for any finite lattice size N.[11] Nevertheless, such a state is indeed a ground state in the *thermodynamic limit* $N \to \infty$. The rest follows the FM case: the state $|\pm z\rangle$ has a global residual symmetry $H = U(1)$, and other ground states are in one-to-one correspondence with the element of G/H.

The essence behind the phenomenon of spontaneous symmetry breaking is that, in the *thermodynamic limit*, the ground states labeled by elements of G/H do not mix due to the infinite energy barriers one has to overcome to move from one ground state to another.

If G/H is continuous, soft excitations exist above a symmetry broken ground state, whose energy vanishes as its wave number approaches zero. This is *Goldstone's theorem*, which can be understood intuitively in our Heisenberg example. Take the FM case. since the ground state is maximally polarized (maximally spin alignment), the low-lying excitations can be created by flipping just one spin, and this excitation can propagate in the crystal. These "Goldstone modes" are called spin waves, or magnons. One usually

---

[11]It can be a nontrivial task to exactly determine the ground state in the AFM case for finite N. But on physical grounds one can argue that a tower of low energy states exist, which all preserve SU(2) symmetry.

describe these excitations in terms of the Holstein–Primakoff (HP) bosons a_j:

$$\boldsymbol{S}_j \cdot \boldsymbol{c}_j = S - n_j, \qquad \boldsymbol{S}_j \cdot (\boldsymbol{a}_j + i\boldsymbol{b}_j) = \sqrt{2S - n_j}\, a_j, \qquad S_j^- = \left(S_j^+\right)^\dagger, \qquad (1.15)$$

where $\boldsymbol{a}_j = \hat{x}, \boldsymbol{b}_j = \hat{y}, \boldsymbol{c}_j = \hat{z}$ in a FM state, $n_j = a_j^\dagger a_j$ is the number operator for a_j. Keeping to quadratic order of the HP bosons and diagonalize the resulting Hamiltonian $H[a, a^\dagger]$, we obtain the dispersion at small ka (a is the lattice constant)

$$\omega_{\boldsymbol{k}} = S|J|(ka)^2. \qquad (1.16)$$

The spin waves in the AFM case can be obtained in a similar way. The Néel-type ground state determines

$$\boldsymbol{a}_j = \hat{x}, \boldsymbol{b}_j = \hat{y}, \boldsymbol{c}_j = \hat{z} \ \text{ for } \ j \in A; \qquad \boldsymbol{a}_j = \hat{x}, -\boldsymbol{b}_j = \hat{y}, \boldsymbol{c}_j = -\hat{z} \ \text{ for } \ j \in B. \qquad (1.17)$$

Plugging them to the formula (1.15) for HP bosons a_j, the resulting Hamiltonian for a_j has a two-sublattice structure. Completing the diagonalization, we find that there are two gapless modes at small ka

$$\omega_{\boldsymbol{k},1} = \omega_{\boldsymbol{k},2} = 2dJSak. \qquad (1.18)$$

In general, spontaneous symmetry breaking gives rise to orders. The ordered state is one of the ground states that transform nontrivially under the broken symmetry and do not overlap with each other in the thermodynamic limit. The order is described by some order parameter—an operator that develops nonzero expectation value in the ordered state as symmetry breaking happens. In the above, the FM (or the Néel) order is characterized by the order parameter[12] $\sum_j S_j^z$ (or $\sum_{j \in A} S_j^z - \sum_{j \in B} S_j^z$). On top of the ordered state

---

[12]The formal definition of an order parameter requires the concept of interpolating field. See e.g.

lies the *Goldstone modes*—these are the low energy excitations that are gapless at long wavelength $k \to 0$. The Goldstone modes appear whenever a continuous symmetry is spontaneously broken[13]. The quadratic mode in the FM case and the two linear modes in the AFM case are all examples of Goldstone modes associated to the symmetry breaking $G/H = SU(2)/U(1) \cong S^2$. These example clearly demonstrates that, for the very same symmetry breaking $G \to H \subset G$ (here G and H are regarded as abstract groups), the details of the Goldstone modes can still differ. In particular, the "folklore" that each generator of the spontaneously broken symmetry[14] corresponds to one Goldstone mode is not universally correct.

In fact the correct counting of the Goldstone modes, as well as their dispersion relations, were only cleared up recently. Here we outline the basic idea for the counting rules; the details can be found in the excellent reviews [163, 9]. Label the generators of the spontaneously broken symmetry as Q_a, with $a = 1, 2, ..., n$, with $n = \dim G/H$. These global generators can be written as the sum of local generators, $Q_a = \sum_i Q_{ai}$. The extra information to determine the number of Goldstone modes other than the number n, roughly speaking, is the noncommutativity of the generators *in the ground state*[15]; any such noncommutative relation would result in two linearly dispersing modes (which are those mentioned in the "folklore") to combine into one quadratic Goldstone mode.

Ref. [9] for detail.

[13]Known as the Goldstone's theorem.

[14]Here and below we assume implicitly that such symmetry is a global continuous symmetry.

[15]This defines the so-called Watanabe–Brauner matrix

$$M_{ab} = -i\langle [Q_a, Q_{bi}] \rangle.$$

In the case of cubic Heisenberg model, the two generators of the broken global symmetry are $\sum_i S_i^x$ and $\sum_i S_i^y$, whose commutator gives the magnetization $S^z = \sum_i S_i^z$. In the AFM case, the expectation value $\langle S^z \rangle$ vanishes, giving two linearly dispersion Goldstone modes as usually expected. In the FM case, however, S^z is an order parameter of the symmetry broken ground state, $\langle S^z \rangle \neq 0$, hence we have only one quadratic Goldstone mode. These two types of Goldstone modes are called type-A and type-B respectively in the literature.

1.2 Quantum spin liquids and their symmetry classifications

1.2.1 Frustrated magnetism and fundamentals of spin liquids

As introduced in the last section, the AFM Heisenberg model on a cubic lattice (or any bipartite lattice) has a Néel-type ground state. In non-bipartite lattices, AFM exchange interaction can lead to unusual behavior. Taking the triangular lattice for example. Regarding spins as classical unit vectors, the AFM Heisenberg model has any "three-sublattice states", i.e. states with a three-site unit cell with $\sum_{\mu=1,2,3} \boldsymbol{S}_\mu = 0$, as its ground state. The ground state manifold is $S^1 \times S^1$. Turning on quantum effects, there is no simple way to determine the true quantum ground state due to the vastly many classically degenerate ground state configurations.

It was proposed, first by Philip Anderson, that nontrivial quantum states can arise

in this context [2]. The proposed state, the "resonating valence bond" (RVB) state, is a particular superposition of dimer[16] coverings on a triangular lattice. The state differs from conventional magnetically ordered states since no order parameters or symmetry breaking exists whatsoever. Therefore, if it is indeed the ground state of the AFM Heisenberg model, it would lie outside Landau's theory of spontaneous symmetry breaking.

The RVB state, although now disproved to be the ground state of the triangular AFM Heisenberg model [182, 166], provides new possibilities in searching for exotic states in magnetic systems. The state is an early prototype of *spin liquids*—a highly correlated spin state that does not order down to temperatures much lower than their exchange interaction scale. This definition, negative in its tone, works perfectly as a practical one but is also a too broad one. What we would like to pursue is the class of intrinsic quantum states that captures the essence of the RVB state. We will call them *quantum spin liquids* (QSLs). Adopting a modern point of view, we list the main properties of QSLs as follows:

- A QSL is a *highly entangled* state. In contrast to magnetically ordered states which are product-like in real space, a QSL state is a superposition of product states, rendering it highly entangled in real space. Entanglement has been a core concept in modern condensed matter physics, especially in the study of exotic quantum states. It is the *defining* property of a QSL state, from which many of the properties mentioned below follow.

---

[16]Here a dimer means a spin singlet state formed by two $S = 1/2$ spins at the ends of a nearest-neighbor bond.

18

- A QSL supports nonlocal excitations that carry *fractional* quantum numbers. In a magnetically ordered state, excitations can all be created by local operators: shedding a light or shooting a neutron to a magnet, a magnon is locally created and propagators in the material. The spin carried by the magnon reflects the flip of a local spin and has the elementary unit of spin one, $S = 1$. In a QSL state, however, a low energy magnon can *fractionalize* into two excitations, called *spinons*, each with $S = 1/2$ and behave as sharp quasiparticles. While the spinons must be created in pairs, the "individualistic" nature of them makes it legitimate to regard each of them as elementary excitations of the system. From theory point of view, each spinon must be created by a nonlocal operator, which is an extensive product of local operators; the energy cost for a spinon, however, is non-extensive, which is made possible precisely because of the highly entangled state: the nonlocal operator, acting on the QSL state, merely "reshuffles the components of the superposition" [138].

- The nonlocal fractionalized excitations may carry nontrivial self and/or mutual statistics. In QSLs in which all excitations are gapped, the excitations may encode information about the *topology* of the system. In two dimensions, the excitations may exhibit anyon statistics. Determining the statistics of these excitations in some cases can be a highly nontrivial task.

- As a byproduct of the lack of symmetry breaking, a QSL usually preserves time reversal symmetry as well as the full symmetry of the lattice. The interplay be-

19

tween symmetry and fractionalization can result in new classification regimes that generalizes Landau's paradigm of symmetry classification. This in fact is one of the main theme of this thesis. Nevertheless, we remind here that a QSL does not necessarily preserve full symmetry and can coexist with magnetic order [137].

1.2.2 Effective description: emergent gauge fields

It has been realized that an effective low-energy theory for QSLs necessarily involves gauge fields. A heuristic argument goes like this: we have just seen that low energy excitations of a QSL are fractionalized, which must be excited in pairs/multiples so that the sum of their quantum numbers makes sense even outside the QSL realm. Effectively, whether these excitations can be viewed as individuals depends on the interaction among them (the fractionalized excitations, and hence the QSL phase, are destroyed if the interaction develops tension). It is therefore essential to study the dynamics of the interaction, or in the language of high energy physics, to study the dynamics of the gauge bosons (they are, after all, the force carrier!). In a larger setting, it is a quite general phenomenon that highly entangled states, such as the fractional quantum Hall effect and the half-filled Landau level, necessitate gauge fields in their effective description. Finally, exactly solvable models that possess highly entangled ground states, such as the toric code model, the Kitaev honeycomb model, and the quantum spin ice model, all can be mapped to a gauge theory. Although a proof for the applicability of gauge theory in highly entangled systems is lacking, it is generally believed to be true. Unlike gauge

bosons in the elementary particle theory, the gauge field in these highly entanglement systems is *emergent*: they are born from the highly entangled ground state, i.e. from the massive superposition of product states.

In this subsection, we provide a formal derivation of how gauge theory appears in a simple AFM Heisenberg model, following Ref. [165, 184]. We hope that this example helps understand the naturalness and prevalence of gauge fields in the theory of QSLs. There are also other exactly solvable spin models in which gauge field can be explicitly derived. These models will be reviewed in Subsection 1.2.3.

Our derivation begins with the attempt of finding the effective theory for the AFM Heisenberg model (1.14) ($J > 0$) in terms of spinons. To start with, consider a representation of $S = 1/2$ spin operators in terms of either Abrikosov fermions $f_{\boldsymbol{r}_\mu}$ or Schwinger bosons $b_{\boldsymbol{r}_\mu}$,

$$\hat{\boldsymbol{S}}_{\boldsymbol{r}_\mu} = \frac{1}{2} a^\dagger_{\boldsymbol{r}_\mu} \boldsymbol{\sigma} a_{\boldsymbol{r}_\mu}, \qquad a_{\boldsymbol{r}_\mu} = \begin{pmatrix} a_{\boldsymbol{r}_\mu,\uparrow} \\ a_{\boldsymbol{r}_\mu,\downarrow} \end{pmatrix}, \quad \text{where } a = f \text{ or } b, \tag{1.19}$$

formally, the bosons b or fermions f—both called *partons*—are mathematical representations of the fractionalized excitations in a spin liquid phase, each carrying a $S = 1/2$ spin. They are introduced to describe the deconfined bosonic or fermionic spinon excitations that are of our interest in the QSL: with the desired fractional spin numbers, the hope is that either the partons, or any linear combinations of them, provide a good description of the spinons. The use of boson or fermion is a matter of choice, which should properly reflect the spinon statistics[17].

---

[17]Both bosonic and fermionic particles can exist in a QSL. In a U(1) spin liquid described by the usual Maxwell theory, the bosonic particles are the electric charges and magnetic monopoles, while a bound

These representations however, are not faithful ones. The partons live in an enlarged Hilbert space at each site $\boldsymbol{r}_\mu$ while the original Hilbert space is recovered under the the constraint

$$a^\dagger_{\boldsymbol{r}_\mu} a_{\boldsymbol{r}_\mu} = 1, \quad a_{\boldsymbol{r}_\mu\uparrow} a_{\boldsymbol{r}_\mu\downarrow} = a^\dagger_{\boldsymbol{r}_\mu\uparrow} a^\dagger_{\boldsymbol{r}_\mu\downarrow} = 0, \quad \text{for} \quad a = b, f. \tag{1.20}$$

As a consequence, the parton description contains redundant information: a local U(1) gauge transformation

$$G: a_{\boldsymbol{r}_\mu} \to e^{i\theta(\boldsymbol{r}_\mu)} a_{\boldsymbol{r}_\mu}, \quad a = b, f, \quad \theta(\boldsymbol{r}_\mu) \in [0, 2\pi) \tag{1.21}$$

leaves $\hat{\boldsymbol{S}}_{\boldsymbol{r}_\mu}$ invariant. In fact, for fermions, such a gauge redundancy can be enlarged to SU(2), which can be seen from the identity

$$\hat{\boldsymbol{S}}_{\boldsymbol{r}_\mu} = \frac{1}{4} \text{Tr}(\Psi^\dagger_{\boldsymbol{r}_\mu} \boldsymbol{\sigma} \Psi_{\boldsymbol{r}_\mu}), \quad \text{with} \quad \Psi_{\boldsymbol{r}_\mu} = \begin{pmatrix} f_{\boldsymbol{r}_\mu,\uparrow} & f^\dagger_{\boldsymbol{r}_\mu,\downarrow} \\ f_{\boldsymbol{r}_\mu,\downarrow} & -f^\dagger_{\boldsymbol{r}_\mu,\uparrow} \end{pmatrix}, \tag{1.22}$$

and from the fact that any site-dependent SU(2) gauge transformation

$$G: \Psi_{\boldsymbol{r}_\mu} \to \Psi_{\boldsymbol{r}_\mu} W(\boldsymbol{r}_\mu), \quad W(\boldsymbol{r}_\mu) \in \text{SU}(2) \tag{1.23}$$

leaves the spins $\hat{\boldsymbol{S}}_{\boldsymbol{r}_\mu}$ invariant.

Any quantity written in terms of the original spin degrees of freedom can be expressed in terms of partons. we illustrate this using the fermions f. The partition function for the AFM Heisenberg model (1.14), in particular, becomes

$$Z = \int D[f, \bar{f}; a] e^{-S[f,\bar{f};a]}, \tag{1.24}$$

state formed out of them—a *dyon*—is fermionic.

22

with

$$S[f, \bar{f}; a] = S[f, \bar{f}] - \sum_i \left\{ a_{0,i}^3 (f_i^\dagger f_i - 1) + \left[(a_{0,i}^1 + i a_{0,i}^2) f_{i\uparrow} f_{i\downarrow} + h.c. \right] \right\}, \qquad (1.25a)$$

$$S[f, \bar{f}] = \int_0^\beta d\tau \, \bar{f}_i \partial_\tau f_i - H[f, \bar{f}], \qquad (1.25b)$$

$$H[f, f^\dagger] = \frac{J}{8} \sum_{\langle i,j \rangle} \sum_{\alpha,\beta=\uparrow,\downarrow} \left(2 f_{i\alpha}^\dagger f_{i\beta} f_{j\beta}^\dagger f_{j\alpha} - f_{i\alpha}^\dagger f_{i\alpha} f_{j\beta}^\dagger f_{j\beta} \right), \qquad (1.25c)$$

where i, j are shorthand notation for $\boldsymbol{r}_\mu, \boldsymbol{r}'_\nu$. The auxiliary fields $a_{0,i}^l$ are introduced to constrain the Hilbert space; they have their own fluctuations.

In order to make progress with the path integral in Eq. (1.25), one must make some approximation. Traditionally, it is assumed that the path integral is dominated by nonzero equal-time expectation values of the following quantities

$$\chi_{ij} = \langle f_i^\dagger f_j \rangle, \qquad \Delta_{ij} = \langle f_{i\uparrow} f_{j\downarrow} \rangle, \qquad a_0^l = \langle a_{0,i}^l \rangle, \qquad (1.26)$$

this is essentially a mean-field treatment, ignoring any time-dependent fluctuations in Δ_{ij}, χ_{ij}, and $a_{0,i}^l$. Note that the mean-field decoupling is by no means unique, and the above decoupling in terms of the spin singlet hopping and pairing channels are the most common ones considered to be compatible with the SU(2) spin symmetry of the Heisenberg model. The time-dependent fluctuations, not considered in a mean-field Hamiltonian, are exactly the *gauge fluctuations*: indeed, parameterizing the phase fluctuations of χ as $e^{i a_{ij}}$, an effective low-energy Lagrangian can be written as

$$L^{(0)} = \sum_i \bar{f}_i (\partial_\tau - a_0) f_i + \frac{3}{8} \sum_{\langle i,j \rangle} \left(J \chi e^{i a_{ij}} \bar{f}_i f_j + h.c. \right) + \text{other terms} \qquad (1.27)$$

in which the phase fluctuation a_{ij} can exactly be viewed as a gauge field. Standard gauge

theory analysis can then be applied to study these fluctuations beyond the mean-field level.

How to determine the actual gauge degree of freedom in a QSL? This is not a trivial question. In a two-dimensional QSL where all the fractional excitations (i.e. matter fields) are gapped, the gauge field cannot be U(1) since such a phase is unstable to confinement [121]. A $\mathbb{Z}_2$ gauge field has gapped excitations and does not show at zero energy of the spectrum. In some models, the gauge type can be determined from the original degree's of freedom; but a larger gauge group is always exposed to the possibility of Higgs transition. In these scenarios, identifying the gauge fields requires both analytical and numerical efforts.

In the next subsection, we introduce two important models—the toric code model and the quantum spin ice model, which are known to host a $\mathbb{Z}_2$ QSL in 2D and a U(1) QSL in 3D respectively. Special focus will be on how a gauge structure emerges and how a QSL–non-QSL transition is characterized by the interplay between the matter fields (i.e. the fractionalized excitations) and the gauge fields.

1.2.3   Case study: toric code, quantum spin ice, and beyond

The toric code model on a square lattice is defined by

$$H_{\text{TC}} = -K_P \sum_p \underbrace{\prod_{i \in p} \sigma_i^z}_{P_p} - K_S \sum_s \underbrace{\prod_{i \in s} \sigma_i^x}_{S_s}, \qquad K_P > 0, K_S > 0, \tag{1.28}$$

where p and s respectively label plaquettes and stars, both consisting of four NN bonds of the square lattice. The Pauli operators σ_i^x and σ_i^z, labeled by index i, live *on these*

bonds.

This model is exactly solvable due to the extensive commutativity among P_p and S_s:

$[P_p, P_{p'}] = [S_s, S_{s'}] = [P_p, S_s] = 0$, for all the plaquettes p, p' and stars s, s'. It is then easy

to see that the ground states of the toric code are any states that satisfy $P_p = S_s = 1$ for

all p and s. It turns out that there are only four such states (assuming periodic boundary

conditions) distinguished by nonlocal parity operators but all are highly entangled state.

The Hamiltonian H_{TC} has a gauge structure $\sigma_i^z \equiv \sigma_{rr'}^z \to \eta_r \sigma_{rr'}^z \eta_{rr'}$ where $\eta = \pm 1$ are $\mathbb{Z}_2$

variables and we denoted the bond i by its endpoints r, r'. In this sense, the toric code

can be mapped to a $\mathbb{Z}_2$ gauge theory.

What are the fractionalized excitations in the toric code? Corresponding to the

two terms in the Hamiltonian, the elementary excitations are a *single plaquette defect*

$P_p = -1$, which we call an m particle, and a *single star defect* $S_s = -1$, which we call

an e particle. Obviously, since the elementary operator σ_i^x (or σ_i^z) always affects two

adjacent plaquettes (or stars), the m particle (or e particle) can be created only in pairs.

Also, perhaps less obviously, e are m are both bosons. The creation of a particle pair (e

or m) has a finite energy cost, however, once the pair is created, each particle can travel

arbitrarily far from the other, without causing extra energy. This is a concrete realization

of the fractionalized spinon excitations[18] we depicted in Subsection 1.2.1.

A transition out of the $\mathbb{Z}_2$ QSL phase can happen by reducing the excitation energy

of, say, the m particle to zero.[19] The bosonic m particle condenses, and the field lines

---

[18]Due to the duality between e and m, either can be viewed as the spinons.

[19]Physically, reducing the excitation of energy of the m particle can be achieved with the term $h_x \sum_i \sigma_i^x$, with a finite value of h_x. A similar story happens for the e particle as well, in which case a

emanating from them (represented by strings of σ^z operators) fluctuate wildly. This completely pins down the value of the σ^x fields, meaning the ground state is a simple product state of σ_i^x for all i, and consequently the e particles are confined since the energy of separating a pair of e particles scales with the separation.[20]

The toric code is a concrete realization of $\mathbb{Z}_2$ gauge theory, often also called $\mathbb{Z}_2$ *topological order*. We mentioned briefly that another model, the Kitaev's honeycomb model[21], lies in the same category for some choice of exchange parameters, but otherwise realizes a *gapless* $\mathbb{Z}_2$ QSL, which can be regarded as a $\mathbb{Z}_2$ gauge theory with gapless matter. Kitaev's honeycomb model is, in some sense, a more realistic model as compared to the toric code, and the materialization is a hot topic in current research, see Ref. [62] for a review.

The pyrochlore lattice consists of an FCC lattice of a pair of corner-sharing tetrahedra as unit cells. The lattice and symmetry information is detailed in Appendix A.1. We consider the XXZ model on pyrochlore:

$$H = \sum_{\langle i,j \rangle} J_z S_i^z S_j^z + J_\perp (S_i^x S_j^x + S_i^y S_j^y), \qquad (1.29)$$

here the z direction of the spin is not a global one; rather, the local direction of $S_i^z = 1/2$ is defined by the vector that points from site i to the center of the "down" tetrahedron that contains site i. In the pure Ising limit, $J_\perp = 0$, the Hamiltonian H is a classical

---

term $h_z \sum_i \sigma_i^z$ needs to be added with finite h_z.

[20]What we left unmentioned is the nontrivial mutual statistics between e and m: spatially exchanging them produces a π phase change in the wave function. This provides another viewpoint on the confinement of e: since the ground state is a superposition of different m states, the mutual statistics of e and m forbids e to propagate coherently.

[21]We refer the readers to Kitaev's original paper [78] which explains the model in detail. But the paper contains much more beyond!

one with commuting spins S_z. The ground state is any configuration that satisfies the "two-in two-out" rule, with two $S^z = 1/2$ and two $S^z = -1/2$ spins on each "down" tetrahedron. In fact, this Ising model describes the physics of classical electromagnetism. The two-in two-out rule resembles the geometrical organization of water ice, and is named the *classical spin ice*.

The massively degenerate classical ground states hinted at a potential quantum spin liquid state. In the following, we switch on the $J_\perp$ term and focus on the strong Ising AFM limit, $J_z \gg J_\perp > 0$. Perturbation theory gives an effective Hamiltonian

$$H_{\text{ring}} = -\frac{K}{2} \sum_{\hexagon_p} (S_1^+ S_2^- S_3^+ S_4^- S_5^+ S_6^- + \text{H.c.}),\tag{1.30}$$

where $K \sim J_\perp^3/J_z^2$, $S_i^\pm = S_i^x \pm i S_i^y$, and we used $\hexagon_p$ to denote an elementary hexagon ring with neighboring sites $i = 1, 2, ..., 6$. The local symmetry is generated by simultaneously rotation all the four spins in tetrahedron t along their respective z axis by the same amount α: $G_t(\alpha) = \exp(i\alpha \sum_{i \in t} S_i^z)$, where α is a U(1) angle.

By introducing a pair of lattice gauge fields—the electric field $E_{rr'} = S_i^z + 1/2$ and the vector gauge potential $e^{\pm iA_{rr'}} = S_i^\pm$—that live on the dual diamond bonds rr' (whose midpoint is the pyrochlore site i), it can be shown that $[E_{rr'}, A_{rr'}] = i$, and the Hamiltonian H_{ring} can be mapped to a gauge theory model

$$H = -K \sum_{\hexagon_d} \cos(\text{curl}A) + \frac{U}{2} \sum_{rr'} \left(E_{rr'} - \frac{\epsilon_r}{2} \right)^2,\tag{1.31}$$

where $\epsilon_r = \pm 1$ for r being the center of the up or down tetrahedron. Since the gauge field A is an angular variable, this is a *compact* U(1) lattice gauge theory. A compact U(1) theory differs from a non-compact U(1) theory by the existence of magnetic monopoles—

the m particles. Whether the difference matters is to ask, equivalently, whether it is legitimate to expand the cosine. Whenever this expansion is valid, the cosine term simply gives the magnetic energy B^2, and the Hamiltonian realizes a *deconfined phase*[22]: an *emergent* Maxwell theory of electromagnetism, with gapless (emergent) photon modes.

We then look at the excitations. As in the $\mathbb{Z}_2$ QSL case, we have the e and m particles; the former is really nothing but an *emergent* electric charge (only assumed to be bosonic for now), while the latter, monopoles, are the topological defect of a compact U(1). In the deconfined phase, m is gapped. Once becoming gapless, the monopoles m drives a confinement transition out of the deconfined QSL phase and the resulting state is some short-range entangled, product-like state. On the other hand, the bosonic e particle, when become gapless, can drive a Higgs transition, which does not necessarily terminate the QSL; for example, a two-charge condensate is a "partial" Higgs transition and can give rise to a $\mathbb{Z}_2$ QSL.

In the analysis of U(1) quantum spin ice above we assumed that e and m particles are both bosons. This is not necessarily the case. In Ref. [159] and later in [187, 113], all possible statistics and symmetry classes of e and m in a three-dimensional QSL are obtained assuming various global symmetries. The major assumption of these works is that both e and m are gapped excitations. This excludes a large class of U(1) QSL with gapless spinon excitations on the pyrochlore lattice, which we will discuss in Chapter 5.

---

[22]Also known as the Coulomb phase. We remind the reader that such a phase is unstable in 2D unless in presence of gapless matter fields.

1.2.4 Projective symmetry group

While the intactness of symmetries should not be regarded as a defining property of QSL states, symmetry does have important effects for QSLs. Upon imposing symmetries, a spin liquid phase may split (or "fractionalize") into several distinct phases that all preserve the symmetry action. The phases are distinguished by the distinct quantum numbers carried by the fractionalized excitations under the symmetry action. These spin liquids phases are called symmetric spin liquids, and the corresponding symmetries form a *projective symmetry group* (PSG). The classification of symmetric spin liquids can be viewed as a symmetry analysis of the PSG acting on fractionalized excitations (in our case, the bosonic or fermionic spinons). The purpose of this section is to describe the procedures for this classification. Later in Chapters 4 and 5 we will use the framework developed here to classify symmetric $\mathbb{Z}_2$ and U(1) spin liquids on the pyrochlore lattice.

To start with, one expresses spins in terms of Schwinger bosons or Abrikosov fermions introduced in Eq. (1.19). At the mean-field level, they are governed by a quadratic Hamiltonian, commonly known as the mean-field ansatz. As we mentioned, the enlargement of the parton Hilbert space and the gauge redundancy must be properly treated to validate the parton description.

The PSG method is a way to resolve this redundancy in the parton description of a spin liquid with full lattice symmetries (the symmetric spin liquid). The crucial step is to realize that physical symmetries act *projectively* on the parton operators, and that seemingly different parton Hamiltonians describe the same physics if they are related

by gauge transformations. Conversely, if two parton Hamiltonians cannot be related by gauge transformations, they must carry different projective representations of the physical symmetry—this suggests that the classification of projective symmetry corresponds classification of symmetric spin liquids. We now formulate this statement in a more concrete way. Consider a spin–orbit coupled spin system on some lattice. Under a space group operation $\mathcal{O}$ the spins transform as in Eq. (1.11). According to Eq. (1.22), we naïvely expect that the partons transform as

$$\mathcal{O} \colon \Psi_{\boldsymbol{r}_\mu} \to U_{\mathcal{O}}^\dagger \Psi_{\mathcal{O}(\boldsymbol{r}_\mu)}. \tag{1.32}$$

However, due to the SU(2) gauge redundancy, any operation $\mathcal{O}$ can be accompanied by a site-dependent SU(2) gauge transformation of the form in Eq. (1.23). The partons thus transform projectively as

$$\widetilde{\mathcal{O}} = G_\mathcal{O} \circ \mathcal{O} \colon \quad \begin{aligned} b_{\boldsymbol{r}_\mu} &\to U_\mathcal{O}^\dagger b_{O(\boldsymbol{r}_\mu)} e^{i\phi_\mathcal{O}[\mathcal{O}(\boldsymbol{r}_\mu)]}, \\ \Psi_{\boldsymbol{r}_\mu} &\to U_\mathcal{O}^\dagger \Psi_{O(\boldsymbol{r}_\mu)} W_\mathcal{O}[\mathcal{O}(\boldsymbol{r}_\mu)], \end{aligned} \tag{1.33}$$

where the symbol "∘" indicates that the projective operation $\widetilde{\mathcal{O}}$ is the composition of the physical symmetry operation $\mathcal{O}$ and the gauge transformation $G_\mathcal{O}$. Due to the notational similarity, we shall use the fermion notation in the second line to denote also the boson notation in the first line, as long as no confusion is caused.

The projective symmetry can be extended to include internal symmetries, and here we consider time reversal operation $\mathcal{T}$ as an example. The spins transform under $\mathcal{T}$ as $\hat{\boldsymbol{S}}_{\boldsymbol{r}_\mu} \xrightarrow{\mathcal{T}} \mathcal{K}^\dagger U_\mathcal{T} \hat{\boldsymbol{S}}_{\boldsymbol{r}_\mu} U_\mathcal{T}^\dagger \mathcal{K}$, where $U_\mathcal{T} = i\sigma^2$, and $\mathcal{K} = \mathcal{K}^\dagger = \mathcal{K}^{-1}$ applies complex conjugation to everything on its right. For group relations involving time reversal, special care must

30

be taken due to the presence of the complex conjugation $\mathcal{K}$. The bosonic spinons are found to transform as

$$\widetilde{\mathcal{T}} = G_{\mathcal{T}} \circ \mathcal{T}: b_{\boldsymbol{r}_\mu} \rightarrow e^{i\phi_{\mathcal{T}}(\boldsymbol{r}_\mu)} \mathcal{K} U_{\mathcal{T}}^\dagger b_{\boldsymbol{r}_\mu}. \tag{1.34}$$

Note that $[\mathcal{K}, U_{\mathcal{T}}] = 0$ because $U_{\mathcal{T}}$ is real.

For Abrikosov fermions, however, using the special property of the SU(2) algebra, one can design the projective action of $\mathcal{T}$ on Ψ to be unitary (see App. A.8 for detailed derivation):

$$\widetilde{\mathcal{T}} = G_{\mathcal{T}} \circ \mathcal{T}: \Psi_{\boldsymbol{r}_\mu} \rightarrow U_{\mathcal{T}} \Psi_{\boldsymbol{r}_\mu} W_{\mathcal{T}}(\boldsymbol{r}_\mu), \tag{1.35}$$

Note that this does not modify the anti-unitary nature of time reversal symmetry.

For a symmetric spin liquid, the projective operations $\widetilde{\mathcal{O}}$ and $\widetilde{\mathcal{T}}$ generate the symmetry group of the parton Hamiltonian, commonly known as the projective symmetry group. The classification of symmetric spin liquids amounts to the classification of PSGs. To achieve this, one needs to find all the gauge-inequivalent solutions for the gauge transformations $G_{\mathcal{O}}$ and $G_{\mathcal{T}}$ that are consistent with the symmetry group of the system. Any group relation of Eq. (A.4) can be written in the general form of

$$\mathcal{O}_1 \circ \mathcal{O}_2 \circ \cdots = 1, \tag{1.36}$$

we consider the gauge-enriched group relation

$$\widetilde{\mathcal{O}}_1 \circ \widetilde{\mathcal{O}}_2 \circ \cdots = (G_{\mathcal{O}_1} \circ \mathcal{O}_1) \circ (G_{\mathcal{O}_2} \circ \mathcal{O}_2) \circ \cdots = \mathcal{G}, \tag{1.37}$$

where $\mathcal{G}$ is a pure gauge transformation and corresponds to the identity operation for the spins. We say that $\mathcal{G}$ is an element of the invariant gauge group (IGG), the group of all pure gauge transformations that leave the parton Hamiltonian invariant. The IGG

31

transformation on each site is a subgroup of SU(2), typically $\mathbb{Z}_2$ or U(1). In most cases, there exists a gauge choice (the canonical gauge [165]) in which the IGG transformation can be made "global" of the form $\mathcal{G} = e^{i\sigma^3\chi}$ with a constant χ. In this thesis, we will be classifying both $\mathbb{Z}_2$ and U(1) spin liquids, therefore we consider both IGG $= \mathbb{Z}_2$ and U(1), for which $\chi = \{0, \pi\}$ and $\chi \in [0, 2\pi)$, respectively.

Making use of the general conjugation rule

$$\mathcal{O}_i \circ G_{\mathcal{O}_j} \circ \mathcal{O}_i^{-1} \colon \Psi_{\boldsymbol{r}_\mu} \to \Psi_{\boldsymbol{r}_\mu} W_{\mathcal{O}_j}[\mathcal{O}_i^{-1}(\boldsymbol{r}_\mu)], \tag{1.38}$$

which follows directly from Eqs. (1.32) and (1.33), Eq. (1.37) can be rewritten as

$$G_{\mathcal{O}_1} \circ (\mathcal{O}_1 \circ G_{\mathcal{O}_2} \circ \mathcal{O}_1^{-1}) \circ (\mathcal{O}_1 \circ \mathcal{O}_2 \circ G_{\mathcal{O}_3} \circ \mathcal{O}_2^{-1} \circ \mathcal{O}_1^{-1}) \circ \cdots = \mathcal{G}, \tag{1.39}$$

which then becomes a matrix equation:

$$W_{\mathcal{O}_1}(\boldsymbol{r}_\mu) W_{\mathcal{O}_2}[\mathcal{O}_1^{-1}(\boldsymbol{r}_\mu)] W_{\mathcal{O}_3}\{\mathcal{O}_2^{-1}[\mathcal{O}_1^{-1}(\boldsymbol{r}_\mu)]\} \cdots = \mathcal{G}, \tag{1.40}$$

this reduces to, for the bosons, a phase equation

$$\phi_{\mathcal{O}_1}(\boldsymbol{r}_\mu) + \phi_{\mathcal{O}_2}[\mathcal{O}_1^{-1}(\boldsymbol{r}_\mu)] + \phi_{\mathcal{O}_3}\{\mathcal{O}_2^{-1}[\mathcal{O}_1^{-1}(\boldsymbol{r}_\mu)]\} + \cdots = n\pi \mod 2\pi. \tag{1.41}$$

The PSG classification is obtained by listing all group relations and finding all solutions to the corresponding matrix equation (1.40) (or phase equation (1.41)). We emphasize that solutions must be discriminated by the principle of gauge equivalence, rather than resemblance. Indeed, by means of a general gauge transformation G as in Eq. (1.23), the gauge-enriched group relations in Eq. (1.37) can be rewritten as

$$(G \circ G_{\mathcal{O}_1} \circ \mathcal{O}_1 \circ G^{-1}) \circ (G \circ G_{\mathcal{O}_2} \circ \mathcal{O}_2 \circ G^{-1}) \circ \cdots = \mathcal{G}, \tag{1.42}$$

which transforms $W_{\mathcal{O}_i}(\boldsymbol{r}_\mu)$ according to

$$W_{\mathcal{O}_i}(\boldsymbol{r}_\mu) \to W(\boldsymbol{r}_\mu)W_{\mathcal{O}_i}(\boldsymbol{r}_\mu)W^{-1}[\mathcal{O}_i^{-1}(\boldsymbol{r}_\mu)]. \tag{1.43}$$

This indicates that two seemingly distinct solutions to the PSG equations can in fact be equivalent.

1.3 Experimental probes for magnetic materials

1.3.1 Specific heat, magnetization, and susceptibility

To diagnose spin liquid physics in a candidate material, thermodynamic properties are usually measured first since they are easy to carry out in a laboratory. The first goal would be to establish the absence of magnetic ordering at low temperature. A simple measure is the frustration parameter $f = |\Theta_{\mathrm{CW}}|/T_f$. Here Θ_{CW} is the *Curie–Weiss temperature* obtained from a fit to the high-temperature susceptibility χ. In an insulating magnet that is our focus here, the susceptibility obeys the Curie–Weiss form

$$\chi = \chi_0 + \frac{C}{T + \Theta_{\mathrm{CW}}}, \tag{1.44}$$

where χ_0 is a temperature-independent term that mostly receives contribution from the *Van Vleck* susceptibility resulted from the field-induced admixture of the higher-lying levels of the multiplet. In the second term, C is the *Curie constant*, which does not contain much information about the exchange interaction and is only a reflection of the size of the magnetic moment. The information about exchange interaction is hidden in

the Curie–Weiss temperature Θ_{CW}: in a mean-field type calculation, we have

$$\Theta_{\mathrm{CW}} = \mathrm{Const.}\, \mathcal{J}\, C, \tag{1.45}$$

where $\mathcal{J}$ is the exchange interaction[23]. Then a positive (negative) Θ_{CW} corresponds to antiferromagnetic (ferromagnetic) exchanges. The second quantity, T_f, usually is the actually ordering temperature which is determined from any nonanalytic behavior (such as divergence, cusp, etc.) in a $\chi - T$ plot. The temperature range $\Theta_{\mathrm{CW}} \gg T > T_f$ defines a *cooperative paramagnetic regime* in which the frustration effect overwhelms and is a natural place to look for a QSL.

The magnetization M is another simple measurement and contains roughly the same amount of information as the susceptibility χ.[24] In a mean-field-type calculation, M as a function of temperature T and external field H can be written as

$$m - \chi_0 H = gJB_J(x), \qquad x = J\left(g\mu_B H - \mathcal{J}(m - \chi_0 H)\right), \tag{1.46}$$

where $B_J(x)$ is the Brillouin function which reduces to the familiar hyperbolic tangent $B(x) = \tanh x$ for $J = 1/2$. The g-factor describes the response to an external magnetic field. Here we assumed g to be a scalar, but its general form in the Hamiltonian is a tensor

$$H_{\mathrm{Zeeman}} = -\mu_B H^\mu \sum_i g_i^{\mu\nu} S_i^\nu, \tag{1.47}$$

and the tensor structure can be obtained from symmetry principle.

The magnetization and susceptibility measurement both contain single ion contribu-

---

[23]We use a calligraphic $\mathcal{J}$ to distinguish it from the angular momentum number J. $\mathcal{J}$ is also called the Weiss molecular field constant, and the mean-field theory is also called the Weiss molecular theory.
[24]Formally the magnetization M is the first derivative of free energy F with respect to external field H: $M = -\frac{\partial F}{\partial H}$, whereas magnetic susceptibility χ is the second derivative $\chi(T) = -\frac{1}{V}\frac{\partial^2 F}{\partial H^2}$.

tions at the zeroth order, and sometimes it is quite hard to separate the correlation (i.e. exchange) effects from these quantities.

The measurement which requires interaction between spins to interpret is the low temperature, zero-field specific heat. Underlying this is the assumption that other contributions such as phonons, nucleus, do not contribute at the temperature measured, an assumption that must be justified. The phonon contribution to specific heat is easy to determine in both experiment and theory—experimentally one usually fabricate the nonmagnetic analogue of the magnetic compound (for rare-earth materials, for example, replace the magnetic element with the nonmagnetic element lutetium), and subtract the specific heat curve $C_p - T$ of the nonmagnetic twin from that of the magnetic compound. Assuming the remaining contribution comes purely from magnetic moment, one compares the residual curve with the high-temperature expansion result for the specific heat

$$C_p \sim \frac{C_0}{T^2}, \tag{1.48}$$

where $C_0 = \frac{1}{k_B} \mathrm{Tr}[H^2] \propto \mathcal{J}^2$. This suggests that the magnetic contribution to high temperature heat capacity is pure interaction effect.

The in-field magnetic heat capacity, however, contains single-ion effect. At high field, low temperature heat capacity for a $J_{\mathrm{eff}} = 1/2$ system takes the Schottky form

$$C_{\mathrm{Schottky}} = n \frac{\Delta^2}{T^2} \frac{e^{\Delta/T}}{(1 + e^{\Delta/T})^2}, \tag{1.49}$$

which describes the heat capacity of a two-level system with energy gap the Zeeman gap $\Delta = 2\mu_B g J B$.

So far we have seen that the interaction effect is hidden in the Curie–Weiss temper-

ature obtained from susceptibility measurement, as well as the constant in the magnetic high temperature heat capacity. It is quite common that the exchange effect extracted from these two approaches show variances since in either approach many other factors can influence the result. For example, at high enough temperature, the heat capacity will surely include contributions from crystal field excitations.

In summary, one usually compare the high-temperature thermodynamic response result with a high-temperature expansion of a putative spin Hamiltonian determined from symmetry principles in order to make connection between the macroscopic measurements and microscopic descriptions. For system whose spin Hamiltonian and g-factor are of a simple enough form this can often give us a lot of information. However, it is inevitable that high-temperature expansion include many other unwanted contributions that blur this analysis. A major complement to these experiments are spectroscopic measurements, which we introduce below.

1.3.2 Spectroscopy

Inelastic neutron scattering is the process during which the neutron scatters off the material with a spin flip. The inelastic neutron scattering cross-section can be theoretically derived

$$\frac{d\sigma}{d\Omega dE} \propto F(q) \left(\delta_{\alpha\beta} - \frac{q^\alpha q^\beta}{q^2} \right) \sum_{\boldsymbol{r}_\mu, \boldsymbol{r}'_\nu} e^{i\boldsymbol{q}\cdot(\boldsymbol{r}_\mu - \boldsymbol{r}'_\nu)} \int dt dt' e^{-i\omega(t-t')} \langle S^\alpha_{\boldsymbol{r}_\mu}(t) S^\beta_{\boldsymbol{r}'_\nu}(t') \rangle. \qquad (1.50)$$

If the material is magnetically ordered, the scattering is primarily a two-body neutron–magnon scattering, with definite energy–momentum transfer between them. In a QSL, the scattering is a three-body (or multibody) scattering between neutron and a pair (or multiple) of spinons. Assume the spinons have momenta $\boldsymbol{k}_1$ and $\boldsymbol{k}_2$, a smooth signal is produced at each momentum transfer $\boldsymbol{q}$, where the intensity is spread out over a continuum of frequencies ω, only constrained by the momentum sum $\boldsymbol{k}_1 + \boldsymbol{k}_2 = \boldsymbol{q}$. The high energy neutron scattering can be used to measure crystal field excitations.

While the existence of a broad continuum in the inelastic neutron scattering is a good indication of a QSL phase, it is not sufficient to claim the observation of fractionalized spinon excitations from it alone. First of all, a multi-magnon excitation is always a possibility. Second, a quasiparticle description of the low energy excitations may not exist at all. In short, inelastic neutron scattering is a powerful tool to diagnose spin liquid physics, but in most case it does not qualify as a smoking-gun measurement for the QSL phase.

In addition to neutron scattering measurements, the resonant inelastic x-ray scattering have been increasingly applied as a probe of magnetism. The technique typically detects small changes in a resonant atomic transition, and consequently the energy resolution is limited as far as current experiments (a few tens of meV, as compared to $\sim 0.1\,\mathrm{meV}$ in for neutrons) are concerned. However this is an active and rapidly changing experimental field, where capabilities have witnessed major improvement in the past years. Compared to neutron scattering, x-ray scattering has the advantage of being able

to treat samples with much smaller sizes while maintaining good momentum resolution. However, x-ray resonant processes is much more complicated than neutrons (see the equivalence of Eq. (1.50) in Ref. [141]) and can involve other types of excitations. This can blur the information about the magnetism in the material.

There are still other powerful probes which we mention briefly. The nuclear magnetic resonance (NMR) probe the local magnetic fields of the spin degrees of freedom via the hyperfine interaction with nuclear levels. The relaxation time $1/T_1$ measures the local magnetic susceptibility (in the zero-frequency limit) which is related to the magnetic density of states. Alternatively, the local magnetic fields is measured in muon spin resonance (μSR) experiments, which can distinguish and is highly sensitive to static moments (which suggest the existence of conventional long range order) and dynamical moments of spin liquids. For other probes, we refer the readers to the superb review [138].

1.4 Outline of the thesis

1.4.1 Theoretical and experimental study of the frustrated triangular lattice antiferromagnet NaYbO$_2$

In chapter 2, we investigate NaYbO$_2$, which hosts an ideal triangular lattice of effective $J_{\text{eff}} = 1/2$ moments with no inherent site disorder. No signatures of conventional magnetic order appear down to $50\,\text{mK}$, strongly suggesting a quantum spin liquid ground

state. We observe a two-peak specific heat and a nearly quadratic temperature dependence, in agreement with expectations for a two-dimensional (2D) Dirac spin liquid. Application of a magnetic field strongly perturbs the quantum disordered ground state and induces a clear transition into a collinear ordered state, consistent with a long-predicted up–up–down structure for a triangular-lattice XXZ Hamiltonian driven by quantum fluctuations. The observation of spin liquid signatures in zero field and quantum-induced ordering in intermediate fields in the same compound demonstrates an intrinsically quantum disordered ground state. We conclude that $NaYbO_2$ is a model, versatile platform for exploring spin liquid physics with full tunability of field and temperature.

Using the symmetry of the delafossite lattice we determine the symmetry-allowed exchange interactions on the nearest-neighbor in-plane and inter-layer bonds. Restricting to the in-plane Hamiltonian, we study all the possible three-sublattice magnetic orders consistent with the observed order in $NaYbO_2$, both with and without a magnetic field. We then consider the perturbative effect of couplings between the layers. We find that the presence of a high degree of degeneracy even once the inter-layer spin–orbit interactions have been included indicates that the interlayer coupling of the three-sublattice order is frustrated even with the most general exchange interactions. This suggests a strong suppression of ordering when the 2D exchanges are in this regime, in zero magnetic field. Finally, we present the simulation result for the dynamic spin structure factor using linear spin wave theory.

1.4.2 LiYbO$_2$ and Heisenberg model on a stretched diamond lattice

Chapter 3 presents an investigation of an alternative, frustrated diamond lattice framework in the material LiYbO$_2$. This material can be viewed as containing a stretched diamond lattice of Yb^{3+} moments, and it falls within a broader family of ALnX_2 (A = alkali, Ln = lanthanide, X = chalcogenide) materials where the lattice structure is dictated by the ratio of lanthanide ion radius to alkali plus chalcogenide radii. Results from magnetization, susceptibility, heat capacity, and neutron scattering reveals a rich magnetic phase diagram of LiYbO$_2$: Long-range incommensurate spiral magnetic order of $\boldsymbol{k} = (0.384, \pm 0.384, 0)$ forms in the ground state, which seemingly manifests through a two-step ordering process via a partially ordered intermediate state. Upon applying an external magnetic field, magnetic order becomes commensurate with the lattice with $\boldsymbol{k} = (1/3, \pm 1/3, 0)$ through a "lock-in" phase transition. Remarkably, the majority of this behavior in LiYbO$_2$ can be captured in the Heisenberg $J_1 - J_2$ limit where the magnetic Yb^{3+} ions are split into two interpenetrating A-B sublattices. This model was explicitly derived and tuned for LiYbO$_2$, and it is directly related to a physical elongation of the diamond lattice Heisenberg $J_1 - J_2$ model. Notably, however, variance between the observed and predicted phasing of Yb moments on the bipartite lattice as well as the emergence of an intermediate, partially disordered state suggests the presence of interactions/fluctuation effects not captured in the classical $J_1 - J_2$ Heisenberg framework. We finally model the observed "lock-in" transition energetically from a sym-

metry point of view and show that increasing the magnetic field will inevitably induce an incommensurate-to-commensurate transition. Exploring the nature of the intermediate ordered state is promising future steps in single-crystal studies.

1.4.3 Pyrochlore I: competing orders from $\mathbb{Z}_2$ spin liquid perspective

Chapter 4 combines the two threads mentioned above—magnetic order and QSL physics— by utilizing the connection of symmetry to emergent gauge structure described by the PSG. The embedding of the physical symmetries into the PSG can then lead to a unification of distinct symmetry-breaking orders that are unrelated in classical physics. Such a unified description of seemingly unrelated magnetic orders is the main motivation behind this study. Generally, a QSL state can be connected to magnetically ordered states by considering the condensation patterns that emerge when the energy of a bosonic QSL excitation is brought to zero.

We first employ the PSG method for *Schwinger bosons* to obtain a full classification of QSLs with $\mathbb{Z}_2$ gauge structure on the pyrochlore lattice. While standard parton constructions also allow U(1) and SU(2) gauge structures, we consider the $\mathbb{Z}_2$ gauge structure due to its simplicity (gauge field is gapped and does not enter the low energy sector) and richness (a single U(1) PSG class can be further split into several $\mathbb{Z}_2$ PSG classes upon lowering the gauge symmetry from U(1) to $\mathbb{Z}_2$). We use Schwinger bosons rather than Abrikosov fermions (which will be considered in Chapter 5) to immediately obtain

a bosonic excitation, the elementary Schwinger boson itself, that can condense at the phase transition point out of the QSL.

As a result of our PSG analysis, we find 16 different $\mathbb{Z}_2$ QSLs on the pyrochlore lattice. We use a standard mean-field description to study the 0-flux QSLs, in which translation symmetry acts linearly (i.e., as in classical physics) on the Schwinger bosons. The PSG method also allows us to describe phase transitions from these QSLs to magnetically ordered phases. Condensing the Schwinger bosons, we identify 15 different ordering patterns, and call them "paraphases", since each of them actually unifies several distinct symmetry-breaking orders. We find that, generically, these orders are intertwined, necessarily appearing together at the phase transition out of the QSL, and that conventional spin orders are in many cases accompanied by inversion-breaking "hidden" orders.

The phase transitions corresponding to these 15 paraphases fall into two dynamical classes of $z = 1$ and $z = 2$ quantum criticality, exhibiting critical modes with linear and quadratic dispersions, respectively. We uncover the mathematical structure discriminating between these two classes, related to Hamiltonian diagonalizability, and derive their effective field theories, along with their most important experimental signatures. In particular, we use mean-field theory to compute static and dynamic spin structure factors for each of the 15 paraphases. Finally, by comparing the magnetic orders associated with each paraphase to those observed in experiments, we identify a set of likely QSL phases that might be relevant to real-world pyrochlore materials.

1.4.4 Pyrochlore II: classification of $U(1)$ and $\mathbb{Z}_2$ spin liquid and nodal line spin liquid

As a more in-depth study of symmetry fractionalizations on the pyrochlore lattice, in Chapter 5 we apply the PSG method for *Abrikosov fermions* to give a complete classification of symmetric QSLs on the pyrochlore lattice with either $\mathbb{Z}_2$ or $U(1)$ gauge type. For each gauge type, we first consider only space group symmetry, and later add time reversal symmetry. We consider generic cases where we allow spin–orbit coupling in the underlying spin system and do not require $SU(2)$ spin rotation symmetry. By following the general PSG principle to solve the gauge–symmetry consistency equations, we find that there can be at most 18 and 28 symmetric quantum spin liquids preserving the pyrochlore PSG for the $U(1)$ and $\mathbb{Z}_2$ gauge types, respectively. When time-reversal symmetry is imposed, the number of possible symmetric spin liquids is reduced to 16 for the $U(1)$ type and is increased to 48 for the $\mathbb{Z}_2$ type. For each class, the most general symmetry-allowed spinon mean-field Hamiltonian is given. Importantly, we find that a large family of spinon Hamiltonians possesses gapless nodal lines along the four equivalent (111) directions of the Brillouin zone. We call this unusual nodal structure a "nodal star" and show that it is stable at the mean-field level as it is protected by the projective threefold rotation and screw symmetries of the system. We then go beyond the mean-field level and consider a full-fledged low energy theory of the spinon nodal star coupled to a $U(1)$ gauge field. Specifically, we obtain thermodynamic properties of the system by computing the photon contribution to the free energy. We find that the two most

dominant low temperature contributions to the specific heat are $C \sim T^{3/2}$ from the bare spinons and $C \sim T^{3/2}/\ln T$ from the photon–spinon interactions. This scaling of the low temperature specific heat may serve as a clear evidence for the experimental discovery of a nodal star U(1) QSL.

Chapter 2

Frustrated triangular lattice antiferromagnet in delafossites: application to NaYbO$_2$

2.1 Introduction

The triangular lattice antiferromagnet is a long-studied archetype of geometrically-driven magnetic frustration that has been widely explored both theoretically and experimentally. While the ideal Heisenberg antiferromagnet develops three-sublattice 120° order, perturbing away from this limit realizes a rich phase space including QSL phases [110, 13]. Early studies of triangular QSL candidates mainly focused on organic materials. It was only found recently that several classes of rare earth oxides have model planes of equilat-

eral triangles of $4f$ moments form in a high symmetry setting. The archetypal material in this class is $YbMgGaO_4$, originally proposed as a quantum spin liquid (QSL) candidate due its lack of long-range magnetic order and the observation of a low-temperature continuum of magnetic excitations [89, 88, 91, 92, 118]. However, chemical disorder in $YbMgGaO_4$, endemic to the mixed occupancies of Mg and Ga atoms on the same crystallographic site, has clouded interpretation [93, 92, 91, 146, 170, 118, 90, 89, 88], and several other possibilities were suggested in place of a spin liquid state [185, 76, 101].

The rare earth moments in compounds of the form $NaRO_2$ (R=rare earth ions) are known to form an ideal triangular lattice in the α-$NaFeO_2$ ($R\bar{3}m$) structure. Previous studies suggest that they realize a large degree of magnetic frustration [59, 96, 3], and $NaYbO_2$ in particular stands out as an appealing candidate material. Specifically, the $NaYbO_2$ lattice promotes enhanced exchange through short nearest neighbor bonds, where the Yb moments occupy high-symmetry sites that forbid Dzyaloshinskii-Moriya interactions. This combined with large crystal field splitting between the ground state and first excited doublet [118, 90] render this lattice an appealing framework.

We start by presenting experimental result of $NaYbO_2$. Zero field susceptibility data collected down to $50\,mK$ reveal no signatures of spin freezing or glassiness, and heat capacity data collected over the same temperature range reveal only a broad two-peak structure–a common signature of the onset of short-range correlations in materials thought to host quantum disordered ground states [180, 31, 111, 45]. This disordered state is strongly perturbed via the application of a magnetic field that, under modest

fields ($H \approx 3\,\text{T} - 5$ T), induces antiferromagnetic order consistent with an up-up-down plateau state for the triangular lattice.

We then proceed to the theoretical modeling and understanding of the experimental results via a classical in-field magnetic order analysis and spin wave theory. We show that the disordered state and the *up-up-down* order at intermediate fields reflect an underlying XXZ Hamiltonian with enhanced fluctuations due to interlayer frustration. We examine the detailed field dependence of low-energy continuum of scattering about the $\boldsymbol{Q} = (1/3, 1/3, 0)$ two-dimensional antiferromagnetic ordering zone center. Our spin-wave calculations qualitatively capture the field evolution of dynamics endemic to the *up-up-down* phase, an anomalous band of excitations above the single-magnon cutoff is identified in the ordered state.

2.2 Main results

Polycrystalline $NaYbO_2$ was synthesized and characterized via neutron powder diffraction measurements. Figure 2.1(a) shows the structure at $1.6\,\text{K}$, revealing that the structure retains its $R\bar{3}m$ symmetry with fully occupied Na and O sites. The local $D_{3\text{d}}$ distorted YbO_6 octahedra and bond lengths are illustrated, and a similar YbO_6 environment in $YbMgGaO_4$ is known to generate a large $38\,\text{meV}$ splitting between the first excited state and the ground state doublet [118, 90]. At low temperatures, the ground state therefore behaves as an isolated $J_{\text{eff}} = 1/2$ Kramers doublet. Nearest-neighbor Yb-Yb distances were refined to $3.3507(1)\,\text{Å}$ at $300\,\text{K}$, consistent with previous reports [59, 96, 3], and
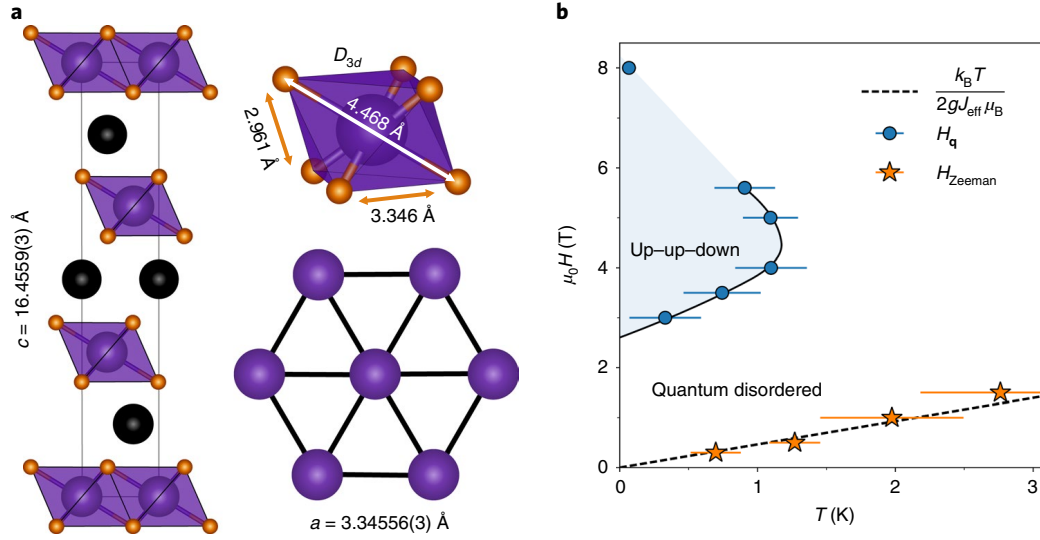
Figure 2.1: Crystal structure and magnetic (H, T) phase diagram of $NaYbO_2$. (a), Refined $NaYbO_2$ structure ($1.6\,K$, $R\bar{3}m$) contains equilateral triangular layers of D_{3d} YbO_6 distorted octahedra separated by $3.346\,Å$. Sodium cations refine to full occupation, creating a uniform chemical environment surrounding the triangular layers. Purple spheres, Yb atoms; black spheres, Na atoms; brown spheres, O atoms. (b), Low-temperature phase boundary between quantum disordered and antiferromagnetic ordered states in $NaYbO_2$, plotted as a function of field and temperature, extracted from a.c. susceptibility and neutron-scattering experiments. The dashed line denotes the boundary of Zeeman-driven quenching of a minority fraction of free Yb moments under field, above which free moments are quenched. These free moments coexist with a quantum disordered ground state. Values in parentheses and error bars indicate one standard deviation. k_B is the Boltzmann constant, H_q denotes the onset temperature of the up–up–down ordered state and H_{Zeeman} denotes the suppression in magnetic susceptibility observed due to the quenching of a small fraction of free Yb moments.

naively support enhanced exchange relative to other frustrated Yb-based compounds.

Characterizing this exchange, magnetic susceptibility and magnetization data are plotted in Figs. 2.2 and 2.3. Below $50\,\mathrm{K}$, the Van Vleck contribution to the susceptibility is negligible. The data from $20\,\mathrm{K}-100\,\mathrm{K}$ were modeled by Curie–Weiss fits of the form $\frac{1}{\chi-\chi_0} = \left(\frac{C}{T-\theta_{CW}}\right)^{-1}$ shown in Fig. 2.2(a) and yield a local moment value of $2.63(8)\,\mu_{\mathrm{B}}$ with an antiferromagnetic Curie–Weiss $\theta_{CW} = -10.3(8)\,\mathrm{K}$. This value is substantially enhanced relative to YbMgGaO$_4$ ($\theta_{CW} = -4\,\mathrm{K}$ [93, 92, 146, 118]), consistent with enhanced exchange. The local moment generated from the Curie–Weiss fits suggests a heightened g-factor, which was validated via electron paramagnetic resonance (EPR) measurements (Fig. 2 (a) inset). A powder averaged g-factor of $g_{avg} = 3.2$ implies a local moment of $2.77\,\mu_{\mathrm{B}}$ for a $J = 1/2$ system—a value only 5 higher than the moment extracted from susceptibility data. Fits to the EPR line shape reveal a highly anisotropic g-factor of $g_{ab} = 3.294(8)$ and $g_c = 1.726(9)$, corresponding to the triangular ab-plane and c-axis respectively.

While the saturated moment for this system is then expected to be approximately $1.6\,\mu_{\mathrm{B}}/\mathrm{Yb}$, $M(H)$ measurements collected at $2\,\mathrm{K}$ up to $9\,\mathrm{T}$ (Fig. 2.2(b)) were only able to polarize Yb moments up to $1\,\mu_{\mathrm{B}}$, consistent with significant θ_{CW} exchange. Fig. 2.2(c) shows zero-field AC susceptibility data collected down to $50\,\mathrm{mK}$. No signatures of freezing, frequency dependence, or long-range order are observed. Instead, $\chi'(T)$ continues to diverge as the sample is cooled, generating an empirical frustration parameter $\theta_{CW}/T_{\mathrm{AF}} > 500$. As we will later argue, this zero-field state is an inherently quantum disordered state
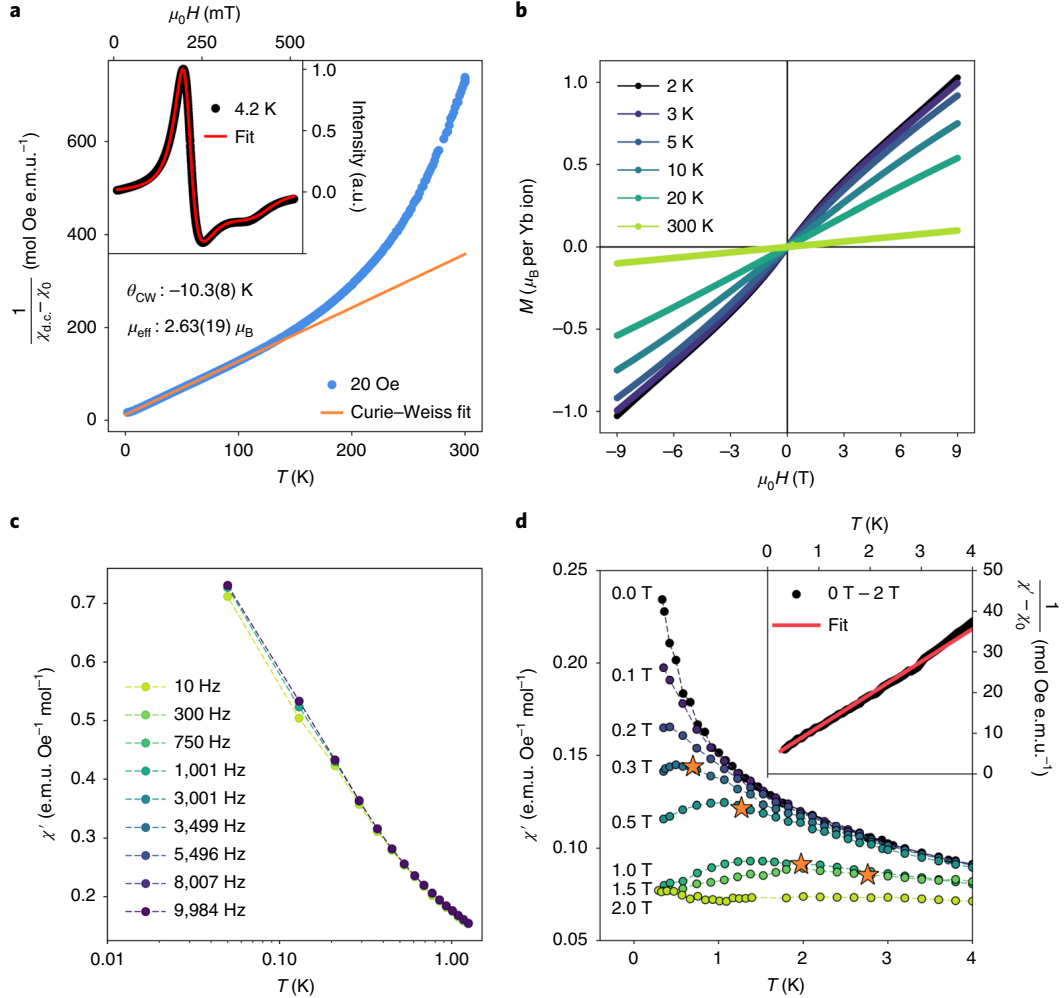
Figure 2.2: Low-field magnetization and magnetic susceptibility data. (a), Low-temperature Curie–Weiss fit to the constant field magnetic susceptibility $\chi_{\text{d.c.}}$ in temperature range free from Van Vleck contributions from high-energy crystal field doublets (where the majority of trivalent Yb ions are in the $J_{\text{eff}} = 1/2$ ground state). A large mean-field interaction strength of $-10.3(8)$ K with an effective local moment, μ_{eff}, of $2.63(19)\,\mu_{\text{B}}$ is fit with a temperature-independent $\chi_0 = 0.0053(3)$ e.m.u. mol^{-1} background term. Inset: EPR data collected at 4.2 K fit to anisotropic g-factors of $g_{ab} = 3.294(8)$ and $g_c = 1.726(9)$. (b), Isothermal magnetization versus field data reaching only 67% of the expected $1.5\mu_{\text{B}}$ per Yb ion polarized moment under $\mu_0 H = 9$ T. (c), Temperature and frequency dependence of a.c. magnetic susceptibility $\chi'(T)$ from 50 mK to 4 K under zero field. (d), $\chi'(T)$ data collected under applied magnetic fields. A minority fraction of free Yb moments are quenched at low temperatures and high fields, resulting in a peak in $\chi'(T)$, and the downward inflection parameterizing this Zeeman splitting is denoted by orange stars. Inset shows field-subtracted 0 T–2 T $\chi'(T)$ data between 1 K and 3 K and a Curie- Weiss fit quantifying the fraction of free Yb moments in the system, as described in the text. Values in parentheses and error bars indicate one standard deviation. a.u., arbitrary units.
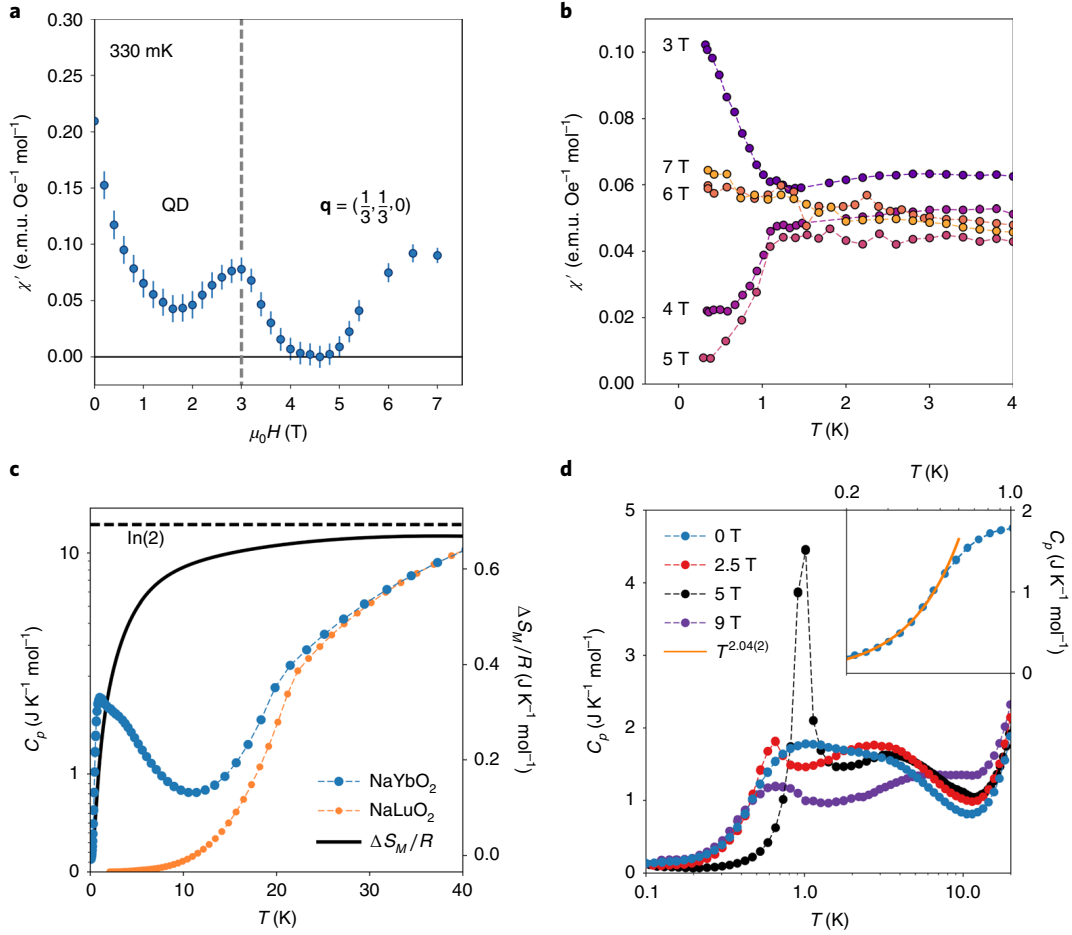
Figure 2.3: High-field magnetic susceptibility and heat capacity data. (a), $\chi'(H)$ data collected at 330 mK showing the phase boundary (dashed line) between the quantum disordered (QD) ground state and magnetically ordered $\mathbf{q} = (1/3, 1/3, 0)$ state near 3 T. A second transition back into the quantum disordered state or a quantum paramagnetic phase begins at higher fields. (b), $\chi'(T)$ data collected under a series of magnetic fields that traverse the ordered state; 4 T and 5 T $\chi'(T)$ data illustrate the onset of the ordered phase below 1 K, while 6 T and 7 T data suggest partial re-entry into a disordered magnetic state. (c), Specific heat of $NaYbO_2$ measured down to 80 mK under zero field and overplotted with the non-magnetic $NaLuO_2$. analogue. The resulting magnetic entropy ΔS_M approaches 95% of $R \ln(2)$. (d), Values of $C_p(T)$ under varying magnetic fields. The lower peak centered around 1 K develops a sharp anomaly at 5 T, indicative of the phase transition into the $\mathbf{q} = (1/3, 1/3, 0)$ state that is suppressed by 9 T. The inset shows the low-temperature portion of the 0 T $C_p(T)$ data fit to a power law. The resulting fit to $T^{2.04}$ is shown as a solid yellow line through the data. Error bars denote one standard deviation of the data.

dressed by a small fraction of free Yb moments that are quenched in a magnetic field.

$\chi'(T)$ data collected under a variety of H fields are plotted in Fig. 2.2(d). Under small H, the divergence in $\chi'(T)$ is suppressed and a maximum appears. The temperature of this maximum increases with field until $\mu_0 H = 2\,\mathrm{T}$ is reached, beyond which $\chi'(T)$ becomes nearly temperature independent. The inflection in $\chi'(T)$ increases linearly with H and is plotted in Fig. 2.1(b). This matches the expected Zeeman splitting of isolated $J_{\mathrm{eff}} = 1/2$ moments $\Delta E = 2\mu_{\mathrm{B}} g_{\mathrm{avg}} J_{\mathrm{eff}} H$ and suggests that $\chi'(T)$ at $\mu_0 H = 2\,\mathrm{T}$ represents the remaining majority of the correlated/bound Yb moments. As an estimate of the fraction of free spins, $\mu_0 H = 0\,\mathrm{T}$ data were fit to a Curie–Weiss form after removing the majority response accessed at $\mu_0 H = 2\,\mathrm{T}$. Fits to a Curie–Weiss form between 1-4 K (Fig. 2.2(d)) are described by a model of 14.4(6)% free spins with a full moment of 2.63 μ_{B} and a $\theta_{CW} = -0.45(4)\,\mathrm{K}$. 2 K $M(H)$ data plotted in Supplementary Fig 2 (d) were also fit to a two-component model of Brillouin-like free spins and exchange-field-bound moments which yielded a free spin fraction of approximately 7%. These fits roughly parameterize the limit of a free spin fraction in the material and suggest that free spins coexist with a quantum disorder ground state.

At higher fields, the nearly temperature-independent $\chi'(T)$ at 2 T evolves into a ordered state. Isothermal $\chi'(H)$ data at $330\,\mathrm{mK}$ plotted in Fig. 2.3 (a) show an increase in the susceptibility as a phase boundary is traversed at 3 T followed by near total suppression of $\chi'(H)$ at 5 T. For $\mu_0 H > 5\,\mathrm{T}$, $\chi'(H)$ begins to recover suggesting a higher field phase boundary—one marking the quenching of the ordered state as spins are fur-

ther polarized toward a quantum paramagnetic phase. $\chi'(T)$ data collected across the ordered regime are plotted in Fig. 2.3(b) and show a sharp transition into below 1 K at $\mu_0 H = 4$ T. The likely origin of the enhancement in $\chi'(T)$ upon entering the ordered state at 3 T is due to the proximity of the quantum critical point associated with the nearby 0 K phase boundary. These quantum fluctuations are suppressed crossing the finite temperature phase boundaries away from this point.

To further characterize NaYbO$_2$, heat capacity measurements were performed. Fig. 2.3(c) shows the zero-field $C(T)$ of both NaYbO$_2$ and a nonmagnetic comparator NaLuO$_2$ plotted from 80 mK to 40 K. Consistent with susceptibility data, no sharp anomaly indicative of the onset of long-range order is observed in NaYbO$_2$. Instead, a broad feature comprised of two peaks is apparent—one peak centered near 1 K and the other near 2.5 K. Two peaks in $C(T)$ are predicted in a number of theoretical models for both triangular [162, 72] and kagome-based [40, 151] Heisenberg lattices where a quantum spin liquid state appears. Integrating $S_{\mathrm{mag}}(T)$ data with the lattice contribution subtracted yields a magnetic entropy reaching 95% of R ln(2), consistent with the nominal $J_{\mathrm{eff}} = 1/2$ magnetic doublet of NaYbO$_2$.

Upon applying magnetic field, data in Fig. 2.3(d) show the 2.5 K peak in $C_p(T)$ shifts upward in temperature similar to other frustrated magnets; however, under 5 T, a sharp anomaly appears near 1 K and is coincident with the downturn in $\chi'(T)$ at this field. Under 9 T, this sharp peak broadens and shifts lower in temperature as the system is driven into the disordered state. $S_{\mathrm{mag}}(T)$ integrated under 5 T matches that of 0 T and

the lowest temperature $C_p(T)$ is strongly suppressed once order is generated. This is consistent with the suppression of low energy spin fluctuations upon entering the ordered state, which return when the high field quantum paramagnetic phase is approached. Determining the precise form of the zero-field $C_p(T)$ is complicated by a nuclear Schottky feature that dominates below 100 mK ; however attempts to do so away from this feature yield a $C(T) \propto T^2$ as shown in the inset of Fig. 2.3(d).

Low temperature neutron scattering measurements were also performed. Fig. 2.4(a) shows temperature subtracted (330 mK–1.6 K) diffraction data and the absence of zero-field long-range magnetic order. Field subtracted data at 450 mK plotted in Fig. 2.4(b) reveal that under 5 T, new superlattice reflections appear at the $\boldsymbol{Q} = (1/3, 1/3, 0)$, $(1/3, 1/3, 1)$, and $(1/3, 1/3, 3)$ positions. Given the symmetry constraints of the $R\bar{3}m$, structure, these either represent a 120° noncollinear spin structure or an up-up-down pattern of spin order. The absence of a reflection at $\boldsymbol{Q} = (1/3, 1/3, 2)$ suggests the field-induced order is collinear. Additionally, magnetic intensity appears at the $\boldsymbol{Q} = (0, 0, 3)$ position, consistent with the two-$\boldsymbol{q}$ structure ($\boldsymbol{q} = (1/3, 1/3, 0) + \boldsymbol{q} = (0, 0, 0)$) expected for the equal moment up-up-down state [46]. The best fit to this model is shown in Fig. 2.4(c) where spins refine to be oriented nearly parallel to the $(1, -1, -1)$ direction with an ordered moment $1.36 \pm 0.1 \, \mu_{\mathrm{B}}$. This value is less than the $1.6 \, \mu_{\mathrm{B}}$ expected likely due to the presence of a minority fraction of free moments as well as the influence of remnant fluctuations in the ordered state. Magnetic peaks are resolution-limited with a minimum spin-spin correlation length of $\xi_{\mathrm{min}} = 450 \, \text{Å}$. Further data collected at 67 mK
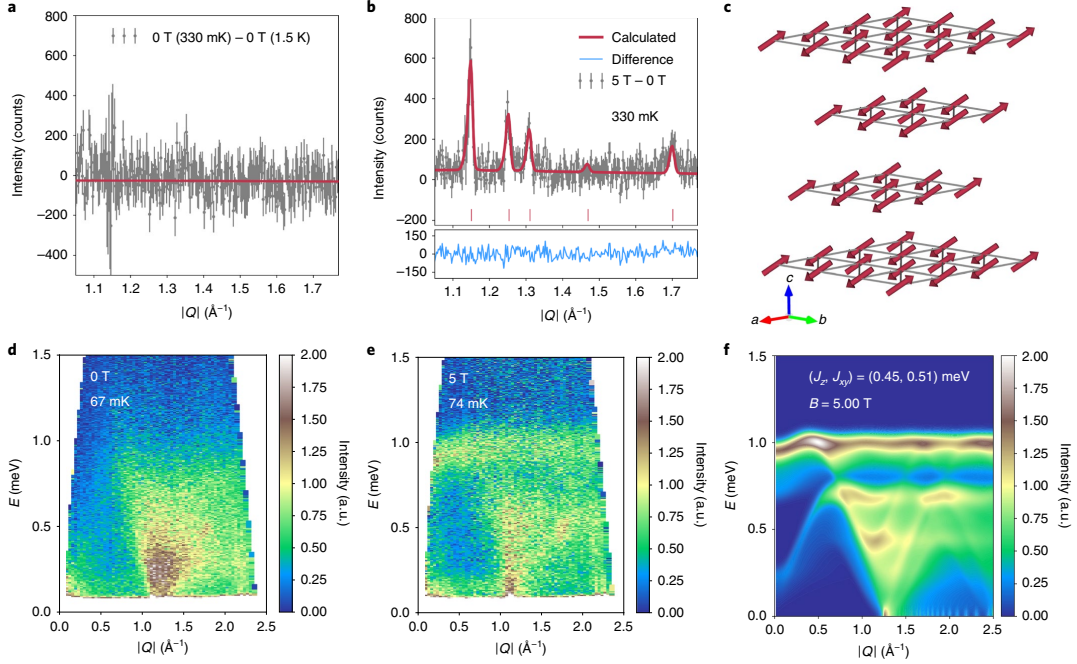
Figure 2.4: Neutron diffraction and inelastic neutron-scattering data. (a), Temperature-subtracted neutron powder diffraction data $(330\,\text{mK} - 1.5\,\text{K})$ collected under $0\,\text{T}$, showing the absence of low-temperature magnetic order. The red line is a constant fit to the subtracted data. (b), Under an applied field of $5\,\text{T}$ at $450\,\text{mK}$, new magnetic peaks appear at $(1/3, 1/3, z)$ positions $(z = 0, 1, 3)$, corresponding to an ordering wave vector of $\boldsymbol{q} = (1/3, 1/3, 0)$. The data were refined by analyzing field-subtracted data $(5\,\text{T} - 0\,\text{T})$, which are constrained by the suppressed $(1/3, 1/3, 2)$ reflection. (c), The best fit to the $5\,\text{T}$ induced magnetic state using the two-$\boldsymbol{q}$ structure $\boldsymbol{q} = (1/3, 1/3, 0) + \boldsymbol{q} = (0, 0, 0)$ is generated by a collinear spin structure with Yb moments of $1.36(10)\,\mu_{\text{B}}$. The displayed structure aligns moments approximately along the $< 1, -1, -1 >$ direction and has six symmetrically equivalent structures generated by threefold in-plane rotational and mirror symmetries. (d), Inelastic neutron-scattering spectrum collected at $67\,\text{mK}$ and $0\,\text{T}$. (e), Inelastic neutron-scattering spectrum collected at $74\,\text{mK}$ and $\mu_0 H = 5\,\text{T}$. (f), Linear spin wave calculations showing the powder-averaged $S(Q, E)$ for a two-dimensional triangular lattice of anisotropic Yb^{3+} moments of NaYbO_2 in a $5\,\text{T}$ field and three-sublattice ordering. Error bars denote one standard deviation of the data.

determine the low temperature, magnetic field phase boundaries [14].

Inelastic scattering data plotted in Figs. 2.4(d) and 2.4(e) reveal a dramatic renormalization of the low energy spin dynamics upon transitioning from the quantum disordered state into the up-up-down phase. The zero field data shows a diffuse spectrum of excitations centered about the $(1/3, 1/3, L)$-type wave vectors, and upon applying a $5\,\mathrm{T}$ field, much of this spectral weight is shifted into the elastic channel and a nearly flat band of excitations centered at $1\,\mathrm{meV}$. Powder averaged linear spin wave calculations assuming a purely two-dimensional triangular lattice in a $5\,\mathrm{T}$ magnetic field reproduce this flat feature, and the simulated $S(\boldsymbol{Q}, \omega)$ is plotted in Fig. 2.4(f). This simulation was generated using nearest neighbor coupling with a nearly Heisenberg Hamiltonian with a slight easy-plane anisotropy, $J_z = 0.45\,\mathrm{meV}$, $J_{xy} = 0.51\,\mathrm{meV}$. The subtle downturn at low $\boldsymbol{Q}$ of the emergent $1\,\mathrm{meV}$ band requires a slight easy-plane anisotropy as discussed in Subsection 2.6.2.

We now discuss the implications of our results. The similar YbO_6 octahedra of $NaYbO_2$ and $YbMgGaO_4$ intimate that the local crystal fields and in-plane exchange couplings between Yb ions are comparable; however, the main distinction between the two systems is the much shorter inter-plane distance in $NaYbO_2$. This suggests that the interlayer coupling is non-negligible, and therefore, a minimal Hamiltonian should include nearest neighbor bonds within the planes and between neighboring layers. Based

on the structure, a symmetry analysis leads to the following exchange Hamiltonian:

$$H_{2d} = \sum_{\langle ij \rangle} \left\{ J_{xy} \left(S_i^x S_j^x + S_i^y S_j^y \right) + J_z S_i^z S_j^z \right.$$
$$\left. + J_c \left(\hat{\boldsymbol{e}}_{ij} \cdot \boldsymbol{S}_i \right) \left(\hat{\boldsymbol{e}}_{ij} \cdot \boldsymbol{S}_j \right) + J_{cz} \left[\left(\hat{\boldsymbol{z}} \cdot \hat{\boldsymbol{e}}_{ij} \times \boldsymbol{S}_i \right) S_j^z + \left(\hat{\boldsymbol{z}} \cdot \hat{\boldsymbol{e}}_{ij} \times \boldsymbol{S}_j \right) S_i^z \right] \right\}. \quad (2.1)$$

$$H' = \sum_{\langle\langle ij \rangle\rangle} \left\{ J'_{xy} \left(S_i^x S_j^x + S_i^y S_j^y \right) + J'_z S_i^z S_j^z \right.$$
$$\left. + J'_c \left(\hat{\boldsymbol{f}}_{ij} \cdot \boldsymbol{S}_i \right) \left(\hat{\boldsymbol{f}}_{ij} \cdot \boldsymbol{S}_j \right) + J'_{cz} \left[\left(\hat{\boldsymbol{f}}_{ij} \cdot \boldsymbol{S}_i \right) S_j^z + \left(\hat{\boldsymbol{f}}_{ij} \cdot \boldsymbol{S}_j \right) S_i^z \right] \right\}, \quad (2.2)$$

Eq. (2.1) contains interactions within a triangular layer, and Eq. (2.2) between layers. The unit vectors $\hat{\boldsymbol{e}}_{ij}$ are oriented along the ij bond, and $\hat{\boldsymbol{f}}_{ij}$ is a unit vector along the projection of the ij bond into the ab-plane. The in-plane Hamiltonian H_{2d} is identical to that in YbMgGaO$_4$ but rewritten here (following Iaconis et al. [69]) in a more physically transparent "compass model" form. The interlayer exchange in the second line also has a compass-like structure. We expect that this form applies to the full family of delafossite-like antiferromagnets, ARX_2, with dipolar Kramer's doublets on the R site, sharing the space group 166.

H_{2d} notably contains a wide range of phase space favoring three types of classical orders: (1) three-sublattice 120° structures; (2) collinear two-sublattice stripe phases; and (3) out-of-plane Ising anisotropy with up-up-down structures. Because we do not observe zero-field order, and we expect that interplane exchange is substantial, we infer that the interactions in H' should be frustrated by the in-plane order or correlations. Consideration of the coupling between layers uniquely singles out the three-sublattice

120° structure: to leading order, only this in-plane order allows the staggered magnetization to effectively cancel the exchange field between neighboring planes [14]. This is even true to a large extent also for the anisotropic J_c' and J_{cz}' couplings.

Using this deduction that $NaYbO_2$ has 120° correlations, we expect fluctuations amongst many classically degenerate or nearly degenerate states to strongly suppress order. Furthermore, recent DMRG studies of H_{2d} find that for $S = 1/2$ quantum spins, a spin liquid state indeed occurs in a corner of the classically 120° ordered phase space with moderate J_{cz} coupling [186]. Consequently, it is plausible that a spin liquid state occurs in $NaYbO_2$, and if so, it is likely to be smoothly connected to the spin liquid of the two-dimensional problem. The optimal spin liquid ground state for the 2d model based on variational parton calculations [69] is a U(1) Dirac state with gapless fermionic spinons described theoretically as a 2+1-dimensional conformal field theory: QED_3. The second implication of our Hamiltonian in this regime is that, on applying a magnetic field, the degeneracy is strongly lifted. This is because a large part of the zero-field cancellation is reliant on the specific 120° structure of the in-plane ground state, which is modified by the application of a magnetic field. Therefore, it is natural to expect ordering to become more robust in an applied magnetic field. The three-sublattice $(1/3, 1/3, 0)$ wave vector is indeed germane to triangular antiferromagnets in a magnetic field, which stabilize a quantized magnetization plateau at 1/3 saturation in XXZ models [154, 35].

With this in mind, we return to a discussion of the data. Theory predicts the 2d U(1) Dirac state to have $C_p(T)$ quadratic in temperature, consistent with measurements

[123]. An alternate explanation of T^2 specific heat might come from the degenerate line of spiral states found by Rastelli and Tassi for the zero-field rhombohedral XXZ model [125], which has 2d-like spin fluctuations despite 3d coupling. The incommensurate long-range order of the Rastelli-Tassi spiral does not appear in our measurements, however, the field-induced Bragg peaks seen in experiment are consistent with the three-sublattice plateau states that emerge in the XXZ model in a field [154, 117]. Indeed, the magnetization at $5\,\mathrm{T}$, where the ordered phase is maximal, is approximately 1/3 of the expected saturation moment and corresponds to a plateau where $\chi(T) = \partial M/\partial H$ reaches zero. The best fit to neutron diffraction data further corresponds to the equal moment, two-$\boldsymbol{q}$ *up-up-down* structure of the plateau state.

The two peaks observed in the zero field $C_p(T)$ of $NaYbO_2$ evoke a number of theoretical models of Heisenberg spins on both triangular [162, 72] and kagome [40, 151] lattices that predict dual entropy anomalies upon cooling into spin liquid ground states. Both peaks are rarely observed experimentally and interpretations of the nature of each peak vary with the specific model. Exact diagonalization studies of the XXZ Hamiltonian on a triangular lattice predict a high temperature peak corresponding to the formation of trimers of doublet states (i.e. short-range correlations) followed by a lower temperature peak that marks the onset of a quantum spin singlet state [72]. Recent work exploring the $S = 1/2$ triangular lattice using tensor renormalization group techniques predicts a dual $C_p(T)$ anomaly with the lower temperature peak signifying the onset of short-range/incipient order and the upper peak reflective of the onset of gapped low energy,

chiral fluctuations [31]. The ratio of peak temperatures predicted in this $S = 1/2$ model $T_l/T_h \approx 0.36$ is consistent with those observed in NaYbO$_2$ and the $J \approx 5$ K inferred from the model is reasonably close to the θ_{CW} determined from susceptibility data.

Our data demonstrate that the nearly ideal triangular lattice of Yb ions in NaYbO$_2$ realize an unconventional quantum disordered ground state. Unlike the majority of other spin-liquid candidates such as Herbertsmithite ZnCu$_3$(OH)$_6$Cl$_2$ [60], the ground state in NaYbO$_2$ can be driven into an intermediate ordered regime in relatively weak magnetic fields. The origin of the small fraction of free spins coexisting with this ground state remains an open question; however, they are not reflective of trivial disorder, which favours the least collinear state [105]. Additionally, rather than hosting a purely two-dimensional network of spins where the two-dimensionality precludes long-range order such as in Ba$_8$CoNb$_6$O$_{24}$ [129, 36], interlayer geometric frustration is critical to the exclusion of order in NaYbO$_2$. This reflects the strong perturbation field provides to a complex interplay between interlayer frustration and the nearly degenerate ground states inherent to the XXZ triangular lattice Hamiltonian. Due to this, NaYbO$_2$ uniquely stands able to provide considerable insight into the critical phase behavior manifest at the phase boundaries between the ordered and quantum disordered states in a chemically-ideal frustrated triangular lattice.

2.3 Symmetry and exchange interactions

In this section, we discuss the symmetries and show that the symmetry-allowed exchange interactions on the nearest-neighbor in-plane and inter-layer bonds have the form given in the main text. In $NaYbO_2$, the magnetic Yb atoms live on the sites of 2d triangular lattices with "ABC" stacking in the vertical direction. This is a rhombohedral lattice. Specifically, the system has space group 166, $R\bar{3}m$. We assume that the there is an effective spin-1/2 operator transforming like a pseudo-vector on each Yb site. The exchange interactions on a bond are constrained by the subgroup of the full space group which preserves that bond, i.e. which leaves the center of the bond unchanged. We discuss the intra-layer and inter-layer bonds in turn below.

In this and the following Supplemental section, it will be useful to establish notation. In conventional rhombohedral coordinates, we specify positions using dimensionless coordinates so that

$$\boldsymbol{r}_{mnl} = m\boldsymbol{a}_1 + n\boldsymbol{a}_2 + l\boldsymbol{c}, \tag{2.3}$$

with vectors

$$\boldsymbol{a}_1 = a(1,0,0), \quad \boldsymbol{a}_2 = a(-\frac{1}{2}, \frac{\sqrt{3}}{2}, 0), \quad \boldsymbol{c} = c(0,0,1). \tag{2.4}$$

Note that $\boldsymbol{c}$ is not the primitive translation but a conventional one. The primitive translation is $(2\boldsymbol{a}_1 + \boldsymbol{a}_2 + \boldsymbol{c})/3$. This connects a layer at $l = 0$ to $l = 1/3$.

2.3.1 NN in-plane bonds

All the in-plane bonds are equivalent by rotations and translations. So we can deduce the exchange on all of them by considering one. Specifically, we consider one whose center is at coordinates $(1/2, 0, 0)$. This is the middle of a bond along the x axis in cartesian coordinates. This point is the 9e Wyckoff position, with site symmetry group 2/m. The point group is generated by 2 $\mathbb{Z}_2$ operations, which we can take as: (1) inversion through the bond center and (2) a C_2 rotation about the axis along the bond. Composing these two gives a third (not independent) element, a mirror reflection through the plane normal to the bond. Using these operations, we learn from inversion that there is no DM coupling. Then applying the C_2 operation, for a bond along x, the sites are *not* interchanged but $S_i^y \to -S_i^y$ and $S_i^z \to -S_i^z$. This means the general exchange matrix for a bond connecting the two sites along this direction is

$$
J_{NN,\boldsymbol{x}} = \begin{pmatrix} J_1 & 0 & 0 \\ 0 & J_2 & J_4 \\ 0 & J_4 & J_3 \end{pmatrix}. \tag{2.5}
$$

Now we obtain the exchange for an arbitrary pair of in-plane NN spins by rotation. The general form is given in Eq. (2.1). This form is equivalent to that written down in Ref. [92]. The relation between the form used here and the one in Ref. [92] can be found in Ref. [69].

2.3.2   Out of plane bonds

The out of plane bonds are not vertical, but connect each spin in a layer to three spins above and three spins below. As above, we consider the point symmetry group of a mid-point of such a bond. An example is the point $(1/3, 1/6, 1/6)$ in lattice coordinates. This is the mid-point of a bond whose projection into the xy plane is at a 30 degree angle to the x axis, i.e which bisects a triangle of the triangular plane. This is the 9d Wyckoff position, which *also* has site symmetry 2/m. The group is the same as for the in-plane bond, but the symmetries are slightly different. The two generators in this case can be considered as: (1) inversion and (2) a C_2 rotation which is about an axis which bisects the bond and is parallel to the xy plane. The two composed together give the third non-trivial operation in the point group which is a mirror plane which contains the bond and is normal to the xy plane. The difference from the previous case is the orientation of the C_2 axis or the plane of the mirror. The result is that the effective exchange interaction has a very slightly different form from Eq. (2.1), and is given in Eq. (2.2). Note that the vectors $\hat{\boldsymbol{e}}_{ij}$ appearing in Eq. (2.1) are oriented along the triangular axes, while the vectors $\hat{\boldsymbol{f}}_{ij}$ appearing in Eq. (2.1) bisect these directions. The other difference from Eq. (2.1) is that in Eq. (2.2), the final term has no cross product. That is a result of the different orientation of rotation axis/mirror plane in this second situation. This completes the symmetry analysis of interactions.

2.4 Classical phases and frustration in two dimensions

In this section, we discuss aspects of the classical ground states of the model Hamiltonian given in Eq. (2.1), and to what extent frustration arises therein. Since we expect that the interlayer interactions are small compared to the intralayer ones in practice, we begin by discussing what is known for the two dimensional model, with all interlayer interactions turned off.

The Hamiltonian 2.1 has already been extensively studied. It is a simple extension of the "compass" model on the triangular lattice, which had been considered long ago. Collecting results from many papers [69, 186, 100, 89], there are three types of classical ground states which emerge for nearly all parameters in the antiferromagnetic regime: a three-sublattice 120° planar state, and two collinear stripe states, which differ from one another only in the direction of their spin polarization.

2.4.1 Classical three-sublattice states

First we consider the three-sublattice 120° states. It is helpful to rewrite the Hamiltonian a bit more explicitly. For a single layer, we can write

$$H_{2d} = \sum_i \sum_{\mu=1,2,3} \left\{ J_{xy} \left(S_i^x S_{i+\mu}^x + S_i^y S_{i+\mu}^y \right) + J_z S_i^z S_{i+\mu}^z + J_c \left(\boldsymbol{a}_\mu \cdot \boldsymbol{S}_i \right) \left(\boldsymbol{a}_\mu \cdot \boldsymbol{S}_{i+\mu} \right) \right. $$
$$ \left. + J_{cz} \left[\left(\hat{\boldsymbol{z}} \cdot \boldsymbol{a}_\mu \times \boldsymbol{S}_i \right) S_{i+\mu}^z + \left(\hat{\boldsymbol{z}} \cdot \boldsymbol{a}_\mu \times \boldsymbol{S}_{i+\mu} \right) S_i^z \right] \right\}. $$

Here we took $\boldsymbol{a}_3 = -\boldsymbol{a}_1 - \boldsymbol{a}_2$.

Now consider a general three-sublattice state, in which for site $i = (m, n)$ in lattice coordinates

$$\boldsymbol{S}_{m,n} = S\boldsymbol{n}_{\mathrm{Mod}[-m-n,3]}, \tag{2.6}$$

with three classical fixed length vectors $\boldsymbol{n}_s$ with $s = 0, 1, 2$ labeling the three sublattices. For such a state, the energy becomes

$$3E_{2d}/(NS^2) = \sum_{s=0,1,2} \left\{ 3J_{xy} \left(n_s^x n_{s-1}^x + n_s^y n_{s-1}^y \right) + 3J_z n_s^z n_{s-1}^z + J_c \sum_\mu \left(\boldsymbol{a}_\mu \cdot \boldsymbol{n}_s \right) \left(\boldsymbol{a}_\mu \cdot \boldsymbol{n}_{s-1} \right) \right.$$
$$\left. + J_{cz} \sum_\mu \left[\left(\hat{\boldsymbol{z}} \cdot \boldsymbol{a}_\mu \times \boldsymbol{n}_s \right) n_{s-1}^z + n_s^z \left(\hat{\boldsymbol{z}} \cdot \boldsymbol{a}_\mu \times \boldsymbol{n}_{s-1} \right) \right] \right\}$$

Here we have written sublattice s modulo 3. The sum over μ can be carried out explicitly. The last term vanishes because $\sum_\mu \boldsymbol{a}_\mu = 0$. In the second last term, we use $\sum_\mu \boldsymbol{a}_\mu \boldsymbol{a}_\mu^T = (3/2)\mathrm{diag}(1, 1, 0)$. We obtain

$$3E_{2d}/(NS^2) = \sum_{s=0,1,2} \left[3 \left(J_{xy} + \frac{J_c}{2} \right) \left(n_s^x n_{s-1}^x + n_s^y n_{s-1}^y \right) + 3J_z n_s^z n_{s-1}^z \right]. \tag{2.7}$$

We observe the remarkable emergence of U(1) symmetry of the classical energy, despite the anisotropy of the Hamiltonian. This is a well-known accidental degeneracy which occurs for many compass models.[114] Note that vanishing effect of in-plane anisotropy and the complete absence of any effect from J_{cz} is general for any three-sublattice state with this unit cell, whether the spins be collinear, coplanar, or otherwise. It would also hold within any Curie–Weiss mean field treatment which would allow for variable magnitude of the local spin expectation values. The three-sublattice ordered state occurs when the first term above dominates, and the spins consequently orient in the plane with

three different sublattice orientations at 120° angles to one another. Frustration is evident in this ordered pattern by the fact that the classical energy is independent of the overall angle of the spins within the XY plane, which is not related to any symmetry of the model.

Note that when J_z is sufficiently large, the lowest energy configurations of the three sublattice state become Ising like, with spins oriented normal to the plane. However, in this regime the global ground states are actually not of the three-sublattice form, but rather the stripe states we consider next.

2.4.2   Classical stripe phases

If the compass interaction J_c dominates, it is natural to select spins to be aligned or anti-aligned along appropriate neighbors. For example, if we take $J_c < 0$, the compass coupling for an $\boldsymbol{a}_1 = \hat{\boldsymbol{x}}$ bond would favor spins oriented along the x direction forming ferromagnetic chains along this axis. Let us just assume to start a two-sublattice structure, so that

$$\boldsymbol{S}_{m,n} = S\boldsymbol{n}_{\text{Mod}[n,2]}, \tag{2.8}$$

i.e. with ferromagnetic chains along x. Inserting this into Eq. (2.6), we obtain an energy

$$\begin{aligned}
\frac{2E}{NS^2} =& J(2 + 4\boldsymbol{n}_0 \cdot \boldsymbol{n}_1) + J_z \left(4n_0^z n_1^z + (n_0^z)^2 + (n_1^z)^2\right) \\
&+ J_c \left((n_0^x)^2 + (n_1^x)^2 + n_0^x n_1^x + 3n_0^y n_1^y\right) + J_{cz}XX,
\end{aligned} \tag{2.9}$$

where we did not write the expression for the J_{cz} term, because we are going to focus on in-plane order (favored for negative J_z). Assuming in-plane order, i.e. $n_a^z = 0$, the

66

energy is minimized for spins aligned along the y direction:

$$\boldsymbol{n}_0 = -\boldsymbol{n}_1 = \pm\hat{\boldsymbol{y}}, \qquad \frac{2E}{NS^2} = -2J_{xy} - 3J_c. \tag{2.10}$$

The above equations describe two solutions for stripe states, which are translations and time-reversals of one another. There are another four such states, obtain by C_3 rotations of these two, where the ferromagnetic stripes lie along other axes. Note this sixfold degeneracy of the stripe states is *not* accidental, but symmetry mandated. There is no accidental degeneracy within the stripe ground states, and hence we may regard them as less frustrated than the 120° three sublattice states.

One can compare the energy for these states to that for the 120° states, by examining Eq. (2.7). For the 3 sublattice states, one has $\boldsymbol{n}_s \cdot \boldsymbol{n}_{s-1} = -1/2$. One obtains the energy per spin in the two cases as

$$E_{120}/(NS^2) = -\frac{3}{2}J_{xy} - \frac{3}{4}J_c, \qquad E_{stripe}/(NS^2) = -J_{xy} - \frac{3}{2}J_c. \tag{2.11}$$

Clearly the 120 degree state is better for small J_c and the stripe state is better for larger J_c. One finds the stripe is favorable once $J_c > 2/3J_{xy}$.

2.4.3   Adding magnetic field

Now we study the classical ground state of the two dimensional model (2.1) in presence of a magnetic field. The field dependence enters the Hamiltonian through the Zeeman term. For the rest of this subsection we will work under the assumption of a general three-sublattice state. Then the four-term Hamiltonian (2.1) reduces to an XXZ model as was shown in Eq. (2.7).

We further allow an onsite anisotropy term along the z direction. The Hamiltonian then reads

$$H = \sum_{\langle i,j \rangle} J_z S_i^z S_j^z + J_{xy}(S_i^x S_j^x + S_i^y S_j^y) + D \sum_i (S_i^z)^2 - \sum_i \mu_B g_{\mu\nu} B^\mu S_i^\nu, \qquad (2.12)$$

where $\mu, \nu = x, y, z$, $g_{\mu\nu} = \mathrm{diag}(g_{xy}, g_{xy}, g_z)$. We now proceed to study the classical phases of this model.

The main conclusions from our previous study [14] of this Hamiltonian are: (1) the ground state is a three-sublattice $120°$ structure that (2) evolves into a canted phase with an external field, which becomes a canted up-up-down structure depending on the field strength and direction, and (3) a good fit to the inelastic neutron scattering powder-averaged spectrum of $NaYbO_2$ is produced at $J_{xy} = 0.51$ meV and $J_z = 0.45$ meV.

We now use $d = a, b, c$ to label the three sublattices, and define $S_d^\mu = S n_d^\mu$, where $\boldsymbol{n}_d$ is a unit vector. We further define $\Sigma^\mu = \sum_d n_d^\mu$, then the classical ground state is obtained by minimizing the following quantity

$$E = \frac{H}{3NS^2 J_{xy}/2} = A(\Sigma^z - h_z)^2 + (\Sigma^x - h_x)^2 + (\Sigma^y - h_y)^2 - \delta \sum_d (s_d^z)^2 - C, \quad (2.13)$$

where N is the number of sites in the 2D lattice, and we have defined

$$A = r^{-1} = \frac{J_z}{J_{xy}}, \quad (h_x, h_y, h_z) = \frac{\mu_B}{3S} \left(\frac{g_{xy}B^x}{J_{xy}}, \frac{g_{xy}B^y}{J_{xy}}, \frac{g_z B^z}{J_z} \right),$$

$$\delta = A - 1 - \frac{2D}{3J_{xy}}, \quad C = \frac{\frac{H_z^2 J_{xy}}{3J_z^2} + \frac{H_{xy}^2}{3J_{xy}} - 9J_{xy}S^2}{3S^2 J_{xy}}. \qquad (2.14)$$

We then write $\boldsymbol{n}_d = (\sin\theta_d \cos\phi_d, \sin\theta_d \sin\phi_d, \cos\theta_d)$ and take the derivatives with respect

68

to angular variables,

$$\frac{\partial E}{\partial \theta_d} = 0 \;\; \Rightarrow \;\; A(\Sigma^z - h_z)s_d^{xy} - (\Sigma^x - h_x)s_d^z \frac{s_d^x}{s_d^{xy}} - (\Sigma^y - h_y)s_d^z \frac{s_d^y}{s_d^{xy}} - \delta s_d^z s_d^{xy} = 0, \quad (2.15\text{a})$$

$$\frac{\partial E}{\partial \phi_d} = 0 \;\; \Rightarrow \;\; (\Sigma^x - h_x)s_d^y - (\Sigma^y - h_y)s_d^x = 0, \quad\quad\quad\quad\quad (2.15\text{b})$$

where $s_d^{xy} = (s_d^x)^2 + (s_d^y)^2$ (we will use similar notation for other quantities). We then

have the following two cases:

Case 1: If $\Sigma^x - h_x$ and $\Sigma^y - h_y$ do not vanish at the same time: suppose $\Sigma^y - h_y \neq 0$,

then we have $\frac{\Sigma^x - h_x}{\Sigma^y - h_y} = \frac{s_d^x}{s_d^y}$, the order is coplanar in the plane containing z axis. Therefore

we are actually minimizing

$$E_{\text{coplanar}} = A(\Sigma^z - h_z)^2 + (\Sigma^{xy} - h_{xy})^2 - \delta \sum_d (s_d^z)^2. \quad\quad (2.16)$$

This will be treated in detail below.

Case 2: Otherwise, we have

$$\Sigma^x - h_x = \Sigma^y - h_y = 0. \quad\quad\quad\quad\quad\quad (2.17)$$

Plugging this into Eq. (2.15a), we see that

$$s_d^{xy} \left[\delta s_d^z - A(\Sigma^z - h_z) \right] = 0, \quad\quad\quad\quad\quad (2.18)$$

has four cases, depending on how many $s_d^{xy} = 0$; note that if two or all three $s_d^{xy} = 0$

then the situation is included in the first case. Therefore we only need analyze two

possibilities.

The first is if $s_d^{xy} \neq 0$ for all $d = a, b, c$, then we must have

$$s_a^z = s_b^z = s_c^z = \frac{Ah_z}{\delta - 3A},$$
(2.19)

In other words, the spins have equal z component. We call this the "canted-I" phase. This solution should be considered only when $s^z = |\frac{Ah_z}{\delta - 3A}| \leq 1$ and $3\sqrt{1 - (s^z)^2} \leq h_{xy}$, i.e.

$$\frac{h_{xy}^2}{9} + \frac{h_z^2}{(3 - \delta/A)^2} \leq 1.$$
(2.20)

The ground state manifold is a degenerate 1D parameter space, resulting from the different ways the xy in-plane vectors satisfy Eq. (2.17). Note that in this case the three equations for θ_d are all independent, but the three equations for ϕ_d are reduced to just two equations. Therefore we should get a 1D degenerate classical ground state manifold.

The second possibility is to suppose $s_a^{xy} = 0$ and $s_b^{xy} = s_c^{xy} \equiv s^{xy} \neq 0$, then we must have $s_b^z = s_c^z$. We call this the "canted-II" phase. In this case there are already four equations therefore the spins are uniquely determined, leaving no classical ground state degeneracy. This solution should be considered only when $s^{xy} = \sqrt{1 - (s^z)^2} \geq h_{xy}/2$, i.e.

$$\frac{h_{xy}^2}{4} + \frac{(s_a^z - h_z)^2}{(2 - \delta/A)^2} \leq 1, \qquad s_a^z = \pm 1.$$
(2.21)

In summary, the classical ground state of the Hamiltonian (2.12) can only be one of the following types: coplanar (in which the order plane must contain the z axis), collinear, "canted-I" (in which the three spins have the same z component), or "canted-II" (in which one spin lies along z and the other two have the same z component). For generic

70

field directions, only the "canted-I" states can form a 1D degenerate classical ground state manifold.

2.4.4   Classical phase diagram

In the following we will set the onsite ion term $D = 0$, which means $\delta = A - 1$. We now present a concrete phase diagram for the Hamiltonian in the (A, h_{xy}, h_z) phase space. For an illustration of the phase diagram, see Fig. 2.5.

Easy-plane anisotropy: In the easy-plane anisotropy region $(0 < A < 1)$, the phase diagram can been analytically obtained [14]

$$
\begin{cases}
\frac{h_{xy}^2}{9} + \frac{h_z^2}{(1/A+2)^2} \geq 1 : & \text{"paramagnetic" phase;} \\
\frac{h_{xy}^2}{9} + \frac{h_z^2}{(1/A+2)^2} < 1 : & \text{"canted-I" phase.}
\end{cases}
\tag{2.22}
$$

The phase boundary is the same as Eq. (2.20) if we take the equality. The "paramagnetic" phase has a unique classical ground state while in the "canted-I" phase the classical ground states are accidentally degenerate and form a one-dimensional manifold, subject to the constraints (2.17) and (2.19).

Easy-axis anisotropy: In the easy-axis anisotropy region $(A > 1)$, three phases exist: the "paramagnetic" phase, the "Y" phase and the "V" phase. We define the "V" phase to be such that two of the spins have identical orientation which is different from the third one, while we define the "Y" phase to be such that the orientation of each is different

71

from the other two. the complete phase diagram is

$$
\begin{cases}
\frac{h_{xy}^2}{(A+2)^2} + \frac{h_z^2}{(1/A+2)^2} \geq 1: & \text{"paramagnetic" phase;} \\[2ex]
\frac{h_{xy}^2}{(A+2)^2} + \frac{h_z^2}{(1/A+2)^2} < 1 \text{ and } h_z \geq h_{z,0}(A, h_{xy}): & \text{"V" phase;} \\[2ex]
h_z \leq h_{z,0}(A, h_{xy}): & \text{"Y" phase,}
\end{cases}
\tag{2.23}
$$

where we have defined critical $h_{z,0}(A, h_{xy})$, which is a function of A and h_{xy}. $h_{z,0}$ is determined from the following group of equations, taking the smallest positive nonzero solution for $h_{z,0}$:

$$
\begin{aligned}
A(a + c - h_z)\sqrt{1 - a^2} &= a(\sqrt{1 - a^2} + \sqrt{1 - c^2} - h_{xy}), \\
A(2a - h_z)\sqrt{1 - c^2} &= c(2\sqrt{1 - a^2} - h_{xy}), \\
c &= h_z - a^3(A^{-1} - 1) - 2a.
\end{aligned}
\tag{2.24}
$$

the corresponding solution for the other variables $a = n_a^z = n_b^z$ and $c = n_c^z$ gives the z component of the three spins in the "V" phase. The first two equations simply come from the saddle point equation (2.15a); the last equation originates from the fact that, at the vicinity of the phase boundary between "V" and "Y" the energy (2.16) (note now $\delta = A - 1$) takes the form $E_{\text{coplanar}} \sim \text{Const.} + \mathcal{O}(a - b)^3$, i.e. when expanding E_{coplanar} in powers of $a - b$ both the first and second order terms must vanish (in fact the third order vanishes too). The analytical solution of Eqs. (2.24) to h_z is hard; however, when A is small enough ($A < 2$ for a numerical estimation), the solution for h_z can be well approximated by the empirical form

$$
h_z = \frac{1}{A}\left(1 - \frac{h_x}{2 + A}\right)^2 \left[b + (1 - b)\left(1 - \frac{h_x}{2 + A}\right)\right]^2
\tag{2.25}
$$

72

with appropriate choice of b as a fitting parameter. Note in the limit $h_{xy} = 0$ (perpendicular field) we recover the result $h_{z,0} = 1/A$ for the boundary between the "Y" and the "V" phases, and $h_{z,1} \equiv 1/A + 2$ for the boundary between the "V" phase and the fully polarized phase [108]. Note also that a special type of the "V" state, the *up-up-down* state, should be distinguished as another distinct phase in the $h_{xy} = 0$ limit, but such a phase loses its meaning as soon as an in-plane field component is turned on.

Applying these results to NaYbO$_2$, which carries easy-plane exchange couplings $J_z = 0.45\,\mathrm{meV}$ and $J_{xy} = 0.51\,\mathrm{meV}$, we are left only with two phases: the "canted-I" phase and the "paramagnetic" phase. The critical field for the onset of the "paramagnetic" phase is

$$B_{z,\mathrm{c}} = 21.15\,\mathrm{T}, \qquad B_{xy,\mathrm{c}} = 12.03\,\mathrm{T}, \tag{2.26}$$

and when the field is oriented in other directions, the corresponding critical B_c interpolates between these two values.

We note here that the canted-I phase does not exactly match the experimentally reported *up-up-down* state. A slightly canted *up-up-down* state can however form within the manifold of allowed canted-I states. This may be beyond the detection of the current powder measurements, or, alternatively, we envision that quantum fluctuations or other exchange interactions may lead to a slightly different ground state from those predicted in the purely 2D classical XXZ phase diagram. Despite this difference, the dynamics calculated from the classical 2D model are likely to be relatively insensitive to small differences in the ordered phase such as a small degree of noncollinear canting predicted
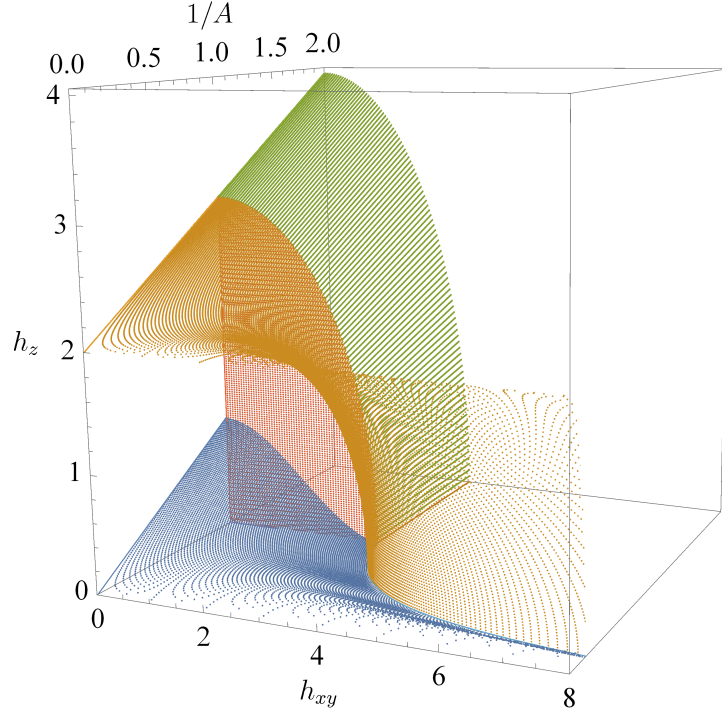
Figure 2.5: Classical phase diagram of the 2D XXZ model on a triangular lattice in presence of magnetic field. The 3D phase space is parameterized by (h_{xy}, A^{-1}, h_z), where $h_{xy} = \sqrt{h_x^2 + h_y^2}$. Only first octant $(h_{xy} \geq 0, A^{-1} \geq 0, h_z \geq 0)$ is considered. The blue surface separates the "Y" and the "V" phases; the red plane separates the phases between the $A < 1$ and the $A > 1$ regions; the green surface separates the "canted-I" and the "paramagnetic" phases in the region $A < 1$, and the orange surface separates the "V" and the "paramagnetic" phases in the region $A > 1$.

in the present model.

2.5 Inter-layer effects

Next we consider the effect of couplings between the layers. We regard the inter-layer couplings always as small compared to the intra-layer ones. Thus to a first approximation, we ask how the interlayer Hamiltonian, H', behaves when *projected* into the space of states whose order or correlations is set by the 2d interactions.

2.5.1 Three-sublattice regime

If the 2d system is in the regime with three-sublattice correlations, we should consider the energy of an arbitrary state with the three-sublattice structure *in each layer*, and find the energy due to interlayer couplings. We further assume that the system is periodic under translation by three layers. There will then be 9 sublattices, labeled by a sublattice index $s = 0, \ldots, 9$. We can define this by the condition

$$\boldsymbol{S}_i = S\boldsymbol{n}_s, \qquad \boldsymbol{r}_i = m\boldsymbol{a}_1 + n\boldsymbol{a}_2 + \frac{l}{3}(2\boldsymbol{a}_1 + \boldsymbol{a}_2 + \boldsymbol{c}), \qquad s = 3\mathrm{Mod}[l, 3] + \mathrm{Mod}[-m - n, 3]. \tag{2.27}$$

Now we can express the inter-layer energy in terms of the 9 sublattice magnetizations $\boldsymbol{n}_s$:

$$9E_{il}/(NS^2) = \sum_{l=0}^{2} \sum_{p=0}^{2} \sum_{q=0}^{2} \left\{ J'_{xy} \left(n^x_{s(l,p)} n^x_{s'(l,p,q)} + n^y_{s(l,p)} n^y_{s'(l,p,q)} \right) + J'_z n^z_s n^z_{s'} \right.$$
$$\left. + J'_c \left(\boldsymbol{f}_q \cdot \boldsymbol{n}_s \right) \left(\boldsymbol{f}_q \cdot \boldsymbol{n}_{s'} \right) + J'_{cz} \left[\left(\boldsymbol{f}_q \cdot \boldsymbol{n}_s \right) n^z_{s'} + n^z_s \left(\boldsymbol{f}_q \cdot \boldsymbol{n}_{s'} \right) \right] \right\},$$

where

$$s(l, p) = 3l + p, \qquad s'(l, p, q) = 3\mathrm{Mod}[l + 1, 3] + \mathrm{Mod}[p + q, 3], \tag{2.28}$$

and

$$\boldsymbol{f}_q = \begin{pmatrix} \cos\left(\frac{\pi}{6} + \frac{2\pi q}{3}\right) \\ \sin\left(\frac{\pi}{6} + \frac{2\pi q}{3}\right) \\ 0 \end{pmatrix}. \tag{2.29}$$

The first two terms can be readily rewritten to simplify the energy to

$$9E_{il}/(NS^2) = \sum_{l=0}^{2} \left\{ J'_{xy} \left(m_l^x m_{l+1}^x + m_l^y m_{l+1}^y \right) + J'_z m_l^z m_{l+1}^z + \sum_{pq} \left(J'_c \left(\boldsymbol{f}_q \cdot \boldsymbol{n}_s \right) \left(\boldsymbol{f}_q \cdot \boldsymbol{n}_{s'} \right) \right. \right.$$
$$\left. \left. + J'_{cz} \left[\left(\boldsymbol{f}_q \cdot \boldsymbol{n}_s \right) n_{s'}^z + n_s^z \left(\boldsymbol{f}_q \cdot \boldsymbol{n}_{s'} \right) \right] \right) \right\},$$

where

$$\boldsymbol{m}_l = \sum_{p=0}^{2} \boldsymbol{n}_{3l+p} \tag{2.30}$$

is the total magnetization per unit cell of layer l. Note that in this case the last two terms do not drop out or simplify as they do for the intralayer couplings, because the sublattice indices s and s' are a function of q, which means the q sum is not trivial.

Examining Eq. (2.30), we see that the XXZ type inter-layer couplings J'_{xy} and J'_z depend on the spin configurations only through the layer magnetizations $\boldsymbol{m}_l$. This *vanishes* in the three-sublattice states favored by the 2d interactions. Thus, at this level, the interlayer XXZ exchanges are completely ineffective at coupling the layers and creating 3d order. This is simply because each spin is symmetrically coupled to three spins on a triangle in the layers above and below it, whose sum is zero. Thus the J'_{xy} and J'_z interactions are fully frustrated by the 2d three-sublattice order.

This conclusion is perturbative in J'_{xy} and J'_z. But in fact the frustration is even stronger. For the XXZ model with $J_c = J'_c = J_{cz} = J'_{cz} = 0$, Rastelli and Tassi[125] have found the exact classical ground states for arbitrary $J_{xy}, J_z, J'_{xy}, J'_z$. In a wide regime, the ground states form a *line of degenerate spirals* which are *close* to the three-sublattice 120° state but have in general an incommensurate wavevector with an *arbitrary* component

76

k_z normal to the plane. The continuous family of spiral wavevectors echoes the full frustration in the perturbative limit, and shows that frustration remains in the XXZ model non-perturbatively.

We now return to the perturbative analysis, and consider the effects of the anisotropy terms J'_c and J'_{cz}. We suppose each layer has a $120°$ three-sublattice configuration, and ask how they are coupled. A general form for such a configuration is

$$\hat{\boldsymbol{n}}_{lp} = \begin{pmatrix} \cos(\frac{2\pi\sigma_l p}{3} + \phi_l) \\ \sin(\frac{2\pi\sigma_l p}{3} + \phi_l) \\ 0 \end{pmatrix}, \tag{2.31}$$

where $\sigma_l = \pm 1$ is the vector spin chirality of the triad of three spins in layer l, and $s = 3l + p$ as usual. For this ansatz, $\boldsymbol{m}_l = 0$. The inter-layer energy becomes

$$
\begin{aligned}
9E_{il}/(NS^2) &= J'_c \sum_{l,p,q} \cos\left(\frac{2\pi\sigma_l p}{3} + \phi_l - \frac{\pi}{6} - \frac{2\pi q}{3}\right) \cos\left(\frac{2\pi\sigma_{l+1}(p+q)}{3} + \phi_{l+1} - \frac{\pi}{6} - \frac{2\pi q}{3}\right) \\
&= \frac{J'_c}{2} \sum_{l,p,q} \left[\cos\left(\frac{2\pi(\sigma_l p + \sigma_{l+1}(p+q))}{3} + \phi_l + \phi_{l+1} - \frac{\pi}{3} - \frac{4\pi q}{3}\right)\right. \\
&\qquad\qquad \left. + \cos\left(\frac{2\pi(\sigma_l p - \sigma_{l+1}(p+q))}{3} + \phi_l - \phi_{l+1}\right)\right] \\
&= \frac{J'_c}{2} \sum_{l,p,q} \cos\left(\frac{2\pi(\sigma_l p + \sigma_{l+1}(p+q))}{3} + \phi_l + \phi_{l+1} - \frac{\pi}{3} - \frac{4\pi q}{3}\right).
\end{aligned}
$$

One immediately sees that, because we took an in-plane configuration, J'_{cz} drops out trivially. In passing to the last line we noticed that the sum over q always gives zero in the final term of the previous line, and so dropped it. The final form may also vanish under summation. The sum over q will vanish here unless $\sigma_{l+1} = -1$, in which case the q dependence drops inside the cosine. Then we see that the sum over p will vanish unless

$\sigma_l = -\sigma_{l+1} = +1$. So finally we have

$$9E_{il}/(NS^2) = \frac{9}{2}J'_c\sum_l \cos\left(\phi_l + \phi_{l+1} - \frac{\pi}{3}\right)\delta_{\sigma_l,1}\delta_{\sigma_{l+1},-1}. \qquad (2.32)$$

Actually in this analysis we do not need to assume threefold periodicity in the c direction, and can take l to just sum over all the layers in the crystal.

Based on Eq. (2.32), we can address how frustrated the remaining J'_c inter-layer coupling is. First, if the chiralities are the same in all layers then the energy due to J'_c vanishes. This is entirely independent of the overall angle ϕ_l within each layer. Second, a pair of adjacent layers can lower its energy by choosing the "lower" one (smaller z) to have "positive" chirality $\sigma_l = 1$ and the upper one negative, and then choosing $\phi_l + \phi_{l+1} = -2\pi/3$ (for $J'_c > 0$). However, the J'_c interaction between the upper layer and the next layer then is guaranteed to vanish, as is the interaction between the lower layer and the next lower one. So the best configuration is one in which layers alternate chirality and gain energy from every other pair. There are two possible staggered orders of chirality. For example, we can take $\sigma_l = (-1)^l$. In this case the energy lowering comes from the interaction between spins with even l and those with odd $l + 1$. Moreover, spins in those pairs of layers are correlated, while between these pairs there is no correlation. For $2N$ layers there are N free angles ϕ_{2n} remaining. So there is still quite a bit of degeneracy. However, it is also clear that, in this pattern of spins, translational symmetry by 3 in the vertical direction is necessarily broken.

In summary: the presence of a high degree of degeneracy even once the J'_c interactions have been included indicates that the interlayer coupling of the three-sublattice order is

frustrated even with the most general exchange interactions. This suggests a strong suppression of ordering when the 2d exchanges are in this regime, in zero magnetic field (which we have assumed).

2.5.2 Stripe regime

Now we suppose the individual layers are in the stripe regime of the classical phase diagram. We consider the effect of interlayer interactions on these stripes to see how they couple together to form 3d order. Suppose, as in Eq. (2.10), the spins in the layer $z = l = 0$ order into ferromagnetic stripes along the x axis, with spins oriented along y. Now consider the next exchange field on the spins in the layer at $z = 1/3$. Each spin in that layer receives contributions from three spins from a triangle in the $z = 0$ layer. Consequently, even for simple Heisenberg or XY coupling J' between the layers, there is a net exchange field on each site in the $z = 1/3$ layer, which aligns those spins into a unique preferred pattern in the next layer. This pattern also consists of ferromagnetic chains along x and moments along y. If one assumes antiferromagnetic J', each spin on the $z = 1/3$ layer is antiparallel to two spins on the triangle below it. Repeating this process leads to a globally determined ordering pattern. The interlayer coupling in the stripe state is therefore *unfrustrated* and the ground state degeneracy of the stripe is just that of a single layer, i.e. 6.

The 3d ordering pattern that results in the way just described has symmetry under a three-dimensional translation by the vector $\boldsymbol{t} = (-\boldsymbol{a}_1 - 2\boldsymbol{a}_2 + \boldsymbol{c})/3$. So due to the

79

in-plane doubled unit cell, in total it has just a doubled unit cell.

The lack of frustration of the interlayer coupling in the stripe state suggests that a system whose 2d interactions favor the stripe order will likely stabilize 3d ordering through the inter-layer interactions. Since this does not occur in $NaYbO_2$, we argue by contradiction that this material is likely to be in the parameter regime in which the 2d exchanges favor three-sublattice 120° order and not the stripe state. This corresponds to the XXZ regime with not too strong J_c interactions.

2.6 Simulation for the dynamic spin structure factor

In this section, we study the excitations of the 2d triangular XXZ model using linear spin wave theory and present simulation results for the dynamic spin structure factors.

2.6.1 Linear spin wave theory

Define an orthogonal basis $(\boldsymbol{p}_s, \boldsymbol{q}_s, \boldsymbol{n}_s)$ for each classical spin $\boldsymbol{n}_s$, $s = 0, 1, 2$. The standard Holstein-Primakoff transformation is

$$\boldsymbol{S}_i \cdot \boldsymbol{p}_s = \sqrt{2S}\frac{a_i + a_i^\dagger}{2}, \qquad \boldsymbol{S}_i \cdot \boldsymbol{q}_s = \sqrt{2S}\frac{a_i - a_i^\dagger}{2i}, \qquad \boldsymbol{S}_i \cdot \boldsymbol{n}_s = S - a_i^\dagger a_i, \qquad (2.33)$$

or

$$\boldsymbol{S}_i = \sqrt{2S}M_s K \begin{pmatrix} a_i \\ a_i^\dagger \end{pmatrix} + \boldsymbol{n}_s(S - a_i^\dagger a_i), \qquad (2.34)$$

where $a_i^\dagger$ and a_i are the boson creation and annihilation operators for spin excitations, and we defined

$$M_s = \begin{pmatrix} \boldsymbol{p}_s & \boldsymbol{q}_s \end{pmatrix} \qquad \text{and} \qquad K = \frac{1}{2}\begin{pmatrix} 1 & 1 \\ -i & i \end{pmatrix}. \tag{2.35}$$

Plugging Eq. (2.34) into the Hamiltonian (2.12) (setting $D = 0$), keeping terms only of the order S and doing a Fourier transform, we arrive at a quadratic Hamiltonian for the bosons:

$$H_{2d,B}[a, a^\dagger] = \sum_{\boldsymbol{k} \in \mathrm{BZ}^+} \Phi_{\boldsymbol{k}}^\dagger \mathcal{H}(\boldsymbol{k}) \Phi_{\boldsymbol{k}}, \tag{2.36}$$

where BZ^+ is half of the Brillouin zone which is mapped to the other half by momentum inversion, and we defined $\Phi_{\boldsymbol{k}} = \left(a_{\boldsymbol{k},0}, a_{\boldsymbol{k},1}, a_{\boldsymbol{k},2}, a_{-\boldsymbol{k},0}^\dagger, a_{-\boldsymbol{k},1}^\dagger, a_{-\boldsymbol{k},2}^\dagger \right)^T$,

$$\mathcal{H}(\boldsymbol{k}) = \begin{pmatrix} J_0 & [J_{0,1}]_{11} & [J_{2,0}]_{11}^* & 0 & [J_{0,1}]_{12} & [J_{2,0}]_{21}^* \\ [J_{0,1}]_{11}^* & J_1 & [J_{1,2}]_{11} & [J_{0,1}]_{21}^* & 0 & [J_{1,2}]_{12} \\ [J_{2,0}]_{11} & [J_{1,2}]_{11}^* & J_2 & [J_{2,0}]_{12} & [J_{1,2}]_{21}^* & 0 \\ 0 & [J_{0,1}]_{21} & [J_{2,0}]_{12}^* & J_0 & [J_{0,1}]_{22} & [J_{2,0}]_{22}^* \\ [J_{0,1}]_{12}^* & 0 & [J_{1,2}]_{21} & [J_{0,1}]_{22}^* & J_1 & [J_{1,2}]_{22} \\ [J_{2,0}]_{21} & [J_{1,2}]_{12}^* & 0 & [J_{2,0}]_{22} & [J_{1,2}]_{22}^* & J_2 \end{pmatrix}, \tag{2.37}$$

and

$$J_{s,s+1} = 2S \left(\sum_{\mu=1,2,3} e^{i\boldsymbol{k}\cdot\boldsymbol{a}_\mu} \right) K^\dagger M_s^\dagger J M_{s+1} K, \tag{2.38}$$

$$J_s = -3S\boldsymbol{n}_s^T J(\boldsymbol{n}_{s+1} + \boldsymbol{n}_{s-1}) + \mu_B \boldsymbol{B}^T g \boldsymbol{n}_s, \tag{2.39}$$

where $J \equiv \mathrm{diag}(J_{xy}, J_{xy}, J_z)$, $g = \mathrm{diag}(g_{xy}, g_{xy}, g_z)$. Combined with our knowledge of the classical ground state spin configuration in Sec. 2.4.4, the following can be deduced:

- The diagonal entries (2.39) are the classical energy cost of a spin flip $\boldsymbol{S} \to -\boldsymbol{S}$. The flip changes the exchange energy $-3S\boldsymbol{n}_s^T J(\boldsymbol{n}_{s+1} + \boldsymbol{n}_{s-1})$ and the Zeeman energy

$\mu_B \boldsymbol{B}^T g \boldsymbol{n}_s$. The off-diagonal entries (2.38) describe quantum fluctuations due to boson hopping.

- In the easy-plane limit $r > 1$, since all three classical spins have the same z component $n_s^z = \frac{m_z}{r+2}$, we have

$$J_s = 3S J_{xy}, \qquad s = 0, 1, 2. \tag{2.40}$$

At $\Gamma = (0, 0)$ the spectrum is gapless, due to the Goldstone mode of the broken U(1) symmetry. Furthermore, at K $= (0, \pm\frac{4\pi}{3\sqrt{3}a})$, the Hamiltonian is purely diagonal, and the energy is just the value of J_s in (2.40), which is three fold degenerate.

- In the extreme easy-axis limit $r \ll 1$ with a perpendicular field $\boldsymbol{B} = (0, 0, 1)B$, the system is classical and again we are left with only diagonal elements in the Hamiltonian. The ground state in a large magnetic field range is the up-up-down state with excitation energy

$$J_0 = J_1 = \mu_B g_z B, \qquad J_2 = 6J_z S - \mu_B g_z B. \tag{2.41}$$

Finally, let us comment on the criterion of selecting the classical ground state $\boldsymbol{n}_{0,1,2}$ which serves as the input to linear spin wave theory. The issue arises when the classical ground state is degenerate (as in the "canted" phase), and different states in the degeneracy manifold may lead to different dynamic spin structure factor patterns. Whenever degeneracy happens, it can be shown that a classical ground state is fully determined by the choice of in-plane components of the spin vector, $\boldsymbol{m}_s = (n_s^x, n_s^y, 0)$. Without loss of generality we define $|\boldsymbol{m}_0| \leq |\boldsymbol{m}_1| \leq |\boldsymbol{m}_2|$. Our criterion is always to pick $\boldsymbol{n}_{0,1,2}$ such that

$\boldsymbol{m}_0$ and $\boldsymbol{m}_1$ have the smallest angle between them. This criterion is chosen to mimic the fact that, in real triangular systems, quantum fluctuation tends to favor states in the degenerate manifold in which spins are maximally collinear.

2.6.2   Dynamic spin structure factor

The dynamic spin structure factor, by definition, is

$$\mathcal{S}(\boldsymbol{k},\omega) = \sum_{\mu,\nu}(\delta_{\mu\nu} - (\hat{\boldsymbol{k}})_\mu(\hat{\boldsymbol{k}})_\nu)\sum_{s,s'}\langle m_s^\mu(-\boldsymbol{k},-\omega)m_{s'}^\nu(\boldsymbol{k},\omega)\rangle, \tag{2.42}$$

where $m_s^\mu(\boldsymbol{k},\omega) = \mu_B \sum_\kappa g^{\mu\kappa}S_s^\kappa(\boldsymbol{k},\omega)$, and $\hat{\boldsymbol{k}}$ is the unit vector with orientation of $\boldsymbol{k}$. After some derivation, we can write $S(\boldsymbol{k},\omega)$ concisely as

$$\mathcal{S}(\boldsymbol{k},\omega) = \sum_{e=1,2,3} 2S\mu_B^2\delta(\omega - \lambda_{\boldsymbol{k}}^e)\left[V^\dagger(\boldsymbol{k})\widetilde{Q}^\dagger\widetilde{M}^\dagger g^\dagger\left(1_{3\times3} - \hat{\boldsymbol{k}}\hat{\boldsymbol{k}}^T\right)g\widetilde{M}\widetilde{Q}V(\boldsymbol{k})\right]_{e,e}, \tag{2.43}$$

where we defined $\widetilde{M} = \begin{pmatrix} \boldsymbol{p}_0 & \boldsymbol{p}_1 & \boldsymbol{p}_2 & \boldsymbol{q}_0 & \boldsymbol{q}_1 & \boldsymbol{q}_2 \end{pmatrix}$, and $\widetilde{Q} = K \otimes 1_{3\times3}$. V is the matrix that diagonalizes $\mathcal{H}$: $V^\dagger\mathcal{H}V = \Lambda$ with energies stored in the diagonal matrix $\Lambda = \mathrm{diag}(\lambda^1, \lambda^2, \lambda^3, \lambda^1, \lambda^2, \lambda^3)$. Commutation relation of the bosons in the old and the new bases requires $V(\sigma_3 \otimes 1_{3\times3})V^\dagger = \sigma_3 \otimes 1_{3\times3}$.

To connect to the experiment, we define the momentum-orientation-averaged spin structure factor

$$\overline{\mathcal{S}}_{\boldsymbol{B}}(k,\omega) = \frac{1}{4\pi}\int_\pi^0 \sin\theta d\theta \int_0^{2\pi} d\phi\, S_{\boldsymbol{B}}(k\sin\theta\cos\phi, k\sin\theta\sin\phi, \omega), \tag{2.44}$$

where we have used subscript $\boldsymbol{B}$ to remind us of the field dependence. Furthermore, we

83

define the magnetic-orientation-averaged spin structure factor

$$\bar{\bar{\mathcal{S}}}(k,\omega) = \frac{1}{4\pi}\int_\pi^0 \sin\theta_B d\theta_B \int_0^{2\pi} d\phi_B\, \bar{\mathcal{S}}_{B(\sin\theta_B\cos\phi_B,\sin\theta_B,\sin\phi_B,\cos\theta_B)}(k,\omega). \qquad (2.45)$$

Admittedly, such a spin structure factor (2.45) in which the momentum and magnetic field orientations are *independently* averaged does not fully correspond to the experimental measurement: the neutron scattering measurement averages over the grain orientations of the powder sample, which is equivalent to averaging over momentum and magnetic field orientations that are *locked* with a definite relation. Nevertheless our choice of averaging is justified by the robust spectral features (e.g. the isolated high energy flat intensity) observed in a large region with easy-plane near-Heisenberg exchange and in the extreme easy-axis region.

Now we describe the results for the dynamic spin structure factors. We present two representative parameter points near the Heisenberg limit: the first one has weak easy-axis anisotropy with $(J_z, J_{xy}) = (0.5, 0.45)\,\text{meV}$, and the second one has weak easy-plane anisotropy with $(J_z, J_{xy}) = (0.45, 0.51)\,\text{meV}$. The magnetic field is set to be $5\,\text{T}$ in both cases but its orientation is varied. The simulated structure factor plots are shown in Fig. 2.6.

$(J_z, J_{xy}) = (0.5, 0.45)\,meV$. When the magnetic field is along z direction, the classical ground state has a coplanar three-sublattice order [see Fig. 2.6(a)]. The lowest energy band becomes gapless at Γ (Goldstone mode), corresponding to zero energy structure factor intensity at $|\boldsymbol{Q}| \approx 1.25\,\text{Å}^{-1}$. The highest energy band is almost flat on the boundary

of the magnetic order Brillouin zone, which accounts for the structure factor intensity plateau at $0.8\,\mathrm{meV}$. In addition, the highest band has energy minimum at Γ, which is reflected in the downturn of the high energy intensity plateau at small reciprocal lattice $|\boldsymbol{Q}| \to 0$. As the magnetic field develops an in-plane component [see Fig. 2.6(b) for $\theta_B = 75°$], the highest band becomes less flat and the highest band energy at Γ increases; at $\theta_B \approx 70°$ Γ becomes the energy maximum, making the structure factor intensity as $|\boldsymbol{Q}| \to 0$ also at the highest energy. The destruction of the high energy flat bands and the appearance of structure factor intensity at energy maximum as $|\boldsymbol{Q}| \to 0$, both due to large in-plane field component, are generic features of the easy-axis phase region in the parameter range we considered, and consequently one observes an upturn of the high energy intensity as $|\boldsymbol{Q}| \to 0$ in the $\overline{\overline{\mathcal{S}}}(k,\omega)$ plot, with no well-defined isolated high energy intensity plateau.

$(J_z, J_{xy}) = (0.45, 0.51)\,meV.$ When the magnetic field is along z direction the classical ground states form a degeneracy manifold of the "canted" type. Since the z spin component is small in the parameter range we considered [see Fig. 2.6(c)], the spin order is almost coplanar, and consequently the spin structure factor resembles the previous case $(J_z, J_{xy}) = (0.5, 0.45)\,\mathrm{meV}$. In addition to the gapless energy band at Γ (Goldstone mode), threefold energy degeneracy appears at K and its equivalent points [whose energies are given in Eq. (2.40)]. There is no global flat energy bands at high energy, and indeed when the magnetic field is along z, there is no well-defined high energy flat intensity in the structure factor plots. Nevertheless, as the magnetic field develops an in-plane

component, *isolated* structure factor intensity plateau emerges as the magnetic field angle θ_B exceeds $30°$ [see Fig. 2.6(d)) for $\theta_B = 75°$]. The emergence of such isolated intensity plateau due to in-plane field component is a generic feature of the Heisenberg limit with weak easy-plane anisotropy, and persists through $1 < r < 1.6$ in the parameter range we considered. The highest energy band has a local minimum at Γ for all magnetic field orientation (unlike the easy-axis case), which accounts for the downturn of the isolated high energy intensity plateau at small reciprocal lattice $|\boldsymbol{Q}| \to 0$ in the $\overline{\overline{\mathcal{S}}}(k, \omega)$ plot.

Here we present further numerical result of the two-step averaged dynamic spin structure factor $\overline{\overline{\mathcal{S}}}(Q, \omega)$ for various field strengths, see Fig. 2.7. As we expect that the ground state of $NaYbO_2$ is strongly renormalized by quantum fluctuations, this model only captures features in the field-induced ordered state of $NaYbO_2$ where quantum fluctuations in the material are suppressed. Three main features can be observed immediately:

Region 1: Zero energy intensity at the two-dimensional magnetic zone center $\boldsymbol{Q} = (1/3, 1/3, 0)$ ($|Q| = 1.25$ Å^{-1}) can be observed for a large range of field values, indicating the existence of gapless Goldstone mode at Γ point. The zero energy intensity is the highest at zero field with a sharp linear dispersion, and as field starts to increase, such zero energy intensity decreases, while the intensity at low but finite energy begins to develop. The zero energy intensity becomes extremely weak but still observable as the field goes beyond 13 T, and finally vanishes entirely at high field values 22 T. Such behavior of the gapless intensities can be understood from the classical ground state: the ground state belongs to the "canted-I" phase, which forms 1D degenerate ground state manifold

and possesses one Goldstone mode for generic field directions and strength. As field increases, the configuration with in-plane field first reaches critical field at $12\,\mathrm{T}$, and the structure factor of such configuration becomes gapped due to the vanishing of Goldstone modes. As field further increases, more and more configurations reach their critical field and become gapped, and at $B \sim 21\,\mathrm{T}$ the last gapless configuration (corresponding to a perpendicular field) vanishes, leaving behind a fully gapped low energy intensities.

Region 2: A flat intensity region is discernible at fields smaller than $\sim 6\,\mathrm{T}$. At zero field, the flat intensity appears at energy $E \sim 0.8\,\mathrm{meV}$; as field increases, the flat region starts to split and form two flat regions, one moving towards higher energy and the other towards lower energy. The higher energy flat region approaches $E \sim 1.0\,\mathrm{meV}$ at $B = 5\,\mathrm{T}$, which corresponds to the observed flat intensity in neutron scattering experiments at the same field strength. As field further increases, the higher and lower energy flat intensities vanish at $B \sim 6.5\,\mathrm{T}$ and $\sim 8.5\,\mathrm{T}$, respectively.

Region 3: The behavior of the intensities at zero momentum $|Q| \sim 0$ change drastically as field is varied. When the field is small, the zero momentum intensity is weak and at low energy, resulting a visual downturn from the higher energy flat intensities. As field increases, the zero momentum intensity also increases and moves towards higher energies; the downturn finally vanishes at $B = 5.5\,\mathrm{T}$, resulting a globally flat intensity across all the plotted momenta. Further increasing the field will result in an upturn of the zero momentum intensity, meaning the zero momentum intensity further increases and become the highest energy intensity in the plot. The evolution of the zero momentum

87

intensity is closely related to the large in-plane component of the field [14]; after the field exceeds the in-plane critical field $B_{xy,c}$, the configuration with an in-plane field has a gapped spin wave spectrum, which is responsible for the highly dispersed, high intensity branch of the plot.

As a comparison, figures 2.8 shows the field-dependent evolution of the INS spectrum of $NaYbO_2$ powder across a series of fields spanning from 0 T to 10 T. At zero-field, $NaYbO_2$ contains a continuum of excitations from the quantum disordered ground state that evolve into the *up-up-down* ordered phase as reported above [14]. The diffuse continuum is centered about the two-dimensional magnetic zone center $\boldsymbol{Q} = (1/3, 1/3, 0)$ with a bandwidth of approximately 1 meV. With increasing field at base temperature, the spectral weight condenses and splits, with part of it coalescing into the elastic line and part of it pushed upward within a nearly flat, powder-averaged band near 1 meV in the ordered state (Figure 2.8). Upon exiting the ordered state at 10 T, the remaining resolvable scattering in this energy window primarily resides above the two-dimensional magnetic zone center $\boldsymbol{Q} = (1/3, 1/3, 0)$ ($|Q| = 1.25$ Å^{-1}) and the $(0, 0, 3)$ Bragg peak ($|Q| = 1.15$ Å^{-1}).
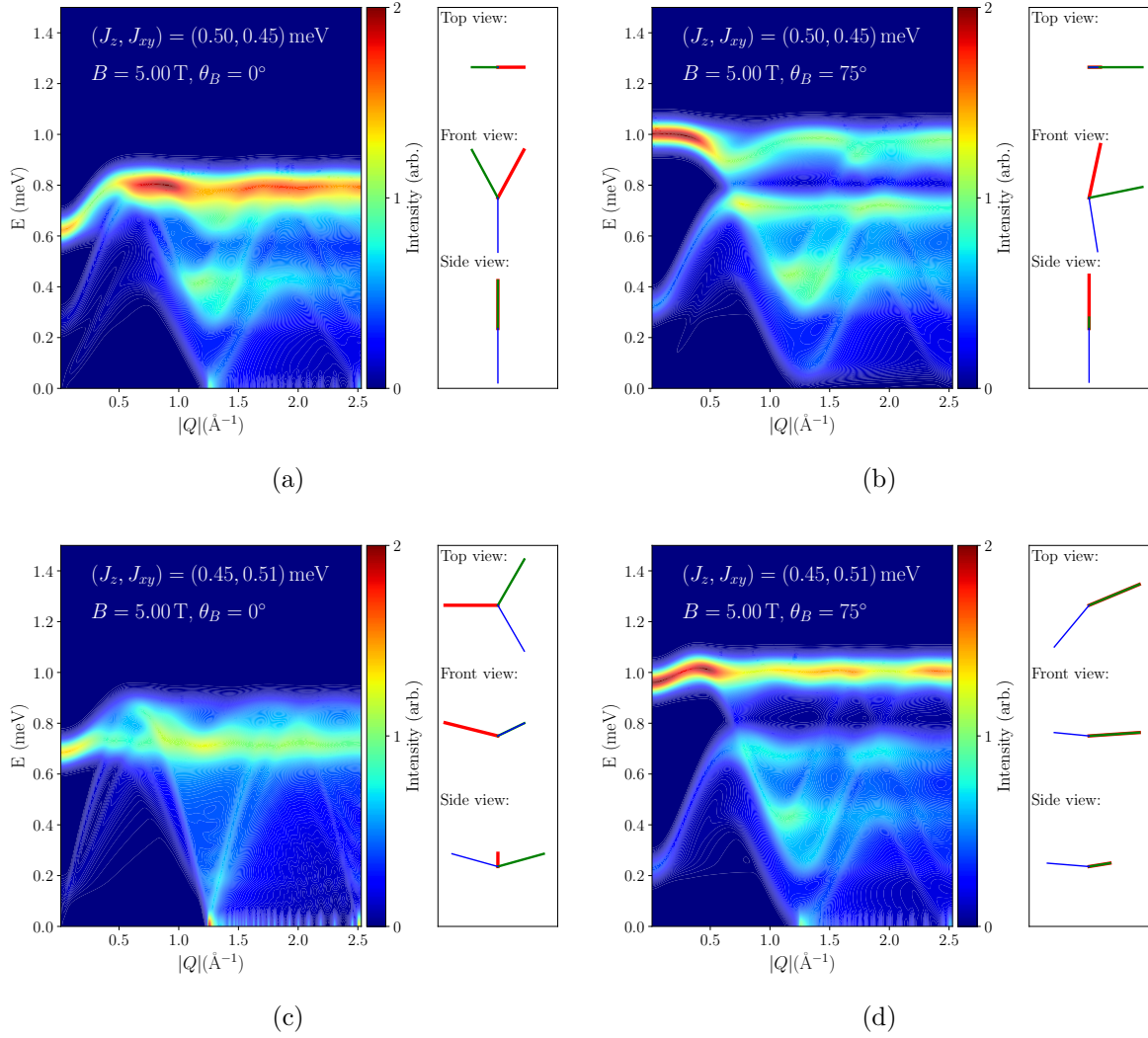
Figure 2.6: Dynamic spin structure factor $\overline{\mathcal{S}}(k, \omega)$ and the classical three-sublattice (red, green and blue) spin ground state from different views. The exchange parameters are (a,b) $(J_z, J_{xy}) = (0.5, 0.45)\,\text{meV}$, and (c,d) $(J_z, J_{xy}) = (0.45, 0.51)\,\text{meV}$. Field strength is fixed at $B = 5\,\text{T}$, while the field orientation is tilted from the z axis with an angle of either (a,c) $\theta_B = 0°$ or (b,d) $\theta_B = 75°$.
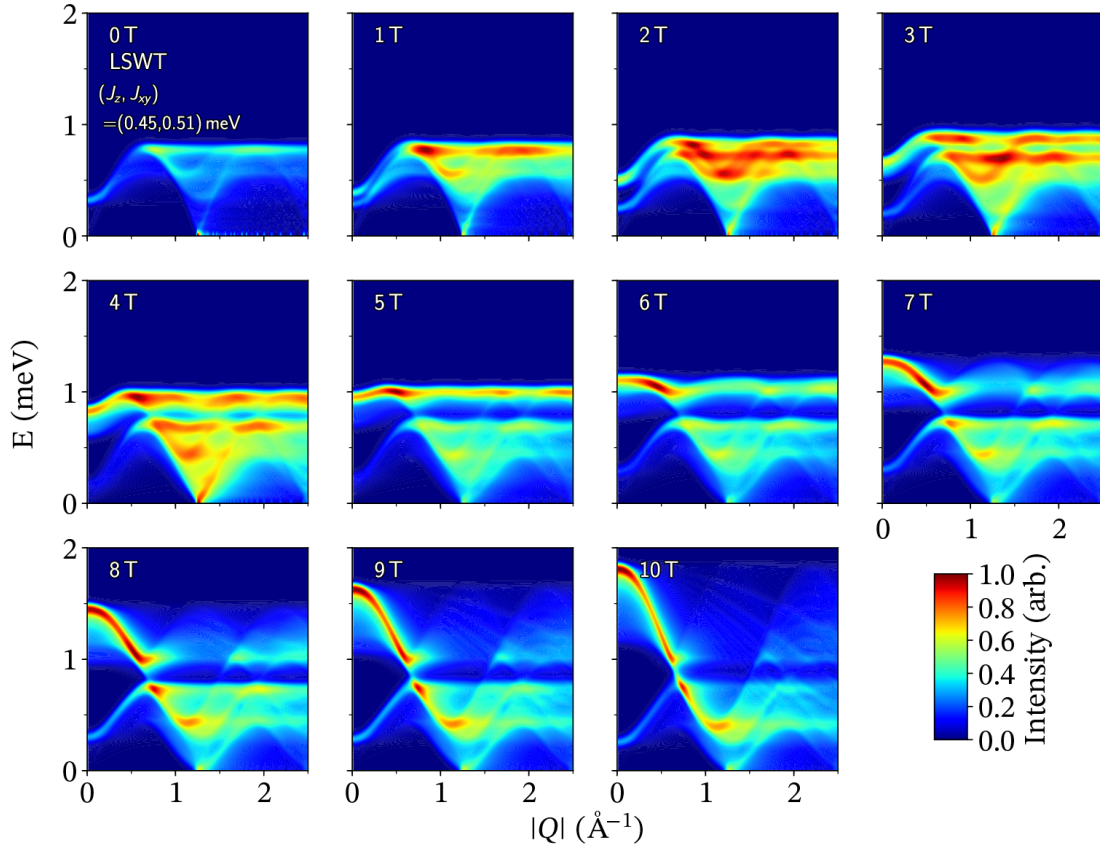
Figure 2.7: Linear spin wave theory (LSWT) calculations showing $S(Q, \hbar\omega)$ as a function of field for powder-averaged Yb^{3+} ions on a two-dimensional triangular lattice assuming three-sublattice ordering derived from the proposed spin model for $NaYbO_2$ [14]. At 0 T, $NaYbO_2$ does not show magnetic ordering, and therefore LSWT fails to capture the continuum of excitations from the quantum disordered ground state.
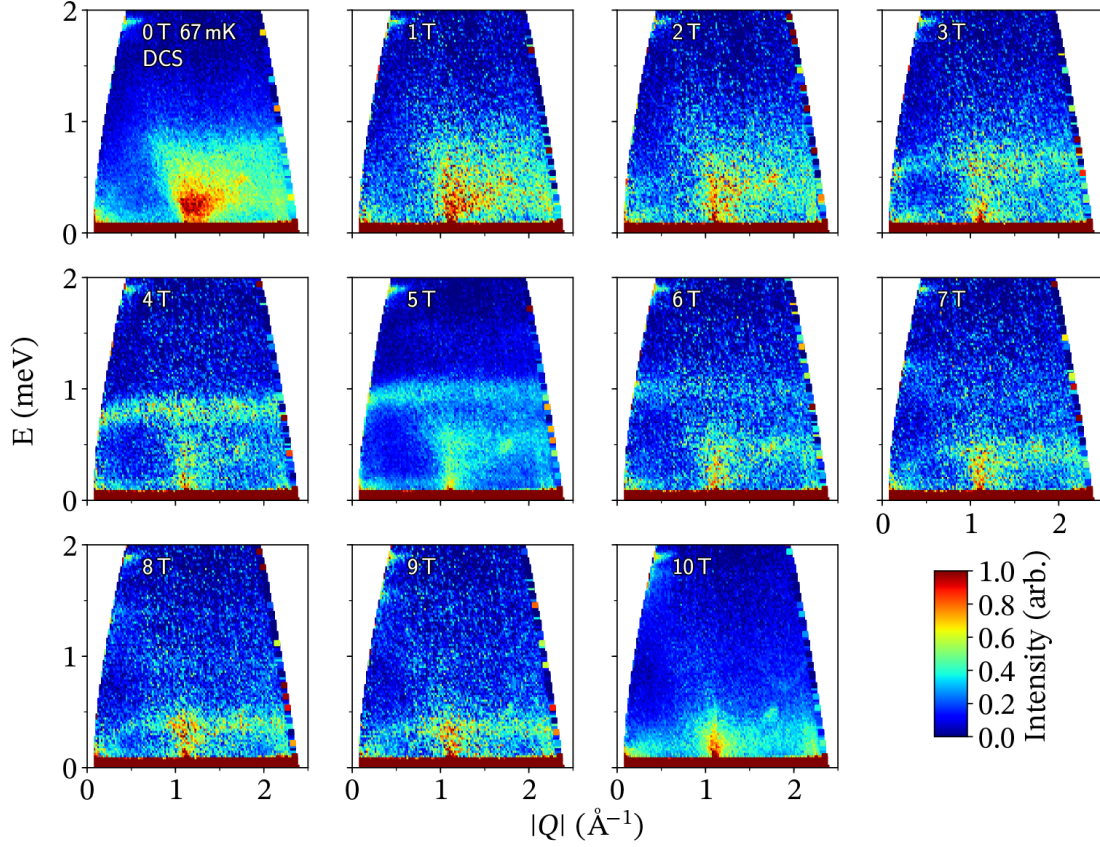
Figure 2.8: Low energy inelastic neutron scattering (INS) spectrum $S(Q, \hbar\omega)$ of NaYbO$_2$ powder at varying fields collected on DCS. With increasing field, NaYbO$_2$ evolves from a gapless quantum disordered ground state $(0 - 2\,\mathrm{T})$ into an up-up-down equal moment magnetic structure $(3 - 8\,\mathrm{T})$ and a field-polarized state at high field $(9 - 10\mathrm{T})$. Data were collected with longer scans at 0, 5, and 10 T to increase resolution. Detector spurions occur at [0.5 Å^{-1}, 1.8 meV] and [1.75 Å^{-1}, 0.4 meV]. Data were collected between 67 – 100 mK.

Chapter 3

Frustrated Heisenberg $J_1 - J_2$ model within the stretched diamond lattice of LiYbO$_2$

3.1   Introduction

In the field of three-dimensionally frustrated magnets, the predominant research focus has centered on the magnetic diamond and pyrochlore lattices [10, 84, 22, 30, 12, 139, 19, 57, 56, 109, 25, 122, 18, 20, 45, 133]. Both of these frameworks appear within the family of transition-metal spinels of the form AB_2X_4 (A, B = transition metal or metalloid, X = chalcogenide), where the diamond and pyrochlore lattices appear on the A- and B-site sublattices, respectively. Strong magnetic frustration within each of these sublattice

types is known to suppress typical Neél order and instead favor the manifestation of unconventional ground states, including classical spin liquids [109, 25], (quantum) spin ices [122, 18, 20, 133], and (quantum) spiral spin liquids [10, 84, 22].

Quantum fluctuations that manifest in the small spin limit on these lattices further suppress magnetic order and can formulate the basis for highly entangled ground states [83, 5, 138, 167, 184, 21]. At this limit, the magnetic diamond lattice has been less thoroughly studied in comparison to the magnetic pyrochlore lattice, as the magnetic pyrochlore lattice also manifests in a large, well-studied family of rare-earth $Ln_2M_2O_7$ (Ln = lanthanide, M = metal or metalloid) compounds [12, 139, 19, 57, 56, 109, 25, 122, 18, 20, 45, 133]. Furthermore, while introducing model $J_{\text{eff}} = 1/2$ lanthanide moments within frustrated magnetic motifs has shown promise in realizing intrinsically quantum disordered states (e.g. $Yb_2Ti_2O_7$ pyrochlore [133, 47] and triangular lattice $NaYbO_2$ [14, 16, 38, 124]), isolating materials that comparably incorporate model f-electron moments within a diamond lattice framework is a challenge.

Frustration within the diamond lattice is best envisioned by dividing the lattice into two interpenetrating face centered cubic (FCC) lattices with two exchange interactions, J_1 and J_2, where in the Heisenberg limit (Figure 3.1) [10, 84, 22].

$$H = J_1 \sum_{\langle i,j \rangle} \boldsymbol{S}_i \cdot \boldsymbol{S}_j + J_2 \sum_{\langle\langle i,j \rangle\rangle} \boldsymbol{S}_i \cdot \boldsymbol{S}_j \tag{3.1}$$

In the two limits where either J_1 or J_2 is zero, this bipartite system is unfrustrated with a conventional Neél ordered ground state. However, when $J_2 > 0$ and $|J_1| > 0$, ordering becomes frustrated. When $J_2/|J_1| \geq 1/8$, the classical interpretation of this
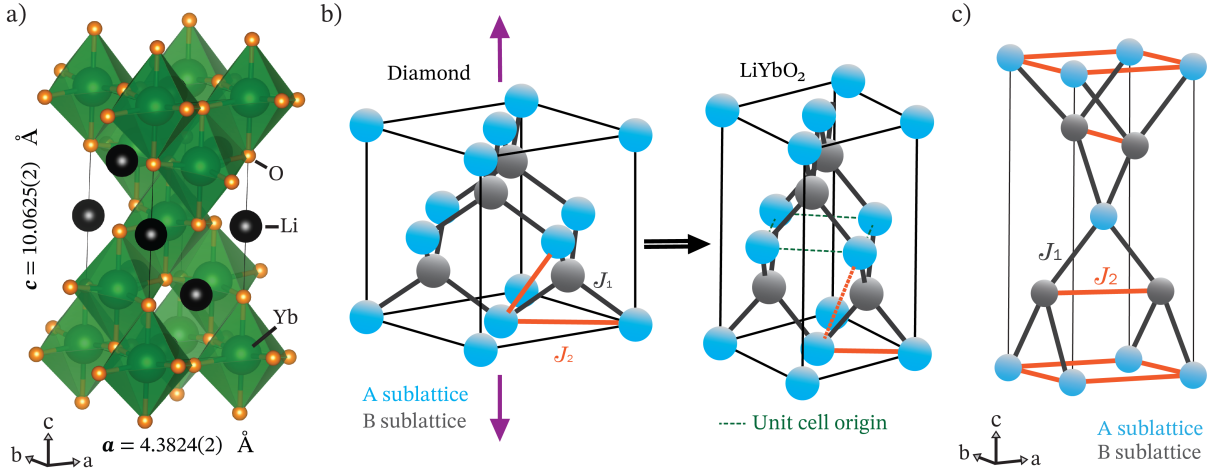
Figure 3.1: a) Crystal structure of $LiYbO_2$ with YbO_6 octahedra shaded in green and black spheres noting the positions of Li ions. b) The frustrated $J_1 - J_2$ model on the diamond lattice consists of two interpenetrating face centered cubic (FCC) sublattices, A and B, with a J_1 (black) magnetic interaction connecting the two sublattices and a J_2 (orange) spanning interactions within an FCC sublattice. When this structure is stretched along one of the cubic axes, the $I4_1/amd$ lattice of $LiYbO_2$ is reproduced where the dashed green line represents the unit cell origin of $LiYbO_2$ shown in panel c). In $LiYbO_2$, the stretched bond (5.909 Å, dashed orange) is 1.527 Å longer than the in-plane J_2 (4.382 Å, solid orange). In the present model for $LiYbO_2$, the stretched bond is assumed negligible in strength relative to the shorter J_2. c) NN (J_1) and NNN (J_2) exchange pathways between Yb-ions in $LiYbO_2$ with Yb ions in the A and B sublattices shaded differently for clarity.

model develops a degenerate ground state manifold of coplanar spin spirals [10, 84, 22]. Each of these spirals can be described by a unique momentum vector, and together the degenerate momentum vectors formulate a spin spiral surface in reciprocal space [10, 84, 22]. The degeneracy of these spin spirals can be lifted entropically via an order-by-disorder mechanism that selects a unique spin spiral state [10, 84, 22], but in the presence of strong quantum fluctuations ($S \leq 1$), long-range order is quenched and a spiral spin liquid ground state manifests that fluctuates about the spiral surface [22].

Identifying materials exhibiting (quantum) spiral spin liquid states derived from this $J_1 - J_2$ model remains an outstanding goal. Transition-metal-based AB_2X_4 spinels have been primarily investigated as potential hosts; however two vexing problems typically occur: (1) non-negligible further neighbor interactions beyond the $J_1 - J_2$ limit arise and lift the degeneracy and (2) weak tetragonal distortions from the ideal $Fm\bar{3}m$ spinel structure appear. For example, detailed investigations of the spinels $MgCr_2O_4$ [158, 4], $MnSc_2S_4$ [44, 71, 79], $NiRh_2O_4$ [22, 26], and $CoRh_2O_4$ [50] have all required expanding the model Hamiltonian to include up to third-neighbor interactions, originating from the large spatial extent of d-orbitals, to describe the generation of their helical magnetic ground states. Within some materials like $NiRh_2O_4$ [22, 26], single ion anisotropies must also be incorporated to digest the experimental results. Complexities with extended interactions beyond the $J_1 - J_2$ limit may also compound with inequivalent exchange pathways that form as the cubic $Fm\bar{3}m$ spinel structure undergoes a distortion to a tetragonal $I4_1/amd$ or $I\bar{4}2d$ space group prior to magnetic ordering (e.g. $NiRh_2O_4$ [22, 26] and $CoRh_2O_4$ [50]).

The tetragonal distortion in spinels can be viewed as a compression of the diamond lattice along one of its cubic axes (opposite to that illustrated in Figure 3.1), and it splits the nominal J_2 of the ideal diamond lattice structure into two different pathways. This disrupts the reciprocal space spiral surface generated in the $J_1 - J_2$ model's cubic limit. Despite these complications common to A-site transition metal spinels, the predictions born from the model Hamiltonian show substantial promise as materials such as $MnSc_2S_4$ [44, 71, 79], $CoAl_2O_4$ [178, 134, 102], and $NiRh_2O_4$ [22, 26] are nevertheless either close

to or partially manifest degenerate spiral spin states. Identifying other crystal struc-

tures that realize comparable physics but with more localized f-electron moments is an

appealing path forward.

Here we present an investigation of an alternative, frustrated diamond lattice frame-

work in the material $LiYbO_2$. This material can be viewed as containing a stretched

diamond lattice of Yb^{3+} moments (Figure 3.1), and it falls within a broader family

of $ALnX_2$ (A = alkali, Ln = lanthanide, X = chalcogenide) materials where the lattice

structure is dictated by the ratio of lanthanide ion radius to alkali plus chalcogenide radii.

Our results show that $LiYbO_2$ realizes the expected ground state derived from a $J_1 - J_2$

Heisenberg model on a tetragonally-elongated diamond lattice and that $J_{\text{eff}} = 1/2$ Yb^{3+}

ions in related materials may act as the basis for applying the Heisenberg $J_1 - J_2$ model

to Ln-ion diamond-like materials. Notably, however, variance between the observed and

predicted phasing of Yb moments on the bipartite lattice as well as the emergence of an

intermediate, partially disordered state suggests the presence of interactions/fluctuation

effects not captured in the classical $J_1 - J_2$ Heisenberg framework.

3.2 Experimental results

3.2.1 Magnetization, susceptibility, and heat capacity results

Figure 3.2 shows the magnetic susceptibility, isothermal magnetization, and a.c. suscepti-

bility measured on powders of $LiYbO_2$. In the low temperature regime where the ground
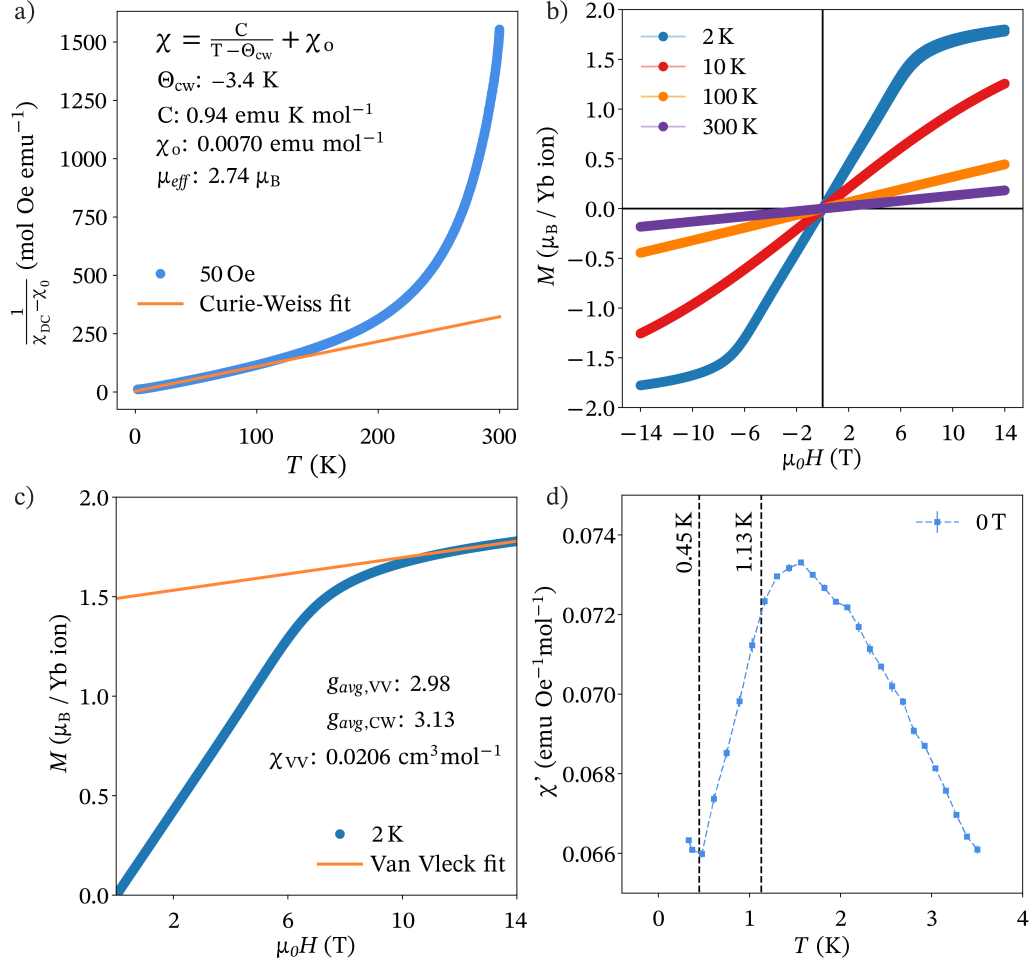
Figure 3.2: a) Temperature dependence of the inverse magnetic susceptibility of LiYbO$_2$. Solid line shows the a Curie–Weiss fit to the data between $20 < T < 100$ K. b) Field dependence of the magnetization collected at a variety of temperatures. c) 2 K isothermal magnetization curve with a linear fit in the saturated state above 10 T. The 0 T intercept ($g_{avg}\mu_B/2$) provides a powder-averaged $g_{avg,VV}$ and the slope provides χ_{VV}. d) a.c. magnetic susceptibility $\chi'(T)$ data collected for $330\,\text{mK} < T < 3.5$ K at zero-field. The two dashes lines at 1.13 K and 0.45 K mark the onset of peaks observed in zero-field heat capacity data.

state Kramers doublet is primarily occupied ($T < 100$ K), data were fit to a Curie–Weiss-type behavior with a $\Theta_{CW} = -3.4$ K and an effective moment $\mu_{eff} = 2.74$ μ_B. This implies a powder-averaged g-factor $g_{avg,CW} = 3.13$ assuming $J_{\text{eff}} = 1/2$ Yb ions. The nonlinearity of the Curie–Weiss fit above 100 K arises due to Van Vleck contribu-
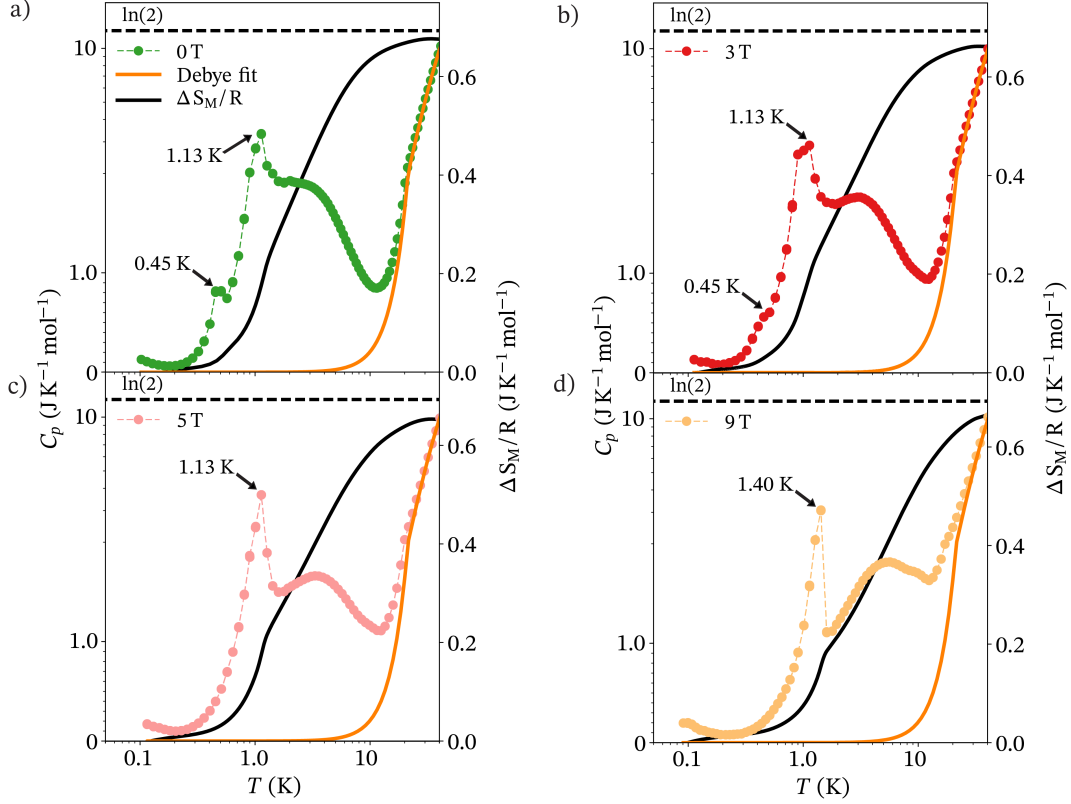
Figure 3.3: a-d) Specific heat $C(T)$ of LiYbO$_2$ collected as a function of temperature under $\mu_0 H = 0$, 3, 4, and 9 T. The integrated magnetic entropy δS_M is overplotted with the data as a black line. Results from a Debye model of lattice contributions to $C(T)$ are shown as orange lines. The horizontal dashed lines represent $R\ln(2)$.

tions to the susceptibility that derive from the CEF splitting of the $J = 7/2$ Yb manifold. In order to independently determine g_{avg}, the χ_{VV} contribution to the total susceptibility was fit in the saturated regime ($\mu_0 H > 10$ T) of the 2 K isothermal magnetization data shown in Figure 3.2. In the near-saturated state, the slope of isothermal magnetization yields $\chi_{VV} = 0.0206\,\mathrm{cm}^3\,\mathrm{mol}_{Yb}^{-1}$ [167], and the intercept of this linear fit with $\mu_0 H = 0$ T was utilized to determine the saturated magnetic moment ($g\mu_B/2$) that corresponds to a powder-averaged $g_{avg,VV} = 2.98$.

Magnetic susceptibility data in Figure 3.2 explore the low temperature magnetic

behavior of LiYbO$_2$. Two low-temperature ($T < 10\,\mathrm{K}$) features appear: The first is a broad cusp in susceptibility centered near $1.5\,\mathrm{K}$ and is an indication of the likely onset of magnetic correlations. The second feature is a small upturn below $0.45\,\mathrm{K}$. When compared with specific heat measurements in Figure 3.3, these two features in $\chi'(T)$ coincide with the two sharp anomalies in $C_p(T)$ at $T_{N1} = 1.13\,\mathrm{K}$ and $T_{N2} = 0.45\,\mathrm{K}$. An additional broad peak also appears in $C(T)$ centered near $2\,\mathrm{K}$, likely indicative of the likely onset of short-range correlations. As discussed later in this manuscript, the two lower temperature peaks in $C_p(T)$ mark the staged onset of long-range magnetic order with T_{N1} marking the onset of partial order with disordered relative phases between the A and B Yb-ion sublattices and with T_{N2} marking the onset of complete order between the two sublattices.

Figure 3.3a) also displays the total magnetic entropy released upon cooling down to $100\,\mathrm{mK}$. Below $200\,\mathrm{mK}$, a nuclear Schottky feature arises from Yb nuclei as similarly observed in NaYbO$_2$ [14]. Integrating C_p/T between $100\,\mathrm{mK}$ and $40\,\mathrm{K}$ shows that 98% of $R\ln(2)$ is reached at $0\,\mathrm{T}$, showing that the ordering is complete by $100\,\mathrm{mK}$. Approximately half of $R\ln(2)$ is released upon cooling through the broad $2\,\mathrm{K}$ peak representing the onset of short range correlations. $C_p(T)$ data were also collected under a series of applied magnetic fields. The onset of T_{N1} stays fixed at $1.13\,\mathrm{K}$ from $0\,\mathrm{T}$ to $5\,\mathrm{T}$ and shifts up to $1.40\,\mathrm{K}$ at $9\,\mathrm{T}$. The $0\,\mathrm{T}$ heat capacity anomaly at $T_{N2} = 0.45\,\mathrm{K}$ begins to broaden at $3\,\mathrm{T}$ into a small shoulder of the initial $1.13\,\mathrm{K}$ transition and vanishes by $5\,\mathrm{T}$. The broad $C_p(T)$ peak marking the onset of short-range correlations near $2\,\mathrm{K}$ shifts to higher

Table 3.1: Coefficients of the magnetic basis vectors creating the helical models of the base temperature magnetic structure of $LiYbO_2$ at $0\,T$ and $3\,T$, where $bv_1 = (100)$, $bv_2 = (010)$, and $bv_3 = (001)$.

atom $(x,\ y,\ z)$	270 mK, 0 T $\mathbf{k} = (0.384, \pm 0.384, 0)$			270 mK, 3 T $\mathbf{k} = (1/3, \pm 1/3, 0)$		
	bv_1	bv_2	bv_3	bv_1	bv_2	bv_3
Yb_1 (0, 0.75, 0.125)	0	-1.26i	1.26	0	-1.26i	1.26
Yb_2 (0, 0.25, 0.875)	0	-1.26i	1.26	0	-1.26i	1.26

temperatures with increasing magnetic field, consistent with a number of other frustrated spin systems [14, 167]. The suppression of the staged T_{N1}-T_{N2} ordering under modest magnetic field strengths suggests that zero-field fluctuations/remnant degeneracy likely influence the ordering behavior.

3.2.2 Neutron diffraction results

To further investigate the low-temperature, ordered state, neutron powder diffraction measurements were performed. Figure 3.4 details the field- and temperature-evolution of magnetic order in $LiYbO_2$ about the T_{N1} and T_{N2} transitions identified in specific heat measurements (Figure 3.3). Magnetic peaks appear in the powder neutron diffraction data below $1\,K$, and three regions of ordering were analyzed: (1) In the zero-field low-temperature, fully ordered state ($T < 450\,mK$); (2) in the zero-field, intermediate ordered state (450 mK$< T < 1\,K$); and (3) in the field-modified ordered state ($T < 450$ mK and $\mu_0 H = 3\,T$). Figure 3.4a) shows the data and structural refinement collected at $1.5\,K$ in the high temperature paramagnetic regime—this is used as nonmagnetic background that is subtracted from the low-temperature data. Figure 3.4b) shows the subtracted data
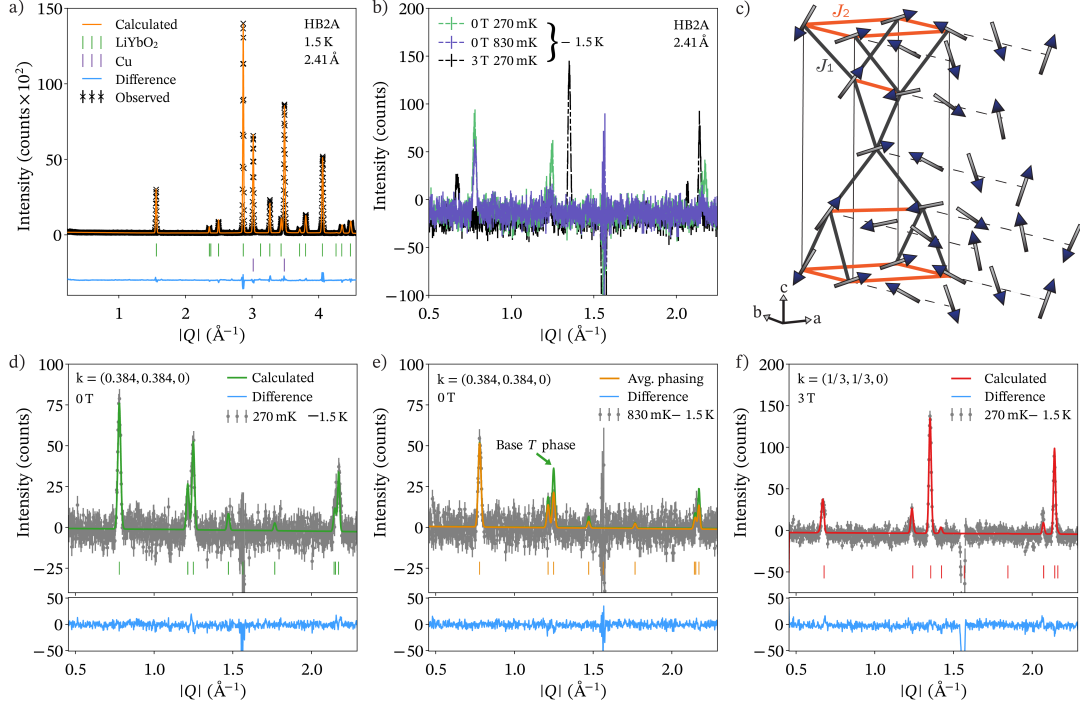
Figure 3.4: Neutron powder diffraction data collected for $LiYbO_2$ at HB-2A at the High Flux Isotope Reactor. a) Fits to the elastic scattering data at $1.5\,K$ reveal only one structural phase. b) Temperature-subtracted diffraction data ($T - 1.5\,K$) revealing a series of new magnetic peaks upon cooling. Additionally, at $270\,mK$ and $3\,T$, another set of magnetic peaks arise. Intensity near $1.5\,Å^{-1}$ results from slight under/over subtraction of the structural peak at that position in a) and is not a magnetic Bragg reflection. c) Helical magnetic structure fit below the ordering transition T_{N2}. d) $270\,mK$ data collected under zero field with the $1.5\,K$ structural data subtracted. Green line shows the resulting fit using the magnetic structure described in the text. e) 830 mK data collected under zero field with the $1.5\,K$ structural data subtracted. The orange line shows the partially disordered, intermediate helical state described in the text and the green line shows a fit using the fully ordered helical structure for comparison. f) $270\,mK$ data collected under $\mu H = 3\,T$ with the $1.5\,K$ structural data subtracted. The red line shows the fit to the commensurate magnetic structure describe in the text.

in each of the above regions overplotted with one another, and each magnetic profile is discussed separately in the following subsections. We note here that in each region, the large difference signal observed slightly above $1.5\,\text{Å}^{-1}$ is due to the slight under/over subtraction of a nuclear reflection.

Region 1: $\mu_0 H = 0\,\textbf{T}$, $T < 450\,\textbf{mK}$

At 270 mK, well below T_{N2}, a series of peaks appear at incommensurate momentum transfers. These new magnetic reflections are described by a doubly-degenerate ordering wave vector of $\boldsymbol{k} = (0.384, \pm 0.384, 0)$. The best fit to the data in this regime corresponds to a helical magnetic structure shown in 3.4c) that is produced from the Γ_1 irreducible representation (Kovalev scheme) of this space group with the three basis vectors $bv_1 = (1, 0, 0)$, $bv_2 = (0, 1, 0)$, and $bv_3 = (0, 0, 1)$. The helical state is defined by a combination of the ordering wave vector $\boldsymbol{k}$ and the helical propagation direction. The latter defines a vector that moments rotate in the plane perpendicular. Best fits for the refinement data were achieved when the helical propagation vector is restricted to the ab-plane. However, all helical propagation directions within the ab-plane produce equivalent fits to the data.

The fit presented in Figure 3.4d) corresponds to the instance where helices propagate along the b-axis with moments rotating within the ac-plane depicted in in Figure 3.4c). Coefficients of the basis vector representation of this fit are shown in Table 3.1. Due to the bipartite nature of this lattice, two magnetic Yb^{3+} atoms are defined in the system (denoted as sublattices A and B), and in effect, this creates a relative phase difference in the moment rotation between the two sites that is experimentally fit at 0.58π. The

ordered magnetic moment refined with this fit is $\mu = 1.26(10)\ \mu_B$, comprising 84% of the expected 1.5 μ_B moment in a $J_{\text{eff}} = 1/2$ system with $g_{avg} = 3$.

Region 2: $\mu_0 H = 0\,\text{T},\ 450\,\text{mK} < T < 1.13\,\text{K}$

As the temperature is increased above T_{N2} to $830\,\text{mK}$ into the intermediate ordered state, incommensurate magnetic reflections with the same ordering wave vector of $\boldsymbol{k} = (0.384, \pm 0.384, 0)$ persist (Figure 3.4e)). Order in this T_{N1} state is seemingly still long-range and the lowest angle reflection can be fit to a Lorentzian peak shape to extract an estimated, minimum correlation length. In both the $270\,\text{mK}$ base temperature and $830\,\text{mK}$ intermediate temperature regimes, the minimum correlation length corresponds to $\approx 364\,\text{Å}$. Modeling the pattern of magnetic peaks in this intermediate temperature regime using the same T_{N2} structure as described above however fails to fully capture the data. As seen in Figure 3.4e), the T_{N2} (green) structure overestimates reflections near $1.2\,\text{Å}^{-1}$.

One potential model for the magnetic order in this intermediate temperature regime is to allow the relative phasing of the A and B magnetic sublattices to become disordered upon warming into the T_{N1} state. In other words, helical magnetic order could establish with $\boldsymbol{k} = (0.384, \pm 0.384, 0)$; however the phasing between Yb-sites would remain disordered prior to selecting a specific phase below T_{N2}. This conjecture was modeled by averaging over ten fits using equally-spaced relative phases from zero to 2π between Yb-sites, and where each fit was calculated using an identical moment size ($1.26\ \mu_b$). This averaged phasing model (Figure 3.4d) orange) captures the relative peak intensi-

ties better than the single-phase model used below T_{N2} and is supported by $C(T)$ data showing that additional entropy freezes out below T_{N2}.

Region 3: $\mu_0 H = 3\,\mathbf{T}$, $T < 450\,\mathbf{mK}$

Upon applying a magnetic field to the low-temperature ordered state below T_{N2}, the magnetic ordering of the system changes. Figure 3.4f) shows that a $\mu_0 H = 3\,\mathrm{T}$ field drives commensurate peaks to appear in place of the incommensurate reflections in the zero-field ordered state. The modified propagation vector corresponds to the doubly-degenerate $\boldsymbol{k} = (1/3, \pm 1/3, 0)$. Although the modified $\boldsymbol{k}$ reflects a locking into a commensurate structure, qualitatively, the details of the ordered state remain similar to the zero-field T_{N2} model. The commensurate $3\,\mathrm{T}$ state is still best represented by an ab-plane helical magnetic structure with basis vector coefficients displayed in Table 3.1. The magnetic moment is refined to be $\mu = 1.26(9)\,\mu_B$ and the two Yb-sublattices differ by a relative phase of 0.42π.

3.2.3 Low-energy magnetic fluctuations

The low-energy spin dynamics of Yb moments in $\mathrm{LiYbO_2}$ were investigated in all three ordered regimes described in the previous section via inelastic neutron scattering measurements. While the powder-averaged data is difficult to interpret given the complexity of the ordered state, Figure 3.5 plots a series of background-subtracted inelastic spectra that qualitatively illustrate a few key points. Below T_{N2} and in zero-field, the bandwidth of spin excitations extends to roughly $1\,\mathrm{meV}$. Spectral weight appears to originate from
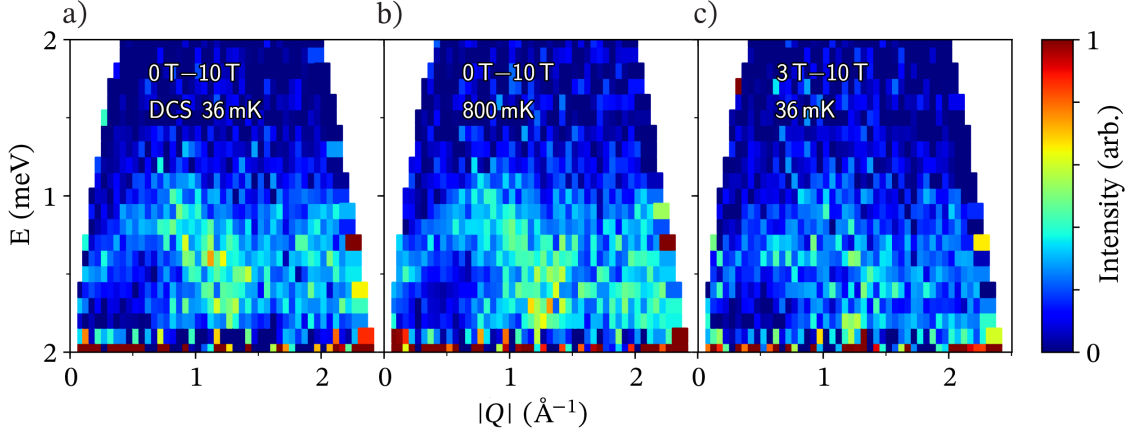
Figure 3.5: Low-energy inelastic neutron scattering (INS) spectra $S(|Q|, \hbar\omega)$ collected on the DCS spectrometer at a) $\mu_0 H = 0\,\mathrm{T}$ and $36\,\mathrm{mK}$, b) $\mu_0 H = 0\,\mathrm{T}$ and $800\,\mathrm{mK}$, and c) $\mu_0 H = 3\,\mathrm{T}$ and $36\,\mathrm{mK}$. All data have data collected at $36\,\mathrm{mK}$ and $10\,\mathrm{T}$ subtracted, where $\mathrm{LiYbO_2}$ enters a field-polarized state, indicated by isothermal magnetization data from Figure 4b).

the magnetic zone centers of $\boldsymbol{k} = (q, \pm q, 0)$ (where $q = 0.384$ at $0\,\mathrm{T}$ and $q = 1/3$ at $3\,\mathrm{T}$) and the Γ point. As the ordered does not change appreciably under moderate fields, the low-energy spectra remain qualitatively similar for both $0\,\mathrm{T}$ and $3\,\mathrm{T}$ data below T_{N2}. Similarly, upon heating from T_{N2} into the T_{N1} state, minimal changes are observed in the inelastic spectra. At $10\,\mathrm{T}$ and $36\,\mathrm{mK}$ however, $\mathrm{LiYbO_2}$ enters a field-polarized state where the low energy spin fluctuations are dramatically suppressed. The removal of low-energy fluctuations in this high-field data was used to subtract out background contributions in the data shown in Figure 3.5. There are slight differences in the dynamics of the $0\,\mathrm{T}$ and $3\,\mathrm{T}$ states in Figure 3.5 that will require future experiments to detail their differences with higher statistics.

3.3   Theoretical analysis

In the following subsections, we construct a classical Heisenberg Hamiltonian to describe the interactions of Yb ions in $LiYbO_2$. We then use this Hamiltonian, extended out to next-nearest neighbors, to model the potential magnetic ground states in $LiYbO_2$ for comparison with experimental data. Spin excitations are then also modeled in the parameter space predicting magnetic order most closely matching that experimentally observed.

3.3.1   Coordinates and symmetry

First we establish the coordinates for the Yb atoms in $LiYbO_2$ by denoting the orthogonal unit cell vectors as $\boldsymbol{a} = a\hat{\boldsymbol{x}}$, $\boldsymbol{b} = a\hat{\boldsymbol{y}}$, and $\boldsymbol{c} = c\hat{\boldsymbol{z}}$, with $a = 4.378\,\text{Å}$, and $c = 10.058\,\text{Å}$. The BCC primitive cell vectors are

$$\boldsymbol{a}_p = \frac{1}{2}(-\boldsymbol{a} + \boldsymbol{b} + \boldsymbol{c}), \quad \boldsymbol{b}_p = \frac{1}{2}(\boldsymbol{a} - \boldsymbol{b} + \boldsymbol{c}), \quad \boldsymbol{c}_p = \frac{1}{2}(\boldsymbol{a} + \boldsymbol{b} - \boldsymbol{c}). \tag{3.2}$$

We choose the origin to be centered on the $\mu = 0$ sublattice ; the other sublattice ($\mu = 1$) has one atom sitting at $\frac{1}{2}\boldsymbol{b} + \frac{1}{4}\boldsymbol{c}$. We introduce the global coordinate (x, y, z) and the sublattice-dependent coordinate $(r_1, r_2, r_3)_\mu$, with $\mu = 0, 1$:

$$\begin{aligned}(r_1, r_2, r_3)_\mu &= r_1\boldsymbol{a}_p + r_2\boldsymbol{b}_p + r_3\boldsymbol{c}_p + \boldsymbol{\delta}_\mu \\ &= \left(\frac{-r_1 + r_2 + r_3}{2}, \frac{r_1 - r_2 + r_3}{2} + \frac{\mu}{2}, \frac{r_1 + r_2 - r_3}{2} + \frac{\mu}{4}\right).\end{aligned} \tag{3.3}$$

On the other hand, we have $(r_1, r_2, r_3)_\mu = (x, y, z) = (y + z - 3\mu/4, x + z - \mu/4, x + y - \mu/2)_\mu$, where $\mu = 0$ if x, y, z all are multiples of $1/2$, and $\mu = 1$ if at least one of x, y, z is not a multiple of $1/2$ (and is a multiple of $1/4$).

The space group for LiYbO$_2$ is $I4_1/amd$ (No. 141). The point group is D_{4h} with 16 elements, generated by the following symmetry operations

$$
\begin{aligned}
S_{2z}: \quad & (r_1, r_2, r_3)_\mu \to (1 + r_2 - r_3 - \mu, 1 + r_1 - r_3, 1 - r_3 - \mu)_\mu, & \text{(3.4a)} \\
S_{4z}: \quad & (r_1, r_2, r_3)_\mu \to (r_2 + \mu, r_2 - r_3, -r_1 + r_2)_{1-\mu}, & \text{(3.4b)} \\
C_{2y}: \quad & (r_1, r_2, r_3)_\mu \to (-r_2 + r_3 + \mu, 1 - r_2, r_1 - r_2 + \mu)_{1-\mu}, & \text{(3.4c)} \\
P: \quad & (r_1, r_2, r_3)_\mu \to (-r_1, -r_2, -r_3)_{1-\mu}. & \text{(3.4d)}
\end{aligned}
$$

In global coordinates, these symmetry operations have the form

$$
\begin{aligned}
S_{2z}: \quad & (x, y, z) \to (\tfrac{1}{2} - x, \tfrac{1}{2} - y, \tfrac{1}{2} + z), & \text{(3.5a)} \\
S_{4z}: \quad & (x, y, z) \to (-y, \tfrac{1}{2} + x, \tfrac{1}{4} + z), & \text{(3.5b)} \\
C_{2y}: \quad & (x, y, z) \to (\tfrac{1}{2} - x, y, \tfrac{3}{4} - z), & \text{(3.5c)} \\
P: \quad & (x, y, z) \to (-x, \tfrac{1}{2} - y, \tfrac{1}{4} - z). & \text{(3.5d)}
\end{aligned}
$$

The minimal set of generators of D_{4h} can be chosen as $\{S_{4z}, C_{2y}, P\}$.

The local environment symmetry for an Yb ion is D_{2d}, which is order-eight, generated by three order-two elements C_{2z}, M, and S (assuming the Yb ion is at the origin):

$$
\begin{aligned}
C_{2z}: \quad & (x, y, z) \to (-x, -y, z), & \text{(3.6a)} \\
M: \quad & (x, y, z) \to (-x, y, z), & \text{(3.6b)} \\
S: \quad & (x, y, z) \to (-y, x, -z). & \text{(3.6c)}
\end{aligned}
$$

The local environment symmetry group D_{2d} is a subgroup of the point group D_{4h}. This can be seen from the following relations:

$$
C_{2z} = S_{4z} T_1^{-1} T_2^{-1} T_3^{-1} S_{4z}, \qquad M = T_1^{-1} T_2^{-1} T_3^{-1} C_{2y} P, \qquad S = P S_{4z}. \qquad \text{(3.7)}
$$

3.3.2 LiYbO$_2$ exchange Hamiltonian

A minimal Hamiltonian describing the NN interactions in LiYbO$_2$ ($I4_1/amd$) following symmetry analysis in the last subsection can be written as

$$H_1 = \sum_{\langle i,j \rangle} J_z S_i^z S_j^z + J_{xy}(S_i^x S_j^x + S_i^y S_j^y) + J_\delta (\boldsymbol{S}_i \cdot \boldsymbol{f}_{ij})(\boldsymbol{S}_j \cdot \boldsymbol{f}_{ij}) + J_{cz}(\boldsymbol{S}_i \cdot \boldsymbol{f}_{ij} S_j^z + S_i^z \cdot \boldsymbol{f}_{ij}\hat{\boldsymbol{z}}),$$

(3.8)

where $\boldsymbol{f}_{ij}$ is the projection of the bond vector $\boldsymbol{e}_{ij}$ onto the basal plane. The symmetry-allowed next nearest-neighbor (NNN) interactions are written as

$$H_2 = \sum_{\langle\langle i,j \rangle\rangle} J'_z S_i^z S_j^z + J'_{xy}(S_i^x S_j^x + S_i^y S_j^y) + J'_\delta (\boldsymbol{S}_i \cdot \boldsymbol{e}_{ij})(\boldsymbol{S}_j \cdot \boldsymbol{e}_{ij}) + \boldsymbol{D}_{ij} \cdot \boldsymbol{S}_i \times \boldsymbol{S}_j, \quad (3.9)$$

where the Dzyaloshinskii-Moriya (DM) vectors for the NNN bonds $\langle ij \rangle$ along $\boldsymbol{a}$ and $\boldsymbol{b}$ are $\boldsymbol{D}_{ij} = (-1)^{\mu(i)}D\boldsymbol{a} \times \hat{\boldsymbol{z}}$ and $\boldsymbol{D}_{ij} = (-1)^{\mu(i)}D\boldsymbol{b} \times \hat{\boldsymbol{z}}$, respectively. Here $\mu(i) = 0, 1$ for the sublattice $i = A, B$, respectively, indicating that the sign of the DM vector alternates between layers.

We hereby restrict our study to the Hamiltonian up to NNN: $H = H_1 + H_2$. For f-orbital ions such as Yb, the anisotropies J_δ and J'_δ are usually negligible, and as a good approximation we take the Heisenberg limit $J_z = J_{xy} = J_1$, and $J'_z = J'_{xy} = J_2$ (the effect of $J_z \neq J_{xy}$ and $J'_z \neq J'_{xy}$ will be discussed in a later subsection). This generates as a physical model the $J_1 - J_2$ Heisenberg Hamiltonian

$$H = J_1 \sum_{\langle ij \rangle} \boldsymbol{S}_i \cdot \boldsymbol{S}_j + J_2 \sum_{\langle\langle ij \rangle\rangle} \boldsymbol{S}_i \cdot \boldsymbol{S}_j \tag{3.10}$$
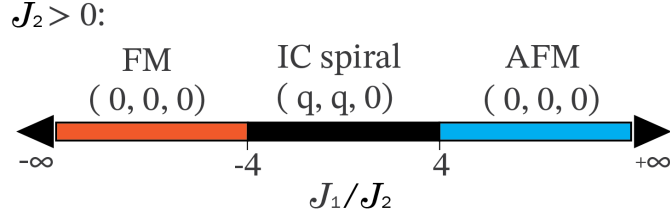
Figure 3.6: Phase diagram of magnetic order in the $J_1 - J_2$ Heisenberg model, assuming $J_2 > 0$, where ferromagnetic (FM), incommensurate (IC) spiral, and antiferromagnetic (AFM) Néel order exist.

3.3.3 The $J_1 - J_2$ model and spiral order

We first look at the $J_1 - J_2$ Heisenberg model on the stretched diamond lattice without the DM term. The classical ground state of this model can be solved exactly. In momentum space, the $J_1 - J_2$ Heisenberg model is written as

$$H = \sum_{\boldsymbol{q},\mu,\nu} \boldsymbol{S}_{\boldsymbol{q},\mu} J_{\boldsymbol{q}}^{\mu\nu} \boldsymbol{S}_{-\boldsymbol{q},\nu}, \tag{3.11}$$

with

$$J_{\boldsymbol{q}}^{11} = J_{\boldsymbol{q}}^{22} = J_2(\cos \boldsymbol{q} \cdot \boldsymbol{a} + \cos \boldsymbol{q} \cdot \boldsymbol{b}),$$

$$J_{\boldsymbol{q}}^{12} = J_{\boldsymbol{q}}^{21*} = J_1 \left(e^{-i\frac{\boldsymbol{q} \cdot \boldsymbol{c}}{4}} \cos \frac{\boldsymbol{q} \cdot \boldsymbol{a}}{2} + e^{i\frac{\boldsymbol{q} \cdot \boldsymbol{c}}{4}} \cos \frac{\boldsymbol{q} \cdot \boldsymbol{b}}{2} \right).$$

Therefore the lower branch of the band is

$$\lambda_{\boldsymbol{q}} = J_{\boldsymbol{q}}^{11} - |J_{\boldsymbol{q}}^{12}|. \tag{3.12}$$

Solving for the minimum of $\lambda_{\boldsymbol{q}}$, the classical ground state is an incommensurate spiral, with wave vector

$$\boldsymbol{q} = \frac{2\pi}{a}(q, q, 0) \quad \text{or} \quad \boldsymbol{q} = \frac{2\pi}{a}(q, -q, 0), \tag{3.13}$$

where

$$q \equiv \begin{cases} \pm \frac{1}{\pi} \arccos \frac{|J_1|}{4J_2}, \\ 0, \end{cases} \quad \text{respectively for} \begin{cases} |J_1| \leq 4J_2, \\ |J_1| > 4J_2. \end{cases}$$

109
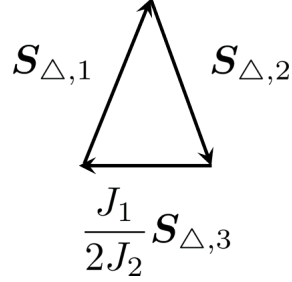
Figure 3.7: The classical ground state condition $\boldsymbol{S}_{\triangle,1} + \boldsymbol{S}_{\triangle,2} + \frac{J_1}{2J_2}\boldsymbol{S}_{\triangle,3} = 0$.

Note that due to the sublattice structure, both the FM and AFM Néel orders have $q = 0$. From now on we assume $J_2 > 0$ since spiral order can appear only for a positive J_2 (Figure 3.6). The experimental value for the doubly-degenerate spiral wave vector is $\frac{2\pi}{a}(0.384, \pm 0.384, 0)$, which gives

$$J_1 = \pm 4\cos(0.384\pi)J_2 = \pm 1.426 J_2. \tag{3.14}$$

The eigenvector corresponding to $\lambda_{\boldsymbol{q}}$ is $u_{\boldsymbol{q}} = \frac{1}{\sqrt{2}}(e^{i\phi_{\boldsymbol{q}}}, 1)^T$, where the phase $\phi_{\boldsymbol{q}} = \pi + \mathrm{Arg} J_{\boldsymbol{q}}^{12}$ determines the relative angle or phase between the spins of the two sublattices. The magnetic order then is

$$\boldsymbol{S}_{\boldsymbol{r}_i} = (0, \cos\boldsymbol{q}\cdot\boldsymbol{r}_i, \sin\boldsymbol{q}\cdot\boldsymbol{r}_i) \tag{3.15}$$

or any coplanar configuration that is related to Eq. (3.15) by a global SO(3) rotation.

A more intuitive, geometrical way to obtain the ground state of the Heisenberg $J_1 - J_2$ Hamiltonian is to rewrite it as the sum over all the "elementary" triangles $\triangle$ that are enclosed by two NN bonds and one NNN bond, where each NNN bond belongs to only one "elementary" triangle while each NN bond is shared by two "elementary" triangles. Concretely, for each $\triangle$, label the two spins connected with an NNN bond as $\boldsymbol{S}_{\triangle,1}$ and

$S_{\triangle,2}$, and the third spin as $S_{\triangle,3}$, we then have:

$$H = \text{Constant} + \frac{J_2}{2} \sum_{\triangle} \left(S_{\triangle,1} + S_{\triangle,2} + \frac{J_1}{2J_2} S_{\triangle,3} \right)^2. \tag{3.16}$$

Written in this way, the classical ground state is the spin configuration that satisfies

$S_{\triangle,1} + S_{\triangle,2} + \frac{J_1}{2J_2} S_{\triangle,3} = 0$ for all $\triangle$. Denote the (orientationless) angle between two

vectors S_1 and S_2 by $\langle S_1, S_2 \rangle$. One easily infers from Figure 3.7 that

$$\langle S_{\triangle,1}, S_{\triangle,3} \rangle = \langle S_{\triangle,2}, S_{\triangle,3} \rangle = \begin{cases} \pi - \arccos \frac{J_1}{4J_2} > \frac{\pi}{2}, & 4J_2 \geq J_1 > 0 \\ \arccos \frac{|J_1|}{4J_2} < \frac{\pi}{2}, & 4J_2 \geq -J_1 > 0 \end{cases},$$

$$\langle S_{\triangle,1}, S_{\triangle,2} \rangle = 2 \arccos \frac{|J_1|}{4J_2}. \tag{3.17}$$

This result agrees with the exact diagonalization result above. When $J_1 = 1.426 J_2 > 0$

with a sublattice phasing of π, the angle between the two spins in a primitive cell is

expected to be $\pi - \arccos(1.426/4) = 1.935 \sim 111°$.

3.3.4 Effect of other terms; phasing and lattice distortion

The $J_1 - J_2$ model reproduces the spiral phase and the incommensurate wave vector in

the ground state of LiYbO$_2$. The angle difference between the nearest spins (111°),

however, does not agree with the best experimental fitting (staggered in alternating 34°

and 172° angles). One plausible explanation is a small lattice distortion that is outside

of resolution of the neutron powder diffraction data.

In this subsection, we study the effect of a lattice distortion on the magnetic order.

We assume a simple scenario in which the lattice distortion results in a displacement

between two sublattices: suppose the $\mu = 1$ sublattice, originally $\delta = a/2 + c/4$ part

from the $\mu = 0$ sublattice, is offset by $\boldsymbol{\varepsilon}$ from the original position, where $\boldsymbol{\varepsilon} = (\epsilon, \epsilon, 0)$. In this case the NN vectors from the Yb ion at the origin become $\frac{a}{2} + \frac{c}{4} + \boldsymbol{\varepsilon}$, $-\frac{a}{2} + \frac{c}{4} + \boldsymbol{\varepsilon}$, $\frac{b}{2} - \frac{c}{4} + \boldsymbol{\varepsilon}$, and $-\frac{b}{2} - \frac{c}{4} + \boldsymbol{\varepsilon}$, which correspond to J_1', J_1'', J_1', J_1'', respectively. Here we assume antiferromagnetic exchange $J_1', J_1'' > 0$ in order to agree with experiment. We can again write down the Hamiltonian in momentum space in the form of Eq. (3.11), with modified off-diagonal element

$$
\begin{aligned}
J_{\boldsymbol{q}}^{12} = J_{\boldsymbol{q}}^{21*} &= \frac{J_1'}{2} \left(e^{i\boldsymbol{q} \cdot \left(\frac{a}{2} + \frac{c}{4} + \boldsymbol{\varepsilon} \right)} + e^{i\boldsymbol{q} \cdot \left(\frac{b}{2} - \frac{c}{4} + \boldsymbol{\varepsilon} \right)} \right) + \frac{J_1''}{2} \left(e^{i\boldsymbol{q} \cdot \left(-\frac{a}{2} + \frac{c}{4} + \boldsymbol{\varepsilon} \right)} + e^{i\boldsymbol{q} \cdot \left(-\frac{b}{2} - \frac{c}{4} + \boldsymbol{\varepsilon} \right)} \right) \\
&= \frac{1}{2} e^{i\boldsymbol{q} \cdot \boldsymbol{\varepsilon}} \left(J_1' e^{i\boldsymbol{q} \cdot \left(\frac{a}{2} + \frac{c}{4} \right)} + J_1' e^{i\boldsymbol{q} \cdot \left(\frac{b}{2} - \frac{c}{4} \right)} + J_1'' e^{i\boldsymbol{q} \cdot \left(-\frac{a}{2} + \frac{c}{4} \right)} + J_1'' e^{i\boldsymbol{q} \cdot \left(-\frac{b}{2} - \frac{c}{4} \right)} \right),
\end{aligned}
\tag{3.18}
$$

where we denote $q_x = \boldsymbol{q} \cdot \boldsymbol{a}$, $q_y = \boldsymbol{q} \cdot \boldsymbol{b}$, and $q_z = \boldsymbol{q} \cdot \boldsymbol{c}$. It is easy to show that

$$
\lambda_{\boldsymbol{q}} \geq J_2 (\cos q_x + \cos q_y) - \sqrt{\frac{J_1'^2}{4} + \frac{J_1''^2}{4} + \frac{1}{2} J_1' J_1'' \cos q_x} - \sqrt{\frac{J_1'^2}{4} + \frac{J_1''^2}{4} + \frac{1}{2} J_1' J_1'' \cos q_y},
\tag{3.19}
$$

hence the energy minimum is reached at $q_x = q_y \equiv q_0$ and $q_z = 0$. Here $q_0 = 0.384 \times 2\pi$ is the required experimental value to minimize $f(q) = J_2 \cos q - \sqrt{\frac{J_1'^2}{2} + \frac{J_1''^2}{2} + J_1' J_1'' \cos q}$, and we get

$$
\cos q_0 = \frac{J_1'^2 J_1''^2 - 4 J_2^2 (J_1'^2 + J_1''^2)}{8 J_2^2 J_1' J_1''},
$$

This equation restricts the value between J_1'/J_2 and J_1''/J_2. Setting $J_1' = J_1'' = J_1$ recovers the previous undistorted result, $J_1 = 4 \cos \frac{q_0}{2} = 4 \cos \pi q$. The eigenvector corresponding

to $\lambda_{\boldsymbol{q}}$ is again $u_{\boldsymbol{q}} = \frac{1}{\sqrt{2}}(e^{i\phi_{\boldsymbol{q}}}, 1)^T$, where we now have

$$\phi_{\boldsymbol{q}_0} = \pi + \boldsymbol{q}_0 \cdot \boldsymbol{\varepsilon} + \arctan\left(\tan\left(\frac{\pi}{4} - \beta\right)\tan\frac{q_0}{2}\right) \approx \pi + \arctan\left(\tan\left(\frac{\pi}{4} - \beta\right)\tan\frac{q_0}{2}\right),$$
(3.20)

and we define $\tan\beta = J_1''/J_1'$. The term $\boldsymbol{q} \cdot \boldsymbol{\varepsilon}$ is small and can be ignored. Eq. (3.20) suggests that the angle difference between NN spins (which is $\phi_{\boldsymbol{q}_0} + q_0/2$) depends on the spiral wave vector and the ratio of NN bond exchange energies. If we plug in $\phi_{\boldsymbol{q}_0} = 360° - 34° = 172°$, then we get $\tan\beta \approx 6$. This means that in our simple lattice distortion scenario, a large exchange ratio is needed in order to reproduce the experimentally observed order.

We note that the DM contribution vanishes if different layers are assumed to have the same order: assume $D \ll J_1, J_2$; suppose the coplanar order is normal to $\boldsymbol{n}$, then the DM interaction in layer l is proportional to $(-1)^{\mu(l)}D(\boldsymbol{a} - \boldsymbol{b}) \cdot \boldsymbol{n} \sin qa$. The sign $(-1)^{\mu(l)}$ indicates that neighboring layers (belonging to different sublattices A and B) have opposite contributions, leading to a vanishing DM energy.

3.3.5   Effect of anisotropy in the $J_1 - J_2$ model

In this subsection we briefly address the effect of anisotropy. Since the classical solution of the original $J_1 - J_2$ Heisenberg model can be mapped to a $J_1 - J_2$ Heisenberg chain, we use a chain representation in the following analysis: the site index in the chain labels the sites in the (110) direction of the original LiYbO$_2$ lattice; in doing so we collapse and treat all the spins in the plane normal to the (110) direction as one spin, since they all

have the same orientation in the Ansatz that we now consider.

We consider an XXZ model with NN and NNN exchange interactions. Denote as $\Delta_{1,2}$ the Ising anisotropy at NN and NNN level, the energy can be written as

$$H = \sum_i J_1(\sin\theta_i \sin\theta_{i+1} + \Delta_1 \cos\theta_i \cos\theta_{i+1}) + J_2(\sin\theta_i \sin\theta_{i+2} + \Delta_2 \cos\theta_i \cos\theta_{i+2}). \quad (3.21)$$

In the Heisenberg limit $\Delta_1 = \Delta_2 = 1$, $H = \sum_i J_1 \cos(\theta_{i+1} - \theta_i) + J_2 \cos(\theta_{i+2} - \theta_i)$, the uniform spiral order is recovered. For general Δ_1 and Δ_2, we assume the Ansatz that $\theta_{2i} = \theta_0 + 2i\phi$, while $\theta_{2i+1} = \theta_{2i} + \phi + \alpha$. The energy under this Ansatz becomes

$$
\begin{aligned}
H = & J_1 \sum_i \frac{\Delta_1 - 1}{2}(\cos(2\theta_0 + (4i+1)\phi + \alpha) + \cos(2\theta_0 + (4i+3)\phi + \alpha)) \\
& + \frac{\Delta_1 + 1}{2}(\cos(\phi + \alpha) + \cos(\phi - \alpha)) \\
& + J_2 \sum_i \frac{\Delta_2 - 1}{2}(\cos(2\theta_0 + (4i+2)\phi) + \cos(2\theta_0 + (4i+4)\phi + 2\alpha)) \\
& + \frac{\Delta_2 + 1}{2}(\cos(2\phi) + \cos(2\phi)).
\end{aligned}
\quad (3.22)
$$

If ϕ is an incommensurate angle (i.e. irrational fraction of 2π), then the first term of each summation averages to zero, and only the last term of each summation survives the average. This recovers the original $J_1 - J_2$ chain with renormalized exchange parameter $J_i \rightarrow J_i \frac{\Delta_i + 1}{2}$, $i = 1, 2$.

Next we consider the possibility of lattice distortion, which is a displacement between two sublattices as mentioned in the main text. In the chain representation, J_1 is now modified to J_1' and J_1'' depending on the bond considered, while Δ_1 is still unique. Then

we have

$$
\begin{aligned}
H = \sum_i & \frac{\Delta_1 - 1}{2}(J_1' \cos(2\theta_0 + (4i+1)\phi + \alpha) + J_1'' \cos(2\theta_0 + (4i+3)\phi + \alpha)) \\
& + \frac{\Delta_1 + 1}{2}(J_1' \cos(\phi + \alpha) + J_1'' \cos(\phi - \alpha)) \\
& + J_2 \sum_i \frac{\Delta_2 - 1}{2}(\cos(2\theta_0 + (4i+2)\phi) + \cos(2\theta_0 + (4i+4)\phi + 2\alpha)) \\
& + \frac{\Delta_2 + 1}{2}(\cos(2\phi) + \cos(2\phi)).
\end{aligned}
\tag{3.23}
$$

Again assume incommensurate ϕ, the first terms of the two sums average to zero, and

we are left with

$$
H/N = \frac{\Delta_1 + 1}{2}((J_1' + J_1'') \cos\alpha \cos\phi + (-J_1' + J_1'') \sin\alpha \sin\phi) + J_2(\Delta_2 + 1)\cos 2\phi, \tag{3.24}
$$

One then first minimizes with respect to α. At $(\cos\alpha, \sin\alpha) = \frac{(-(J_1'+J_1'')\cos\phi, -(-J_1'+J_1'')\sin\phi)}{\sqrt{J_1'^2 + J_1''^2 + 2J_1' J_1'' \cos 2\phi}}$,

H is minimized

$$
H/N = -\frac{\Delta_1 + 1}{2}\sqrt{J_1'^2 + J_1''^2 + 2J_1' J_1'' \cos 2\phi} + J_2(\Delta_2 + 1)\cos 2\phi. \tag{3.25}
$$

Finally, minimizing H with respect to ϕ gives the condition for ϕ

$$
\cos 2\phi = \frac{J_1'^2 J_1''^2 - 4\left(\frac{\Delta_2+1}{\Delta_1+1}\right)^2 J_2^2(J_1'^2 + J_1''^2)}{8\left(\frac{\Delta_2+1}{\Delta_1+1}\right)^2 J_2^2 J_1' J_1''}.
\tag{3.26}
$$

Compare this equation with its Heisenberg limit at $\Delta_1 = \Delta_2 = 1$, we see that the effect

of Ising anisotropy is to renormalize $J_2 \to \frac{\Delta_2+1}{\Delta_1+1} J_2$.

115

3.3.6 Linear spin wave theory

In this subsection, we present simulations of the dynamical structure factor using linear spin wave theory. An undistorted lattice is assumed. Introducing Holstein-Primakoff (HP) bosons

$$\boldsymbol{S}_i \cdot \boldsymbol{a}_i = \sqrt{s}\frac{a_i + a_i^\dagger}{\sqrt{2}}, \ \ \boldsymbol{S}_i \cdot \boldsymbol{b}_i = \sqrt{s}\frac{a_i - a_i^\dagger}{\sqrt{2i}}, \ \ \boldsymbol{S}_i \cdot \boldsymbol{c}_i = s - n_i \tag{3.27}$$

where $\boldsymbol{c}_i = \boldsymbol{u}\cos\widetilde{\boldsymbol{q}}\cdot\boldsymbol{r}_i + \boldsymbol{v}\sin\widetilde{\boldsymbol{q}}\cdot\boldsymbol{r}_i$ is the spin order ($\boldsymbol{u}$ and $\boldsymbol{v}$ are orthogonal unit vectors spanning the order plane), $\boldsymbol{b}_i = \boldsymbol{u}\times\boldsymbol{v}$, and $\boldsymbol{a}_i = \boldsymbol{b}_i\times\boldsymbol{c}_i$. We define $\widetilde{\boldsymbol{q}} = \frac{2\pi}{a}(1-q, 1-q, 0)$ to remind that the angle between NN spins is obtuse in the $J_1 - J_2$ model. The spin wave Hamiltonian is then

$$H = \sum_{\boldsymbol{k}\in\mathrm{BZ}^+} \Phi_{\boldsymbol{k}}^\dagger \mathcal{H}(\boldsymbol{k})\Phi_{\boldsymbol{k}}, \tag{3.28}$$

where $\Phi_{\boldsymbol{k}} = \left(a_{\boldsymbol{k},0}, a_{\boldsymbol{k},1}, a_{-\boldsymbol{k},0}^\dagger, a_{-\boldsymbol{k},1}^\dagger\right)^T$ are the HP bosons in momentum space, and

$$\mathcal{H}(\boldsymbol{k}) = 2\begin{pmatrix} h_{11} & h_{12} & p_{11} & p_{12} \\ h_{12}^* & h_{11} & p_{12}^* & p_{11} \\ p_{11} & p_{12} & h_{11} & h_{12} \\ p_{12}^* & p_{11} & h_{12}^* & h_{11} \end{pmatrix}, \tag{3.29}$$

with

$$h_{11} = J_2 \sum_{\boldsymbol{\delta}=a,b}\left(2s\cos\boldsymbol{k}\cdot\boldsymbol{\delta}\left[\frac{1}{4}(c_{\boldsymbol{\delta}}+1)\right] - sc_{\boldsymbol{\delta}}\right) - J_1 \sum_{\boldsymbol{\delta}=\pm\frac{a}{2}-\frac{c}{4},\pm\frac{b}{2}+\frac{c}{4}}\frac{s}{2}c_{\boldsymbol{\delta}}, \tag{3.30a}$$

$$h_{12} = J_1 \sum_{\boldsymbol{\delta}=\pm\frac{a}{2}-\frac{c}{4},\pm\frac{b}{2}+\frac{c}{4}} se^{i\boldsymbol{k}\cdot\boldsymbol{\delta}}\left[\frac{1}{4}(c_{\boldsymbol{\delta}}+1)\right], \tag{3.30b}$$

$$p_{11} = J_2 \sum_{\boldsymbol{\delta}=a,b} 2s\cos\boldsymbol{k}\cdot\boldsymbol{\delta}\left[\frac{1}{4}(c_{\boldsymbol{\delta}}-1)\right], \tag{3.30c}$$

$$p_{12} = J_1 \sum_{\boldsymbol{\delta}=\pm\frac{a}{2}-\frac{c}{4},\pm\frac{b}{2}+\frac{c}{4}} se^{i\boldsymbol{k}\cdot\boldsymbol{\delta}}\left[\frac{1}{4}(c_{\boldsymbol{\delta}}-1)\right], \tag{3.30d}$$

116
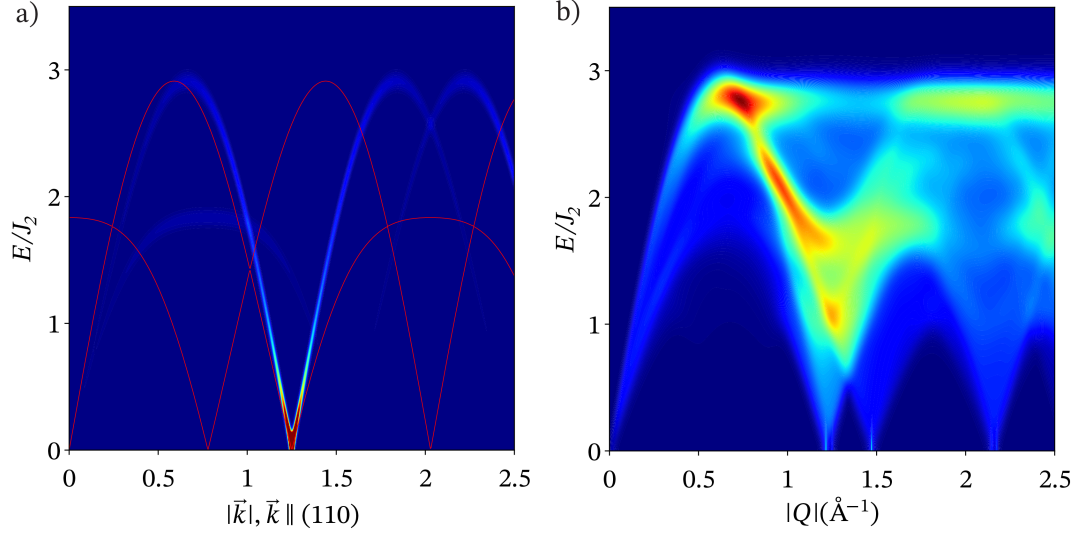
Figure 3.8: a) Spin wave spectrum (red lines) and the structure factor simulation for $J_1 = 1.42565 J_2 > 0$. Both along the (110) direction. b) Angular averaged structure factor for $J_1 = 1.42565 J_2 > 0$.

where we defined

$$c_{\boldsymbol{\delta}} \equiv \cos \widetilde{\boldsymbol{q}} \cdot \boldsymbol{\delta} = \begin{cases} -J_1/4J_2, & \boldsymbol{\delta} \in \text{NN}, \\ 2\left(\frac{J_1}{4J_2}\right)^2 - 1, & \boldsymbol{\delta} \in \text{NNN}. \end{cases} \tag{3.31}$$

The boson canonical commutation relation is preserved by the diagonalization $V_{\boldsymbol{k}}^{\dagger} \mathcal{H}(\boldsymbol{k}) V_{\boldsymbol{k}} = \Lambda_{\boldsymbol{k}}$, $\Phi_{\boldsymbol{k}} = V_{\boldsymbol{k}} \Psi_{\boldsymbol{k}}$, where $V_{\boldsymbol{k}}^{\dagger} J V_{\boldsymbol{k}} = J \equiv \text{Diag}(1, 1, -1, -1)$. Diagonalizing $J\mathcal{H}(\boldsymbol{k})$ then gives the spin wave spectrum $\Lambda = (\lambda_1, \lambda_2, -\lambda_1, -\lambda_2)$, with

$$\lambda_{1,2} = \sqrt{(h_{11} \pm |h_{12}|)^2 - (p_{11} \mp |q_{12}|)^2}. \tag{3.32}$$

The spin wave spectrum (3.32) along the (110) direction is shown in Figure 3.8a. One observes that the spectrum is gapless at

$$\boldsymbol{q} = (0, 0, 0), \quad \pm \frac{2\pi}{a}(q, q, 0), \quad \text{and} \quad \pm \frac{2\pi}{a}(1 - q, 1 - q, 0), \tag{3.33}$$

and the momenta that are related to $\boldsymbol{q}$ by a C_4 rotation along (001) or translation by reciprocal lattice vectors.

117

We then derive an expression for the dynamical structure factor, which is the Fourier transform of spin-spin correlation function. One obtains

$$
\begin{aligned}
\mathcal{S}(\boldsymbol{k}, \omega) &= \sum_{i,j=1}^{3} (\delta_{ij} - (\hat{\boldsymbol{k}})_i (\hat{\boldsymbol{k}})_j) \sum_{\mu,\nu=0}^{1} \langle m_\mu^i(-\boldsymbol{k}, -\omega) m_\nu^j(\boldsymbol{k}, \omega) \rangle \\
&= 2s\mu_B^2 \sum_{e=1}^{4} \delta(\omega - J\lambda_{\boldsymbol{k}-\widetilde{\boldsymbol{q}},e}) \left[V_{\boldsymbol{k}-\widetilde{\boldsymbol{q}}}^\dagger K_1^\dagger g^\dagger P_{\boldsymbol{k}} g K_1 V_{\boldsymbol{k}-\widetilde{\boldsymbol{q}}} \right]_{e,e} \\
&\quad + \delta(\omega - J\lambda_{\boldsymbol{k}+\widetilde{\boldsymbol{q}},e}) \left[V_{\boldsymbol{k}+\widetilde{\boldsymbol{q}}}^\dagger K_1^T g^\dagger P_{\boldsymbol{k}} g K_1^* V_{\boldsymbol{k}+\widetilde{\boldsymbol{q}}} \right]_{e,e} \\
&\quad + \delta(\omega - J\lambda_{\boldsymbol{k},e}) \left[V_{\boldsymbol{k}}^\dagger K_2^\dagger g^\dagger P_{\boldsymbol{k}} g K_2 V_{\boldsymbol{k}} \right]_{e,e},
\end{aligned}
\tag{3.34}
$$

where we defined projector $P_{\boldsymbol{k}} = 1_{3\times 3} - \hat{\boldsymbol{k}}\hat{\boldsymbol{k}}^T$. From Eq. (3.34), it is clear that the structure factor intensity at one $\boldsymbol{k}$ receives contributions from three momenta: $\boldsymbol{k} \pm \widetilde{\boldsymbol{q}}$ and $\boldsymbol{k}$. The simulated structure factor according to Eq. (3.34) is shown in Figure 3.8a) for a specific $(1, 1, 0)$ direction, and in Figure 3.8b) for the angular averaged result. One of the main features at low-energy is the vanishing intensity at Γ and $|\boldsymbol{q}| = \frac{2\sqrt{2}\pi}{a}0.384$, where the spin wave spectrum is gapless, and one would naively expect a strong intensity peak at zero energy due to singular BdG Hamiltonian at these momenta. Physically the "missing" intensity is a consequence of the destructive interference of the two sublattices at Γ and $\boldsymbol{q}$ that leads to vanishing contribution to the structure factor. The same interference pattern is also true for the static structure factor. The perfect cancellation is really a consequence of the (undistorted) $J_1 - J_2$ Heisenberg model. On the other hand, the persistence of high intensities at Γ and $\boldsymbol{q}$ from the neutron experiment suggests this cancellation is partially lifted in the real material due to other effects not captured by the $J_1 - J_2$ Heisenberg model.

3.3.7 Free energy analysis

The classical ground state of the $J_1 - J_2$ Heisenberg model has a global SO(3) symmetry due to the freedom in choosing the spiral plane. Since the lattice only has discrete symmetries, it is likely that this continuous symmetry is lifted due to other effects, such as spin–orbit coupling and fluctuations, and it is the goal of this section to address this issue energetically from a symmetry point of view. Specifically, we will examine the symmetry constraints on the free energy. We first write down the spiral order parameter. Assuming the spiral plane is spanned by two orthogonal vectors $\boldsymbol{u}$ and $\boldsymbol{v}$, the order parameter can be chosen as the Fourier transform of the magnetic order, which can be written as

$$\boldsymbol{d} = e^{i\theta(\boldsymbol{r})}(l\boldsymbol{u} + im\boldsymbol{v}), \tag{3.35}$$

where $\theta(\boldsymbol{r})$ determines the direction of the spins in the spiral plane. While it is a constant in the spiral phase, spatial fluctuation of θ must be considered near the incommensurate-to-commensurate (IC-C) transition. Note we have introduced l and m to account for either perfect circular ($l = m$, no net magnetization), elliptical ($m \neq l > 0$) or linear ($m = 0$) polarization, which correspond to zero, low and high magnetic fields, respectively.

We first look at the zero-field case, $l = m$. Following Lee and Balents [84], we seek to write down the free energy for the order parameter to quadratic order using symmetry considerations. Out of the symmetry generators $T_{1,2,3}$, S_{4z}, C_{2y} and P, the little group of the wave vector $\widetilde{\boldsymbol{q}}$ contains P, $T_{1,2,3}$, S_{4z}^2, and $S_{4z}^3 C_{2y}\colon (x,y,z) \to (y-1/2, x-1/2, 3/2-z)$. Under these symmetries, the order parameter transforms as

$$P: \quad \boldsymbol{d} \to e^{i\pi\widetilde{q}}\boldsymbol{d}^*, \tag{3.36a}$$

$$S_{4z}^2: \quad \boldsymbol{d} \to \mathrm{Diag}(-1,-1,1)\boldsymbol{d}^*, \tag{3.36b}$$

$$T_{1,2}: \quad \boldsymbol{d} \to \boldsymbol{d}, \tag{3.36c}$$

$$T_3: \quad \boldsymbol{d} \to e^{-2i\pi\widetilde{q}}\boldsymbol{d}, \tag{3.36d}$$

$$S_{4z}^3 C_{2y}: \quad \boldsymbol{d} \to \begin{pmatrix} & 1 & \\ 1 & & \\ & & 1 \end{pmatrix} e^{i2\pi\widetilde{q}}\boldsymbol{d}, \tag{3.36e}$$

where the last symmetry operation can be composed with T_3 to get $T_3 S_{4z}^3 C_{2y}: \boldsymbol{d} \to (d_y, d_x, d_z)$. From this, one can write down a free energy density that is quadratic in $\boldsymbol{d}$:

$$f(\boldsymbol{d}) = c_0|\boldsymbol{d}|^2 + c_1(d_1^* d_2 + c.c.) + c_2 d_3^* d_3. \tag{3.37}$$

By minimizing this free energy one finds there are three choices for the spiral plane depending on the value of c_1 and c_2 [84]: the normal of the order plane can be along either (001), $(1\bar{1}0)$, or (110).

The result above applies to a generally incommensurate wave vector $\widetilde{q}$ at zero magnetic field. As the field is switched on, the spiral order ceases to be circularly polarized, and the unequal components $l \neq m$ allow for nonzero net magnetization. As a consequence, some of the symmetry transformations in (3.36) are no longer valid and need to be modified. Nevertheless, we assume that all the symmetry transformations in (3.36) remain approximately valid at small field. Under these assumptions, we proceed to an explanation of the IC-C transition at $3\,\mathrm{T}$. The commensurate phase has a three-unit cell order with corresponding wave vector $\boldsymbol{q} = 2\pi(\frac{1}{3}, \frac{1}{3}, 0)$. In this phase, another term can be added to the free energy density:

$$f_\mathrm{C} = f(\boldsymbol{d}) - \widetilde{c}_6\left((\boldsymbol{d} \cdot \boldsymbol{d})^3 + c.c.\right). \tag{3.38}$$

120

The development of unequal l and m can be further modeled phenomenologically by fourth-order terms in the free energy such as $\beta_2 |\boldsymbol{d} \cdot \boldsymbol{d}|^2 + \chi_1 H^2 (\boldsymbol{d}^* \cdot \boldsymbol{d}) + \chi_2 |\boldsymbol{H} \cdot \boldsymbol{d}|^2$, which we do not discuss here but instead refer to Ref. [183].

In the following, we show that the IC-C transition can be described phenomenologically by a sine-Gordon model. For given J_1 and J_2, assume $\boldsymbol{q}$ is the (generally incommensurate) ground state spiral wave vector, while $\boldsymbol{k}$ is a nearby commensurate wave vector. Assume $\boldsymbol{q} = \boldsymbol{k} + \boldsymbol{\delta k} + \boldsymbol{\nabla}\theta$, where $\boldsymbol{\nabla}\theta$ denotes the spatial fluctuation of the order parameter. The classical energy can be expanded around $\boldsymbol{k}$:

$$\lambda = \lambda_0 + 2\boldsymbol{\delta} \cdot \boldsymbol{\nabla}\theta + \frac{\kappa_{xy}}{2}((\partial_x\theta)^2 + (\partial_y\theta)^2) + \frac{\kappa_z}{2}(\partial_z\theta)^2, \qquad (3.39)$$

where $\lambda_0 = -\frac{J_1^2}{4J_2} - 2J_2$, and the rigidity for θ is

$$\kappa_{xy} = -\frac{a^2}{16J_2}(J_1^2 - 16J_2^2), \qquad \kappa_z = \frac{c^2 J_1^2}{32 J_2}. \qquad (3.40)$$

Importantly, a term linear in the gradient of θ exists, with coefficient $\boldsymbol{\delta} = \kappa_{xy}\boldsymbol{\delta k}$. A full theory for θ then appears as

$$F[\theta] = A \int d^3x \left(\frac{\kappa}{2}(\boldsymbol{\nabla}\theta)^2 + 2\boldsymbol{\delta} \cdot \boldsymbol{\nabla}\theta - c_6 \cos 6\theta \right), \qquad (3.41)$$

where the last term comes from Eq. (3.38) with $c_6 \sim (l^2 - m^2)^3 c_6$. This is the sine-Gordon model that has been analyzed in numerous works; see e.g. Ref. [183]. The basic physics is that the soliton number N of the lowest energy solution to the free energy functional (3.41) distinguishes commensurate phase ($N = 0$) and incommensurate phase ($N = \pm 1$); the C-IC transition then is determined by the energetics of $N = 0$ and $N \neq 0$ configurations, with critical relation $\kappa^2 c_6/4\kappa\delta k = \pi^2/32$ ($\kappa^2 c_6/4\kappa\delta k < \pi^2/32$ gives the incommensurate phase). Since the elliptic polarization is induced by magnetic

121

field, following Ref. [183] we conclude that the coefficient $c_6 \propto (l^2 - m^2)^3 \propto H^6$, and that increasing the magnetic field will inevitably induce an IC-C transition.

3.4   Discussion

LiYbO$_2$ shows a rich magnetic phase diagram (see Figure 3.9) with inherent similarities to the A-site transition metal spinels and the $J_1 - J_2$ diamond lattice model, indicating that the underlying physics of both systems arises from the same bipartite frustration. The $J_1 - J_2$ model on the ideal diamond lattice with $J_2/|J_1| > 1/8$, produces frustrated spiral order with wave vectors directed along the high-symmetry directions of the lattice (e.g. (q, q, q), $(q, q, 0)$, $(0, 0, q)$) and similar spiral order also appears in tetragonaly elongated diamond lattice of LiYbO$_2$ near $|J_1| \leq 4J_2$. Spiral wave vectors in the distorted case are however limited to $(q, \pm q, 0)$, and tetragonal distortion lifts the degeneracy of the spiral spin liquid surface predicted for the perfect diamond lattice [10, 84, 22].

Curiously, in zero-field, the long-range helical ground state forms through two successive magnetic transitions upon cooling. An intermediate state formed upon cooling below T_{N1} is best fit by modeling a spiral state on each Yb-site but with disordered relative phasing between the two spirals. This apparent frustration in the relative phase between magnetic sublattices and the formation of a partially ordered state is also likely reflected in the departure of the relative phasing between Yb-ions within the fully ordered state (below T_{N2}) from the predictions of the Heisenberg $J_1 - J_2$ model. Specifically, the model predicts that moments rotate along all A-to-B sublattice bonds equivalently (i.e. the

angle difference between every NN spin is 111°), while the experimental data suggests that moments rotate in a staggered fashion, where the first A-to-B sublattice bond is 34° and the second is 172°. This generates a magnetic structure in which pairs of spins between the A and B sublattices are nearly aligned antiparallel.

While CEF data suggest the presence of two Yb environments in the lattice, this is not readily apparent in the average structural data, suggesting that the distortion responsible for this is reasonably subtle. Given the large distortion required for the model to produce the experimentally observed phasing between Yb-moments, the possible origin for the phase difference instead lies in the presence of anisotropic exchange interactions in $LiYbO_2$. We note however that, assuming spiral order with a single wave vector q, including Ising type of anisotropy at NN and NNN level does not help in explaining the disagreement between theory and experiment. Resolving the possibility of other anisotropic terms in the Hamiltonian as well as the precise nature of the anomalous state between $0.45\,K < T < 1.13\,K$ will require future single crystal studies.

The incommensurate helical structure in $LiYbO_2$ evolves into a commensurate helical structure when $\mu_0 H = 3\,T$ is applied. A similar type of "lock-in" incommensurate-to-commensurate (IC-C) phase transition occurs in the A-site spinels, originating from magnetic anisotropy on top of the $J_1 - J_2$ model [84]. Anisotropy accounts for the change from an incommensurate $(q, \pm q, 0)$ helical phase to a commensurate one in $MnSc_2S_4$ [84, 44, 71] and $CoCr_2O_4$ [28, 81, 32] with decreasing temperature. In $LiYbO_2$ however, the field-driven "lock-in" phase transition is captured within the sine-Gordon model in

Eq. (3.38) without the need to perturb the Heisenberg $J_1 - J_2$ model.

In fact, a considerable amount of the zero-field magnetic behavior of $LiYbO_2$ is captured at the ideal Heisenberg $J_1 - J_2$ limit. The doubly-degenerate ordering wave vector $(q, \pm q, 0)$ predicted by the model is reproduced in the fits to elastic neutron diffraction data, and the theory predicts that the spiral structure's ordering plane should be along $(0, 0, 1)$, $(1, 1, 0)$, or $(1, \bar{1}, 0)$. Experimental fits in Figure 3.4 and Table 3.1 rule out the $(0, 0, 1)$ ordering plane and the remaining planes of $(a, b, 0)$ can not be distinguished with the present powder data. Future single crystal neutron experiments could reveal if the ordering plane aligns with the energy minimization in the $(1, 1, 0)$ or $(1, \bar{1}, 0)$ planes.

Additionally, the extracted value of $|J_1|/J_2 = 1.426$ from the $J_1 - J_2$ model makes intuitive sense within the chemical lattice. It is unsurprising that the two magnetic interactions would be comparable in strength due to their relative superexchange pathways. In comparison, materials such as $KRuO_4$ [104] and $KOsO_4$ [153, 70] share the same $I4_1/amd$ magnetic sublattice comprised of Ru and Os ions, but break the oxygen-based superexchange connection along J_2. In these systems, magnetic order resides in the $J_2 = 0$ limit of the Heisenberg $J_1 - J_2$ model, where moments order within a Neél antiferromagnetic state and an unfrustrated J_1 [104, 153, 70].

Calculations of low-energy spin excitations with the parameters obtained from the $J_1 - J_2$ model largely reproduce the low-energy INS spectrum in Figures 3.5 and 3.8 with $J_2 \approx 1/3 \, \text{meV}$ and $J_1 \approx 0.475 \, \text{meV}$. One difference appears in the spectral weight at the Γ and $|\boldsymbol{q}| = \frac{2\sqrt{2}\pi}{a} \times 0.384$ positions, where a cancellation of the simulated structure factor

intensity occurs due to destructive interference of the two sublattices at these momenta. This cancellation does not occur in the experimental data due to the difference in phasing between Yb-moments relative to the predictions of the $J_1 - J_2$ model.

Despite this minor deviation, rooted in the relative phasing between the Yb-sublattices, our work establishes that $LiYbO_2$ contains a tetragonally-elongated diamond lattice largely captured by the Heisenberg $J_1 - J_2$ model. To the best of our knowledge, reports of diamond lattices decorated with trivalent lanthanide ions are rare, and, based upon our results, we expect that an ideal diamond lattice decorated with Yb^{3+} moments may reside close to the ideal Heisenberg limit. Such an ideal cubic Ln-ion diamond lattice would be a promising platform for manifesting (quantum) spiral spin liquid states, similar to transition metal spinels, while potentially avoiding the complications of extended exchange interactions born from d-electron systems.

3.5 Conclusions

$LiYbO_2$ provides an interesting material manifestation of localized f-electron moments decorating a frustrated diamond-like lattice. Long-range incommensurate spiral magnetic order of $\boldsymbol{k} = (0.384, \pm 0.384, 0)$ forms in the ground state, which seemingly manifests through a two-step ordering process via a partially ordered intermediate state. Upon applying an external magnetic field, magnetic order becomes commensurate with the lattice with $\boldsymbol{k} = (1/3, \pm 1/3, 0)$ through a "lock-in" phase transition. Remarkably, the majority of this behavior in $LiYbO_2$ can be captured in the Heisenberg $J_1 - J_2$ limit where
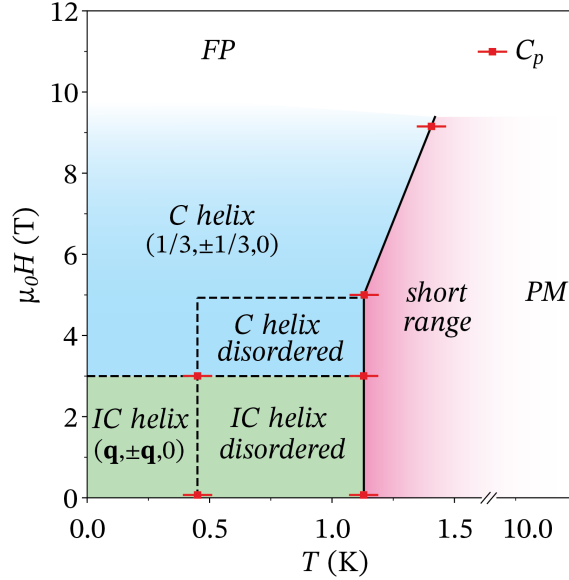
Figure 3.9: Proposed powder-averaged, low-temperature (H, T) diagram of $LiYbO_2$ extracted from a combination of specific heat (C_p) measurements and elastic neutron powder diffraction data. At high temperature, $LiYbO_2$ is in the paramagnetic (PM) phase. Below approximately $10\,K$, specific heat shows a broad feature where roughly half of the magnetic entropy of $R\ln(2)$ is released and signifies the onset of short-range magnetic correlations. A sharp anomaly at $1.13\,K$ at 0, 3, and $5\,T$ and $1.40\,K$ at $9\,T$ in specific heat measurements shows where long-range magnetic order sets in. Combining specific heat data with neutron powder diffraction data suggests that the temperature regime between $0.45\,K$ and $1.13\,K$ consists of a helical magnetic structure with disordered phasing between the two interpenetrating Yb sublattices. The system undergoes a lock-in phase transition from an incommensurate helical structure at zero field to a commensurate structure at $3\,T$.

the magnetic Yb^{3+} ions are split into two interpenetrating A-B sublattices. This model was explicitly re-derived and tuned for $LiYbO_2$, and it is directly related to a physical elongation of the diamond lattice Heisenberg $J_1 - J_2$ model. Differences in the relative phasing of A-B sublattices between the Heisenberg model and the observed magnetic structure suggest additional interactions and quantum effects may be present in $LiYbO_2$. This is possibly related to the observation of crystal field splittings suggesting two Yb environments. Exploring these as well as the nature of the intermediate ordered state

are promising future steps in single-crystal studies.

Chapter 4

Competing orders in pyrochlore magnets from a $\mathbb{Z}_2$ spin liquid perspective

4.1 Introduction

Quantum spin liquids (QSLs) [138] are zero-temperature phases of interacting spin systems which possess intrinsic long-range entanglement and support nonlocal excitations carrying fractionalized quantum numbers. Typically, they respect all symmetries of the underlying lattice, i.e., they exhibit a lack of conventional symmetry-breaking order. The theoretical understanding of QSLs is largely in terms of *emergent* gauge theory, which provides a convenient mathematical framework to describe long-range entanglement, along

with the nonlocal nature of the fractionalized excitations.

In frustrated magnetic systems [5], QSL ground states may control the physics even at (small) finite temperatures, as long as energy dominates over entropy. For two-dimensional spin liquids, this statement is purely asymptotic; at any nonzero temperature $T > 0$, the putative QSL is adiabatically connected to a high-temperature paramagnet. However, some three-dimensional spin liquids, particularly the so-called $\mathbb{Z}_2$ states with Ising-like emergent gauge fields, are more robust, and can persist in the form of a distinct low-temperature phase up to a nonzero critical temperature.

While QSLs are extremely interesting from a conceptual perspective, it is far from obvious to realize them in experimental materials, or even realistic spin Hamiltonians. Traditionally, most studies considered spin-rotation-invariant Heisenberg systems on geometrically frustrated two-dimensional lattices. However, it has recently been recognized that magnetic systems with strong spin–orbit coupling provide a promising alternative avenue to QSLs [167, 51, 127, 69]. In general, these systems have a large number of magnetically anisotropic terms, leading to exchange frustration as well as an extended parameter space, and are thus expected to harbor QSL ground states on a wide range of two- and three-dimensional lattices.

The most widely studied such three-dimensional structure is the pyrochlore lattice, consisting of periodically arranged corner-sharing tetrahedra. Experimentally, two large families of materials, the pyrochlore spinels and the rare-earth pyrochlores, provide vast real-world possibilities [45] to test theoretical predictions on the pyrochlore lattice. In the

2000s, it was predicted that certain antiferromagnetic pyrochlore models could support a U(1) QSL phase [63] [the "U(1)" means that the gauge field belongs to the Lie algebra of the U(1) group and that the emergent charges are characterized by integers related to the generating charge of U(1)], which is a simulacrum of electromagnetic gauge theory in high-energy physics. In 2011/2012, theoretical applications of this idea to realistic models emerged, suggesting the presence of a U(1) spin liquid in the so-called "quantum spin ice" pyrochlore materials [133, 137]. So far, these predictions remain to be confirmed in experiments, even though there are some promising recent developments [65, 64, 49, 149, 150, 143, 155, 147, 157].

Another thread recurring in the experimental study of rare-earth pyrochlores is the close competition amongst several weakly ordered states [55]. Several hints at this competition are present in the family of Yb pyrochlores, $Yb_2B_2O_7$, which have a systematic structural evolution across the series $B =$ Ge, Ti, Pt, Sn. While the germanate orders antiferromagnetically, the remaining members of the family have ferromagnetic ground states, suggesting the close proximity of at least these two phases. In each material, the specific heat is peaked at a temperature of 2-4 K, while the maximum ordering temperature is 0.6 K in the germanate and half or less than that in the rest of the family. These findings indicate the onset of strong spin correlations well above the ordering temperature, but an inability of the system to decide upon its ground state. The weak ferromagnetic ground state in $Yb_2Ti_2O_7$ is also famously mercurial, changing its character substantially with sample variations [17]. Theoretically, a classical analysis indeed

finds close competition amongst several distinct phases [172], but a quantum picture of this phase competition is not yet available.

In this work, we combine the two threads of phase competition and QSL physics by utilizing the connection of symmetry to emergent gauge structure. This connection is mathematically described by the projective symmetry group (PSG), proposed by Wen in 2002 [165], which encapsulates the fact that, in a QSL, the group operations of the physical symmetry group are interleaved with those of the emergent gauge group. The embedding of the physical symmetries into the PSG can then lead to a unification of distinct symmetry-breaking orders that are unrelated in classical physics. Such a unified description of seemingly unrelated magnetic orders is the main motivation behind the present study.

The PSG also offers a straightforward method to classify QSLs in the presence of symmetry. Concretely, the PSG specifies a distinct set of transformation rules for the emergent matter and gauge fields in each QSL phase, corresponding to a given PSG class. Employing the PSG method, an entire zoo of QSLs has been found on the square [130], triangular [97], kagome [99], honeycomb [177], star [34], and hyperkagome [67] lattices, to give a few notable examples. Generally, these QSLs can be connected to magnetically ordered states by considering the condensation patterns that emerge when the energy of a bosonic QSL excitation is brought to zero [11, 29, 87].

In this chapter, we employ the PSG method to obtain a full classification of QSLs with $\mathbb{Z}_2$ gauge structure on the pyrochlore lattice using Schwinger bosons [135, 161, 160,

174, 106, 23, 68]. While standard parton constructions also allow U(1) and SU(2) gauge structures, we consider the $\mathbb{Z}_2$ gauge structure for two reasons. First, it is the simplest one: quasiparticles in a $\mathbb{Z}_2$ QSL are weakly interacting because the gauge field itself is gapped. Second, it is also the richest one: a single U(1) PSG class can be further split into several $\mathbb{Z}_2$ PSG classes if the gauge symmetry is lowered from U(1) to $\mathbb{Z}_2$. We use Schwinger bosons rather than Abrikosov fermions [136] to immediately obtain a bosonic excitation, the elementary Schwinger boson itself, that can condense at the phase transition out of the QSL.

As a result of our PSG analysis, we find 16 different $\mathbb{Z}_2$ QSLs on the pyrochlore lattice. We use a standard mean-field description to study the 0-flux QSLs, in which translation symmetry acts linearly (i.e., as in classical physics) on the Schwinger bosons. The PSG method also allows us to describe phase transitions from these QSLs to magnetically ordered phases. Condensing the Schwinger bosons, we identify 15 different ordering patterns, and call them "paraphases", since each of them actually unifies several distinct symmetry-breaking orders. We find that, generically, these orders are intertwined, necessarily appearing together at the phase transition out of the QSL, and that conventional spin orders are in many cases accompanied by inversion-breaking "hidden" orders.

The phase transitions corresponding to these 15 paraphases fall into two dynamical classes of $z = 1$ and $z = 2$ quantum criticality, exhibiting critical modes with linear and quadratic dispersions, respectively. We uncover the mathematical structure discriminating between these two classes, related to Hamiltonian diagonalizability, and derive their

effective field theories, along with their most important experimental signatures. In particular, we use mean-field theory to compute static and dynamic spin structure factors for each of the 15 paraphases. Finally, by comparing the magnetic orders associated with each paraphase to those observed in experiments, we identify a set of likely QSL phases that might be relevant to real-world pyrochlore materials.

The rest of the chapter is organized as follows. First, in Sec. 4.2, we summarize our main results on the different QSL phases and the corresponding phase transitions out of them ("paraphases"). In Sec. 5.2, we employ the PSG method, deriving the PSG classes, and constructing a mean-field theory for each PSG class. In Sec. 5.3, we analyze the mean-field theories of our QSL phases, describing phase transitions out of them, and establishing the two dynamical classes with critical exponents $z = 1, 2$. In Sec. 5.4, we move on to the experimental signatures of our phase transitions, describing the heat capacity and the spin structure factors, and also introducing the concept of intertwined and hidden orders. Finally, in Sec. 5.5, we discuss our results and connect them to existing experimental data. Detailed derivations and lengthy formulas are given in the Appendices for reference.

4.2 Main results

Table 4.1: Most important characteristics of the 15 critical "paraphases" corresponding to phase transitions between the six 0-flux $\mathbb{Z}_2$ spin-liquid phases [labeled as 0-($n_{\overline{C}_6 S}\, n_{ST_1}\, n_{\overline{C}_6}$)] and a rich variety of magnetically ordered phases. Each paraphase is labeled by the condensation momenta (see Table IV for notation) where the spinons become gapless and condense at the phase transition. For each critical theory, experimental signatures are given in terms of the dynamical critical exponent, the low-temperature behavior of the heat capacity, and the low-energy features of the dynamic spin structure factor (see Fig. 4.4). For each magnetically ordered phase obtained by spinon condensation, it is specified whether various orders are generically present (+) or absent (0), including conventional spin orders, such as all-in-all-out (AIAO) order, XY antiferromagnetic (AFM) order [$\Psi_{2,3}$], ferromagnetic (FM) order, and Palmer-Chalker (PC) order [Ψ_4], as well as inversion-breaking "hidden" orders.

Spin-liquid phases	Critical "paraphases"				Magnetically ordered phases				
	Condensation momenta	Dynamical exponent	Heat capacity: $C_V \propto T^x$	Dynamic spin structure factor	Spin orders				Hidden orders
					AIAO	AFM	FM	PC	
0-(001)	Γ	$z=2$	$x=\frac{3}{2}$	Gapless at Γ Weak in the low-energy limit	0	0	+	0	+
	L	$z=2$	$x=\frac{3}{2}$	Gapless at Γ and X Weak in the low-energy limit	+	+	+	+	+
	Λ	$z=2$	$x=1$	Gapless along $\Gamma \to$ X and K $\to \Gamma \to$ L $\to$ U Low-energy weight at all momenta	Unclear at NN level				+
0-(010)	Γ	$z=2$	$x=\frac{3}{2}$	Gapless at Γ Weak in the low-energy limit	0	0	+	+	0
	Λ	$z=1$	$x=2$	Gapless along $\Gamma \to$ X and K $\to \Gamma \to$ L $\to$ U	Unclear at NN level				0
0-(100)	Γ	$z=2$	$x=\frac{3}{2}$	Gapless at Γ Weak in the low-energy limit	+	+	0	0	0
	Λ	$z=1$	$x=2$	Gapless along $\Gamma \to$ X and K $\to \Gamma \to$ L $\to$ U	Unclear at NN level				0
0-(101)	Γ	$z=2$	$x=\frac{3}{2}$	Gapless at Γ Weak in the low-energy limit	+	+	0	0	+
	W	$z=1$	$x=3$	Gapless at Γ, X, and $\frac{2}{3}$K Singular in the low-energy limit	+	+	+	+	+

	Point	z	x						Description
	X	$z=1$	$x=3$	+	+	0	+	+	Gapless at Γ and X Singular in the low-energy limit
0-(110)	Γ	$z=1$	$x=3$	0	+	0	0	0	Gapless at Γ Characteristic lower edge of the spectrum
	Λ	$z=1$	$x=2$		Unclear at NN level				Gapless along $\Gamma \to X$ and $K \to \Gamma \to L \to U$
	Γ	$z=2$	$x=\frac{3}{2}$	+	+	+	0	+	Gapless at Γ Weak in the low-energy limit
0-(111)	W	$z=1$	$x=3$	+	+	+	+	+	Gapless at Γ, X, and $\frac{2}{3}$K Singular in the low-energy limit
	X	$z=1$	$x=3$	+	+	+	0	+	Gapless at Γ and X Singular in the low-energy limit

From our PSG classification scheme, we find that there are 16 different $\mathbb{Z}_2$ PSG classes of Schwinger bosons, corresponding to 16 inequivalent $\mathbb{Z}_2$ QSL phases, on the pyrochlore lattice. Out of these 16 different QSLs, there are eight 0-flux QSLs and eight π-flux QSLs. For each QSL, we construct a general quadratic mean-field Hamiltonian for the Schwinger bosons containing all onsite, nearest neighbor (NN), and next-nearest neighbor (NNN) terms allowed by symmetry. However, for simplicity, we focus on the 0-flux QSLs and restrict the mean-field Hamiltonian to onsite and NN terms. At such a NN level, two out of eight 0-flux Hamiltonians have an enlarged U(1) gauge symmetry, and we thus concentrate on the remaining six 0-flux Hamiltonians with $\mathbb{Z}_2$ gauge symmetry.

In each of the six corresponding $\mathbb{Z}_2$ QSL phases, the Schwinger bosons can be identified as elementary spinon excitations carrying fractionalized quantum numbers. If the chemical potential is tuned to its critical value, there is a phase transition driven by the condensation of these bosonic spinons. Depending on the particular patterns of spinon condensation, we describe 15 different critical "paraphases" out of the six QSL phases. The most important characteristics of these paraphases, labeled by their parent QSL phases and the condensation momenta of the spinons, are tabulated in Table 4.1.

For each paraphase, the spinon spectrum is gapless at the critical point by construction. The effective field theory of the critical point is characterized by the low-energy spinon dispersion, $\omega \sim k^z$, in terms of the dynamical critical exponent, which is either $z = 1$ or $z = 2$. These two dynamical classes give rise to distinct sets of experimental signatures. For a start, the power-law exponent x of the low-temperature heat capacity,

136

$C_V \sim T^x$, is determined by the dynamical exponent z and the dimensionality of the condensation manifold, i.e., if the spinons condense at points or along lines in the Brillouin zone (BZ). Also, the dynamical exponent gives rise to universal features in the static and dynamic spin structure factors, which appear on top of more detailed characteristics specific to given paraphases. In particular, when approaching zero energy, the spectral weight in the dynamic structure factor vanishes for $z = 2$ but diverges for $z = 1$; the divergence in the $z = 1$ case is also observable as a nonanalytic behavior in the static structure factor.

To establish a connection between spinon condensation and the resulting magnetic orders, restricted to zero momentum for simplicity, we investigate the transformation rules of the possible order parameters under the point group O_h of the pyrochlore lattice. For each paraphase, we determine which magnetic orders generically appear, concentrating in particular on the conventional spin orders seen in the experiments: the all-in-all-out, antiferromagnetic, ferromagnetic, and Palmer-Chalker orders. In doing so, we learn two important general lessons on magnetic orders obtained by spinon condensation. First, several distinct orders may be intertwined, i.e., they necessarily accompany each other, even though they are completely unrelated on the classical level. Second, the conventional spin orders may emerge together with more exotic inversion-breaking "hidden" orders.

4.3 Classification result

4.3.1 Projective symmetry group

The detailed solution of the PSG equations is presented in Appendix A.5. The PSG results for the phases are

$$\phi_{T_1}(\boldsymbol{r}_\mu) = 0, \tag{4.1a}$$

$$\phi_{T_2}(\boldsymbol{r}_\mu) = n_1 \pi r_1, \tag{4.1b}$$

$$\phi_{T_3}(\boldsymbol{r}_\mu) = n_1 \pi (r_1 + r_2), \tag{4.1c}$$

$$\phi_{\mathcal{T}}(\boldsymbol{r}_\mu) = 0, \tag{4.1d}$$

$$\phi_{\overline{C}_6}(\boldsymbol{r}_\mu) = \left[\frac{n_{\overline{C}_6}}{2} + (n_1 + n_{ST_1})\delta_{\mu=1,2,3} \right] \pi$$
$$+ n_1 \delta_{\mu=2,3} \pi r_1 + n_1 \delta_{\mu=2} \pi r_3 + n_1(r_1 r_2 + r_1 r_3), \tag{4.1e}$$

$$\phi_S(\boldsymbol{r}_\mu) = \left[(-)^{\delta_{\mu=1,2,3}} \frac{n_1 + n_{ST_1}}{2} + \delta_{\mu=2} n_{\overline{C}_6 S} \right] \pi + (n_1 \delta_{\mu=1,2} - n_{ST_1})\pi r_1$$
$$+ (n_1 \delta_{\mu=2} - n_{ST_1})\pi r_2 + n_1 \delta_{\mu=1,2}\pi r_3 - \frac{1}{2} n_1 \pi (r_1 + r_2)(r_1 + r_2 + 1), \tag{4.1f}$$

where n_1, $n_{\overline{C}_6 S}$, n_{ST_1}, and $n_{\overline{C}_6}$ are four $\mathbb{Z}_2$ parameters, each being either 0 or 1. Therefore, we find that there are 16 gauge-inequivalent $\mathbb{Z}_2$ PSG classes, corresponding to distinct $\mathbb{Z}_2$ quantum spin liquids, which we label by the notation $n_1 \pi$-$(n_{\overline{C}_6 S} \, n_{ST_1} \, n_{\overline{C}_6})$. The four $\mathbb{Z}_2$ parameters have concrete interpretations:

- The parameter n_1 comes from the three PSG equations corresponding to $T_i T_{i+1} T_i^{-1} T_{i+1}^{-1} = 1$, which are required by the PSG to share the same $\mathbb{Z}_2$ parameter. Physically, it quantifies the Aharonov-Bohm (AB) phase a spinon accumulates while moving on the closed edge of a plaquette, which is traversed by such a sequence of translations. In the case of $n_1 = 1$ ($n_1 = 0$), the AB phase is π (0), corresponding to a π-flux

(0-flux) spin liquid.

- The parameter $n_{\overline{C}_6}$ comes from the PSG equation corresponding to $\overline{C}_6^6 = 1$. Physically, it describes the AB phase a spinon accumulates after completing six subsequent sixfold rotoinversions. Together with n_{ST_1}, it determines whether or not the sixfold rotoinversion $\overline{C}_6$ acts projectively.

- The parameter n_{ST_1} comes from the PSG equation corresponding to $ST_1 S^{-1} T_3^{-1} T_1 = 1$. Physically, it describes the AB phase a spinon accumulates after completing the operation sequence $ST_1 S^{-1} T_3^{-1} T_1$. Together with n_1 and $n_{\overline{C}_6 S}$ it determines whether or not the screw operation S acts projectively.

- The parameter $n_{\overline{C}_6 S}$ comes from the PSG equation corresponding to $(\overline{C}_6 S)^4 = 1$. Physically, it describes the AB phase a spinon accumulates after completing the operation sequence $(\overline{C}_6 S)^4$.

4.3.2   Construction of mean-field ansätze

We are now in the position to construct the mean-field ansatz for each PSG class. The most general mean-field ansatz for bosonic spinons can be written as

$$H = \sum_{\boldsymbol{r}_\mu, \boldsymbol{r}'_\nu} b^\dagger_{\boldsymbol{r}_\mu} u^h_{\boldsymbol{r}_\mu, \boldsymbol{r}'_\nu} b_{\boldsymbol{r}'_\nu} + b^\dagger_{\boldsymbol{r}_\mu} u^p_{\boldsymbol{r}_\mu, \boldsymbol{r}'_\nu} \left(b^\dagger_{\boldsymbol{r}'_\nu} \right)^T + h.c., \tag{4.2}$$

where $u^h_{\boldsymbol{r}_\mu, \boldsymbol{r}'_\nu}$ and $u^p_{\boldsymbol{r}_\mu, \boldsymbol{r}'_\nu}$ are 2×2 matrices acting on spin space, and the labels "h" and "p" indicate hopping and pairing terms, respectively.

The PSG operators $\widetilde{\mathcal{O}}$ and $\widetilde{\mathcal{T}}$ are the symmetry operators of the Hamiltonian H,

meaning $\widetilde{\mathcal{O}}\colon H \to H$ and $\widetilde{\mathcal{T}}\colon H \to H$. Since the spinons transforms under $\widetilde{\mathcal{O}}$ and $\widetilde{\mathcal{T}}$ according to Eqs. (1.33) and (1.34), the matrices u^h and u^p must transform as

$$
\begin{aligned}
G_{\mathcal{O}}^{\dagger}[\mathcal{O}(\boldsymbol{r}_{\mu})] U_{\mathcal{O}} u^h_{\boldsymbol{r}_{\mu},\boldsymbol{r}'_{\nu}} U_{\mathcal{O}}^{\dagger} G_{\mathcal{O}}[\mathcal{O}(\boldsymbol{r}'_{\nu})] &= u^h_{\mathcal{O}(\boldsymbol{r}_{\mu}),\mathcal{O}(\boldsymbol{r}'_{\nu})}, &\text{(4.3a)}\\
G_{\mathcal{O}}^{\dagger}[\mathcal{O}(\boldsymbol{r}_{\mu})] U_{\mathcal{O}} u^p_{\boldsymbol{r}_{\mu},\boldsymbol{r}'_{\nu}} U_{\mathcal{O}}^{T} G_{\mathcal{O}}^{\dagger}[\mathcal{O}(\boldsymbol{r}'_{\nu})] &= u^p_{\mathcal{O}(\boldsymbol{r}_{\mu}),\mathcal{O}(\boldsymbol{r}'_{\nu})} &\text{(4.3b)}
\end{aligned}
$$

for space-group elements $\mathcal{O} \in \{T_1, T_2, T_3, \overline{C}_6, S\}$ and as

$$
\begin{aligned}
G_{\mathcal{T}}^{\dagger}(\boldsymbol{r}_{\mu}) U_{\mathcal{T}} \left(u^h_{\boldsymbol{r}_{\mu},\boldsymbol{r}'_{\nu}}\right)^{*} U_{\mathcal{T}}^{\dagger} G_{\mathcal{T}}(\boldsymbol{r}'_{\nu}) &= u^h_{\boldsymbol{r}_{\mu},\boldsymbol{r}'_{\nu}}, &\text{(4.4a)}\\
G_{\mathcal{T}}^{\dagger}(\boldsymbol{r}_{\mu}) U_{\mathcal{T}} \left(u^p_{\boldsymbol{r}_{\mu},\boldsymbol{r}'_{\nu}}\right)^{*} U_{\mathcal{T}}^{T} G_{\mathcal{T}}^{\dagger}(\boldsymbol{r}'_{\nu}) &= u^p_{\boldsymbol{r}_{\mu},\boldsymbol{r}'_{\nu}} &\text{(4.4b)}
\end{aligned}
$$

for time reversal $\mathcal{T}$. The respective SU(2) matrices are

$$
\begin{aligned}
U_{T_1} = U_{T_2} = U_{T_3} = \sigma^0, \quad U_{\mathcal{T}} = i\sigma^2, \\
U_{\overline{C}_6} = U_{C_3} = e^{-\frac{i}{2}\frac{2\pi}{3}\frac{(1,1,1)}{\sqrt{3}}\cdot\boldsymbol{\sigma}}, \quad U_S = e^{-\frac{i}{2}\pi\frac{(1,1,0)}{\sqrt{2}}\cdot\boldsymbol{\sigma}}.
\end{aligned} \tag{4.5}
$$

where $\sigma^0 = 1_{2\times 2}$ is the identity matrix. Suppressing the site indices for simplicity, we parameterize the matrices u^h and u^p in the general forms

$$
\begin{aligned}
u^h &= a\sigma^0 + i(b\sigma^1 + c\sigma^2 + d\sigma^3), &\text{(4.6a)}\\
u^p &= \left(a'\sigma^0 + i(b'\sigma^1 + c'\sigma^2 + d'\sigma^3)\right)\cdot i\sigma^2, &\text{(4.6b)}
\end{aligned}
$$

where $a, b, c, d, a', b', c', d'$ are all complex. The additional factor $i\sigma^2$ appearing in u^p ensures that (a, b, c, d) and (a', b', c', d') transform in the same way under the respective unitary conjugations $u^h \to Uu^hU^{\dagger}$ and $u^p \to Uu^pU^T$ for any $U \in \mathrm{SU}(2)$. In both cases, the singlet parameters a and a' transform as scalars, while the triplet parameters $\boldsymbol{b} = (b, c, d)$ and $\boldsymbol{b'} = (b', c', d')$ transform as SO(3) vectors. Indeed, any SU(2) rotation leaves the singlet parameters invariant and performs the corresponding SO(3) rotation

on the triplet vectors: $\boldsymbol{b} \to \mathcal{R}\boldsymbol{b}$ and $\boldsymbol{b}' \to \mathcal{R}\boldsymbol{b}'$. For the generators $\overline{C}_6$ and S, these SO(3) rotations are

$$
\mathcal{R}^{\overline{C}_6} = \begin{pmatrix} & & 1 \\ 1 & & \\ & 1 & \end{pmatrix}, \quad \mathcal{R}^{S} = \begin{pmatrix} & 1 & \\ 1 & & \\ & & -1 \end{pmatrix}, \tag{4.7}
$$

while the translations $T_{1,2,3}$ correspond to trivial SO(3) rotations: $\mathcal{R}^{T_{1,2,3}} = 1_{3\times3}$.

To reduce the number of parameters in the mean-field ansatz, we first consider the effect of time reversal. Substituting Eq. (4.6) into Eq. (4.4), and taking $G_{\mathcal{T}}(\boldsymbol{r}_\mu) = 1$ from Eq. (4.1d), we obtain $(a, b, c, d) = (a^*, b^*, c^*, d^*)$ as well as $(a', b', c', d') = (a'^*, b'^*, c'^*, d'^*)$ and deduce that all 8 parameters of u^h and u^p are real.

Turning to space-group symmetries and using Eq. (4.3), we can then establish relations between the respective parameters of $u^h_{\boldsymbol{r}_\mu,\boldsymbol{r}'_\nu}$ and $u^p_{\boldsymbol{r}_\mu,\boldsymbol{r}'_\nu}$ that correspond to different bonds $\langle \boldsymbol{r}_\mu, \boldsymbol{r}'_\nu \rangle$ of the lattice. In fact, the entire mean-field ansatz in Eq. (4.2) can be constructed up to next-nearest-neighbor level by specifying the 8 real parameters for each of the following three representative bonds:

- onsite "bond" $\boldsymbol{0}_0 \to \boldsymbol{0}_0$:

$$
\begin{aligned}
u^h_{\boldsymbol{0}_0,\boldsymbol{0}_0} &= \alpha\sigma^0 + i(\beta\sigma^1 + \gamma\sigma^2 + \delta\sigma^3), \\
u^p_{\boldsymbol{0}_0,\boldsymbol{0}_0} &= \left(\alpha'\sigma^0 + i(\beta'\sigma^1 + \gamma'\sigma^2 + \delta'\sigma^3)\right) \cdot i\sigma^2,
\end{aligned} \tag{4.8}
$$

- nearest neighbor (NN) bond $\boldsymbol{0}_0 \to \boldsymbol{0}_1$:

$$
\begin{aligned}
u^h_{\boldsymbol{0}_0,\boldsymbol{0}_1} &= a\sigma^0 + i(b\sigma^1 + c\sigma^2 + d\sigma^3), \\
u^p_{\boldsymbol{0}_0,\boldsymbol{0}_1} &= \left(a'\sigma^0 + i(b'\sigma^1 + c'\sigma^2 + d'\sigma^3)\right) \cdot i\sigma^2,
\end{aligned} \tag{4.9}
$$

- next-nearest neighbor (NNN) bond $\boldsymbol{0}_1 \to \boldsymbol{0}_2 - \hat{e}_2$:

$$
\begin{aligned}
u^h_{\boldsymbol{0}_1,\boldsymbol{0}_2-\hat{e}_2} &= A\sigma^0 + i(B\sigma^1 + C\sigma^2 + D\sigma^3), \\
u^p_{\boldsymbol{0}_1,\boldsymbol{0}_2-\hat{e}_2} &= \left(A'\sigma^0 + i(B'\sigma^1 + C'\sigma^2 + D'\sigma^3)\right) \cdot i\sigma^2.
\end{aligned} \tag{4.10}
$$

Table 4.2: Independent mean-field parameters and constraints for the sixteen PSG classes. The parameters not mentioned in this table are enforced to be zero by the constraints. Note that a nonzero onsite chemical potential $\mu = \alpha$ is allowed in all PSG classes. We defined † to be the condition $\beta' = \delta' = \gamma' = \nu$. In the classes superscripted by ‡, the mean-field Hamiltonians appear to be U(1) on the NN level, but recover their $\mathbb{Z}_2$ character upon including NNN terms.

Class $n_1\pi$-	Independent nonzero parameters			Constraints		
$(n_{\overline{C}_6 S} n_{ST_1} n_{\overline{C}_6})$	Onsite	NN	NNN	Onsite	NN	NNN
0-(000)‡	μ	a,c	A,B,D,B'		$c=-d$	$B=C,\ B'=-C'$
0-(001)	μ	a,c,b'	A,B,D,B'		$c=-d,$	$B=C,\ B'=-C'$
0-(010)	μ,ν	a,c,b'	A,B,D,A',B',D'	†	$c=-d,$	$B=C,\ B'=C'$
0-(011)‡	$\mu,$	a,c	A,B,D,A',B',D'		$c=-d,$	$B=C,\ B'=C'$
0-(100)	$\mu,$	b,c'	A,B,D,B'		$c'=d',$	$B=C,\ B'=-C'$
0-(101)	$\mu,$	b,a',c'	A,B,D,B'		$c'=-d',$	$B=C,\ B'=-C'$
0-(110)	μ,ν	b,a',c'	A,B,D,A',B',D'	†	$c'=-d',$	$B=C,\ B'=C'$
0-(111)	$\mu,$	b,c'	A,B,D,A',B',D'		$c'=d',$	$B=C,\ B'=C'$
π-(000)	μ,ν	a,c,b'	B,B'	†	$c=-d$	$B=-C,\ B'=-C'$
π-(001)‡	μ	a,c	B,B'		$c=-d$	$B=-C,\ B'=-C'$
π-(010)	μ	a,c	B,A',B',D'		$c=-d$	$B=-C,\ B'=C'$
π-(011)	$\mu,$	a,c,b'	B,A',B',D'		$c=-d$	$B=-C,\ B'=C'$
π-(100)‡	μ,ν	b,a',c'	B,B'	†	$c'=-d'$	$B=-C,\ B'=-C'$
π-(101)	$\mu,$	b,c'	B,B'		$c'=d'$	$B=-C,\ B'=-C'$
π-(110)	μ	b,c'	B,A',B',D'		$c'=d'$	$B=-C,\ B'=C'$
π-(111)	$\mu,$	b,a',c'	B,A',B',D'		$c'=-d'$	$B=-C,\ B'=C'$

4.3.3 Nontrivial parameter constraints

When constructing the entire mean-field ansatz from the representative bonds in Eqs. (4.8)–(4.10), the significance of using Eq. (4.3) is twofold. On the one hand, most space-group elements map the representative bonds onto different bonds, thereby determining the matrices $u^h_{\boldsymbol{r}_\mu,\boldsymbol{r}'_\nu}$ and $u^p_{\boldsymbol{r}_\mu,\boldsymbol{r}'_\nu}$ for all symmetry-related bonds. On the other hand, some space-group elements map the representative bonds onto themselves, thereby leading to nontrivial constraints on the original 24 parameters.

For simplicity, we first concentrate on the 0-flux PSG classes. Since translation is

trivial [see Eqs. (4.1a)–(4.1c)], we can restrict our attention to a single unit cell, within which bonds are mapped onto each other by elements of the *point group*. Since the point group O_h consists of 48 elements, and there are 4 onsite, 12 NN, and 24 NNN bonds within a single unit cell, which can be viewed as three orbits in the point group, the orbit-stabilizer theorem implies that the onsite, NN, and NNN representative bonds are mapped onto themselves by 12, 4, and 2 point-group elements, respectively. When a bond is mapped onto itself by such a point-group element, nontrivial constraints are obtained on the parameters by comparing the new and the old expressions for $u^h_{\boldsymbol{r}_\mu,\boldsymbol{r}'_\nu}$ and $u^p_{\boldsymbol{r}_\mu,\boldsymbol{r}'_\nu}$. These constraints can be found in Appendix A.2; see Ref. [94] for the detailed solution to these constraints.

In Table 4.2, we present the nonzero parameters of the mean-field ansatz for each of the eight 0-flux and each of the eight π-flux PSG classes up to NNN level, along with any constraints between the parameters. From these nonzero parameters, the entire mean-field ansatz can be constructed via Eq. (4.3). Note that some of the mean-field ansätze in Table 4.2 have an enlarged U(1) gauge symmetry at the NN level which only breaks down to $\mathbb{Z}_2$ when nonzero NNN terms are included.

4.4 Analysis of the mean-field ansätze

The previous section explains how the method of PSG can be used to obtain classes of 0-flux and π-flux mean-field ansätze, which describe distinct phases of $\mathbb{Z}_2$ quantum spin liquids on the mean-field level. In this section, we focus on the 0-flux mean-field

ansätze and study their physical properties in great detail. Since our main goal is to explore the relationship between spin liquids and magnetic orders adjacent to them, we primarily concentrate on the critical field theories and the condensation patterns (i.e., the resulting magnetic orders).

In each mean-field ansatz, we neglect the NNN terms for simplicity, restricting our attention to onsite and NN terms. Since we are interested in $\mathbb{Z}_2$ spin liquids, and two out of eight 0-flux mean-field ansätze have U(1) gauge symmetry at the NN level, we only consider the remaining *six* mean-field ansätze in the rest of the chapter.

4.4.1 Symmetry properties

The PSG method is rooted in symmetry analysis, and it is important to understand how the PSG governs the symmetry of the mean-field Hamiltonians. By means of a Fourier transformation, a general mean-field Hamiltonian [see Eq. (4.2)] can be written in momentum space as

$$H = \sum_{\boldsymbol{k} \in \mathrm{BZ}} B_{\boldsymbol{k}}^{\dagger} \mathcal{H}(\boldsymbol{k}) B_{\boldsymbol{k}}, \tag{4.11}$$

where $B_{\boldsymbol{k}} = \left(b_{\boldsymbol{k},0}, b_{\boldsymbol{k},1}, b_{\boldsymbol{k},2}, b_{\boldsymbol{k},3}, b_{-\boldsymbol{k},0}^{\dagger}, b_{-\boldsymbol{k},1}^{\dagger}, b_{-\boldsymbol{k},2}^{\dagger}, b_{-\boldsymbol{k},3}^{\dagger} \right)^{T}$ is a 16-component vector of operators. The matrix $\mathcal{H}(\boldsymbol{k})$ has the standard Bogoliubov form

$$\mathcal{H}(\boldsymbol{k}) = \begin{pmatrix} U_h(\boldsymbol{k}) & U_p(\boldsymbol{k}) \\ U_p^{\dagger}(\boldsymbol{k}) & U_h^{T}(-\boldsymbol{k}) \end{pmatrix}, \tag{4.12}$$

where $U_h(\boldsymbol{k}) = U_h^{\dagger}(\boldsymbol{k})$ and $U_p(\boldsymbol{k}) = U_p^{T}(-\boldsymbol{k})$, corresponding to hopping and pairing terms, respectively.

The Hamiltonian matrix $\mathcal{H}(\boldsymbol{k})$ combines momenta $\pm\boldsymbol{k}$ and thus assigns a full set of

144

physical degrees of freedom to only half of the BZ. This redundancy in the description leads to an effective charge-conjugation "symmetry", corresponding to the matrix-level constraint

$$U_{\mathcal{C}}^{-1}\mathcal{H}^*(\boldsymbol{k})U_{\mathcal{C}} = \mathcal{H}(-\boldsymbol{k}), \tag{4.13}$$

where we define $U_{\mathcal{C}} = \sigma^1 \otimes 1_{8\times 8}$. The anti-unitary charge-conjugation operator is then given by $U_{\mathcal{C}}\mathcal{K}$, where $\mathcal{K}$ denotes complex conjugation.

Considering physical symmetries, time reversal $\mathcal{T}$ gives rise to an analogous matrix-level constraint

$$U_{\mathcal{T}}^{-1}\mathcal{H}^*(\boldsymbol{k})U_{\mathcal{T}} = \mathcal{H}(-\boldsymbol{k}), \tag{4.14}$$

where we define $U_{\mathcal{T}} = 1_{8\times 8} \otimes (i\sigma^2)$. Correspondingly, the anti-unitary time-reversal operator is $U_{\mathcal{T}}\mathcal{K}$. Note that time reversal acts non-projectively in all PSG classes because we use gauge freedom to fix $\phi_{\mathcal{T}}(\boldsymbol{r}_\mu) = 0$.

In contrast, inversion $I = \overline{C}_6^3$ acts projectively on the spinons and generates the matrix-level constraint

$$U_I^{-1}(\boldsymbol{k})\mathcal{H}(\boldsymbol{k})U_I(\boldsymbol{k}) = \mathcal{H}(-\boldsymbol{k}), \tag{4.15}$$

where $U_I(\boldsymbol{k}) = (\sigma^3)^{n_{\overline{C}_6}} \otimes (U_J \cdot I^2(\boldsymbol{k})) \otimes \sigma^0$, in terms of the 4×4 diagonal form-factor matrix

$$I(\boldsymbol{k}) = \mathrm{Diag}\left(1, e^{i\boldsymbol{k}\cdot\hat{\varepsilon}_1}, e^{i\boldsymbol{k}\cdot\hat{\varepsilon}_2}, e^{i\boldsymbol{k}\cdot\hat{\varepsilon}_3}\right), \tag{4.16}$$

and the diagonal matrix $U_J = \mathrm{Diag}\left((-1)^{n_{ST_1}}, 1, 1, 1\right)$.

The symmetries $\mathcal{C}$, $\mathcal{T}$, and I result in important general spectral features. First, the symmetry $I \circ \mathcal{T}$ guarantees that each energy level is doubly degenerate, according to

145

Kramers theorem. Second, the symmetry $I \circ \mathcal{C}$ leads to an additional double degeneracy for any non-zero-energy level, which is connected to the redundant description in Eqs. (4.11) and (4.12). The two symmetries together thus result in a generic fourfold degeneracy at each energy level $E > 0$ shared by momenta $\pm \boldsymbol{k}$. Note that the degeneracy may be smaller or larger at special time-reversal-invariant momenta ($\boldsymbol{k} = -\boldsymbol{k}$) because there are half as many physical degrees of freedom but, on the other hand, pure point-group symmetries (e.g., inversion) may lead to additional degeneracy.

The degeneracy of zero-energy levels is more subtle as it may be affected by the diagonalizability of the Hamiltonian matrix $\mathcal{H}(\boldsymbol{k})$. Since the low-energy physics is the main focus of our study, this issue will be addressed in a separate section (see Sec. 4.4.4).

4.4.2   Condensation domains: a "phase diagram" for paraphases

The use of bosonic mean-field Hamiltonians, obtained from the spinon decomposition in Eq. (1.19), facilitates the study of phase transitions between spin liquids and magnetically ordered phases. Indeed, by lowering the chemical potential μ, there is a critical chemical potential μ_c at which the bosonic spinons undergo Bose–Einstein condensation at some critical momenta $\boldsymbol{k}_c$ and the system thus develops magnetic order.

For the mean-field Hamiltonian in each PSG class, the critical chemical potential μ_c is a function of the mean-field parameters.While the value of μ_c changes continuously with the mean-field parameters, and this variation of μ_c is thus locally analytic, it globally separates into domains across which the variation of μ_c is non-analytic. These domains
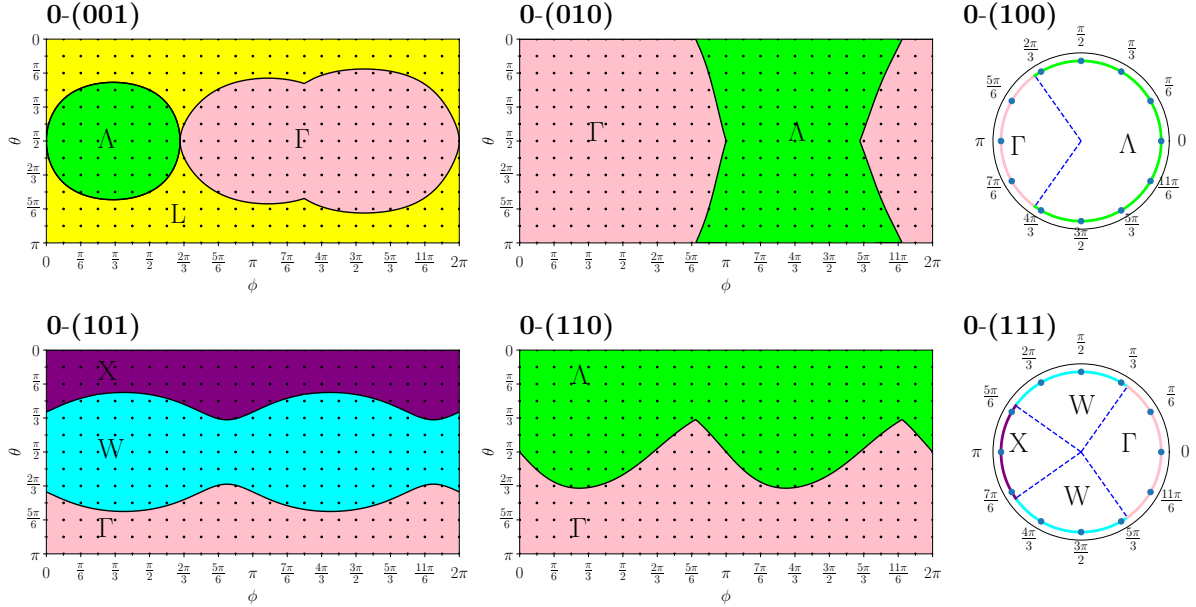
Figure 4.1: Condensation "phase diagrams" for the NN mean-field ansätze of the six 0-flux PSG classes 0-(001), 0-(010), 0-(100), 0-(101), 0-(110), and 0-(111). The complete phase diagram at NN level is 1D for classes 0-(100) and 0-(111), 2D for classes 0-(001) and 0-(101), and 3D for classes 0-(010) and 0-(110). The parameters (ψ, θ, ϕ) are related to the mean-field parameters according to Table 4.6. For the classes 0-(010) and 0-(110), only a 2D slice with $\psi = 0$ is shown. The slices for other values of ψ share the same qualitative behavior as the $\psi = 0$ slice, e.g., they also consist of two phases Γ and Λ.

of analyticity of μ_c are reminiscent of the domains of analyticity of the free energy, which define phases in thermodynamics. However, the analogy is not perfect as each such domain may give rise to several true phases on crossing the phase transition into magnetic order (i.e., when taking $\mu < \mu_c$). We therefore coin the word *paraphases* to describe the distinct domains of analyticity of μ_c. Restated, each paraphase is a connected region of phase space in which the unstable manifold of condensation modes varies smoothly.

Following this logic, the six mean-field Hamiltonians are further divided into 15 para-phases (see Fig. 4.1). The analytical expressions for the paraphase boundaries are given

Table 4.3: Paraphase boundaries of the NN ansätze.

Class	Adjacency	Paraphase boundary
0-(001)	Λ vs L	$2ac + c^2 - b'^2 = 0$
	Γ vs L	$2a^2 + ac - b'^2 = 0$ for $c > a$ and $ac - 4c^2 + b'^2 = 0$ for $c < a$
	Λ vs Γ	$2a + c = b' = 0$
0-(010)	Γ vs Λ	$\sqrt{4(a-c)^2 + 3(\nu - b')^2} = -2a - 4c + \sqrt{3}|\nu + b'|$
0-(100)	Γ vs Λ	$\sqrt{2}b = \pm c'$
0-(101)	Γ vs W	$-2b^2 + 3c'^2 + 2c'a' + a'^2 = 0$, $b > 0$
	X vs W	$-2b^2 + 3c'^2 + 2c'a' + a'^2 = 0$, $b < 0$
0-(110)	Γ vs Λ	$\sqrt{(\nu + a' - 2c')^2 + 2(\nu - a')^2} = 4b + \sqrt{3}|\nu + a' + 2c'|$
0-(111)	Γ vs W	$\sqrt{2}b = \pm c'$
	X vs W	$b = \pm\sqrt{2}c'$

Table 4.4: Possible sets of condensation momenta.

Label	Description
Γ	$(0,0,0)$
L	$\pi(\delta_1, \delta_2, \delta_3)$, where $\delta_1, \delta_2, \delta_3 \in \{1, -1\}$
Λ	$k(\delta_1, \delta_2, \delta_3)$, where $k \in [-\pi, \pi]$ and $\delta_1, \delta_2, \delta_3 \in \{1, -1\}$
X	$X^1 = 2\pi(1,0,0)$, $X^2 = 2\pi(0,1,0)$, $X^3 = 2\pi(0,0,1)$
W	$\pi(2, \pm 1, 0)$ and all permutations of the 3 components

in Table 4.3, while the distinct critical momenta $\boldsymbol{k}_c = \Gamma, L, \Lambda, X, W$ characterizing the various paraphases are explained in Table 4.4. Finally, the distinct expressions for the critical chemical potentials μ_c in the 15 paraphases are listed in Table 4.5.

Note that, for the PSG classes with $n_{ST_1} = 1$, the PSG result for the screw operation S depends on the spatial coordinates, and it is convenient to shift the entire BZ by the translation $\boldsymbol{k} \to \boldsymbol{k} - \pi(1,1,1)$. Such a shift of the BZ can be thought of as a gauge transformation of the spinons, which does not modify any physical quantities on the spin level. This shift is assumed throughout the chapter and is already taken into account when specifying the condensation momenta in Fig. 4.1.

Table 4.5: Critical chemical potential μ for the 15 paraphases.

Paraphase	Critical μ_c
0-(001)Γ	$\mu_c = \max\{-6a, 2a - 8c\}$
0-(001)L	Largest root of $\mu^3 + 2(a + 2c)\mu^2$ $-4(2a^2 - 4ac + 2c^2 + 3b'^2)\mu - 24b'^2(a + 2c) = 0$
0-(001)Λ	$\mu_c = 2a + 4c$
0-(010)Γ	$\mu_c = 2\left(a + 2c + \sqrt{4(a - c)^2 + 3(\nu - b')^2}\right)$
0-(010)Λ	$\mu_c = 2\left(-a - 2c + \sqrt{3}|\nu + b'|\right)$
0-(100)Γ	$\mu_c = -6b$
0-(100)Λ	$\mu_c = 2b + 4\sqrt{2}|c'|$
0-(101)Γ	$\mu_c = -6b$
0-(101)W	Largest root of $\mu^4 - 8(b^2 + 2a'^2 + 4c'^2)\mu^2$ $+64(2a' + c')bc'\mu - 64a'c'(b^2 + 3c'^2)$ $+16(b^2 - 3c'^2)^2 - 32b^2a'^2 + 48a'^4 = 0$
0-(101)X	$\mu_c = 2b + 2\sqrt{2}|a' - c'|$
0-(110)Γ	$\mu_c = 6b + 2\sqrt{3}|\nu + a' + 2c'|$
0-(110)Λ	$\mu_c = -2b + 2\sqrt{(\nu + a' - 2c')^2 + 2(\nu - a')^2}$
0-(111)Γ	$\mu_c = 6b$
0-(111)W	$\mu_c = \max\left\{\pm\sqrt{2}w + \sqrt{2}\sqrt{2b^2 \mp 4\sqrt{2}bw + 7w^2}\right\}$
0-(111)X	$\mu_c = -2b + 2\sqrt{6}|c'|$

Note also that the region Λ supports a one-dimensional manifold of condensation momenta. Since the only physical symmetries are discrete space-group and time-reversal symmetries, this ground-state continuum must be accidental, i.e., the result of restricting the mean-field Hamiltonians to NN level. Indeed, when including infinitesimal NNN parameters, we see that the condensation regions are reduced from Λ to either Γ or L.

4.4.3 Critical spectra

The critical spectra of the 15 paraphases, corresponding to $\mu = \mu_c$ in each case, are shown in Fig. 4.4, along with the associated dynamical spin structure factors, obtained

on the mean-field level. Generically, each of these spectra consists of four bands, which is consistent with the fourfold degeneracy of each band. While certain spectra have distinguishing features, not all paraphases can be *fully* distinguished by their spectra, as some spectral characteristics are shared by multiple paraphases. Among other features, several spectra show a quasi-mirror-reflection symmetry (in terms of energy) between two bands, which accounts for certain high-energy features in the dynamic spin structure factor (see Sec. 4.5.2).

Most importantly, however, the critical paraphases can be divided into two classes, characterized by linear and quadratic dispersions at low energies. In terms of the dynamical critical exponent z, defined by $\omega \sim |k - k_c|^z$ and specified for each paraphase in Table 4.1, these two classes are labeled by $z = 1$ and $z = 2$, respectively. As we later show, paraphases with $z = 1$ and $z = 2$ correspond to different critical field theories, which determine the critical exponents of various physical observables, such as the heat capacity and the magnetic susceptibility, and thus lead to distinct experimental signatures.

4.4.4 Hamiltonian diagonalizability

From a technical point of view, the distinction between $z = 1$ and $z = 2$ theories becomes evident when we try to diagonalize the Hamiltonian matrix in Eq. (5.17). In general, we seek a change of basis for the bosonic operators,

$$B_{\boldsymbol{k}} = V(\boldsymbol{k})\widetilde{B}_{\boldsymbol{k}}, \tag{4.17}$$

such that the Hamiltonian in Eq. (5.16) is of the form

$$H = \sum_{\boldsymbol{k} \in \text{BZ}} \widetilde{B}_{\boldsymbol{k}}^{\dagger} \Lambda(\boldsymbol{k}) \widetilde{B}_{\boldsymbol{k}}, \tag{4.18}$$

where $\Lambda(\boldsymbol{k}) = V^{\dagger}(\boldsymbol{k}) \mathcal{H}(\boldsymbol{k}) V(\boldsymbol{k})$ is a 16×16 diagonal matrix, and $V(\boldsymbol{k}) \in \text{SU}(8,8)$ satisfies

$$V(\boldsymbol{k}) J V^{\dagger}(\boldsymbol{k}) = J, \qquad J = \sigma^3 \otimes 1_{8 \times 8}, \tag{4.19}$$

ensuring that this change of basis is a canonical transformation. The matrices $\Lambda(\boldsymbol{k})$ and $V(\boldsymbol{k})$ can be found by solving the generalized eigenvalue problem

$$J\mathcal{H}(\boldsymbol{k}) \boldsymbol{a}_{\boldsymbol{k},i} = \lambda_{\boldsymbol{k},i} \boldsymbol{a}_{\boldsymbol{k},i}, \tag{4.20}$$

where the eigenvalues $\lambda_{\boldsymbol{k},i}$ give the diagonal elements of the matrix $J\Lambda(\boldsymbol{k})$ and the eigenvectors $\boldsymbol{a}_{\boldsymbol{k},i}$ form the columns of the matrix $V(\boldsymbol{k})$. However, since $J\mathcal{H}(\boldsymbol{k})$ is not necessarily Hermitian (or even normal), it is not guaranteed that such a matrix $V(\boldsymbol{k})$ actually exists.

In particular, it may happen at the critical chemical potential $\mu = \mu_c$ that there are not enough independent eigenvectors for the zero eigenvalues $\lambda_{\boldsymbol{k}_c} = 0$. Physically, this scenario means that we cannot diagonalize our critical Hamiltonian by a canonical transformation of bosonic creation and annihilation operators, and instead we must decompose our complex operators $B_{\boldsymbol{k}}$ according to

$$B_{\boldsymbol{k}} = \frac{1}{\sqrt{2}} (\hat{X}_{\boldsymbol{k}} + i\hat{P}_{\boldsymbol{k}}), \tag{4.21}$$

where $\hat{X}_{\boldsymbol{k}}$ and $\hat{P}_{\boldsymbol{k}}$ are 16-dimensional vectors of real operators, analogous to the position and momentum operators in first quantization. In terms of these new operators, the

analog for the change of basis in Eq. (4.17) is

$$\begin{pmatrix} \hat{X}_{\boldsymbol{k}} \\ \hat{P}_{\boldsymbol{k}} \end{pmatrix} = W(\boldsymbol{k}) \begin{pmatrix} \hat{Y}_{\boldsymbol{k}} \\ \hat{Q}_{\boldsymbol{k}} \end{pmatrix}, \tag{4.22}$$

where the 32×32 matrix $W(\boldsymbol{k})$ satisfies

$$W(\boldsymbol{k})\mathcal{E}W^T(\boldsymbol{k}) = \mathcal{E}, \qquad \mathcal{E} = i\sigma^2 \otimes 1_{16\times16}. \tag{4.23}$$

Using this canonical change of basis, the Hamiltonian can then be brought to the diagonal

form

$$H = \sum_{\boldsymbol{k},i} \alpha_{\boldsymbol{k},i}\hat{y}_{\boldsymbol{k},i}^2 + \beta_{\boldsymbol{k},i}\hat{q}_{\boldsymbol{k},i}^2, \tag{4.24}$$

where $\hat{y}_{\boldsymbol{k},i}$ and $\hat{q}_{\boldsymbol{k},i}$ are the components of $\hat{Y}_{\boldsymbol{k}}$ and $\hat{Q}_{\boldsymbol{k}}$, respectively, and the new eigenvalues

are related to the original ones by

$$\lambda_{\boldsymbol{k},i}^2 = \alpha_{\boldsymbol{k},i}\beta_{\boldsymbol{k},i}. \tag{4.25}$$

Importantly, however, unlike the original method of diagonalization, $B_{\boldsymbol{k}} \to \widetilde{B}_{\boldsymbol{k}}$, which

may fail if $J\mathcal{H}(\boldsymbol{k})$ is a defective matrix, the alternative method of diagonalization,

$(\hat{X}_{\boldsymbol{k}}, \hat{P}_{\boldsymbol{k}}) \to (\hat{Y}_{\boldsymbol{k}}, \hat{Q}_{\boldsymbol{k}})$, always works.

For any zero mode i at a critical momentum $\boldsymbol{k}_c$, we have $\alpha_{\boldsymbol{k}_c,i}\beta_{\boldsymbol{k}_c,i} = 0$ from Eq. (4.25).

The diagonalizability of the critical Hamiltonian $\mathcal{H}(\boldsymbol{k}_c)$ is then determined by the follow-

ing simple criterion:

- If $\alpha_{\boldsymbol{k}_c,i} = \beta_{\boldsymbol{k}_c,i} = 0$, the Hamiltonian can be diagonalized in the original basis of

  creation and annihilation operators;

- Otherwise, either $\alpha_{\boldsymbol{k}_c,i} = 0$, $\beta_{\boldsymbol{k}_c,i} \neq 0$ or $\alpha_{\boldsymbol{k}_c,i} \neq 0$, $\beta_{\boldsymbol{k}_c,i} = 0$; the Hamiltonian is

  not diagonalizable in any creation-annihilation-operator basis, meaning that the

SU(8,8) transformation is singular.

To understand how these two scenarios for the diagonalizability lead to theories of $z = 2$ and $z = 1$ types, respectively, we now switch to the language of path integrals and consider the critical low-energy actions.

4.4.5 Effective low-energy theories

Our phase transitions from spin liquids to magnetic orders, driven by a change in the chemical potential μ, are prototypes of quantum critical points (QCPs). At such a QCP, one can write down an effective theory in terms of the low-energy degrees of freedom. We assume a single condensing eigenmode obtained from the Hamiltonian $\mathcal{H}(\boldsymbol{k}_c)$, denoted by $\widetilde{b}_{\boldsymbol{k}_c}$. Including spatial fluctuations, we promote this eigenmode to a field $\phi(\tau, \boldsymbol{x})$ and consider the imaginary-time action $S = \int \mathcal{L} \, d^3 x \, d\tau$. If the Hamiltonian is diagonalizable, the critical Lagrangian becomes

$$\mathcal{L} = \overline{\phi} \left(\partial_\tau - \mu_{ij} \partial_i \partial_j \right) \phi, \tag{4.26}$$

describing a massless field ϕ at the QCP. The corresponding action is invariant under the rescaling

$$\tau \to \tau e^{-l}, \qquad x \to x e^{-l/2}, \qquad \phi \to \phi e^{3l/4}, \tag{4.27}$$

from which we can immediately deduce that the dynamical critical exponent is $z = 2$.

However, the mass of ϕ should be generally considered as a tensor of real fields χ and π, which are the real and imaginary components of ϕ, such that

$$\phi = \chi + i\pi. \tag{4.28}$$

153

In the Hamiltonian language, these two components correspond to the "position" and "momentum" operators in Eq. (4.21). Consequently, if the Hamiltonian is not diagonalizable, only one of these components is massless at the QCP. Assuming without loss of generality that χ is massive and π is massless, the critical Lagrangian becomes

$$\mathcal{L} = 2i\chi\partial_\tau\pi + r^2\chi^2 - \pi\nu_{ij}\partial_i\partial_j\pi. \tag{4.29}$$

By integrating out the massive field χ and rescaling the massless field as $\pi \to r\pi$, we finally obtain

$$\mathcal{L}_{\text{eff}} = \pi\left(\partial_\tau^2 - \widetilde{\nu}_{ij}\partial_i\partial_j\right)\pi. \tag{4.30}$$

This effective action is invariant under the rescaling

$$\tau \to \tau e^{-l}, \qquad x \to x e^{-l}, \qquad \pi \to \pi e^{l}, \tag{4.31}$$

from which we can immediately deduce that the dynamical critical exponent is $z = 1$.

These two distinct QCPs, characterized by critical exponents $z = 2$ and $z = 1$, respectively, are reminiscent of the QCPs governing phase transitions from quantum paramagnets to XY antiferromagnets [179]. If such a transition is induced by an external magnetic field, the QCP is described by the $z = 2$ critical theory in Eq. (4.26), while if the transition is induced by pressure and is thus time-reversal symmetric, the QCP is described by the $z = 1$ critical theory in Eq. (4.30).

4.4.6 Spin condensation: order patterns

We are now ready to describe the spin orders obtained by condensing the spinons in each of the 15 critical paraphases. When the chemical potential μ reaches its critical value

Table 4.6: Parametrization of the NN mean-field ansätze using generalized spherical coordinates (ψ, θ, ϕ) for the phase diagram in Fig. 4.1.

Class	Independent nonzero parameters up to NN terms and parameterized by
0-(001)	$(a, c, b') = (\sin\theta\cos\phi, \sin\theta\sin\phi, \cos\theta)$
0-(010)	$(\nu, a, c, b') = (\cos\psi, \sin\psi\sin\theta\cos\phi, \sin\psi\sin\theta\sin\phi, \sin\psi\cos\theta)$
0-(100)	$(b, c') = (\cos\phi, \sin\phi)$
0-(101)	$(b, a', c') = (\cos\theta, \sin\theta\cos\phi, \sin\theta\sin\phi)$
0-(110)	$(\nu, b, a', c') = (\cos\psi, \sin\psi\cos\theta, \sin\psi\sin\theta\cos\phi, \sin\psi\sin\theta\sin\phi)$
0-(111)	$(b, c') = (\cos\phi, \sin\phi)$

μ_c, certain spinons $\widetilde{b}_{\boldsymbol{k}_c}$ at critical momenta $\boldsymbol{k}_c$ condense and thereby acquire macroscopic occupation numbers $\langle\widetilde{b}_{\boldsymbol{k}_c}\rangle$. We can then use these $\langle\widetilde{b}_{\boldsymbol{k}_c}\rangle$ as order parameters and detect spin orders by looking at order parameter bilinears, which, according to the spinon decomposition in Eq. (1.19), recover spin expectation values.

So far, several types of orders have been successfully identified in pyrochlore materials, most of which do not break translation symmetry. These zero-momentum orders correspond to representations of the point group O_h and can thus be analyzed by the standard representation theory of groups. We will defer such an effort to the next section. In this subsection, we select several paraphases with definite ordering signatures and explicitly calculate the spin expectation values via condensing spinons. This way, we capture a limited set of orders, which correspond to irreducible representations (irreps) of the tetrahedral group T_d (see Appendix A.3), and show that all such orders can be obtained from at least one of the six $\mathbb{Z}_2$ spin liquids. We mainly restrict ourselves to NN terms in the spinon Hamiltonian but include NNN terms whenever necessary.

One must bear in mind that the simplified irrep analysis on these explicit spin-

condensation orders may be incomplete. For example, we will find from such an analysis that pure all-in-all-out order may be obtained in the paraphase 0-(100)Γ, while a full representation-theory analysis in Sec. 4.5.3 leads to Table 4.9, which indicates that all-in-all-out order is always intertwined with some hidden orders (i.e., it can never appear alone). Still, the naïve spin-condensation analysis in this subsection is a good starting point to build some insight into how the six spin liquids are physically distinct from each other.

All-in-all-out order

We consider the paraphase 0-(100)Γ, but also remark that the paraphases 0-(101)Γ and 0-(111)Γ give similar results. At the critical chemical potential μ_c, the zero-energy subspace is twofold degenerate. The zero-energy eigenvectors are obtained from Eq. (4.20) and are given by the time-reversal partners $\boldsymbol{a}$ and $U_{\mathcal{T}}\boldsymbol{a}^*$. After condensing these two modes, the corresponding operators $\widetilde{b}_{1,2}$ acquire macroscopic occupation numbers $\langle \widetilde{b}_i \rangle = r_i e^{i\phi_i}$, with $i = 1, 2$, implying $\langle B_{\boldsymbol{k}_c} \rangle = \sum_{i=1,2} \boldsymbol{a}_i r_i e^{i\phi_i}$ at the critical momentum $\boldsymbol{k}_c = \Gamma$. In terms of the 12-component vector $\mathbf{S} = (\boldsymbol{S}_0, \boldsymbol{S}_1, \boldsymbol{S}_2, \boldsymbol{S}_3)$ of the spin components on the four sublattices, we have, up to a global coefficient,

$$\mathbf{S} = r\mathbf{S}^r + \cos(\phi_1 - \phi_2)\mathbf{S}^c + \sin(\phi_1 - \phi_2)\mathbf{S}^s, \tag{4.32}$$

where $r = (r_1^2 - r_2^2)/(2r_1 r_2)$, and $\mathbf{S}^{r,c,s}$ are three equimodular and mutually orthogonal vectors (see Appendix A.3 for detail). Using the basis for the irreducible representations of T_{d} (see Appendix A.3), it can be shown that this paraphase generically supports two

156

orders: the all-in-all-out order and the AFM order. One can obtain pure all-in-all-out order [see Fig. 4.2(a) for illustration] by setting particular values for the condensation parameters $r_{1,2}$ and $\phi_{1,2}$.

XY antiferromagnetic order

The paraphase 0-(110)Γ has a non-diagonalizable critical Hamiltonian, because $\mathcal{H}$ has four zero-energy eigenvalues, but the nullspace of $J\mathcal{H}$ is only two dimensional, spanned by the time-reversal partners $\boldsymbol{a}$ and $U_{\mathcal{T}}\boldsymbol{a}^*$. We therefore switch to the position-momentum representation $(\hat{x}, \hat{p})$, according to Eq. (4.21). The critical Hamiltonian is then diagonalized by a basis change $(\hat{x}, \hat{p}) \to (\hat{y}, \hat{q})$ and takes the low-energy form

$$H = \hat{q}_1^2 + \hat{q}_2^2 + 0 \cdot \hat{y}_1^2 + 0 \cdot \hat{y}_2^2, \tag{4.33}$$

which contains two gapless modes $\hat{y}_1$ and $\hat{y}_2$. To minimize the energy, we must have $\langle \hat{q}_i \rangle = 0$ and, due to the uncertainty principle, $\hat{y}_i$ must fluctuate maximally. In terms of $y_i = \langle \hat{y}_i \rangle$, we then find $\langle B_{\boldsymbol{k}_c} \rangle = \boldsymbol{b} y_1 + U_{\mathcal{T}} \boldsymbol{b} y_2$ at $\boldsymbol{k}_c = \Gamma$ for some vector $\boldsymbol{b}$ determined by $\boldsymbol{a}$, and the final result for spin configuration becomes

$$\begin{aligned} \mathbf{S} \quad &\propto \quad (C, -S_2, -S_1, C, S_2, S_1, -C, -S_2, S_1, -C, S_2, -S_1), \\ &S_1 = \sin\left(\frac{\pi}{12} - \theta\right), \quad S_2 = \sin\left(\frac{\pi}{4} + \theta\right), C = \cos\left(\frac{\pi}{12} + \theta\right), \end{aligned}$$

where $\cos\theta = y_1^2 - y_2^2$ and $\sin\theta = y_1 y_2/2$. This spin configuration, shown in Fig. 4.2(b), corresponds to the "XY" order of the irrep E obtained in Eq. (39) of Ref. [172] after a redefinition $\theta \to \theta - \frac{\pi}{12}$.
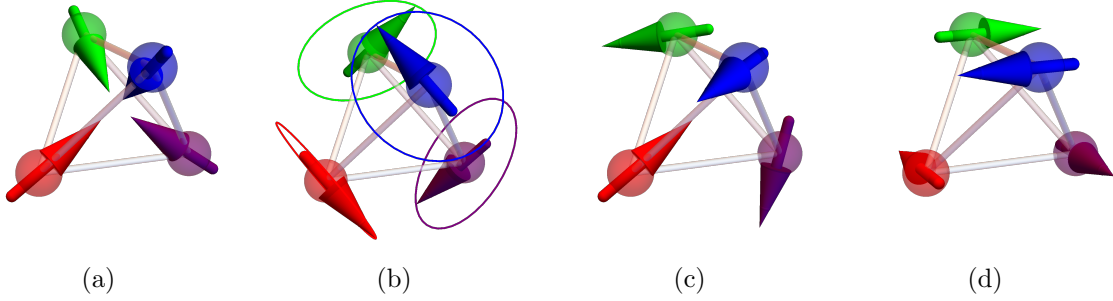
Figure 4.2: Typical spin order for (a) the paraphases 0-(100)Γ, 0-(101)Γ, and 0-(111)Γ (all-in all-out order), (b) the paraphase 0-(110)Γ (the XY order), (c) the paraphase 0-(001)Γ (ferrimagnetic order), and (d) the paraphase 0-(101)X (the Palmer-Chalker order).

Ferromagnetic order: collinear and non-collinear

For the paraphase 0-(001)Γ, all pairing terms vanish at the Γ point at the NN level and, solving the hopping part at μ_c, we find that the zero-energy subspace is spanned by the time-reversal partners $\boldsymbol{a}$ and $U_{\mathcal{T}}\boldsymbol{a}^*$. There are two cases depending on the expression for μ in terms of the mean field parameters. When $\mu = -6a$, all four spins point in the same direction, which is the collinear FM order. When $\mu = 2a - 8c$, the spin vector $\mathbf{S}$ follows Eq. (4.32), where $\mathbf{S}^{r,c,s}$ are three equimodular and mutually orthogonal vectors (see Appendix A.3 for detail). A typical spin configuration of such ferrimagnetic nature is shown in Fig. 4.2(c).

Palmer-Chalker order

The paraphase 0-(101)X has a non-diagonalizable critical Hamiltonian, because $\mathcal{H}$ has eight zero-energy eigenvalues, but the nullspace of $J\mathcal{H}$ is only four dimensional. Switching to the $(\hat{x}, \hat{p})$ representation and diagonalizing the Hamiltonian via the basis change

158

$(\hat{x}, \hat{p}) \to (\hat{y}, \hat{q})$, we find that there are four gapless modes $\hat{y}_{1,2,3,4}$ for each of the three critical momenta $\boldsymbol{k}_c = \mathrm{X}^{1,2,3}$. The expression for $\langle B_{\boldsymbol{k}_c} \rangle$ thus contains 12 real parameters: the expectation values of the maximally fluctuating modes $\hat{y}_{1,2,3,4}$ at each critical momentum. Although most choices of these condensation parameters give an order with an enlarged unit cell, some special cases respect translation symmetry. For instance, if condensation is restricted to X^1, the spin configuration, shown in Fig. 4.2(d), corresponds to a Palmer-Chalker order, transforming under the irrep T_2.

Non-uniform spinon condensations and partial orders

The spin expectation values $\boldsymbol{S}_{0,1,2,3}$ for the paraphase 0-(010)Γ have different amplitudes on different sublattices, invalidating the irrep analysis that presupposed classically ordered states of fixed-length spins. There is no a priori reason to rule out such a non-uniform spin-amplitude state. It does, however, correspond to a more "exotic" ordered phase in which the spin is more ordered on some sublattices than others. This type of partially ordered state has been proposed in the material $\mathrm{Gd}_2\mathrm{Ti}_2\mathrm{O}_7$ [27, 74] and in various theoretical models.

Spinon line orders

The line orders Λ appearing in classes 0-(001), 0-(010), 0-(100), and 0-(110) have accidental degeneracies, higher than demanded by the lattice symmetry. This extra degeneracy is an artifact of the restriction to NN ansätze, and should reduce to discrete condensation momenta in the presence of further-neighbor terms. If we include infinitesimal NNN

159

terms to the mean-field ansatz, using Table 4.2, we indeed see that line condensation along Λ shrinks to point condensation at either Γ or L. However, if we increase these NNN terms, the condensation points are shifted away from these high-symmetry points.

Due to the large NNN parameter space, we were unable to exhaustively study the effect of NNN terms on the NN mean-field ansatz. However, for some purposes, the NN level ansätze may be adequate. For example, as we explore in the next section, the line minima contribute to substantial low-energy continua in the dynamical spin structure factor. This feature should persist at intermediate energies when small NNN terms are included.

Multi-spinon condensation orders

Spinon condensation at multiple critical momenta, in the paraphases 0-(001)L, 0-(101)X/W, and 0-(111)X/W, allows for richer physics and is often accompanied by an enlargement of the unit cell. As an example, we look at the paraphase 0-(001)L: there are two independent zero-energy modes at each critical momentum L, and the four inequivalent L momenta thus give rise to an eight-dimensional zero-energy subspace. The 16-component zero-energy modes at these critical momenta have a complicated expression and do not form a representation of T_d, thereby leading to non-uniform spinon condensation, as discussed above. Indeed, if condensation is restricted to one of the four inequivalent L momenta, we find that three of the four sublattices have the same spin amplitude, while the fourth sublattice has a different one.

4.5 Experimental signatures

4.5.1 Critical behavior of the heat capacity

For each critical paraphase, the low-temperature heat capacity is expected to follow a power law whose exponent is determined by the low-energy spinon density of states in the critical theory. Indeed, depending on the dynamical exponent z and the spinon condensation manifold (i.e., if spinons condense at points or along lines), this low-energy density of states follows different power laws $g(\epsilon) \sim \epsilon^\alpha$, where the possible values of α are listed in Table 4.7. The thermal energy due to spinon excitations at temperature T is then given by

$$E \sim \int d\epsilon\, g(\epsilon)\, \frac{\epsilon}{\exp(\epsilon/T) - 1} \propto T^{2+\alpha}, \tag{4.34}$$

and the heat capacity takes the form

$$C_V = \frac{dE}{dT} \propto T^{1+\alpha}. \tag{4.35}$$

We remark that line condensation is not stable against generic perturbations, corresponding to further-neighbor terms in the mean-field ansatz. Consequently, at the lowest temperatures, we expect that the line-condensation paraphases are governed by the same exponents as their point-condensation counterparts. Nevertheless, if the NN mean-field ansatz is a good first approximation, there is an intermediate temperature range in which the approximate line condensation in such paraphases becomes manifest and therefore the line-condensation exponents in Table 4.7 are experimentally observable.

161

Table 4.7: Power-law exponents of the low-energy spinon density of states and the corresponding low-temperature heat capacity for critical theories of dynamical exponents $z = 1, 2$ where spinons condense at points or along lines.

Condensation manifold	Dynamical exponent	Density of states: $g(\epsilon) \propto \epsilon^\alpha$	Heat capacity: $C_V \propto T^x$
Point(s)	$z = 2$	$\alpha = \frac{1}{2}$	$x = \frac{3}{2}$
	$z = 1$	$\alpha = 2$	$x = 3$
Line(s)	$z = 2$	$\alpha = 0$	$x = 1$
	$z = 1$	$\alpha = 1$	$x = 2$

4.5.2 Critical spin structure factors

In this subsection, we present the most direct signatures of our critical points between magnetic orders and their parent spin liquids by computing both the static and the dynamic spin structure factors for the 15 paraphases. While our calculation is based on mean-field theory, it still serves as a reference point for classifying the possible spinon spectra in pyrochlore magnets.

The static structure factor (SSF) is defined as the spatial Fourier transform of the equal-time spin-spin correlation function,

$$S(\boldsymbol{q}) = \frac{1}{N} \sum_{\boldsymbol{r}_\mu, \boldsymbol{r}'_\nu, \alpha} \left\langle \hat{S}^\alpha_{\boldsymbol{r}_\mu} \hat{S}^\alpha_{\boldsymbol{r}'_\nu} \right\rangle e^{i\boldsymbol{q} \cdot (\boldsymbol{r}_\mu - \boldsymbol{r}'_\nu)}, \tag{4.36}$$

where $\alpha = x, y, z$. We calculate this quantity using the critical mean-field ansätze in Sec. 5.3. Writing the 16×16 matrix $V(\boldsymbol{k})$ in Eq. (4.17) as

$$V(\boldsymbol{k}) = \begin{pmatrix} V_{11}(\boldsymbol{k}) & V_{12}(\boldsymbol{k}) \\ V_{21}(\boldsymbol{k}) & V_{22}(\boldsymbol{k}) \end{pmatrix}, \tag{4.37}$$
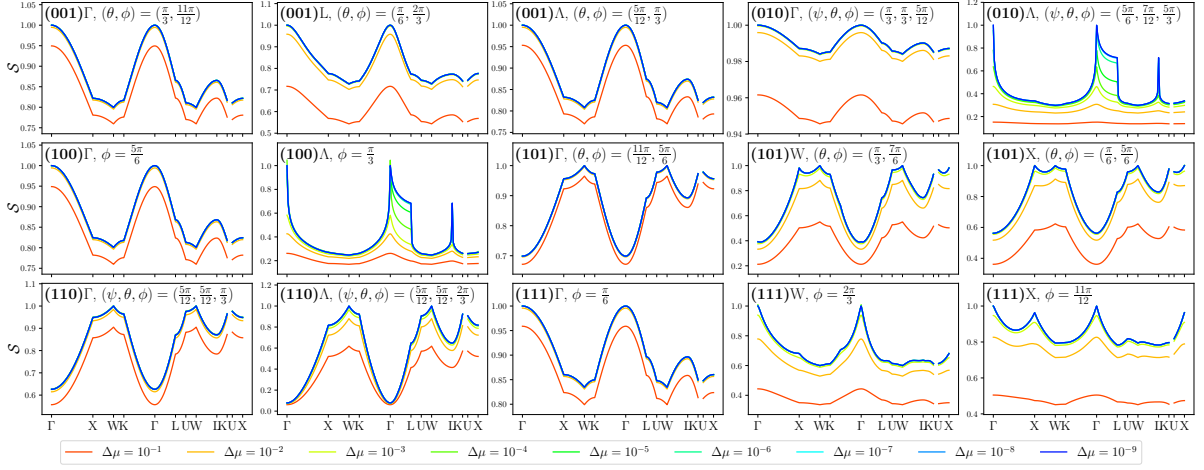
Figure 4.3: Static spin structure factors for representative points in each of the 15 para-phases along the high-symmetry path in the Brillouin zone. The chemical potential μ is above the critical condensation value by $\Delta\mu = 10^{-1}, 10^{-2}, ..., 10^{-9}$ (in arbitrary units). The vertical axis is the spectral weight $\mathcal{S}$ normalized by the maximum intensity of the $\Delta\mu = 10^{-9}$ line along the path. In each paraphase, denoted by its PSG class and con-densation momenta, the representative point is specified by the mean-field parameters.

where the 8×8 blocks generally satisfy

$$V_{11}^*(\boldsymbol{k}) = V_{22}(-\boldsymbol{k}), \qquad V_{12}^*(\boldsymbol{k}) = V_{21}(-\boldsymbol{k}) \tag{4.38}$$

due to charge-conjugation "symmetry", the SSF becomes

$$\mathcal{S}(\boldsymbol{q}) = \frac{1}{2N} \sum_{\boldsymbol{k},\alpha} \text{Tr} \left[U^\alpha(\boldsymbol{k}, \boldsymbol{q}) \left(U^\alpha(\boldsymbol{k}, \boldsymbol{q}) \right)^\dagger \right] \tag{4.39}$$

in terms of the auxiliary 8×8 matrices

$$U^\alpha(\boldsymbol{k}, \boldsymbol{q}) = W^\alpha(\boldsymbol{k}, \boldsymbol{q}) + \left(W^\alpha(-\boldsymbol{k} + \boldsymbol{q}, \boldsymbol{q}) \right)^T, \quad W^\alpha(\boldsymbol{k}, \boldsymbol{q}) = V_{12}^\dagger(\boldsymbol{k}) \left(I(\boldsymbol{q}) \otimes \sigma^\alpha \right) V_{11}(\boldsymbol{k} - \boldsymbol{q}), \tag{4.40}$$

where $I(\boldsymbol{q})$ is the 4×4 diagonal form-factor matrix defined in Eq. (4.16). The resulting SSFs for representative points in each of the 15 paraphases are plotted in Fig. 4.3 for chemical potentials $\mu = \mu_c + 10^{-\delta}$, where $\delta = 1, 2, \ldots, 9$, and μ_c is the critical value given

in Table 4.5. When numerically computing the SSF, we ensure convergence by taking a momentum-space grid that does not contain any condensation momenta $\boldsymbol{k}_c$.

For chemical potentials well above the critical value μ_c, the SSFs of the 15 paraphases (not shown here) can be partitioned into two classes, depending on the sum of the $\mathbb{Z}_2$ parameters $n_{\overline{C}_6 S} + n_{ST_1} + n_{\overline{C}_6}$ characterizing the parent spin liquid. Plotted along the high-symmetry path in the BZ, the SSFs of the $n_{\overline{C}_6 S} + n_{ST_1} + n_{\overline{C}_6} =$ odd paraphases and those of the $n_{\overline{C}_6 S} + n_{ST_1} + n_{\overline{C}_6} =$ even paraphases resemble each other after an appropriate reflection in energy. This relation between the two classes qualitatively survives as the chemical potential approaches its critical value (see Fig. 4.3). For example, depending on the the the sum $n_{\overline{C}_6 S} + n_{ST_1} + n_{\overline{C}_6}$ being even or odd, the SSF has either a valley or a peak at the Γ point. The distinction between the two behaviors can be traced back to Eqs. (4.39) and (4.40). Since the SSF is the squared trace norm of the matrix U^α, which in turn is the sum of two matrices W^α, there is a cross term from the product of the two matrices W^α, physically corresponding to the spinon pairing channel $\langle b^\dagger_{\boldsymbol{k}_1,\mu\sigma_1} b^\dagger_{\boldsymbol{k}_3,\nu\sigma_3} \rangle \langle b_{\boldsymbol{k}_1-\boldsymbol{q},\mu\sigma_2} b_{\boldsymbol{k}_3+\boldsymbol{q},\nu\sigma_4} \rangle$, and we numerically find this cross term to be negative for the $n_{\overline{C}_6 S} + n_{ST_1} + n_{\overline{C}_6} =$ even paraphases and positive for the $n_{\overline{C}_6 S} + n_{ST_1} + n_{\overline{C}_6} =$ odd paraphases. Nevertheless, a deeper understanding of this connection to $n_{\overline{C}_6 S} + n_{ST_1} + n_{\overline{C}_6}$ remains to be found.

Also, there are general differences between the SSFs of the paraphases governed by $z = 1$ and $z = 2$ critical theories, respectively. For most of the $z = 1$ paraphases, as the chemical potential approaches its critical value, the SSF becomes a non-differentiable function at certain momenta $\boldsymbol{q}$. This feature is clearly observable in Fig. 4.3 for the
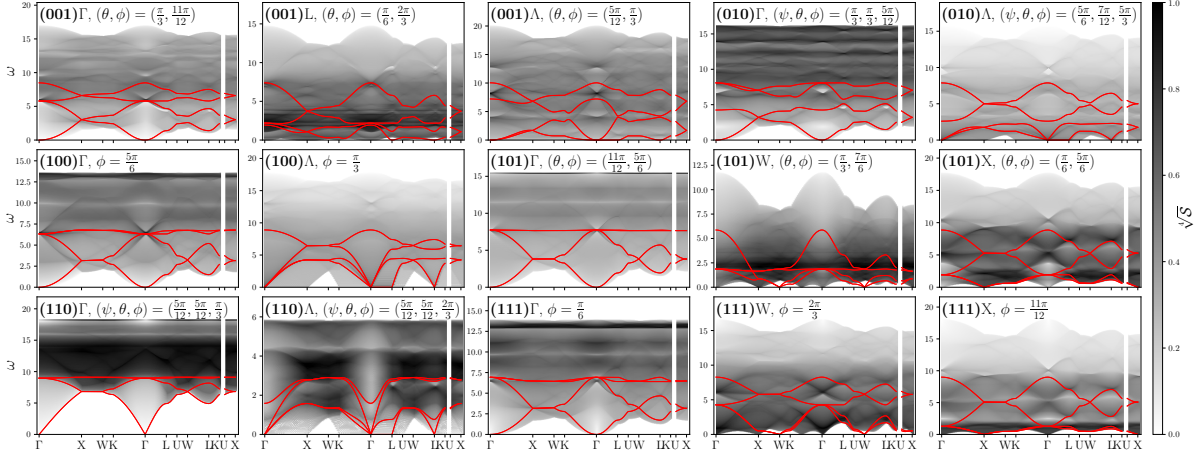
Figure 4.4: Dynamic spin structure factors (gray) and spinon spectra (red) for representative points in each of the 15 paraphases along the high-symmetry path in the Brillouin zone. The vertical axis is the energy ω in arbitrary units, while the gray scale is the quartic root of the spectral weight (power is chosen such that maximum resolution is ensured), $\sqrt[4]{\mathcal{S}}$, normalized by its maximum intensity along the path. The chemical potential μ is 10^{-9} above the critical condensation value. In each paraphase, denoted by its PSG class and condensation momenta, the representative point is specified by the mean-field parameters.

paraphases 0-(010)Λ, 0-(100)Λ, 0-(101)W, 0-(111)W, 0-(111)X at the Γ point and for the

paraphases 0-(101)W, 0-(101)X, 0-(111)W, 0-(111)X at the X point. However, not all

$z = 1$ paraphases conform to this rule; the SSFs of the paraphases 0-(110)Γ and 0-(110)Λ

do not reveal any singular behavior along the high-symmetry path in the BZ. Instead,

they resemble the SSFs of $z = 2$ paraphases, which are smooth across the entire BZ.

To understand these features, we consider the dynamic structure factor (DSF), which

provides further information on the dynamics of spinons. This quantity is defined as the

spatial and temporal Fourier transform of the spin-spin correlation function,

$$\mathcal{S}(\omega, \boldsymbol{q}) = \frac{1}{2\pi N} \int_{-\infty}^{\infty} dt \sum_{\boldsymbol{r}_\mu, \boldsymbol{r}'_\nu, \alpha} \left\langle \hat{S}^\alpha_{\boldsymbol{r}_\mu}(t) \hat{S}^\alpha_{\boldsymbol{r}'_\nu} \right\rangle e^{i(\omega t + \boldsymbol{q} \cdot (\boldsymbol{r}_\mu - \boldsymbol{r}_\nu))}, \tag{4.41}$$

165

and, using the mean-field ansätze in Sec. 5.3, it takes the general form [94]

$$
\begin{aligned}
S(\omega, \boldsymbol{q}) =& \frac{1}{N} \sum_{\mu,\nu} e^{i\boldsymbol{q}\cdot(\hat{\varepsilon}_\mu - \hat{\varepsilon}_\nu)} \sum_{\sigma_1,\sigma_2,\sigma_3,\sigma_4,\alpha} (\sigma^\alpha)_{\sigma_1,\sigma_2} (\sigma^\alpha)_{\sigma_3,\sigma_4} \sum_{\rho_1,\rho_2} \sum_{\tau_1,\tau_2} \sum_{\boldsymbol{k}} \delta\left(\omega - \lambda_{-\boldsymbol{k},\rho_1\tau_1} - \lambda_{\boldsymbol{k}-\boldsymbol{q},\rho_2\tau_2}\right) \\
& \cdot \Big[(V_{12}(\boldsymbol{k}))^*_{\mu\sigma_1,\rho_1\tau_1} (V_{11}(\boldsymbol{k}-\boldsymbol{q}))_{\mu\sigma_2,\rho_2\tau_2} (V_{11}(-\boldsymbol{k}))^*_{\nu\sigma_3,\rho_1\tau_1} (V_{12}(-\boldsymbol{k}+\boldsymbol{q}))_{\nu\sigma_4,\rho_2\tau_2} \\
& \quad + (V_{12}(\boldsymbol{k}))^*_{\mu\sigma_1,\rho_1\tau_1} (V_{11}(\boldsymbol{k}-\boldsymbol{q}))_{\mu\sigma_2,\rho_2\tau_2} (V_{11}(\boldsymbol{k}-\boldsymbol{q}))^*_{\nu\sigma_3,\rho_2\tau_2} (V_{12}(\boldsymbol{k}))_{\nu\sigma_4,\rho_1\tau_1} \Big].
\end{aligned}
\tag{4.42}
$$

The critical ($\mu = \mu_c$) DSFs and the corresponding spinon spectra are plotted in Fig. 4.4 for representative points in each of the 15 paraphases.

Focusing on universal low-energy features, we first observe that each DSF has characteristic points or regions where it is gapless (i.e., finite at small ω). Since the DSF describes spin dynamics, and each spin is decomposed into two spinons, the DSF is gapless at momenta $\boldsymbol{q}$ that are appropriate sums of spinon condensation momenta $\boldsymbol{k}_c$ such that $\boldsymbol{q} = \boldsymbol{k}_{c,1} + \boldsymbol{k}_{c,2}$. Consequently, we can establish a one-to-one correspondence between the potential spinon condensation momenta described in Table 4.4 and the gapless points or regions of the DSF plotted in Fig. 4.4; see Table 4.8 for this correspondence.

We also notice that the DSF has different low-energy behavior in the paraphases governed by $z = 1$ and $z = 2$ critical theories, respectively. For the $z = 1$ paraphases 0-(010)Λ, 0-(100)Λ, 0-(101)W, 0-(111)W, and 0-(111)X, the weight of the low-energy DSF is concentrated around zero energy, while for the $z = 2$ paraphases 0-(001)Γ, 0-(100)Γ, 0-(101)Γ, and 0-(111)Γ, the low-energy DSF gradually vanishes as the energy is decreased to zero.

These low-energy features in the DSF can be understood from a scaling analysis of

166

Table 4.8: One-to-one correspondence between the potential set of momenta at which the spinons condense at the critical point and the set of momenta at which the corresponding dynamic structure factor is gapless along the high-symmetry path in Fig. 4.4; these set of momenta can be points A or sections A → B between two points A and B.

Spinon condensation momenta	Gapless points or regions in dynamic structure factor
Γ	Γ
L	Γ, X
X	Γ, X
W	Γ, X, $\frac{2}{3}$K
Λ	Γ → X, K → Γ → L → U

the critical field theories in Eqs. (4.26) and (4.30). The DSF is the expectation value of a four-point correlation function in the condensation fields; using Wick's theorem, this expectation value can be written as the convolution of two Green's functions,

$$\mathcal{S}_z(\omega, \boldsymbol{q}) \sim \int d^3\boldsymbol{k}\, d\omega'\, G_z(\omega', \boldsymbol{k}) G_z(\omega - \omega', \boldsymbol{q} - \boldsymbol{k}), \tag{4.43}$$

where $G_z(\omega, \boldsymbol{k})$ are labeled by the dynamical critical exponents z of corresponding field theories:

$$G_1(\omega, \boldsymbol{k}) = \frac{1}{\omega^2 + \mu_{ij}k_i k_j}, \qquad G_2(\omega, \boldsymbol{k}) = \frac{1}{\omega + \widetilde{\nu}_{ij}k_i k_j}. \tag{4.44}$$

Inserting $G_z(\omega, \boldsymbol{k})$ into Eq. (4.43), and evaluating the integrals over ω' and $\boldsymbol{k}$, we obtain the scaling behaviors

$$\mathcal{S}_{z=1}(\omega, \boldsymbol{q}) \sim \log(\omega)\, f_1\left(q/\omega\right), \qquad \mathcal{S}_{z=2}(\omega, \boldsymbol{q}) \sim \sqrt{\omega}\, f_2\left(\sqrt{q}/\omega\right), \tag{4.45}$$

where f_1 and f_2 are some general functions. At the momentum with gapless DSF, corresponding to $\boldsymbol{q} = 0$, the DSF at $\omega \to 0$ thus diverges in the $z = 1$ case and vanishes in the $z = 2$ case. This result qualitatively explains the low-energy DSF features described above. Furthermore, it elucidates why the SSFs of the $z = 1$ paraphases have

singularities at specific momenta, which precisely coincide with the gapless momenta of the corresponding DSFs. We stress again that there are $z = 1$ paraphases, for example, 0-(110)Γ, which have SSFs and DSFs following $z = 2$ behavior. Such a discrepancy may occur if a coefficient in the critical theory accidentally vanishes for the NN mean-field ansatz.

Finally, we remark that the DSFs of several paraphases have high-energy points exhibiting large spectral weights at the Γ point. In fact, whenever such points exist, there is a quasi-mirror-reflection symmetry (in terms of energy) between two spinon bands, such that the two band energies satisfy $\lambda_{\boldsymbol{k},1} + \lambda_{\boldsymbol{k},2} = E$ for all momenta $\boldsymbol{k}$. Due to this "symmetry", these two bands can contribute strongly at the Γ point close to energy E, resulting in an increased spectral weight as well as a Dirac-like texture. However, we emphasize that the high-energy part of the DSF depends on specific details and is not to be taken too seriously; only the low-energy part of the DSF captures the universal physics in the given paraphase.

Table 4.9: Analysis of the zero-momentum ($\boldsymbol{K} = 0$) order parameters for the paraphases characterized by single-point and multi-point condensation (i.e., excluding line condensation). For each paraphase, the complex (ϕ) or real (χ) condensation fields are specified; the zero-momentum order parameters are then bilinears of these fields with total momentum $\boldsymbol{K} = 0$ and transform under various irreducible representations of the point group O_{h}. For some paraphases, distinct order parameters are intertwined such that they must appear together at condensation; for each paraphase characterized by single-point condensation, the order parameters are arranged into classes C (marked by curly brackets) such that there must be at least one nonzero order parameter from each class C. The number of quadratic scalars in terms of the order parameters is also specified; if there is only one such scalar, all order parameters are in different classes and hence are maximally intertwined.

Paraphase	Condensation fields	Real dimension of order-parameter space at $\boldsymbol{K} = 0$	Decomposition into irreducible representations (i.e., distinct orders)	Number of scalars quadratic in order parameters	General intertwining between irreducible representations $C_1 \oplus \cdots \oplus C_q$
0-(001)Γ	$\phi_{1,2}$	10	$A_{1\mathrm{g}} \oplus T_{1\mathrm{g}} \oplus 2T_{2\mathrm{u}}$	1	$\{A_{1\mathrm{g}}\} \oplus \{T_{1\mathrm{g}}\} \oplus \{T_{2\mathrm{u}}\}$
0-(001)L	ϕ_{1-8} (2 per $\boldsymbol{k}_c$)	40	$A_{1\mathrm{g}} \oplus A_{2\mathrm{g}} \oplus E_{\mathrm{g}} \oplus 2T_{1\mathrm{g}} \oplus 2T_{2\mathrm{g}}$ $\oplus 2A_{1\mathrm{u}} \oplus 2E_{\mathrm{u}} \oplus 2T_{1\mathrm{u}} \oplus 4T_{2\mathrm{u}}$		
0-(010)Γ	$\phi_{1,2}$	10	$A_{1\mathrm{g}} \oplus T_{1\mathrm{g}} \oplus 2T_{2\mathrm{g}}$	1	$\{A_{1\mathrm{g}}\} \oplus \{T_{1\mathrm{g}}\} \oplus \{T_{2\mathrm{g}}\}$
0-(100)Γ	$\phi_{1,2}$	10	$A_{1\mathrm{g}} \oplus 3A_{2\mathrm{g}} \oplus 3E_{\mathrm{g}}$	6	$\{A_{1\mathrm{g}}\} \oplus \{A_{2\mathrm{g}}\} \oplus \{E_{\mathrm{g}}\}$
0-(101)Γ	$\phi_{1,2}$	10	$A_{1\mathrm{g}} \oplus A_{2\mathrm{g}} \oplus E_{\mathrm{g}} \oplus 2A_{1\mathrm{u}} \oplus 2E_{\mathrm{u}}$	4	$\{A_{1\mathrm{g}}\} \oplus \{A_{2\mathrm{g}}, E_{\mathrm{g}}\} \oplus \{A_{1\mathrm{u}}, E_{\mathrm{u}}\}$
0-(101)W	χ_{1-24} (8 per $\pm\boldsymbol{k}_c$)	48	$2A_{1\mathrm{g}} \oplus A_{2\mathrm{g}} \oplus 3E_{\mathrm{g}} \oplus T_{1\mathrm{g}}$ $\oplus 2T_{2\mathrm{g}} \oplus 2A_{1\mathrm{u}} \oplus A_{2\mathrm{u}}$ $\oplus 3E_{\mathrm{u}} \oplus 3T_{1\mathrm{u}} \oplus 4T_{2\mathrm{u}}$		
0-(101)X	χ_{1-12} (4 per $\boldsymbol{k}_c$)	30	$A_{1\mathrm{g}} \oplus 2A_{2\mathrm{g}} \oplus 3E_{\mathrm{g}} \oplus T_{2\mathrm{g}} \oplus 2A_{1\mathrm{u}}$ $\oplus A_{2\mathrm{u}} \oplus 3E_{\mathrm{u}} \oplus T_{1\mathrm{u}} \oplus 2T_{2\mathrm{u}}$		
0-(110)Γ	$\chi_{1,2}$	3	$A_{1\mathrm{g}} \oplus E_{\mathrm{g}}$	1	$\{A_{1\mathrm{g}}\} \oplus \{E_{\mathrm{g}}\}$
0-(111)Γ	$\phi_{1,2}$	10	$A_{1\mathrm{g}} \oplus A_{2\mathrm{g}} \oplus E_{\mathrm{g}} \oplus 2A_{2\mathrm{u}} \oplus 2E_{\mathrm{u}}$	4	$\{A_{1\mathrm{g}}\} \oplus \{A_{2\mathrm{g}}, E_{\mathrm{g}}\} \oplus \{A_{2\mathrm{u}}, E_{\mathrm{u}}\}$
0-(111)W	χ_{1-24} (8 per $\pm\boldsymbol{k}_c$)	48	$A_{1\mathrm{g}} \oplus 2A_{2\mathrm{g}} \oplus 3E_{\mathrm{g}} \oplus 2T_{1\mathrm{g}}$ $\oplus T_{2\mathrm{g}} \oplus A_{1\mathrm{u}} \oplus 2A_{2\mathrm{u}}$ $\oplus 3E_{\mathrm{u}} \oplus 4T_{1\mathrm{u}} \oplus 3T_{2\mathrm{u}}$		
0-(111)X	χ_{1-12} (4 per $\boldsymbol{k}_c$)	30	$2A_{1\mathrm{g}} \oplus A_{2\mathrm{g}} \oplus 3E_{\mathrm{g}} \oplus T_{1\mathrm{g}} \oplus A_{1\mathrm{u}}$ $\oplus 2A_{2\mathrm{u}} \oplus 3E_{\mathrm{u}} \oplus 2T_{1\mathrm{u}} \oplus T_{2\mathrm{u}}$		

4.5.3 General order parameters: hidden and intertwined orders

The naïve spin-condensation analysis of magnetic orders in Sec. 4.4.6 is far from complete as it presumes that any zero-momentum order transforms under a representation of T_d and thus ignores the possibility of hidden orders transforming under inversion-odd representations of the full pyrochlore point group $O_\mathrm{h} = T_\mathrm{d} \times C_\mathrm{i}$, where C_i is the $\mathbb{Z}_2$ group consisting of inversion and identity. One simple example of such a hidden order is the alternating expansion and contraction of tetrahedra realized in the "breathing" pyrochlores [116, 77, 126]. In this subsection, we analyze zero-momentum orders more comprehensively by identifying all possible order parameters in terms of the condensing spinon fields and constructing the most general Ginzburg–Landau (GL) theory that is compatible with the point group O_h of the pyrochlore lattice. Such an analysis has been previously done for several problems building on the PSG framework [11, 6, 7].

When the spinons condense at the critical point, certain bosonic modes at the condensation momenta $\boldsymbol{k}_c$ become macroscopically occupied, and the expectation values of their bosonic operators thus become classical condensation fields. For the $z = 2$ critical points, the condensation fields ϕ_n are complex, while for the $z = 1$ critical points, the condensation fields χ_n are real. Importantly, these fields themselves are not valid order parameters as they carry a $\mathbb{Z}_2$ gauge charge and transform projectively under the point group. Indeed, the projective transformation rules of ϕ_n and χ_n under the generators of the point group can be explicitly obtained from the corresponding transformation rules

of the original bosonic operators $b_{\boldsymbol{k}_c,\mu}$ (see also Appendix A.3):

$$I: \quad b_{\boldsymbol{k},\mu} \to (-1)^{n_{ST_1}\delta_{\mu=0}} e^{i\boldsymbol{k}\cdot\hat{e}_\mu} b_{-\boldsymbol{k},\mu}, \tag{4.46a}$$

$$C_3: \quad b_{\boldsymbol{k},\mu} \to U_{C_3}^\dagger b_{(k_z,k_x,k_y),C_3(\mu)}, \tag{4.46b}$$

$$S: \quad b_{\boldsymbol{k},\mu} \to (-1)^{\delta_{\mu=3}n_{ST_1}+\delta_{\mu=2}n_{\overline{C}_6 S}} e^{i\boldsymbol{k}\cdot\hat{e}_\mu} U_S^\dagger b_{(k_y,k_x,-k_z),S(\mu)}, \tag{4.46c}$$

where $C_3(\mu) = 0, 2, 3, 1$ and $S(\mu) = 3, 1, 2, 0$ for the respective sublattices $\mu = 0, 1, 2, 3$. The simplest possible order parameters are then the bilinears of the condensation fields, corresponding to total momentum $\boldsymbol{K} = 0$, which are gauge invariant and transform as linear, generically reducible, representations of the point group. For each paraphase, the irrep decomposition of this reducible representation is given in Table 4.9. We now discuss the physical implications of this decomposition.

The scalar irrep $A_{1\mathrm{g}}$ corresponds to a quadratic invariant, i.e., a "mass" term in the GL theory, which drives the phase transition between the spin-liquid phase and the magnetically ordered phase. For almost all paraphases, it appears only once in the reducible representation, which indicates that all components of the condensation occur together by symmetry. The bilinear term transforming under the scalar irrep is $\sum_n \chi_n^2$, where we decompose any complex fields into real fields as $\phi_n = \chi_{2n-1} + i\chi_{2n}$. The effective GL theory governing the phase transition is then

$$\mathcal{L} = \sum_n (\nabla \chi_n)^2 + r \sum_n \chi_n^2 + O(\chi^4). \tag{4.47}$$

When $A_{1\mathrm{g}}$ appears more than once in the reducible representation [for the paraphases

171

0-(101)W and 0-(111)X], it signals an accidental degeneracy, which should be lifted when going beyond the NN level.

The remaining irreps, denoted by standard labels, correspond to various order parameters that describe distinct scenarios of symmetry breaking (see Table 4.10). Irreps with the subscript "g" are even under inversion and correspond to the conventional spin orders discussed in Ref. [172]. The single-spin order parameters of such spin orders are straightforward to detect with neutron scattering. In contrast, irreps with the subscript "u" are odd under inversion and correspond to more unconventional hidden orders. The order parameters of these inversion-breaking orders always contain multiple spin operators and are thus harder to detect [58]. However, in our case, they are also accompanied by a spontaneous breaking of inversion symmetry, which may be observed as a "breathing" distortion of the pyrochlore lattice.

Table 4.9 indicates that one paraphase can give rise to several distinct order parameters. In general, the presence or absence of a given order parameter is determined by the particular form of the GL theory governing the phase transition. However, for some paraphases, we can argue that several distinct orders are intertwined in the sense that they always accompany one another, regardless of the GL parameters. This highly nontrivial result emerges because the magnetically ordered phases are obtained by condensing fractionalized excitations (spinons) that transform projectively under symmetries.

To analyze the general intertwining between distinct orders for a given paraphase, we form an orthogonal basis for the (real) order parameters $\{\Psi_{R,1}, \cdots, \Psi_{R,N_R}\}$ that

172

Table 4.10: Irreducible representations of the point group O_h and the corresponding symmetry-breaking orders. For some representations, simple examples of order parameters are provided in terms of the spins $\boldsymbol{S}_i$ at sites i, where $\boldsymbol{r}_i$ is the vector from site i to the center of the nearest "up" tetrahedron, $\boldsymbol{n}_{i,j}$ is the vector from site i to site j, and $\lambda_{i,j} = \pm 1$ for bonds $\langle i, j \rangle$ in "up" and "down" tetrahedra, respectively. Note that the scalar representation $A_{1\mathrm{g}}$ does not break any symmetries and hence does not correspond to any order.

Irrep	Dim.	Standard name of corresponding order	Simple example of order parameter in terms of spins
$A_{1\mathrm{g}}$	1	(N/A)	1
$A_{2\mathrm{g}}$	1	All-in-all-out	$\sum_i \boldsymbol{r}_i \cdot \boldsymbol{S}_i$
E_{g}	2	XY antiferromagnet	
$T_{1\mathrm{g}}$	3	Ferromagnet	$\sum_i \boldsymbol{S}_i$
$T_{2\mathrm{g}}$	3	Palmer-Chalker	$\sum_i \boldsymbol{r}_i \times \boldsymbol{S}_i$
$A_{1\mathrm{u}}$	1		$\sum_{\langle i,j \rangle} \lambda_{i,j} (\boldsymbol{S}_i \cdot \boldsymbol{S}_j)$
$A_{2\mathrm{u}}$	1		$\sum_{\langle i,j \rangle} \boldsymbol{n}_{i,j} \cdot (\boldsymbol{S}_i \times \boldsymbol{S}_j)$
E_{u}	2		
$T_{1\mathrm{u}}$	3		$\sum_{\langle i,j \rangle} (\boldsymbol{r}_i \times \boldsymbol{n}_{i,j}) \times (\boldsymbol{S}_i \times \boldsymbol{S}_j)$
$T_{2\mathrm{u}}$	3		$\sum_{\langle i,j \rangle} \boldsymbol{n}_{i,j} \times (\boldsymbol{S}_i \times \boldsymbol{S}_j)$

transform under each distinct irrep R. Note that N_R is the product of the irrep dimension and the multiplicity of the irrep in the reducible representation. Since each symmetry acts on the vector $(\Psi_{R,1}, \cdots, \Psi_{R,N_R})$ by an orthogonal matrix, the quadratic term $W_R = \sum_{j=1}^{N_R} \Psi_{R,j}^2$ must be a scalar transforming under $A_{1\mathrm{g}}$. This scalar can be interpreted as the "weight" of the given irrep; since it is a function of the condensation fields χ_n, it may vanish for some special configurations of these fields, indicating the absence of the corresponding order. In contrast, the total weight of all irreps,

$$W_0 = \sum_R W_R = \sum_R \sum_{j=1}^{N_R} \Psi_{R,j}^2 \propto \left(\sum_n \chi_n^2 \right)^2, \tag{4.48}$$

is nonzero for all field configurations, indicating that at least one order must always be present.

For each paraphase, however, the irreps R may be partitioned into classes $C_1 \oplus \cdots \oplus C_q$ (see Table 4.9) such that the total weight of each class $C = \{R_1, \cdots, R_{N_C}\}$, containing some nontrivial subset of all irreps, is proportional to the total weight of all irreps,

$$W_C = \sum_{R \in C} W_R = \sum_{R \in C} \sum_{j=1}^{N_R} \Psi_{R,j}^2 \propto W_0, \tag{4.49}$$

and is thus nonzero for all configurations of the condensation fields. Consequently, at least one order from each class C must always be present, regardless of the GL parameters. In the most extreme scenario, when each irrep forms its own class, such that $W_R \propto W_0$ for all irreps R, the orders are maximally intertwined, i.e., all of them must appear together. For certain paraphases, one can argue for this scenario by counting all possible quadratic scalars that can be formed from the order parameters or, equivalently, all possible fourth-order scalars that can be formed from the condensation fields. There is always at least one such scalar, $(\sum_n \chi_n^2)^2$; however, if there is only one such scalar, it is clear that the weight W_R of each irrep R must be proportional to this scalar, and all orders must therefore be simultaneously present.

While we do not analyze the general intertwining between distinct orders in all para-phases, we observe from the particular examples studied (see Table 4.9) that the presence of intertwined orders is a common feature of magnetically ordered phases obtained by spinon condensation on the pyrochlore lattice. In particular, for parent spin liquids with $n_{\overline{C}_6} = 1$, where inversion symmetry acts projectively on the spinons, we generically antic-ipate the (already intertwined) spin orders to be also accompanied by inversion-breaking hidden orders.

4.6 Discussion

4.6.1 Summary

In this chapter, we gave a complete classification of spin–orbit-coupled $\mathbb{Z}_2$ spin liquids on the pyrochlore lattice by using the PSG method for Schwinger bosons. We studied the mean-field Hamiltonians of the six 0-flux spin liquids at the NN level and examined the critical field theories that describe phase transitions to ordered phases via spinon condensation. We found two crucially different classes of critical field theories, characterized by dynamical exponents $z = 1$ and $z = 2$, respectively, which have distinct properties ranging from Hamiltonian diagonalizability to experimental observables. Moreover, we investigated the zero-momentum orders obtained from spinon condensation, both by a naïve spin-condensation analysis and by the representation theory of the full pyrochlore point group O_{h}. We found that seemingly unrelated orders are generically intertwined with each other and that conventional spin orders are often accompanied by more exotic inversion-breaking "hidden" orders. Finally, we calculated several physical observables for our critical theories, including the heat capacity, as well as the static and dynamic spin structure factors, which may be compared with experimental data.

4.6.2 Possible implications

Many pyrochlore materials have been experimentally confirmed to possess one of the spin orders discussed in this chapter. For example, $Yb_2Pt_2O_7$ has ferromagnetic order

[24], while $Nd_2Zr_2O_7$ possesses all-in-all-out order [86]. Since all of these spin orders can appear as a result of spinon condensation from one of our $\mathbb{Z}_2$ spin liquids, one can contemplate the possibility that some of these materials are proximate to such a spin liquid.

As a particular example, one may consider $Er_2Ti_2O_7$, which is confirmed to have a Ψ_2 antiferromagnetic ground state. The Ψ_2 ground state is selected from the Γ_5 irrep, containing both Ψ_2 and Ψ_3 states, as a result of order-by-disorder mechanism, possibly aided by virtual crystal-field effects [61, 140, 115, 73, 128]. This Ψ_2 ground state is quite stable, which suggests that, if it is obtained from an instability of a spin liquid, such an instability should uniquely prefer E_g order. Consulting Table 4.9, we see that the paraphase Γ of the PSG class 0-(110) has a single nontrivial irrep E_g, which is not intertwined with any other orders. Hence, if $Er_2Ti_2O_7$ is proximate to a spin liquid, a natural candidate for its parent spin liquid is the one corresponding to the PSG class 0-(110).

One motivation of this work was to understand the puzzling experiments on $Yb_2B_2O_7$, where B = Ge, Ti, Sn. These three compounds have distinct ground states: the Ge compound is antiferromagnetic [54], while the Ti [48] and Sn [176] compounds are ferromagnetic, at least when any order can be clearly identified. The Ti compound is also sensitive to disorder. Despite the disparate ground states, inelastic neutron scattering gives very similar spectra for all three materials [53], consisting of continuum weight over the entire Brillouin zone down to the lowest energies resolvable in the measure-

176

ments. This observation suggests that the relevant excitations are characteristic of some common underlying structure, which is distinct from the usual spin waves tied to the individual ordered states. The approach in this work gives one possible explanation: the excitations may be the spinons of a parent spin-liquid state.

To identify a potential parent spin liquid, we seek a PSG class from which both antiferromagnetic and ferromagnetic orders can be obtained through the same condensation paraphase. It is clear from Table 4.1 that such classes exist; the classes 0-(001), 0-(101) and 0-(111) all satisfy this criterion. Therefore, the proximity to a spin liquid corresponding to either of these classes can potentially explain the observed excitation spectra. Looking at the dynamic spin structure factors in Fig. 4.4, we indeed see that many of the critical structure factors in these classes [e.g., 0-(001)L, 0-(101)W, and 0-(111)X] have a large scattering continuum over the entire Brillouin zone down to a very small fraction of the spin-excitation bandwidth. It would be interesting to attempt a more quantitative comparison with the experimental data, which would require, at the very least, a careful consideration of effects beyond mean-field theory.

If the scattering continua in the Yb pyrochlores are reflections of a parent spin liquid, it also suggests that hidden order may be present in these materials [53]. Indeed, from the last column of Table 4.1, we see that the paraphases 0-(001), 0-(101) and 0-(111) all include hidden orders breaking inversion symmetry. Searching for such inversion-breaking orders may be an incisive test of the physical picture presented in this work; if such an order is identified, a full characterization may be assisted by the associated

177

order parameters in Table 4.10. We note that hidden order may also participate in the specific-heat anomalies of the Yb pyrochlores [53].

4.6.3 Future directions

The present chapter explored the physics of proximity to a broad class of quantum spin liquids on the pyrochlore lattice. Nevertheless, several assumptions in the analysis could be modified or relaxed in future work. We focused on $\mathbb{Z}_2$ spin liquids and used the framework of bosonic spinons; it would be interesting to consider $U(1)$ spin liquids and explore fermionic spinons as well. The fermionic approach does not, however, provide a simple mean-field way to study magnetic instabilities, which is straightforward with bosonic spinons by condensing them.

In addition, the PSG results may be further exploited even within the framework of bosonic spinons. We concentrated on the 0-flux NN mean-field Hamiltonians for simplicity, assuming that NNN terms do not qualitatively change our results. This assumption, however, is not necessarily true; in certain cases, a NNN term one-tenth as strong as a NN term can already change the condensation momenta. Moreover, the π-flux PSG classes may exhibit interesting physics of their own. These PSG classes have a fourfold enlarged unit cell due to nontrivial translational PSG along the $\hat{e}_2$ and $\hat{e}_3$ directions, which leads to a 64×64 mean-field Hamiltonian in terms of the parameters in Table 4.2. Multi-spinon condensation may further enlarge the magnetic unit cell. In turn, this enlargement results in a complex spinon spectrum that probably requires a more

computational approach.

We also presumed that the full symmetry group of the pyrochlore lattice is preserved at the level of the spin Hamiltonian. However, there is a large family of "breathing" pyrochlore materials [116, 77, 126] that explicitly break inversion symmetry ($Fd\bar{3}m \rightarrow F\bar{4}3m$) by expansion and contraction of alternating tetrahedra. One material from this family, $Ba_3Yb_2Zn_5O_{11}$, was reported to remain disordered down to 0.38 K [77], and a gauge mean-field theory, distinct from the spinon approach in this work, predicts that this material may experience a non-symmetry-breaking transition between a paramagnet and a quantum spin ice [142]. It would be interesting to see how this material (and the phase transition predicted for it) fits into a pyrochlore PSG classification.

Finally, the PSG method can be connected to the energetics of realistic spin Hamiltonians. Indeed, our mean-field spinon states can in principle be used as variational wave functions, as can their so far unexplored fermionic counterparts. Calculating variational energies for these wave functions would require a major effort in variational Monte Carlo in three dimensions; it is well beyond the present work but is quite worthwhile to explore.

Chapter 5

U(1) and $\mathbb{Z}_2$ symmetric spin liquids in pyrochlore: a fermionic classification

5.1 Introduction

Quantum spin liquids (QSLs) are zero temperature phases of quantum magnets in which localized spins evade magnetic long-range order due to strong quantum fluctuations and form liquid-like states [138]. Such states are fundamentally characterized by intrinsic long-range entanglement and support nonlocal excitations carrying fractionalized quantum numbers. These nonlocal fractionalized excitations interact with each other via an emergent gauge field. Therefore, QSLs are naturally described in terms of gauge theories.

At a coarse level, different QSLs can be classified by their underlying low energy effective theories. Depending on whether a mass exists, the fractionalized spinon exci-

tations (the matter fields) may or may not bear relevance to the low energy description of QSLs. The gauge field may also be gapless as is a U(1) gauge field of photons, or gapped as is a $\mathbb{Z}_2$ gauge field which is of topological nature. All these types have been extensively studied in two dimensions (2D). Perhaps the most well-known $\mathbb{Z}_2$ QSL is the Kitaev model on the 2D honeycomb lattice: this model supports either gapped or gapless Majorana fermions [78]. On the other hand, a compact U(1) gauge theory is confined in 2D [121], and a QSL corresponding to the deconfined phase can appear only in the presence of gapless matter fields. So far, the two most studied examples are spinon Fermi surface and Dirac U(1) QSLs. On the experimental side, promising Kitaev materials include a family of honeycomb iridates [152] and α-RuCl$_3$ [8], and new proposals are still in progress [62]. A spinon Fermi surface U(1) QSL has been speculated to emerge in the 2D layered triangular materials YbMgGaO$_4$ and NaYbSe$_2$ [118, 146, 37], while a U(1) Dirac QSL may be relevant for the 2D layered kagome material Herbertsmithite [123, 173]. The recent material NaYbO$_2$ may also realize a Dirac U(1) spin liquid [38, 14]. These spin liquid candidates provide a natural ground for the experimental realization of exotic quantum phenomena such as quantum electrodynamics in three dimensional spacetime (QED3) and 2D topological order.

Moving to the three-dimensional (3D) world, arguably the most studied examples are QSLs on the pyrochlore lattice. Consisting of corner-sharing tetrahedra, the geometrically frustrated pyrochlore lattice has been proposed to host a QSL phase since the birth of the concept of QSLs [1]. An important theoretical advance occurred in 2004:

through a rigorous mapping, Ref. [63] showed that the pyrochlore Heisenberg model with local Ising anisotropy has a U(1) QSL phase, commonly known as quantum spin ice, which is described by the Maxwell theory at low energies. Since then, the properties of such pyrochlore QSLs have been extensively studied [63, 137, 175, 171], and numerous experiments have reported liquid-like behaviors in rare-earth pyrochlore materials [148, 150, 43, 49, 85].

Given the interest in quantum spin ice that realizes a prototypical low energy theory, it is compelling to ask whether there are other spin liquids whose low energy theory is of a new prototype. In a narrower sense, this amounts to asking if gauge fields can interact with novel forms of gapless matter fields. This has indeed been considered in other works. For example, Refs. [169, 107] considered a class of QSLs with symmetry protected quadratic spinon band touchings for the triangular spin liquid candidates $Ba_3NiSb_2O_9$, κ-$(BEDT\text{-}TTF)_2Cu_2(CN)_3$, and $EtMe_3Sb[Pd(dmit)_2]_2$. In three dimensions, Refs. [67, 82] studied possible symmetric spin liquids on the hyperkagome lattice and found that certain classes possess gapless nodal lines of spinons along high symmetry paths in the Brillouin zone. A similar conclusion was drawn in Ref. [23] for a QSL on the pyrochlore lattice. However, in these two 3D examples it is not clear whether such gapless nodal structures are stable against perturbations. Nodal lines of excitations also appear in other spin liquids, which are either robust against gauge fluctuations [103, 112] or symmetry protected [181].

Another more systematic, yet formal, way of classifying QSLs is based on their sym-

metry properties. Due to the absence of magnetic long-range order, a QSL state usually preserves the full symmetry of the lattice and it may also preserve time reversal symmetry. Crucially, due to the emergent gauge structure, the fractionalized excitations of the system carry a *projective* representation of the symmetry group—a representation of the group extension of the original symmetry group by the gauge structure. The classification of symmetric spin liquids can therefore be achieved by classifying all the distinct projective representations for a given lattice symmetry and a given gauge group type. In his seminal work [165], Wen coined this procedure the classification of projective symmetry groups (PSGs). The PSG approach has led to many fruitful results in our understanding of symmetric spin liquids. For example, we now know that there are at most 20 different $\mathbb{Z}_2$ QSL classes on the kagome [99] and triangular [97] lattices with distinct projective symmetries for fermionic spinons, while the analogous numbers for the 3D hyperkagome [82] and hyperhoneycomb [66] lattices are 3 and 160, respectively. The idea of the PSG has also been applied to the pyrochlore lattice, in the hope of identifying experimental spin liquid candidates within the classification [11, 23, 29, 33, 94].

In this work, we apply the PSG method for Abrikosov fermions to give a complete classification of symmetric QSLs on the pyrochlore lattice with either $\mathbb{Z}_2$ or U(1) gauge type. For each gauge type, we first consider only space group symmetry, and later add time reversal symmetry. In general, we allow spin–orbit coupling in the underlying spin system and do not require SU(2) spin rotation symmetry. By following the general PSG principle to solve the gauge-symmetry consistency equations, we find that there can be

at most 18 and 28 symmetric quantum spin liquids preserving the pyrochlore PSG for the U(1) and $\mathbb{Z}_2$ gauge types, respectively. When time-reversal symmetry is imposed, the number of possible symmetric spin liquids is reduced to 16 for the U(1) type and is increased to 48 for the $\mathbb{Z}_2$ type. For each class, the most general symmetry-allowed spinon mean-field Hamiltonian is given. Importantly, we find that a large family of spinon Hamiltonians possesses gapless nodal lines along the four equivalent (111) directions of the Brillouin zone. We call this unusual nodal structure a "nodal star" and show that it is stable at the mean-field level as it is protected by the projective threefold rotation and screw symmetries of the system. We then go beyond the mean-field level and consider a full-fledged low energy theory of the spinon nodal star coupled to a U(1) gauge field. Specifically, we obtain thermodynamic properties of the system by computing the photon contribution to the free energy. We find that the two most dominant low temperature contributions to the specific heat are $C \sim T^{3/2}$ from the bare spinons and $C \sim T^{3/2}/\ln T$ from the photon–spinon interactions. This scaling of the low temperature specific heat may serve as a clear evidence for the experimental discovery of a nodal star U(1) QSL.

The rest of the chapter is organized as follows. In Sec. 5.2, we apply the PSG procedure to the classification of pyrochlore QSLs with or without time reversal symmetry. In Sec. 5.3, we construct mean-field Hamiltonians for the fermionic spinons and analyze their symmetry properties. We prove that several mean-field Hamiltonians obtained from the U(1) PSG possess symmetry protected nodal lines. In Sec. 5.4, we construct a continuum model for the spinon nodal lines coupled to a U(1) gauge field, and consider the

thermodynamic properties of the system. Finally, we summarize and discuss our results in Sec. 5.5.

5.2 Classification result

We first solve the PSG equations obtained from space group symmetries. The PSG equations for $U(1)$ and $\mathbb{Z}_2$ gauge groups are solved in App. A.6 and App. A.7, respectively. The results are presented in Table 5.1 for the $U(1)$ gauge group and in Table 5.2 for the $\mathbb{Z}_2$ gauge group. We find 18 gauge-inequivalent PSG solutions for the $U(1)$ gauge type and 28 gauge-inequivalent PSG solutions for the $\mathbb{Z}_2$ gauge type. As a result, there can be at most 18 $U(1)$ and 28 $\mathbb{Z}_2$ symmetric spin liquids, ignoring possible time reversal symmetry. Both the $U(1)$ and the $\mathbb{Z}_2$ solutions have the following form:

$$
\begin{align}
W_{T_i}(\boldsymbol{r}_\mu) &= e^{i\sigma^3 \phi_{T_i}(\boldsymbol{r}_\mu)}, \quad i = 1, 2, 3, \tag{5.1a} \\
W_{\overline{C}_6}(\boldsymbol{r}_\mu) &= W_{\overline{C}_6,\mu} e^{i\sigma^3 \phi_{\overline{C}_6}(\boldsymbol{r}_\mu)}, \tag{5.1b} \\
W_S(\boldsymbol{r}_\mu) &= W_{S,\mu} e^{i\sigma^3 \phi_S(\boldsymbol{r}_\mu)}, \tag{5.1c}
\end{align}
$$

with

$$
\begin{align}
\phi_{T_1}(\boldsymbol{r}_\mu) &= 0, \tag{5.2a} \\
\phi_{T_2}(\boldsymbol{r}_\mu) &= -\chi_1 r_1, \tag{5.2b} \\
\phi_{T_3}(\boldsymbol{r}_\mu) &= \chi_1(r_1 - r_2), \tag{5.2c} \\
\phi_{\overline{C}_6}(\boldsymbol{r}_\mu) &= -\chi_1 r_1(r_2 - r_3) - [2\chi_{ST_1} + 2\chi_1 + (\delta_{\mu,2} - \delta_{\mu,3})\chi_1]r_1 + \delta_{\mu,2}\chi_1 r_3, \tag{5.2d} \\
\phi_S(\boldsymbol{r}_\mu) &= \chi_1 \left[\frac{(r_1 + 1)r_1}{2} - \frac{(r_2 + 1)r_2}{2} - r_1 r_2 \right] + [(\delta_{\mu,1} - \delta_{\mu,2})\chi_1 + (2\chi_1 - \chi_{ST_1})]r_1 \\
&\quad + [(2\delta_{\mu,1} - \delta_{\mu,2})\chi_1 + 3\chi_{ST_1}]r_2 + [(\delta_{\mu,1} - \delta_{\mu,2}) + 2]\chi_1 r_3. \tag{5.2e}
\end{align}
$$

The parameters χ_1 and χ_{ST_1} are elements of the IGG defined on the right-hand sides of the PSG equations obtained from Eq. (A.4). Concretely:

- The parameter χ_1 is associated with $T_i T_{i+1} T_i^{-1} T_{i+1}^{-1} = 1$, and physically quantifies the Aharonov-Bohm (AB) phase a spinon accumulates under such a sequence of translations. The AB phase is a gauge invariant quantity. In U(1) PSG, such a phase is allowed to take on values 0, π and $\pi/2$. They give rise to zero-flux, π-flux and $\frac{\pi}{2}$-flux spin liquids, respectively. The $\frac{\pi}{2}$-flux spin liquid explicitly breaks time reversal symmetry since a $\frac{\pi}{2}$ flux changes sign under time reversal operation. In $\mathbb{Z}_2$ PSG, only 0- and π-flux spin liquids are found.

- The parameter χ_{ST_1} is associated with $ST_1 S^{-1} T_3^{-1} T_1 = 1$, and physically quantifies the AB phase a spinon accumulates under the sequence of operations $ST_1 S^{-1} T_3^{-1} T_1$. Such a phase is allowed to take on values 0 and π in both U(1) and $\mathbb{Z}_2$ PSGs.

$W_{\overline{C}_6,\mu}$ and $W_{S,\mu}$ in Eqs. (5.1b) and (5.1c) are the SU(2) matrices at the origin, $\boldsymbol{r}_\mu = 0$, which depend on additional discrete parameters as given in Tables 5.1 and 5.2 for the two gauge types. The parameters $\chi_{\overline{C}_6 S}$, $\chi_{\overline{C}_6}$ and $\chi_{S\overline{C}_6}$ are elements of the IGG associated with $(\overline{C}_6 S)^4 = 1$, $I^2 = 1$ and $(IS)^3 = 1$, respectively, and have the same AB phase interpretation as explained above. We note that two additional parameters $w_{\overline{C}_6}$ and w_S appear in the U(1) PSG classification: they are $\mathbb{Z}_2$-valued ($w = 0, 1$) and determine whether or not the SU(2) matrices $W_{\overline{C}_6,\mu}$ and $W_{S,\mu}$ belong to the IGG. It is necessary to introduce these two parameters in the U(1) case a priori in order to simplify the SU(2) PSG equations to U(1) phase equations for $\phi_\mathcal{O}(\boldsymbol{r}_\mu)$. This is not required in the $\mathbb{Z}_2$ case,

since the phases $\phi_{\mathcal{O}}(\boldsymbol{r}_\mu)$ are $\mathbb{Z}_2$-valued and commute with $W_{\overline{C}_6,\mu}$ and $W_{S,\mu}$. The SU(2) equations for $W_{\overline{C}_6,\mu}$ and $W_{S,\mu}$, however, do rely on an additional discrete parameter j in some classes (see Table 5.2).

In the second step, we include the time reversal operation $\mathcal{T}$ in the symmetry group. In an appropriate gauge, the solution for time reversal operation can be chosen as

$$W_{\mathcal{T}}(\boldsymbol{r}_\mu) = i\sigma^1 \tag{5.3}$$

for U(1) gauge type and

$$W_{\mathcal{T}}(\boldsymbol{r}_\mu) = i\eta_\mu \sigma^k \tag{5.4}$$

for $\mathbb{Z}_2$ gauge type, where $k = 1, 2, 3$ depends on the PSG class and $\eta_\mu = \pm$ is a sublattice-dependent sign factor. Applying this gauge choice and the space group PSG solutions in Eq. (5.1) to the time reversal PSG equations associated with Eqs. (A.4i) and (A.4j), we obtain the PSG solutions for time reversal invariant symmetric spin liquids. We find that there are 16 classes for the U(1) gauge type and 48 classes for the $\mathbb{Z}_2$ gauge type. We list these classes again in Tables 5.1 and 5.2 for U(1) and $\mathbb{Z}_2$ gauge groups, respectively and explicitly mark the data that are specific to the time reversal symmetric classes.

Table 5.1: The 18 U(1) PSG classes of pyrochlore space group symmetry only and 16 U(1) PSG classes of pyrochlore space group symmetry combined with time reversal symmetry. The tabulation is such that the latter are embedded in the former; and that daggered square brackets "[ ]†" are used to enclose data that are specific to the former. The parameters χ_1, χ_{ST_1}, and $\chi_{\overline{C}_6 S}$ are discrete elements of the IGG and $w_{\overline{C}_6}$ and w_S are $\mathbb{Z}_2$-valued parameters introduced in the canonical gauge. Together they label the U(1) PSG classes. The gauge fixing of the SU(2) matrices $W_{\overline{C}_6,\mu}$ and $W_{S,\mu}$ defined in Eq. (5.1) is given.

χ_1	χ_{ST_1}	$\chi_{\overline{C}_6 S}$	$w_{\overline{C}_6}$	w_S	$(W_{\overline{C}_6,0}, W_{\overline{C}_6,1}, W_{\overline{C}_6,2}, W_{\overline{C}_6,3})$	$(W_{S,0}, W_{S,1}, W_{S,2}, W_{S,3})$	Number of classes $[\#]^\dagger$	#
0 or π	0	0 or π	0	0	$(1,1,1,e^{i\sigma^3(\chi_1-\chi_{ST_1})})$	$(1, e^{i\sigma^3(\chi_{ST_1}+\chi_{\overline{C}_6 S})}, 1, e^{i\sigma^3\chi_1})$	$[4]^\dagger$	4
0 or π	0	0 or π	0	1	$(1,1,1,e^{i\sigma^3(\chi_1-\chi_{ST_1})})$	$(i\sigma^1, i\sigma^1 e^{i\sigma^3(\chi_{ST_1}+\chi_{\overline{C}_6 S})}, i\sigma^1, i\sigma^1 e^{i\sigma^3\chi_1})$	$[4]^\dagger$	4
0 or π	0	0 or π	1	0	$(i\sigma^1, i\sigma^1, i\sigma^1, i\sigma^1 e^{i\sigma^3(\chi_1-\chi_{ST_1})})$	$(1, e^{i\sigma^3(\chi_{ST_1}+\chi_{\overline{C}_6 S})}, 1, e^{i\sigma^3\chi_1})$	$[4]^\dagger$	4
0 or π	0	0 or π	1	1	$(i\sigma^1, i\sigma^1, i\sigma^1, i\sigma^1 e^{i\sigma^3(\chi_1-\chi_{ST_1})})$	$(i\sigma^1, i\sigma^1 e^{i\sigma^3(\chi_{ST_1}+\chi_{\overline{C}_6 S})}, i\sigma^1, i\sigma^1 e^{i\sigma^3\chi_1})$	$[4]^\dagger$	4
$\left[\frac{\pi}{2}\right]^\dagger$	$[\pi]^\dagger$	$[0 \text{ or } \pi]^\dagger$	$[0]^\dagger$	$[1]^\dagger$	$\left[(1,1,1,e^{i\sigma^3(\chi_1-\chi_{ST_1})})\right]^\dagger$	$\left[(i\sigma^1, i\sigma^1 e^{i\sigma^3(\chi_{ST_1}+\chi_{\overline{C}_6 S})}, i\sigma^1, i\sigma^1 e^{i\sigma^3\chi_1})\right]^\dagger$	$[2]^\dagger$	0

Table 5.2: The 28 $\mathbb{Z}_2$ PSG classes of pyrochlore space group symmetry combined with time reversal symmetry. The tabulation is such that if a class of the latter is derived from a class of the former then they are written in the same line; and that the double-daggered double-square brackets "$[[\ ]]^{\ddagger}$" are used to enclose data that are specific to the latter. The parameters χ_1, χ_{ST_1}, $\chi_{\overline{C}_6 S}$, $\chi_{S\overline{C}_6}$, and $\chi_{\overline{C}_6}$ are discrete elements of the IGG and j is an extra parameter introduced during solving the PSG equations. Together they label the $\mathbb{Z}_2$ PSG classes. The gauge fixing of the SU(2) matrices $W_{\overline{C}_6,\mu}$ and $W_{S,\mu}$ defined in Eq. (5.1), and the time reversal SU(2) matrix defined in Eq. (5.4) for $\mu = 0$ is given ($k = 1, 2, 3$ corresponds to different gauge fixing). The time reversal parameters $\chi_{\tau\overline{C}_6}$ and $\chi_{\tau S}$ are related to η_μ in Eq. (5.4) by $(\eta_0, \eta_1, \eta_2, \eta_3) = (1, \eta_{\tau\overline{C}_6}\eta_{\tau S}, \eta_{\tau S}, \eta_{\tau S})$. We defined the shorthand notation $W_{S,2}^{\pi\pi 0} = e^{i\chi_{\overline{C}_6 S} i\sigma^{k+1}} e^{i\frac{\pi}{6}\sigma^{k-1}}$.

χ_1	χ_{ST_1}	$\chi_{\overline{C}_6 S}$	$\chi_{S\overline{C}_6}$	$\chi_{\overline{C}_6}$	j	$[[\,\chi_{\tau\overline{C}_6}\,\chi_{\tau S}\,W_{\tau,0}\,]]^{\ddagger}$	$(W_{\overline{C}_6,0}, W_{\overline{C}_6,1}, W_{\overline{C}_6,2}, W_{\overline{C}_6,3})$	$(W_{S,0}, W_{S,1}, W_{S,2}, W_{S,3})$	#	$[[\#]]^{\ddagger}$
0 or π	χ_1	0 or π	0	0	—	$[[\,0\ \ 0\ \ i\sigma^k\,]]^{\ddagger}$	$(1,1,1,1)$	$(1,1,e^{i\chi_{\overline{C}_6 S}},1)$	4	$[4]^{\ddagger}$
0 or π	χ_1	0 or π	π	π	—	$[[\,0\ \ 0\ \ i\sigma^k\,]]^{\ddagger}$; $[[\,0\ \ \pi\ \ i\sigma^{k-1}\,]]^{\ddagger}$	$(-i\sigma^k,1,1,i\sigma^k)$	$(1,1,e^{i\chi_{\overline{C}_6 S}},1)$	4	$[8]^{\ddagger}$
0 or π	$-\chi_1$	0	π	0	1	$[[\,0\ \ \pi\ \ i\sigma^{k-1}\,]]^{\ddagger}$	$(-e^{i\chi_{\overline{C}_6 S}}e^{i\frac{\pi j}{3}\sigma^{k-1}},1,1,1)$	$(1,i\sigma^k,i\sigma^k e^{i\frac{\pi j}{3}\sigma^{k-1}},1)$	2	$[2]^{\ddagger}$
0 or π	$-\chi_1$	0	π	0	3	$[[\,0\ \ 0\ \ i\sigma^k\,]]^{\ddagger}$; $[[\,0\ \ \pi\ \ i\sigma^{k-1}\,]]^{\ddagger}$	$(-e^{i\chi_{\overline{C}_6 S}}e^{i\frac{\pi j}{3}\sigma^{k-1}},1,1,1)$	$(1,i\sigma^k,i\sigma^k e^{i\frac{\pi j}{3}\sigma^{k-1}},1)$	2	$[4]^{\ddagger}$
0 or π	$-\chi_1$	π	π	0	0	$[[\,0\ \ 0\ \ i\sigma^k\,]]^{\ddagger}$; $[[\,0\ \ \pi\ \ i\sigma^{k-1}\,]]^{\ddagger}$	$(-e^{i\chi_{\overline{C}_6 S}}e^{i\frac{\pi j}{3}\sigma^{k-1}},1,1,1)$	$(1,i\sigma^k,i\sigma^k e^{i\frac{\pi j}{3}\sigma^{k-1}},1)$	2	$[4]^{\ddagger}$
0 or π	$-\chi_1$	π	π	0	2	$[[\,0\ \ \pi\ \ i\sigma^{k-1}\,]]^{\ddagger}$	$(-e^{i\chi_{\overline{C}_6 S}}e^{i\frac{\pi j}{3}\sigma^{k-1}},1,1,1)$	$(1,i\sigma^k,i\sigma^k e^{i\frac{\pi j}{3}\sigma^{k-1}},1)$	2	$[2]^{\ddagger}$
0 or π	$-\chi_1$	0 or π	0	π	—	$[[\,0\ \ 0\ \ i\sigma^k\,]]^{\ddagger}$; $[[\,\pi\ \ \pi\ \ i\sigma^{k-1}\,]]^{\ddagger}$	$(i\sigma^k,1,1,i\sigma^k)$	$(1,i\sigma^k,e^{i\chi_{\overline{C}_6 S}}i\sigma^k,1)$	4	$[8]^{\ddagger}$
0 or π	$-\chi_1$	0 or π	π	π	0	$[[\,0\ \ \pi\ \ i\sigma^{k-1}\,]]^{\ddagger}$	$(e^{i\frac{\pi}{6}\sigma^{k-1}},1,1,i\sigma^{k-1})$	$(1,i\sigma^k,W_{S,2}^{\pi\pi 0},1)$	4	$[4]^{\ddagger}$
0 or π	$-\chi_1$	0 or π	π	π	1	$[[\,0\ \ \pi\ \ i\sigma^k\,]]^{\ddagger}$; $[[\,\pi\ \ 0\ \ i\sigma^k\,]]^{\ddagger}$; $[[\,\pi\ \ \pi\ \ i\sigma^{k+1}\,]]^{\ddagger}$	$(-i\sigma^{k-1},1,1,i\sigma^{k-1})$	$(1,i\sigma^k,e^{i\chi_{\overline{C}_6 S}}i\sigma^k,1)$	4	$[12]^{\ddagger}$

189

It is worth pointing out that including time reversal symmetry to the PSG has opposite effects on the U(1) and the $\mathbb{Z}_2$ classes. In U(1) PSG, the presence of time reversal symmetry forbids the two $\frac{\pi}{2}$-flux PSG classes (last line of Table 5.1), thereby reducing the total number of PSG classes from 18 to 16. On the other hand, in $\mathbb{Z}_2$ PSG, adding time reversal symmetry introduces two additional discrete parameters $\chi_{\mathcal{T}\overline{C}_6}$ and $\chi_{\mathcal{T}S}$ in the labeling of the time reversal invariant classes (see columns 7 and 8 of Table 5.2). These two parameters are the IGG elements associated with Eq. (A.4j) for $\mathcal{O} = \overline{C}_6$ and S, respectively, and characterize the phases that a spinon acquires in completing the corresponding spacetime processes. We find that 20 classes obtained from the pure space group PSG are further "fractionalized" as a result of these additional parameters, thereby increasing the total number of PSG classes from 28 to 48. In U(1) PSG, $\chi_{\overline{C}_6\mathcal{T}}$ and $\chi_{S\mathcal{T}}$ do not increase the number of classes since they are fully determined by the $\mathbb{Z}_2$ parameters $w_{\overline{C}_6}$ and w_S that are already introduced for the pure space group PSG. The phenomenon described here in fact also happens in the classification of other projective lattice symmetries: it is generally true that adding time reversal symmetry will increase the number of $\mathbb{Z}_2$ PSG classes and reduce the number of U(1) PSG classes.

5.3   Analysis of the mean-field ansätze

The PSG classification in the last section provides the symmetry constraints on constructing Hamiltonians that describe fractionalized spinons in symmetric U(1) and $\mathbb{Z}_2$ spin liquids. Since the gauge fields are deconfined in a spin liquid phase, a good de-

scription for the spinons is already achieved at the mean-field level. In this section, we present a complete list of parton mean-field Hamiltonians for symmetric spin liquids on the pyrochlore lattice. These Hamiltonians can either be analyzed in their own right, or serve as a first step towards a more realistic description of spin liquids upon adding spinon interactions or fluctuating gauge fields.

5.3.1 Construction of the mean-field ansätze

We are now in the position to construct the mean-field ansatz for each PSG class. The most general mean-field ansatz for fermionic spinons can be written as

$$
H = \sum_{\alpha=0,x,y,z} H^\alpha, \qquad H^\alpha = \sum_{\boldsymbol{r}_\mu, \boldsymbol{r}'_\nu} H^\alpha_{\boldsymbol{r}_\mu, \boldsymbol{r}'_\nu},
$$

$$
H^\alpha_{\boldsymbol{r}_\mu, \boldsymbol{r}'_\nu} = \mathrm{Tr}\left[\sigma^\alpha \Psi_{\boldsymbol{r}_\mu} u^{(\alpha)}_{\boldsymbol{r}_\mu, \boldsymbol{r}'_\nu} \Psi^\dagger_{\boldsymbol{r}'_\nu}\right],
$$

(5.5)

where $u^{(\alpha)}_{\boldsymbol{r}_\mu, \boldsymbol{r}'_\nu}$ with $\alpha = 0, x, y, z$ contain all the sixteen real parameters for the bond $\boldsymbol{r}_\mu \to \boldsymbol{r}'_\nu$,

$$
\begin{aligned}
u^{(0)}_{\boldsymbol{r}_\mu, \boldsymbol{r}'_\nu} &= ia^0_{\boldsymbol{r}_\mu, \boldsymbol{r}'_\nu} 1 - (b^0_{\boldsymbol{r}_\mu, \boldsymbol{r}'_\nu}\sigma^1 + c^0_{\boldsymbol{r}_\mu, \boldsymbol{r}'_\nu}\sigma^2 + d^0_{\boldsymbol{r}_\mu, \boldsymbol{r}'_\nu}\sigma^3), \\
u^{(x)}_{\boldsymbol{r}_\mu, \boldsymbol{r}'_\nu} &= a^x_{\boldsymbol{r}_\mu, \boldsymbol{r}'_\nu} 1 + i(b^x_{\boldsymbol{r}_\mu, \boldsymbol{r}'_\nu}\sigma^1 + c^x_{\boldsymbol{r}_\mu, \boldsymbol{r}'_\nu}\sigma^2 + d^x_{\boldsymbol{r}_\mu, \boldsymbol{r}'_\nu}\sigma^3), \\
u^{(y)}_{\boldsymbol{r}_\mu, \boldsymbol{r}'_\nu} &= a^y_{\boldsymbol{r}_\mu, \boldsymbol{r}'_\nu} 1 + i(b^y_{\boldsymbol{r}_\mu, \boldsymbol{r}'_\nu}\sigma^1 + c^y_{\boldsymbol{r}_\mu, \boldsymbol{r}'_\nu}\sigma^2 + d^y_{\boldsymbol{r}_\mu, \boldsymbol{r}'_\nu}\sigma^3), \\
u^{(z)}_{\boldsymbol{r}_\mu, \boldsymbol{r}'_\nu} &= a^z_{\boldsymbol{r}_\mu, \boldsymbol{r}'_\nu} 1 + i(b^z_{\boldsymbol{r}_\mu, \boldsymbol{r}'_\nu}\sigma^1 + c^z_{\boldsymbol{r}_\mu, \boldsymbol{r}'_\nu}\sigma^2 + d^z_{\boldsymbol{r}_\mu, \boldsymbol{r}'_\nu}\sigma^3).
\end{aligned}
$$

(5.6)

Note that 1 denotes the 2×2 identity matrix.

The bond parameters are subject to constraints provided by the PSG. The PSG operators $\widetilde{\mathcal{O}}$ and $\widetilde{\mathcal{T}}$ are the symmetry operators of the Hamiltonian H, meaning $\widetilde{\mathcal{O}}\colon H \to H$ and $\widetilde{\mathcal{T}}\colon H \to H$. Since the spinons transform under $\widetilde{\mathcal{O}}$ and $\widetilde{\mathcal{T}}$ according to Eqs. (1.33) and (1.35), we have the following rules:

- For a general translation $\boldsymbol{t} = t_1\boldsymbol{e}_1 + t_2\boldsymbol{e}_2 + t_3\boldsymbol{e}_3$, we have

$$u^{(\alpha)}_{\boldsymbol{r}_\mu,\boldsymbol{r}'_\nu} = u^{(\alpha)}_{(\boldsymbol{r}-\boldsymbol{t})_\mu,(\boldsymbol{r}'-\boldsymbol{t})_\nu} e^{i\sigma^3[t_2(r'_1-r_1)-t_3(r'_1-r_1-r'_2+r_2)]\chi_1}; \tag{5.7}$$

- For space-group elements $\mathcal{O} \in \{\overline{C}_6, S\}$, the singlet and the triplet parts transform

  as

$$
\begin{aligned}
W_\mathcal{O}[\mathcal{O}(\boldsymbol{r}_\mu)]u^{(0)}_{\boldsymbol{r}_\mu,\boldsymbol{r}'_\nu}W^\dagger_\mathcal{O}[\mathcal{O}(\boldsymbol{r}'_\nu)] &= u^{(0)}_{\mathcal{O}(\boldsymbol{r}_\mu),\mathcal{O}(\boldsymbol{r}'_\nu)}, \\
W_\mathcal{O}[\mathcal{O}(\boldsymbol{r}_\mu)]u^{(i)}_{\boldsymbol{r}_\mu,\boldsymbol{r}'_\nu}\mathcal{R}^\mathcal{O}_{ij}W^\dagger_\mathcal{O}[\mathcal{O}(\boldsymbol{r}'_\nu)] &= u^{(j)}_{\mathcal{O}(\boldsymbol{r}_\mu),\mathcal{O}(\boldsymbol{r}'_\nu)},
\end{aligned} \tag{5.8}
$$

  where the SO(3) matrices $\mathcal{R}^{\overline{C}_6}$ and $\mathcal{R}^S$ were given in Eq. (4.7).

- For time reversal $\mathcal{T}$,

$$u^\alpha_{\boldsymbol{r}_\mu,\boldsymbol{r}'_\nu} = -W_\mathcal{T}(\boldsymbol{r}_\mu)u^\alpha_{\boldsymbol{r}_\mu,\boldsymbol{r}'_\nu}W^\dagger_\mathcal{T}(\boldsymbol{r}'_\nu). \tag{5.9}$$

By solving Eqs. (5.7)-(5.9) for the sixteen real parameters at each bond, we obtain the

mean-field ansätze for the PSG classes.

The pyrochlore bonds can be categorized into equivalence classes (or orbits) of the

space group, where the bonds within each class are related by space group transforma-

tions, while the bonds in different classes are unrelated. In order to obtain the complete

mean-field ansatz, it suffices to obtain the mean-field solution for one representative bond

of each equivalence class. We choose and express these representative bonds as follows:

- We use the Greek letters $\alpha,\beta,\gamma,\delta$ to parameterize the representative onsite bond

  $(0,0,0)_0 \to (0,0,0)_0$, the Latin small letters a,b,c,d to parameterize the represen-

  tative nearest-neighbor bond $(0,0,0)_0 \to (0,0,0)_1$, and the Latin capital letters

  A,B,C,D to parameterize the representative next-nearest-neighbor (NNN) bond

$(0, 0, 0)_1 \to (0, -1, 0)_2.$

- Take the representative NN bond for example. In an ansatz for the $\mathbb{Z}_2$ PSG without time reversal symmetry, all the 16 terms in Eq. (5.6) may be nonvanishing. We then use eight complex numbers $a_h, b_h, c_h, d_h, a_p, b_p, c_p, d_p$ to paramaterize the 16 real parameters in this bond: explicitly, we write (omitting the bond label $(0, 0, 0)_0 \to (0, 0, 0)_1$)

$$
\begin{aligned}
u^{(0)} &= i\mathrm{Re}a_h 1 - \mathrm{Re}a_p \sigma^1 - \mathrm{Im}a_p \sigma^2 - \mathrm{Im}a_h \sigma^3, \\
u^{(x)} &= \mathrm{Re}b_h 1 + i(\mathrm{Re}b_p \sigma^1 + \mathrm{Im}b_p \sigma^2 + \mathrm{Im}b_h \sigma^3), \\
u^{(y)} &= \mathrm{Re}c_h 1 + i(\mathrm{Re}c_p \sigma^1 + \mathrm{Im}c_p \sigma^2 + \mathrm{Im}c_h \sigma^3), \\
u^{(z)} &= \mathrm{Re}d_h 1 + i(\mathrm{Re}d_p \sigma^1 + \mathrm{Im}d_p \sigma^2 + \mathrm{Im}d_h \sigma^3).
\end{aligned}
\tag{5.10}
$$

In the $U(1)$ PSG, we only have hopping bilinears, therefore the σ^1 and σ^2 terms in Eq. (5.6) vanish, and we parameterize Eq. (5.6) as

$$
\begin{aligned}
u^{(0)} &= i\mathrm{Re}a 1 - \mathrm{Im}a \sigma^3, \quad u^{(x)} = \mathrm{Re}b 1 + i\mathrm{Im}b \sigma^3, \\
u^{(y)} &= \mathrm{Re}c 1 + i\mathrm{Im}c \sigma^3, \quad u^{(z)} = \mathrm{Re}d 1 + i\mathrm{Im}d \sigma^3.
\end{aligned}
\tag{5.11}
$$

The symmetry relations (5.7), (5.8), and (5.9) impose constraints on these parameters, and the numbers of independent real bond parameters are usually smaller than 16 or 8 in the $\mathbb{Z}_2$ and $U(1)$ ansätze, respectively. To determine the independent bond parameters, one needs to find all the symmetry operations (the so called "stabilizers" of the symmetry group) that leave the representative bonds invariant. As an example, time reversal symmetry leaves any bond invariant. In the $U(1)$ case, applying the time reversal PSG in Eq. (5.3) to Eq. (5.9) reduces the bond parameterization in Eq. (5.11)

to

$$u^{(0)} = -\text{Im}a\sigma^3, \quad u^{(x)} = i\text{Im}b\sigma^3,$$
$$u^{(y)} = i\text{Im}c\sigma^3, \quad u^{(z)} = i\text{Im}d\sigma^3. \tag{5.12}$$

In the $\mathbb{Z}_2$ case, applying the time reversal PSG in Eq. (5.4) to Eq. (5.9) reduces the

bond parameterization in Eq. (5.10) depending on the value of η_μ for $\mu = 0, 1$:

$$u^{(0)} = -\text{Re}a_p\sigma^1 - \text{Im}a_p\sigma^2, \quad u^{(x)} = i(\text{Re}b_p\sigma^1 + \text{Im}b_p\sigma^2),$$
$$u^{(y)} = i(\text{Re}c_p\sigma^1 + \text{Im}c_p\sigma^2), \quad u^{(z)} = i(\text{Re}d_p\sigma^1 + \text{Im}d_p\sigma^2) \tag{5.13}$$

for $\eta_0 = \eta_1$ and

$$u^{(0)} = i\text{Re}a_h1 - \text{Im}a_h\sigma^3, \quad u^{(x)} = \text{Re}b_h1 + i\text{Im}b_h\sigma^3,$$
$$u^{(y)} = \text{Re}c_h1 + i\text{Im}c_h\sigma^3, \quad u^{(z)} = \text{Re}d_h1 + i\text{Im}d_h\sigma^3 \tag{5.14}$$

for $\eta_0 = -\eta_1$. Note that the form of Eq. (5.14) coincides with that of a U(1) ansatz

[see Eq. (5.11)]. However, pairing terms (in which parameters have a subscript "p") do

appear for other bonds (e.g., the representative NNN bond), and this is generally not a

U(1) ansatz.

The final result of the mean-field parameters for representative bonds up to NNN are

presented in Table 5.3 for the U(1) PSG and Table 5.4 for the $\mathbb{Z}_2$ PSG. The effect of time

reversal symmetry has also been addressed therein.

Table 5.3: Independent mean-field parameters and constraints for the 18 U(1) PSG classes of pyrochlore space group symmetry only and 16 U(1) PSG classes of pyrochlore space group symmetry combined with time reversal symmetry. The tabulation is such that the latter are embedded in the former; and that daggered square brackets "[ ]†" are used to enclose data that are specific to the former. The parameters not referenced are enforced to be zero. Note the zero- and π-flux PSG have identical free mean-field parameters up to NNN bonds, but this is no longer true when considering 3rd-nearest-neighbor bonds.

Class	Independent nonzero parameters			Constraints	
$\chi_1 - (w_{\bar{C}_6} w_S) - (\chi_{S T_1} \chi_{\bar{C}_6 S})$	Onsite	NN	NNN	NN	NNN
0- or π-(0 0)-(0 0)	Imα	Imα, Imc	ImA, [ReB]†, ImB, ImD	Im$c = -$Imd	$B = -C^*$
0- or π-(0 0)-(0 π)	Imα	Imb, [Rec]†	ImA, [ReB]†, ImB, ImD	[Re$c = Red$]†	$B = -C^*$
0- or π-(0 1)-(0 0)	—	Imc	[ReB]†, ImB	Im$c = Imd$	$B = -C$
0- or π-(0 1)-(0 π)	—	[Rec]†	[ReB]†, ImB	[Re$c = Red$]†	$B = -C$
0- or π-(1 0)-(0 0)	—	Imc	ImA, [ReB]†, ImB, ImD	Im$c = Imd$	$B = -C^*$
0- or π-(1 0)-(0 π)	—	[Rec]†	ImA, [ReB]†, ImB, ImD	[Re$c = Red$]†	$B = -C^*$
0- or π-(1 1)-(0 0)	—	Imα, Imc	[ReB]†, ImB	Im$c = -$Imd	$B = -C$
0- or π-(1 1)-(0 π)	—	Imb, [Rec]†	[ReB]†, ImB	[Re$c = Red$]†	$B = -C$
$\left[\frac{\pi}{2} - (0\ 1) - (\pi\ 0)\right]^\dagger$	[$-$]†	[Imc]†	[ReB, ImB]†	[Im$c = Imd$]†	[$B = -C$]†
$\left[\frac{\pi}{2} - (0\ 1) - (\pi\ \pi)\right]^\dagger$	[$-$]†	[Rec]†	[ReB, ImB]†	[Re$c = Red$]†	[$B = -C$]†

Table 5.4: Independent mean-field parameters and constraints for the 28 $\mathbb{Z}_2$ PSG classes of pyrochlore space group symmetry only and 48 $\mathbb{Z}_2$ PSG classes of pyrochlore space group symmetry combined with time reversal symmetry. The tabulation uses the double-daggered double-square brackets "[[ ]]‡" to enclose data that are specific to the latter, and whenever a class of the latter is derived from a class of the former then a symbol "↳" is used to specify their relation. Also we set $k = 1$ (see Table 5.2 for the definition of k). The parameters not referenced are enforced to be zero. We denoted $F_2 = \{$Imα_h, Im$\alpha_p\}$, $F_4 = \{$Imα_h, Imc_h, Imα_p, Im$c_p\}$, $F_5 = \{$ReB_h, ImA_p, Imα_p, Im$c_p\}$, $F_6 = \{$ImA_h, ImB_h, ImD_h, ImA_p, ImB_p, Im$D_p\}$.

Class $(\chi_1 \chi_{S T_1})-$	Independent nonzero parameters	Constraints (NN and NNN)

$(\chi_{\overline{C}_6 S}\chi_{S\overline{C}_6}\chi_{\overline{C}_6})_j$	Onsite	NN	NNN	
$(00)-$ or $(\pi\pi)-(000)$	$\text{Im}\alpha_h, \alpha_p$	$\text{Im}a_h, \text{Im}c_h, a_p, c_p$	$\text{Im}A_h, B_h, \text{Im}D_h, A_p, B_p, D_p$	$\text{Im}d_h = -\text{Im}c_h, c_p = -d_p, C_h = -B_h^*, B_p = C_p$
$\hookrightarrow [[(\chi_{T\overline{C}_6}\chi_{TS}) = (00)]]^{\ddagger}$	$[F_2]]^{\ddagger}$	$[[F_4]]^{\ddagger}$	$[F_6]]^{\ddagger}$	[[Constraints inherited from above]]‡
$(00)-$ or $(\pi00)$	$\text{Im}\alpha_h, \alpha_p$	$\text{Im}b_h, \text{Re}c_h, b_p$	$\text{Im}A_h, B_h, \text{Im}D_h, A_p, B_p, D_p$	$\text{Re}d_h = \text{Re}c_h, C_h = -B_h^*, B_p = C_p$
$\hookrightarrow [[(\chi_{T\overline{C}_6}\chi_{TS}) = (00)]]^{\ddagger}$	$[F_2]]^{\ddagger}$	$[[\text{Im}b_h, \text{Im}b_p]]^{\ddagger}$	$[F_6]]^{\ddagger}$	[[Constraints inherited from above]]‡
$(00)-$ or $(\pi\pi)-(0\pi\pi)$	$\text{Re}\alpha_p$	$\text{Re}a_h, c_h, \text{Im}c_p$	$A_h, B_h, D_h, \text{Im}A_p, B_p, \text{Im}D_p$	$d_h = -c_h^*, \text{Im}d_p = \text{Im}c_p, C_h = B_h, C_p = -B_p^*$
$\hookrightarrow [[(\chi_{T\overline{C}_6}\chi_{TS}) = (00)]]^{\ddagger}$	$[-]]^{\ddagger}$	$[[\text{Im}c_h, \text{Im}c_p]]^{\ddagger}$	$[F_6]]^{\ddagger}$	[[Constraints inherited from above]]‡
$\hookrightarrow [[(\chi_{T\overline{C}_6}\chi_{TS}) = (\pi0)]]^{\ddagger}$	$[\text{Re}\alpha_p]]^{\ddagger}$	$[[\text{Re}a_h, c_h]]^{\ddagger}$	$[A_h, B_h, D_h]]^{\ddagger}$	[[Constraints inherited from above]]‡
$(00)-$ or $(\pi\pi)-(\pi\pi\pi)$	$\text{Re}\alpha_p$	$\text{Re}b_h, \text{Re}c_p$	$A_h, B_h, D_h, \text{Im}A_p, B_p, \text{Im}D_p$	$\text{Re}d_p = \text{Re}c_p, rC_h = B_h, C_p = -B_p^*$
$\hookrightarrow [[(\chi_{T\overline{C}_6}\chi_{TS}) = (00)]]^{\ddagger}$	$[-]]^{\ddagger}$	$[-]]^{\ddagger}$	$[F_6]]^{\ddagger}$	[[Constraints inherited from above]]‡
$\hookrightarrow [[(\chi_{T\overline{C}_6}\chi_{TS}) = (\pi0)]]^{\ddagger}$	$[\text{Re}\alpha_p]]^{\ddagger}$	$[[\text{Re}b_h]]^{\ddagger}$	$[A_h, B_h, D_h]]^{\ddagger}$	[[Constraints inherited from above]]‡
$(0\pi)-$ or $(\pi0)-(0\pi0)_1$	$-$	$\text{Re}b_h, \text{Re}c_p$	$B_h, \text{Re}A_p, B_p, \text{Re}D_p$	$\text{Im}b_h = \sqrt{3}\text{Re}b_h, \text{Im}c_p = \sqrt{3}\text{Re}c_p, c_p = d_p,$ $\text{Im}A_p = -\sqrt{3}\text{Re}A_p, C_h = -B_h,$ $\text{Im}D_p = -\sqrt{3}\text{Re}D_p, C_p = e^{-\frac{2\pi}{3}i}B_p^*$
$\hookrightarrow [[(\chi_{T\overline{C}_6}\chi_{TS}) = (0\pi)]]^{\ddagger}$	$[-]]^{\ddagger}$	$[[\text{Re}b_h]]^{\ddagger}$	$[\text{Re}A_p, B_p, \text{Re}D_p]]^{\ddagger}$	[[Constraints inherited from above]]‡
$(0\pi)-$ or $(\pi0)-(0\pi0)_3$	$\text{Re}\alpha_p$	$\text{Re}b_h, \text{Re}c_p$	$B_h, \text{Re}A_p, B_p, \text{Re}D_p$	$\text{Re}d_p = \text{Re}c_p, C_h = -B_h, C_p = B_p^*$
$\hookrightarrow [[(\chi_{T\overline{C}_6}\chi_{TS}) = (00)]]^{\ddagger}$	$[-]]^{\ddagger}$	$[-]]^{\ddagger}$	$[\text{Im}B_h, \text{Im}B_p]]^{\ddagger}$	[[Constraints inherited from above]]‡
$\hookrightarrow [[(\chi_{T\overline{C}_6}\chi_{TS}) = (\pi0)]]^{\ddagger}$	$[\text{Re}\alpha_p]]^{\ddagger}$	$[[\text{Re}b_h]]^{\ddagger}$	$[\text{Re}A_p, B_p, \text{Re}D_p]]^{\ddagger}$	[[Constraints inherited from above]]‡
$(0\pi)-$ or $(\pi0)-(\pi\pi0)_0$	$\text{Re}\alpha_p$	$\text{Re}a_h, c_h, \text{Im}c_p$	$B_h, \text{Re}A_p, B_p, \text{Re}D_p$	$d_h = -c_h^*, \text{Im}d_p = \text{Im}c_p, C_h = -B_h, C_p = B_p^*$
$\hookrightarrow [[(\chi_{T\overline{C}_6}\chi_{TS}) = (00)]]^{\ddagger}$	$[-]]^{\ddagger}$	$[[\text{Im}c_h, \text{Im}c_p]]^{\ddagger}$	$[\text{Im}B_h, \text{Im}B_p]]^{\ddagger}$	[[Constraints inherited from above]]‡
$\hookrightarrow [[(\chi_{T\overline{C}_6}\chi_{TS}) = (\pi0)]]^{\ddagger}$	$[\text{Re}\alpha_p]]^{\ddagger}$	$[[\text{Re}a_h, c_h]]^{\ddagger}$	$[\text{Re}A_p, B_p, \text{Re}D_p]]^{\ddagger}$	[[Constraints inherited from above]]‡
$(0\pi)-$ or $(\pi0)-(\pi\pi0)_2$	$-$	$\text{Re}a_h, c_h, \text{Re}c_p$	$B_h, \text{Re}A_p, B_p, \text{Re}D_p$	$\text{Im}a_h = -\sqrt{3}\text{Re}a_h, d_h = e^{\frac{\pi}{3}i}c_h^*, \text{Im}c_p = \frac{1}{\sqrt{3}}\text{Re}c_p,$ $d_p = c_p, \text{Im}A_p = \sqrt{3}\text{Re}A_p, C_h = -B_h,$ $C_p = e^{\frac{2\pi}{3}i}B_p^*, \text{Im}D_p = \sqrt{3}\text{Re}D_p$

196

$\hookrightarrow[[(\chi_T\overline{c}_6\chi_{TS})=(0\pi)]]^\ddagger$				
$\hookrightarrow[[(\chi_T\overline{c}_6\chi_{TS})=(0\pi)]]^\ddagger$	$[-]^\ddagger$	$[\text{Re}a_h,\,c_h]]^\ddagger$	$[\text{Re}A_p,\,B_p,\,\text{Re}D_p]]^\ddagger$	[Constraints inherited from above]]‡
$(0\pi)-$ or $(\pi 0)-(00\pi)$	$\text{Re}\alpha_p$	$\text{Im}a_h,\,\text{Im}c_h,\,a_p,\,c_p$	$\text{Re}A_h,\,B_h,\,\text{Re}D_h,\,B_p$	$\text{Im}d_h=-\text{Im}c_h,\,d_p=-c_p,\,C_h=B_h^*,\,C_p=-B_p$
$\hookrightarrow[[(\chi_T\overline{c}_6\chi_{TS})=(00)]]^\ddagger$	$[-]^\ddagger$	$[F_4]]^\ddagger$	$[\text{Im}B_h,\,\text{Im}B_p]]^\ddagger$	[Constraints inherited from above]]‡
$\hookrightarrow[[(\chi_T\overline{c}_6\chi_{TS})=(\pi\pi)]]^\ddagger$	$[\text{Re}\alpha_p]]^\ddagger$	$[a_p,\,c_p]]^\ddagger$	$[\text{Re}A_h,\,B_h,\,\text{Re}D_h]]^\ddagger$	[Constraints inherited from above]]‡
$(0\pi)-$ or $(\pi 0)-(0\pi\pi)_0$	$\text{Re}\alpha_p$	$\text{Im}b_h,\,\text{Re}c_h,\,b_p$	$\text{Re}A_h,\,B_h,\,\text{Re}D_h,\,B_p$	$\text{Re}d_h=\text{Re}c_h,\,C_h=B_h^*,\,B_p=-C_p$
$\hookrightarrow[[(\chi_T\overline{c}_6\chi_{TS})=(00)]]^\ddagger$	$[-]^\ddagger$	$[\text{Im}b_h,\,\text{Im}b_p]]^\ddagger$	$[\text{Im}B_h,\,\text{Im}B_p]]^\ddagger$	[Constraints inherited from above]]‡
$\hookrightarrow[[(\chi_T\overline{c}_6\chi_{TS})=(\pi\pi)]]^\ddagger$	$[\text{Re}\alpha_p]]^\ddagger$	$[b_p]]^\ddagger$	$[\text{Re}A_h,\,B_h,\,\text{Re}D_h]]^\ddagger$	[Constraints inherited from above]]‡
$(0\pi)-$ or $(\pi 0)-(\pi\pi\pi)_0$	$-$	$\text{Re}b_h,\,\text{Re}c_p$	$B_h,\,\text{Re}A_p,\,B_p,\,\text{Re}D_p$	$\text{Im}b_h=-\sqrt{3}\text{Re}b_h,\,\text{Im}c_p=\frac{1}{\sqrt{3}}\text{Re}c_p,\,c_p=d_p,\ \text{Im}A_p=-\frac{1}{\sqrt{3}}\text{Re}A_p,\,C_h=-B_h,\ C_p=e^{-\frac{\pi}{3}i}B_p^*,\,\text{Im}D_p=-\frac{1}{\sqrt{3}}\text{Re}D_p$
$\hookrightarrow[[(\chi_T\overline{c}_6\chi_{TS})=(0\pi)]]^\ddagger$	$[-]^\ddagger$	$[\text{Re}b_h]]^\ddagger$	$[\text{Re}A_p,\,B_p,\,\text{Re}D_p]]^\ddagger$	[Constraints inherited from above]]‡
$(0\pi)-$ or $(\pi 0)-(\pi\pi\pi)_0$	$-$	$\text{Re}a_h,\,c_h,\,\text{Re}c_p$	$B_h,\,\text{Re}A_p,\,B_p,\,\text{Re}D_p$	$\text{Im}a_h=-\sqrt{3}\text{Re}a_h,\,d_h=e^{i\frac{\pi}{3}}c_h^*,\ \text{Im}c_p=-\sqrt{3}\text{Re}c_p,\,c_p=d_p,\,\text{Im}A_p=-\frac{1}{\sqrt{3}}\text{Re}A_p,\ C_h=-B_h,\,C_p=e^{-\frac{\pi}{3}i}B_p^*,\,\text{Im}D_p=-\frac{1}{\sqrt{3}}\text{Re}D_p$
$\hookrightarrow[[(\chi_T\overline{c}_6\chi_{TS})=(0\pi)]]^\ddagger$	$[-]^\ddagger$	$[\text{Re}a_h,\,c_h]]^\ddagger$	$[\text{Re}A_p,\,B_p,\,\text{Re}D_p]]^\ddagger$	[Constraints inherited from above]]‡
$(0\pi)-$ or $(\pi 0)-(0\pi\pi)_1$	$-$	$\text{Re}b_h,\,\text{Im}c_p$	$B_h,\,\text{Im}A_p,\,B_p,\,\text{Im}D_p$	$\text{Im}d_p=\text{Im}c_p,\,C_h=-B_h,\,C_p=-B_p^*$
$\hookrightarrow[[(\chi_T\overline{c}_6\chi_{TS})=(0\pi)]]^\ddagger$	$[-]^\ddagger$	$[\text{Re}b_h]]^\ddagger$	$[\text{Im}A_p,\,B_p,\,\text{Im}D_p]]^\ddagger$	[Constraints inherited from above]]‡
$\hookrightarrow[[(\chi_T\overline{c}_6\chi_{TS})=(\pi 0)]]^\ddagger$	$[-]^\ddagger$	$[\text{Re}b_h]]^\ddagger$	$[\text{Re}B_h,\,\text{Re}B_p]]^\ddagger$	[Constraints inherited from above]]‡
$\hookrightarrow[[(\chi_T\overline{c}_6\chi_{TS})=(\pi\pi)]]^\ddagger$	$[-]^\ddagger$	$[-]^\ddagger$	$[F_5]]^\ddagger$	[Constraints inherited from above]]‡
$(0\pi)-$ or $(\pi 0)-(\pi\pi\pi)_1$	$-$	$\text{Re}a_h,\,c_h,\,\text{Re}c_p$	$B_h,\,\text{Im}A_p,\,B_p,\,\text{Im}D_p$	$d_h=-c_h^*,\,\text{Re}d_p=\text{Re}c_p,\,C_h=-B_h,\,C_p=-B_p^*$
$\hookrightarrow[[(\chi_T\overline{c}_6\chi_{TS})=(0\pi)]]^\ddagger$	$[-]^\ddagger$	$[\text{Re}a_h,\,c_h]]^\ddagger$	$[\text{Im}A_p,\,B_p,\,\text{Im}D_p]]^\ddagger$	[Constraints inherited from above]]‡
$\hookrightarrow[[(\chi_T\overline{c}_6\chi_{TS})=(\pi 0)]]^\ddagger$	$[-]^\ddagger$	$[\text{Re}a_h,\,\text{Re}c_h,\,\text{Re}c_p]]^\ddagger$	$[\text{Re}B_h,\,\text{Re}B_p]]^\ddagger$	[Constraints inherited from above]]‡
$\hookrightarrow[[(\chi_T\overline{c}_6\chi_{TS})=(\pi\pi)]]^\ddagger$	$[-]^\ddagger$	$[\text{Re}c_p,\,\text{Im}c_h]]^\ddagger$	$[F_5]]^\ddagger$	[Constraints inherited from above]]‡

5.3.2 Symmetry properties of the 0-flux ansätze

The symmetry constraints imposed by the PSG given in the last subsection are formulated in real space. For analyzing the properties of the mean-field ansätze, it is more helpful to see how the projective symmetry transformations apply in momentum space. In the 0-flux case ($\chi_1 = 0$), the action of each projective symmetry is simple and can be explicitly given. To start with, we define the Bogoliubov-de Gennes (BdG) basis (where the spin indices are suppressed):

$$\Phi_{\boldsymbol{k}} = \left(f_{\boldsymbol{k},0}, f_{\boldsymbol{k},1}, f_{\boldsymbol{k},2}, f_{\boldsymbol{k},3}, f^{\dagger}_{-\boldsymbol{k},0}, f^{\dagger}_{-\boldsymbol{k},1}, f^{\dagger}_{-\boldsymbol{k},2}, f^{\dagger}_{-\boldsymbol{k},3} \right)^{T}. \tag{5.15}$$

The Hamiltonian is then written as

$$H = \sum_{\boldsymbol{k} \in \mathrm{BZ}^{+}} \Phi^{\dagger}_{\boldsymbol{k}} \mathcal{H}_{\mathrm{BdG}}(\boldsymbol{k}) \Phi_{\boldsymbol{k}}, \tag{5.16}$$

where the momentum sum is over half of the Brillouin zone (BZ) with, say $k_3 > 0$. This Hamiltonian has the standard Bogoliubov form

$$\mathcal{H}_{\mathrm{BdG}}(\boldsymbol{k}) = \begin{pmatrix} \mathcal{H}_{\mathrm{U}(1)}(\boldsymbol{k}) & \mathcal{H}_{p}(\boldsymbol{k}) \\ \mathcal{H}^{\dagger}_{p} & -\mathcal{H}^{T}_{\mathrm{U}(1)}(-\boldsymbol{k}) \end{pmatrix}, \tag{5.17}$$

where $\mathcal{H}_{\mathrm{U}(1)}$ and $\mathcal{H}_{p}$ correspond to the hopping and pairing terms in Eq. (5.6) for the $\mathbb{Z}_2$ PSG. For the U(1) PSG, the pairing terms vanish and the BdG form corresponds to two copies of the U(1) Hamiltonian $\mathcal{H}_{\mathrm{U}(1)}$.

In terms of the BdG Hamiltonian matrix $\mathcal{H}_{\mathrm{BdG}}(\boldsymbol{k})$ describing each 0-flux ansatz, we have the following symmetry constraints:

$$W^{\dagger}_{\overline{C}_6, w_{\overline{C}_6}}(\boldsymbol{k}) \mathcal{H}_{\mathrm{BdG}}(\boldsymbol{k}) W_{\overline{C}_6, w_{\overline{C}_6}}(\boldsymbol{k}) = \mathcal{H}_{\mathrm{BdG}} \left(\overline{C}_6(\boldsymbol{k}) + \mu^3 \phi_{ST_1} \boldsymbol{b}_1 \right), \tag{5.18}$$

$$W_{S,w_S}^\dagger(\boldsymbol{k})\mathcal{H}_{\mathrm{BdG}}(\boldsymbol{k})W_{S,w_S}(\boldsymbol{k}) = \mathcal{H}_{\mathrm{BdG}}\left(S(\boldsymbol{k}) + \mu^3\phi_{ST_1}(\boldsymbol{b}_1 + 3\boldsymbol{b}_3)\right), \qquad (5.19)$$

where $\boldsymbol{b}_i$ (with $i = 1, 2, 3$) are the three reciprocal lattice vectors in units of a^{-1}, while μ^i (with $i = 1, 2, 3$) are the Pauli matrices acting in the particle-hole space $(f, f^\dagger)^T$. The derivation of these equations together with the forms of $W_{\overline{C}_6, w_{\overline{C}_6}}(\boldsymbol{k})$ and $W_{S,w_S}(\boldsymbol{k})$ can be found in App. A.10. We point out that, due to the projective nature of the symmetry transformation, an annihilation operation f can be mapped to either an annihilation operator f or a creation operator $f^\dagger$. Therefore, the unitary matrices $W_{\mathcal{O},w_{\mathcal{O}}}(\boldsymbol{k})$ with $\mathcal{O} = \overline{C}_6, S$ are either off-diagonal (corresponding to $w_{\mathcal{O}} = 1$) or diagonal (corresponding to $w_{\mathcal{O}} = 0$) in the particle-hole space. Let us understand the implications of this property for a U(1) 0-flux ansatz with $w_{\overline{C}_6} = 1$ by considering the action of $I = \overline{C}_6^3$:

$$w_{\overline{C}_6} = 1: \quad W_I^\dagger\mathcal{H}_{\mathrm{U}(1)}(\boldsymbol{k})W_I = -\mathcal{H}_{\mathrm{U}(1)}^*(\boldsymbol{k}) \quad \forall \boldsymbol{k} \in \mathrm{BZ}. \qquad (5.20)$$

Therefore, projective inversion acts like the product of faithful inversion and charge conjugation, which ensures that the energies come in $\pm E(\boldsymbol{k})$ pairs for the entire BZ.

5.3.3 0-flux U(1) ansätze with $w_S = 1$: projective symmetry protected gapless nodal star

Unlike the $w_{\overline{C}_6} = 1$ classes, a 0-flux U(1) ansatz with $w_{\overline{C}_6} = 0$ does not necessarily have energy levels coming in $\pm E(\boldsymbol{k})$ pairs at each momentum $\boldsymbol{k}$. However, in the case of $w_S = 1$ (regardless of $w_{\overline{C}_6}$), there exists a one-dimensional (1D) submanifold in the BZ
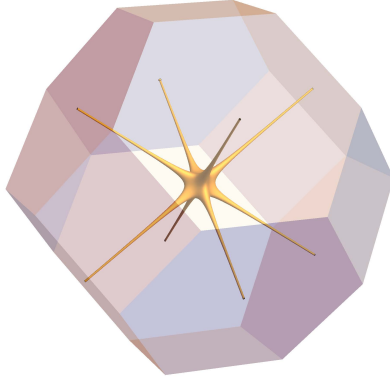
Figure 5.1: Illustration of the nodal star Fermi surface; the contour corresponds to an energy infinitesimally above the Fermi level.

along which this is true. In fact, along this submanifold,

$$\Lambda = \{(\varsigma_1, \varsigma_2, \varsigma_3)k | \varsigma_{1,2,3} = \pm\}, \tag{5.21}$$

the energy levels not only come in $\pm E(\boldsymbol{k})$ pairs, but are always *gapless* at $E = 0$, i.e., there are always two degenerate modes sitting at the Fermi energy. We call this 1D submanifold Λ the *star* manifold, and refer to the gapless modes as the *nodal star* zero modes; see Fig. 5.1 for an illustration. A direct check by adding up to 8th-nearest neighbor bonds with generic bond parameters shows that the zero modes are robust as long as the projective symmetries are intact. This is strong evidence that the nodal star zero modes are not accidental but are protected by the projective symmetries.

Such a nodal star structure has been reported in other contexts. In Ref. [23], Burnell *et al.* studied an SU(2) invariant ansatz with purely imaginary NN hoppings forming $\pi/2$ fluxes on all pyrochlore faces: the so-called "Monopole Flux" state. Such an ansatz preserves charge conjugation, the product of inversion and time reversal $I \circ \mathcal{T}$, and the 24 "proper elements" of the point group O_h, but it breaks the individual time reversal

and inversion symmetries. The 24 "proper elements" and the composed symmetry $I \circ \mathcal{T}$ allow the mapping of one NN bond to all the other NN bonds, while charge conjugation and $I \circ \mathcal{T}$ ensure that the Hamiltonian is real and an odd function of $\boldsymbol{k}$. An algebraic proof was then given to show that the matrix structure on the star submanifold leads to nodal star zero modes and that the symmetries forbid a chemical potential which could otherwise gap out the nodal star. However, the proof relies on the restriction of the hopping to the nearest neighbors, and it is not clear in the proof if the nodal star is truly symmetry protected, i.e., whether further neighbor symmetry allowed hoppings can gap out the nodal star. A similar nodal star state also appears in the bosonic description of a $\mathbb{Z}_2$ spin liquid [94] at the NN level. In that case, it was explicitly shown that an infinitesimal NNN bond amplitude is enough to gap out the nodal line to discrete points.

Here, we provide a proof that the nodal star zero modes appearing in our $w_S = 1$ classes are indeed protected by the projective symmetries, see App. B.1. The proof is algebraic, and can be viewed as a generalized version of that given in Ref. [23]. The proof relies on the following observation: while an unprojective screw symmetry relates the Hamiltonian at momentum $\boldsymbol{k} = (k_x, k_y, k_z)$ with that at momentum $(k_y, k_x, -k_z)$, a projective screw symmetry relates the Hamiltonian at momentum $\boldsymbol{k} = (k_x, k_y, k_z)$ with that at momentum $(-k_y, -k_x, k_z)$. Therefore, focusing on the $(1, 1, 1)$ nodal line without loss of generality, the symmetry operation

$$R \equiv S \circ C_3 \circ C_3 \circ S \circ C_3 \circ S \tag{5.22}$$

leaves the momenta along the nodal line unchanged in the case of a projective S. This

symmetry constrains the Hamiltonian along the nodal line [cf. Eq. (5.20)],

$$W_R^\dagger(k,k,k)\mathcal{H}_{\mathrm{U}(1)}(k,k,k)W_R(k,k,k) = -\mathcal{H}_{\mathrm{U}(1)}^*(k,k,k), \tag{5.23}$$

and implies that the energy levels come in $\pm E(\boldsymbol{k})$ pairs. Considering the analogous action of the threefold rotation C_3 [which also maps (k,k,k) to (k,k,k)],

$$W_{C_3}^\dagger(k,k,k)\mathcal{H}_{\mathrm{U}(1)}(k,k,k)W_{C_3}(k,k,k) = \mathcal{H}_{\mathrm{U}(1)}(k,k,k), \tag{5.24}$$

and the specific forms of $W_R(k,k,k)$ and $W_{C_3}(k,k,k)$, it can then be shown (see App. B.1) that the rank of the matrix $\mathcal{H}_{\mathrm{U}(1)}(k,k,k)$ is at most 6, which implies that it has at least two zero eigenvalues. Since our proof only relies on the symmetry properties of the spinon Hamiltonian, the result universally applies to any fully symmetric mean-field ansatz with a projective screw symmetry ($w_S = 1$), even beyond the NN (or NNN) level. In turn, this suggests that a pyrochlore spin liquid with a nodal star Fermi surface may be commonplace.

Lemma 5.3.1 *define a 6×6 matrix*

$$A(x,y,z) \equiv \begin{pmatrix} x(\sigma_2 - \sigma_3) & y(\sigma_1 - \sigma_2) & z(\sigma_3 - \sigma_1) \\ z(\sigma_1 - \sigma_2) & x(\sigma_3 - \sigma_1) & y(\sigma_2 - \sigma_3) \\ y(\sigma_3 - \sigma_1) & z(\sigma_2 - \sigma_3) & x(\sigma_1 - \sigma_2) \end{pmatrix}, \tag{5.25}$$

(what we will use later is a special case with $(x,y,z) = (c, c', c'^*)$.) then its inverse is

$$(A(x,y,z))^{-1} = \frac{A(x^2 - yz, z^2 - xy, y^2 - xz)}{2(x^3 + y^3 + z^3 - 3xyz)}. \tag{5.26}$$

Furthermore, define a 2×6 matrix

$$B(\alpha, \beta, \gamma, \delta) \equiv \left(\alpha\sigma^0 + (\beta, \gamma, \delta) \cdot \boldsymbol{\sigma}, \alpha\sigma^0 + (\delta, \beta, \gamma) \cdot \boldsymbol{\sigma}, \alpha\sigma^0 + (\gamma, \delta, \beta) \cdot \boldsymbol{\sigma} \right) \tag{5.27}$$

and a 6×2 matrix

$$C(\alpha', \beta', \gamma', \delta') \equiv \begin{pmatrix} \alpha' \sigma^0 + (\beta', \gamma', \delta') \cdot \boldsymbol{\sigma} \\ \alpha' \sigma^0 + (\delta', \beta', \gamma') \cdot \boldsymbol{\sigma} \\ \alpha' \sigma^0 + (\gamma', \delta', \beta') \cdot \boldsymbol{\sigma} \end{pmatrix} \tag{5.28}$$

then for any complex ζ we have (be wary of the switching $\delta \leftrightarrow \gamma$ between B and C below)

$$B(\alpha, \beta, \gamma, \delta) \left(A(x, y, z) \right)^{-1} C(\zeta\alpha, \zeta\beta, \zeta\delta, \zeta\gamma) = 0. \tag{5.29}$$

The proof of this Lemma is elementary.

Now we use the lemma to prove that the existence of nodal star. The U(1) 0-flux mean-field ansätze correspond to an 8×8 matrix $\mathcal{H}_{\mathrm{U}(1)}(\boldsymbol{k})$ in the momentum space, with basis the parton operators $(f_{0\boldsymbol{k}\uparrow}, f_{0\boldsymbol{k}\downarrow}, f_{1\boldsymbol{k}\uparrow}, f_{1\boldsymbol{k}\downarrow}, f_{2\boldsymbol{k}\uparrow}, f_{2\boldsymbol{k}\downarrow}, f_{3\boldsymbol{k}\uparrow}, f_{3\boldsymbol{k}\downarrow})^T$. We abbreviate $\mathcal{H}_{\mathrm{U}(1)}(\boldsymbol{k})$ by $\mathcal{H}(\boldsymbol{k})$ for the rest of this appendix. For U(1) 0-flux states with the PSG number $w_S = 1$, we have the threefold rotation symmetry C_3 along $(1,1,1)$ axis, and the screw symmetry S:

$$\begin{aligned} W_{C_3}^\dagger(\boldsymbol{k}) \mathcal{H}(\boldsymbol{k}) W_{C_3}(\boldsymbol{k}) &= \mathcal{H}(k_z, k_x, k_y), \\ W_S^\dagger(\boldsymbol{k}) \mathcal{H}(\boldsymbol{k}) W_S(\boldsymbol{k}) &= -\mathcal{H}^T(-k_y, -k_x, k_z), \end{aligned} \tag{5.30}$$

notice the second line is *specific* to $w_S = 1$. Now define the operation $R \equiv S \circ C_3 \circ C_3 \circ S \circ C_3 \circ S$. Then we notice that Eqs. (5.23) and (5.24) hold, meaning that R and C_3 both map the momentum (k, k, k) back to itself. Now, assume the most general form of an 8×8 hermitian matrix $\mathcal{H}_{\mathrm{U}(1)}(k, k, k) = [h_{\mu\nu}]$, where $h_{\mu\nu}$ are 2×2 blocks with $\mu, \nu = 0, 1, 2, 3$. Using the special form of $W_{C_3}(k, k, k)$ and $W_R(k, k, k)$, we can show step by step the following:

- $h_{00} = 0$, $h_{11} = c(\sigma^2 - \sigma^3)$, $h_{22} = c(\sigma^3 - \sigma^1)$, $h_{33} = c(\sigma^1 - \sigma^2)$, where c is some real parameter;

- $h_{12} = c'(\sigma^1 - \sigma^2)$, $h_{13} = c'^*(\sigma^3 - \sigma^1)$, $h_{23} = c'(\sigma^2 - \sigma^3)$, where c' is some complex parameter;

- $h_{01} = a''\sigma^0 + (b'', c'', d'') \cdot \boldsymbol{\sigma}$, $h_{02} = a''\sigma^0 + (d'', b'', c'') \cdot \boldsymbol{\sigma}$, and $h_{03} = a''\sigma^0 + (c'', d'', b'') \cdot \boldsymbol{\sigma}$, where (a'', b'', c'', d'') are complex parameters satisfying $a''e^{ik} = -a''^*$, $e^{ik}(-b'', -d'', -c'') = (b''^*, c''^*, d''^*)$.

Therefore the Hamiltonian can be written in the form

$$\mathcal{H}(k, k, k) = \begin{pmatrix} 0 & B \\ C & A \end{pmatrix}, \tag{5.31}$$

where A is a 6×6 block containing h_{ij} blocks with $i, j = 1, 2, 3$, B is a 2×6 block containing h_{01}, h_{02} and h_{03}, and $C = B^\dagger$. Using the above Lemma, we can show that $BA^{-1}C = 0_{2\times2}$, therefore using the standard matrix decomposition, we have

$$\mathcal{H}(k, k, k) = \begin{pmatrix} 1_{2\times2} & BA^{-1} \\ 0 & 1_{6\times6} \end{pmatrix} \begin{pmatrix} 0 & 0 \\ 0 & A \end{pmatrix} \begin{pmatrix} 1_{2\times2} & 0 \\ A^{-1}C & 1_{6\times6} \end{pmatrix}, \tag{5.32}$$

we see that the rank of $\mathcal{H}_{\mathrm{U(1)}}(k, k, k)$ is smaller or equal to 6, i.e. $\mathcal{H}_{\mathrm{U(1)}}(k, k, k)$ at least has two zero eigenvalues. The existence of zero eigenvalues of $\mathcal{H}_{\mathrm{U(1)}}(-k, -k, k)$, $\mathcal{H}_{\mathrm{U(1)}}(-k, k, -k)$ and $\mathcal{H}_{\mathrm{U(1)}}(k, -k, -k)$ then follows.

5.4   Nodal star U(1) spin liquid

In this section, we restrict ourselves to the study of U(1) spin liquids with a gapless nodal star structure as was put forward in the last subsection. Our goal is to develop a full-fledged low energy theory whose degrees of freedom include both the nodal star spinons and the U(1) gauge field. The gauge field has physical consequences and may

lead to observable effects. Such effects have been explored in U(1) spin liquids with a spinon Fermi surface where the U(1) gauge fluctuations lead to $T^{2/3}$ and $T \ln(1/T)$ scaling in the specific heat for two and three spatial dimensions, respectively [145, 110]. These non-Fermi liquid behaviors have been important experimental touchstones for the discovery of spinon Fermi surface U(1) spin liquids. In this regard, it is interesting to ask how gauge fluctuations affect the thermodynamic properties of the nodal star U(1) spin liquid. We hope that the answer to this question provided in this section can serve as a primer for the more interesting properties of the nodal star U(1) spin liquid.

5.4.1 Low energy effective model for spinon nodal bands

In this subsection, we take a specific class of nodal star spin liquid and study its low energy properties in detail. We choose the U(1) class 0–(1 1)–(0 π) and only keep the NN mean-field parameters $b = ib_i$ and $c = c_r$. Although the energy at arbitrary momentum cannot be written in a closed form, the energies along the star $(\varsigma_1 k, \varsigma_2 k, \varsigma_3 k) \in \Lambda$ have a simple expression:

$$E_{1,2} = 0, \quad E_3 = -E_4 = 4\sqrt{2}c_r, \quad E_{5,6} = -E_{7,8} = \sqrt{6b_i^2 + 20c_r^2 - 6(b_i^2 - 2c_r^2)\cos k}. \tag{5.33}$$

For simplicity, we set $b_i = \sqrt{2}c_r$; this specific ansatz should be continuously connected to those at other parameter regions. The low energy dispersion along the nodal lines and

in vicinity of the Γ point is then well described by the following effective Hamiltonian:

$$\mathcal{H}(\boldsymbol{k}) = \boldsymbol{d_k} \cdot \boldsymbol{\sigma}, \qquad (5.34a)$$

$$\boldsymbol{d_k} = \begin{pmatrix} \cos k_3 - \cos k_2 \\ \cos k_1 - \cos k_3 \\ \cos k_2 - \cos k_1 \end{pmatrix}. \qquad (5.34b)$$

Along each momentum section perpendicular to the star lines, the spinon field has the dispersion of a 2+1D Dirac field, where the Dirac velocity $v = \sqrt{3}\sin k$ is a sinusoidal function of the star momentum $(\varsigma_1 k, \varsigma_2 k, \varsigma_3 k)$. In the vicinity of the Γ point, the model can be further simplified by expanding $\boldsymbol{d_k}$:

$$\boldsymbol{d_k} = (k_2^2 - k_3^2, k_3^2 - k_1^2, k_1^2 - k_2^2) + O(k^4). \qquad (5.35)$$

The spinon nodal star creates an interesting instance of U(1) gauge fields interacting with gapless matter. This is in contrast with the quantum spin ice model established in Ref. [63] where the matter fields are gapped and the low energy description is the Maxwell theory.

5.4.2 Nodal star spinons with U(1) gauge field

We now assume that the nodal star spinons are coupled to a U(1) gauge field. The low energy effective Hamiltonian describing the spinon nodal bands in Eq. (5.34a) corresponds to a Lagrangian

$$\mathcal{L}_0 = \psi_k^\dagger(-ik_0 + \mathcal{H}(\boldsymbol{k}))\psi_k, \qquad (5.36)$$

206

where we use the imaginary time formulation and denote $k = (k_0, \boldsymbol{k})$ as the four-momentum in Euclidean spacetime. The U(1) gauge field has a Maxwell term

$$\mathcal{L}_M = \frac{1}{2g^2} A^\mu(k)(k^2 \delta_{\mu\nu} - k_\mu k_\nu) A^\nu(-k), \tag{5.37}$$

which emerges in this low energy effective theory by integrating out the high energy spinon bands. Finally, the gauge field couples to the spinon fields in the form of

$$\begin{aligned}
\mathcal{L}_1 = \sum_q &\; iA^0(-q)\psi^\dagger_{k-q/2}\psi_{k+q/2} + A^i(-q)\psi^\dagger_{k-q/2}\frac{\partial\mathcal{H}(\boldsymbol{k})}{\partial k_i}\psi_{k+q/2} \\
&+ \sum_{q,q'} A^i(q)A^j(q')\psi^\dagger_{k+q'}\frac{\partial^2\mathcal{H}(\boldsymbol{k})}{\partial k_j \partial k_i}\psi_{k-q} + O(A^3),
\end{aligned} \tag{5.38}$$

where the first line is the usual minimal coupling terms and the second line is a diamagnetic coupling term. The complete theory describing the low energy nodal star spinons and the U(1) gauge field is thus

$$\mathcal{L} = \mathcal{L}_0 + \mathcal{L}_M + \mathcal{L}_1 + \mathcal{L}_{gf} + \mathcal{L}_{gh}, \tag{5.39}$$

where we have also included a gauge fixing term and a ghost term for later use [120]:

$$\mathcal{L}_{gf} = \frac{1}{2\xi} k_\mu k_\nu A^\mu(k) A^\nu(-k), \tag{5.40a}$$

$$\mathcal{L}_{gh} = \frac{1}{g^2} \bar{\eta}_k k^2 \eta_k. \tag{5.40b}$$

It is the goal of the next subsection to derive an effective theory for the photon field.
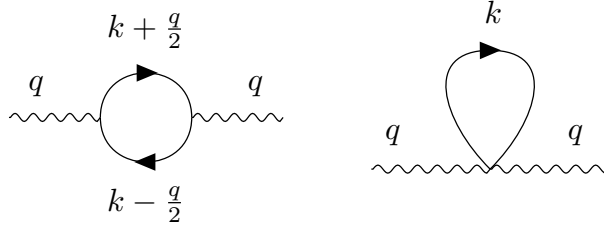
Figure 5.2: The two diagrams for the photon self-energy at one loop level: the "vacuum polarization bubble" (left) and the "tadpole" (right). Solid (wavy) lines denote spinon (photon) propagators.

5.4.3 Vacuum polarization for the emergent photons

We follow the usual perturbative approach to calculate the photon effective action within the random phase approximation (RPA). The validity of this calculation will be commented below.

At one-loop level, the spinon-gauge coupling $\mathcal{L}_1$ produces two diagrams for the photon self-energy, as shown in Fig. 5.2. Due to gauge invariance, the photon self-energy must (i) vanish when $q \to 0$ and (ii) satisfy the Ward identity at small q. We prove these properties at one-loop level in Appendix B.1. We show that, at $q = 0$, the two diagrams of Fig. 5.2, the "vacuum polarization bubble" and the "tadpole", cancel each other. Furthermore, at $q \neq 0$, the corrections to the tadpole are only $O(q^2)$, while, as we will show below, there are corrections to the vacuum polarization bubble at a lower order of q. Therefore, at leading order in q, the photon self-energy can be identified as the q-dependent part of the vacuum polarization bubble. Ignoring a minus sign resulting from the fermion loop, the vacuum polarization bubble reads

$$\Pi^{\mu\nu}(q) = \int \frac{d^4k}{(2\pi)^4} \mathrm{Tr}\left[\Gamma^\mu(\boldsymbol{k})G_0(k+\frac{q}{2})\Gamma^\nu(\boldsymbol{k})G_0(k-\frac{q}{2})\right], \tag{5.41}$$

208

where $G_0(k) = \frac{1}{ik_0 - \mathcal{H}(\boldsymbol{k})}$ is the Green's function for the bare spinon Lagrangian $\mathcal{L}_0$, and the vertex Γ^μ obtained from Eq. (5.38) has the following form:

$$
\begin{aligned}
\Gamma^0(\boldsymbol{k}) &= i1_{2\times2}, & \Gamma^1(\boldsymbol{k}) &= \sin k_1(\sigma^2 - \sigma^3), \\
\Gamma^2(\boldsymbol{k}) &= \sin k_2(\sigma^3 - \sigma^1), & \Gamma^3(\boldsymbol{k}) &= \sin k_3(\sigma^1 - \sigma^2).
\end{aligned}
\tag{5.42}
$$

While the anisotropic forms of the Hamiltonian [Eq. (5.36)] and the vertices [Eq. (5.42)] make it difficult to evaluate the polarization in Eq. (5.41) exactly, it is physically clear that there are two distinct momentum regions in the BZ. These two regions, the star region and the gapped region away from the star, result in different scalings of the photon self energy. The contribution from the gapped region away from the nodal lines, Π_1, is $O(q^2)$, as can be directly seen from expanding the polarization in Eq. (5.41). The final result for Π_1 is constrained by the Ward identity (see Appendix B.1) to have the form of the bare Maxwell term in Eq. (5.37), hence it simply renormalizes the corresponding coupling constant g. In contrast, the contribution from the star region, Π_0, is linear in q *with logarithmic corrections*. This means that Π_0 completely dominates over Π_1 at low energy and small momentum. In the following, we focus on the calculation of Π_0.

We first provide an intuitive understanding for the linear scaling $\Pi_0 \sim |\boldsymbol{q}|$ and the existence of logarithmic corrections. In the BZ, each plane perpendicular to the nodal direction has a Dirac dispersion $E = v|\boldsymbol{k}_\perp|$ with a Dirac velocity $v = \sqrt{3}\sin k_\parallel$ that is a sinusoidal function of the nodal line momentum $(\varsigma_1, \varsigma_2, \varsigma_3)k_\parallel$. Restricted to such a plane, the spinon-gauge coupled system can be viewed as a QED3. The vacuum polarization diagram in QED3 scales linearly in $q_\perp = (q_0, v\boldsymbol{q}_\perp)$ as

$$
\Pi_{\text{QED3}}^{ab} = \sqrt{q_\perp^2}\left(\delta^{ab} - \frac{q_\perp^a q_\perp^b}{q_\perp^2}\right), \quad a = 0, 1, 2.
\tag{5.43}
$$

The polarization of one nodal line branch can therefore be obtained by considering copies of QED3 interacting with each other. To the leading order of q, these QED3 copies are decoupled, and we find that the polarization in the star region, Π_0, summed over these QED3 copies and over different line branches, scales linearly with q. Note, however, that this picture is oversimplified as the vanishing Dirac velocity at the Γ point would lead to unphysical divergence in the limit of $q_0/|\boldsymbol{q}| \to 0$ when integrating over copies of QED3:

$$\int_0^\pi dk_\parallel \Pi_{\text{QED3}}^{00} \sim \int_0^\pi dk_\parallel \frac{1}{\sqrt{q_0^2 + \boldsymbol{q}_\perp^2 \sin^2 k_\parallel}} \xrightarrow{q_0/|\boldsymbol{q}_\perp| \to 0} \text{divergent!} \tag{5.44}$$

In reality, the quadratic dispersion near the Γ point takes over as the Dirac dispersion flattens, which removes the unphysical divergence and introduces a small momentum cutoff θ_0 for the nodal line momentum $k_\parallel$. The cutoff is determined by the criterion that the Dirac dispersion becomes comparable to the quadratic dispersion around the Γ point, $v|\boldsymbol{k}_\perp| \sim \boldsymbol{k}^2$, which gives $\theta_0 \sim |\boldsymbol{k}|$ and thus changes the integration range in Eq. (5.44) as

$$\int_0^\pi dk_\parallel \to \int_{|\boldsymbol{q}|}^{\pi - |\boldsymbol{q}|} dk_\parallel. \tag{5.45}$$

This cutoff introduces a logarithmic correction to the 00, $0i$ and $i0$ components of the polarization tensor.

To understand the scaling behavior of Π_0 in a more rigorous manner, we provide in Appendix B.2 the scaling analysis of the vacuum polarization tensor in Eq. (5.41) for $q_0/|\boldsymbol{q}| \ll 1$. We find that

$$\Pi_0^{00} \sim -|\boldsymbol{q}| \ln \left(\frac{1}{\boldsymbol{q}^2 + \omega^2/\boldsymbol{q}^2} \right) + |\boldsymbol{q}| f_{00}(q_0/\boldsymbol{q}^2), \tag{5.46a}$$

$$\Pi_0^{0i} \sim iq_0 \ln \left(\frac{1}{\boldsymbol{q}^2 + \omega^2/\boldsymbol{q}^2} \right) + \boldsymbol{q}^2 f_{0i}(q_0/\boldsymbol{q}^2), \tag{5.46b}$$

$$\Pi_0^{ij} \sim |\boldsymbol{q}| + |\boldsymbol{q}|^3 f_{ij}(q_0/\boldsymbol{q}^2), \tag{5.46c}$$

where, in each expression, the first and the second terms denote the contributions from the nodal lines and the region near the Γ point, respectively, while $f_{00}(x)$, $f_{0i}(x)$, and $f_{ij}(x)$ are regular functions for any $0 < |x| < 1$. We see that, in all components of the polarization tensor, the contribution from the Γ region is subdominant compared to that from the nodal lines themselves.

The analysis in the preceding two paragraphs allows us to obtain the analytic form of the dominant contribution to the photon self-energy by performing a "QED3 type" calculation for the nodal lines. The detailed calculation can be found in Appendix B.2. Here we stress that the "QED3 type" calculation performed here must be understood with caution. In the usual perturbative calculation of QED3, a large parameter N (the number of fermion flavors) is introduced to ensure the validity of the RPA and the convergence in the infrared (IR) limit. While we introduce no explicit large parameter N in our calculation, such a large N should be understood to be present whenever needed, and we hope that the result can be analytically continued to the $N = 1$ case.

With this caution in mind, we present the final result here: at the leading order of q, the photon self-energy is

$$\Pi(iq_0, \boldsymbol{q}) = \sum_{\varsigma_1, \varsigma_2, \varsigma_3 = \pm 1} \Pi_{\varsigma_1, \varsigma_2, \varsigma_3}(iq_0, \boldsymbol{q}), \tag{5.47}$$

where $\Pi_{\varsigma_1, \varsigma_2, \varsigma_3}(iq_0, \boldsymbol{q})$ is the contribution from the nodal line branch $(\varsigma_1, \varsigma_2, \varsigma_3)$. The

individual contributions are

$$\Pi_{\varsigma_1,\varsigma_2,\varsigma_3}(iq_0, \boldsymbol{q}) = \frac{\sqrt{q_0^2}}{16\sqrt{3}\pi} \begin{pmatrix} \frac{Q^2}{q_0^2}F & -\varsigma_1\frac{Q_1}{q_0}F & -\varsigma_2\frac{Q_2}{q_0}F & -\varsigma_3\frac{Q_3}{q_0}F \\ -\varsigma_1\frac{Q_1}{q_0}F & D_{11}^+ & -\varsigma_1\varsigma_2 D_{33}^- & -\varsigma_1\varsigma_3 D_{22}^- \\ -\varsigma_2\frac{Q_2}{q_0}F & -\varsigma_1\varsigma_2 D_{33}^- & D_{22}^+ & -\varsigma_2\varsigma_2 D_{11}^- \\ -\varsigma_3\frac{Q_3}{q_0}F & -\varsigma_1\varsigma_3 D_{22}^- & -\varsigma_2\varsigma_3 D_{11}^- & D_{33}^+ \end{pmatrix}, \qquad (5.48)$$

with

$$D_{ii}^+ = (1 + \frac{Q_{ii}^2}{Q^2})F + (1 - \frac{Q_{ii}^2}{Q^2})E, \quad D_{ii}^- = \left[(\frac{1}{2} - \frac{Q_{ii}^2}{Q^2})F + (\frac{1}{2} + \frac{Q_{ii}^2}{Q^2})E \right], \quad i = 1, 2, 3,$$
$$(5.49)$$

where

$$F = F(\pi - |\boldsymbol{q}|, -Q^2/q_0^2) - F(|\boldsymbol{q}|, -Q^2/q_0^2), \quad E = E(\pi - |\boldsymbol{q}|, -Q^2/q_0^2) - E(|\boldsymbol{q}|, -Q^2/q_0^2),$$
$$(5.50)$$

are the incomplete elliptic integrals of the first and second kinds, respectively, with elliptic modulus Q/q_0, and

$$Q_1 = 2\varsigma_1 q_1 - \varsigma_2 q_2 - \varsigma_3 q_3, \quad Q_2 = -\varsigma_1 q_1 + 2\varsigma_2 q_2 - \varsigma_3 q_3, \quad Q_3 = -\varsigma_1 q_1 - \varsigma_2 q_2 + 2\varsigma_3 q_3,$$
$$Q_{11}^2 = Q^2 - 3(\varsigma_2 q_2 - \varsigma_3 q_3)^2, \quad Q_{22}^2 = Q^2 - 3(\varsigma_3 q_3 - \varsigma_1 q_1)^2, \quad Q_{33}^2 = Q^2 - 3(\varsigma_1 q_1 - \varsigma_2 q_2)^2,$$
$$Q^2 = \frac{1}{3}(Q_1^2 + Q_2^2 + Q_3^2).$$
$$(5.51)$$

For each branch $(\varsigma_1, \varsigma_2, \varsigma_3)$, $\Pi_{\varsigma_1,\varsigma_2,\varsigma_3}(iq_0, \boldsymbol{q})$ has two zero eigenvalues corresponding to eigenvectors (q_0, q_1, q_2, q_3) and $(0, \varsigma_1, \varsigma_2, \varsigma_3)$; the former one is the longitudinal four-momentum vector. The remaining two nonzero eigenvalues, $\frac{\sqrt{3}}{32\pi}\sqrt{q_0^2}E$ and $\frac{\sqrt{3}}{32\pi}\frac{q_0^2 + \frac{1}{3}Q^2}{\sqrt{q_0^2}}F$, are nondegen-erate; they correspond to one "transverse" eigenvector $(0, \varsigma_1(\varsigma_2 q_2 - \varsigma_3 q_3), \varsigma_2(\varsigma_3 q_3 - \varsigma_1 q_1), \varsigma_3(\varsigma_1 q_1 - \varsigma_2 q_2))$ and one "longitudinal" eigenvector $(-\frac{Q^2}{q_0}, \varsigma_1 Q_1, \varsigma_2 Q_2, \varsigma_3 Q_3)$, where "transverse" and "lon-gitudinal" are understood with respect to the spatial three-momentum (Q_1, Q_2, Q_3). The

212

nondegeneracy here implies that the boost symmetry of the QED3 is broken in our theory, which can be traced back to the "boost symmetry breaking" of the vertices in Eq. (5.42).

The photon self-energy $\Pi(iq_0, \boldsymbol{q})$ contains the longitudinal four-momentum vector as an eigenvector corresponding to eigenvalue zero, which ensures that the Ward identity $q_\mu \Pi^{\mu\nu} = 0$ is preserved. However, since the four star branches have different three-momenta (Q_1, Q_2, Q_3), $\Pi(iq_0, \boldsymbol{q})$ can no longer be decomposed into longitudinal and transverse modes.

Suppose $e_i(iq_0, \boldsymbol{q})$ with $i = 1, 2, 3$ are the three nonzero eigenvalues of $\Pi(iq_0, \boldsymbol{q})$ that correspond to the eigenvectors $v_i(iq_0, \boldsymbol{q})$. The dressed photon Green's function is then

$$D^{\mu\nu}(iq_0, \boldsymbol{q}) = \sum_{i=1}^{3} \frac{P_i^{\mu\nu}}{\frac{1}{g^2}q^2 + e_i(q)} + \xi \frac{q^\mu q^\nu}{q^4}, \tag{5.52}$$

where $P_i^{\mu\nu} = v_i^\mu v_i^\nu$ are the projectors for the $i = 1, 2, 3$ modes. The last term results from the gauge fixing term $\mathcal{L}_{gf}$ in Eq. (5.40a).

We remind the reader that the photon self-energy calculated here is for zero temperature. A finite temperature calculation can also be considered following Ref. [132]. We leave such a calculation to future work.

5.4.4 Photon contribution to thermodynamics

We now proceed to calculate the photon contribution to the thermodynamics. The photon free energy reads

$$F = -\frac{1}{2\beta} \sum_n \int \frac{d^3\boldsymbol{q}}{(2\pi)^3} \left(\ln \det D(i\omega_n, \boldsymbol{q}) + 2\ln \beta^2(\omega_n^2 + \boldsymbol{q}^2) \right), \tag{5.53}$$

where ω_n is the Matsubara frequency and D is the photon Matsubara Green's function. The second term of F comes from the fictitious free energy for the ghost fields η_k in Eq. (5.40b). Half of this fictitious term will cancel the contribution from the gauge fixing term $\xi q^\mu q^\nu / q^4$ in the photon Green's function, while the other half will contribute a positive term $\propto T^4$ to the free energy. Such a term would cancel out the longitudinal mode in the free gauge theory, however, as we will see, this is no longer the case in the full theory when the photons are coupled to the spinons. Converting the Matsubara sum to a contour integral, we then obtain

$$F = \frac{\pi^2}{90}T^4 + \sum_{i=1}^{3} \int_{-\infty}^{+\infty} \frac{d\omega}{2\pi} \frac{1}{e^{\beta\omega} - 1} \int \frac{d^3 q}{(2\pi)^3} \tan^{-1}\left(\frac{-\omega 0^+ + \operatorname{Im} e_i^R(\omega, \boldsymbol{q})}{-\omega^2 + \boldsymbol{q}^2 + \operatorname{Re} e_i^R(\omega, \boldsymbol{q})}\right), \quad (5.54)$$

where $e_i^R(\omega, \boldsymbol{q})$ are the eigenvalues of the retarded polarization $\Pi^R(\omega, \boldsymbol{q}) = \Pi(iq_0 \to \omega^+, \boldsymbol{q})$ with the notation $\omega^+ = \omega + i0^+$. Note that the dressed photon Green's function corresponds to zero temperature and that the temperature dependence of the free energy comes entirely from the Boltzmann function. The momentum-frequency integral in the free energy can be separated into two regions that give different scaling behaviors.

The "dynamic" region: $|\omega|/|\boldsymbol{q}| \geq 2$. In this region, we have $\frac{Q^2}{\omega^2} \leq \frac{4\boldsymbol{q}^2}{\omega^2} \leq 1$, and the elliptic functions E and F are both real. The eigenvalues $e_{1,2,3}^R$ are then purely imaginary due to the prefactor $\sqrt{q_0^2} \to -i\omega$ on the upper half plane in Eq. (5.48). Furthermore, the eigenvalues are of the same amplitude:

$$e_{1,2,3}^R \to -\frac{i\operatorname{sgn}(\omega)}{4\sqrt{3}\pi} \quad \text{when} \quad |\omega|/|\boldsymbol{q}| \to \infty, \quad (5.55)$$

214

which is much larger than $-\omega^2 + \boldsymbol{q}^2$ at small frequency. We then have $\tan^{-1}\left(\frac{\mathrm{Im}\, e_i^R(\omega, \boldsymbol{q})}{-\omega^2 + \boldsymbol{q}^2}\right) \sim$
$-\frac{\pi}{2}\mathrm{sgn}(\omega)$ and, hence, the free energy scales with temperature as

$$F_{\mathrm{dyn}}(T) \sim 3 \int_{-\infty}^{+\infty} \frac{d\omega}{2\pi} \frac{1}{e^{\beta\omega}-1} \frac{\frac{4\pi}{3}}{(2\pi)^3} \frac{\omega^3}{8}\left(-\frac{\pi}{2}\right) = -\frac{\pi^2}{480}T^4, \tag{5.56}$$

where we have dropped an unphysical part $F_{\mathrm{dyn}}(0)$ which is divergent and temperature independent. One notices that the free energy (and other thermodynamic properties, such as the entropy and the specific heat) of each dressed photon is a fraction of that of a free photon, which can be viewed as being contributed by a fractional degree of freedom. Such a phenomenon also appears at infinite coupling of large N QED3 [131].

The "static" region: $|\omega|/|\boldsymbol{q}| \ll 1$. In this region, by using the asymptotic forms of the elliptic functions, the polarization $\Pi^{\mu\nu}$ in Eq. (5.48) agrees with the general scaling form in Eq. (5.46). The Ward identity $\omega\Pi^{00} + q_i\Pi^{i0} = 0$ suggests that $\Pi^{0i} \sim \frac{|\omega|}{|\boldsymbol{q}|}\Pi^{00} \ll \Pi^{00}$. Therefore, the Π^{00} component is decoupled from the 3×3 block of the polarization tensor with spatial indices and is identified with one of the eigenvalues, e_3^R. The remaining eigenvalues $e_{1,2}^R$ then correspond to the two transverse polarization modes. All three eigenvalues $e_{1,2,3}^R$ are generally complex, and we find the following scaling form for them:

$$e_{1,2}^R \sim -i\omega\left[E\left(0, \frac{2\boldsymbol{q}^2}{(\omega^+)^2}\right) - F\left(0, \frac{2\boldsymbol{q}^2}{(\omega^+)^2}\right)\right] \sim |\boldsymbol{q}| - i\frac{\omega^2}{|\boldsymbol{q}|}\mathrm{sgn}(\omega), \tag{5.57a}$$

$$e_3^R \sim i\frac{\boldsymbol{q}^2}{\omega}\left[F\left(\pi - \theta_0, \frac{2\boldsymbol{q}^2}{(\omega^+)^2}\right) - F\left(\theta_0, \frac{2\boldsymbol{q}^2}{(\omega^+)^2}\right)\right]$$

$$\xrightarrow{\theta_0 \sim |\boldsymbol{q}|} |\boldsymbol{q}|\ln\left(\frac{1}{\max\{\frac{|\omega|}{|\boldsymbol{q}|}, |\boldsymbol{q}|\}}\right) + i|\boldsymbol{q}|u\left(\frac{|\omega|}{|\boldsymbol{q}|}\right)\mathrm{sgn}(\omega)\theta\left(\frac{|\omega|}{|\boldsymbol{q}|} - |\boldsymbol{q}|\right), \tag{5.57b}$$

where $u(\frac{|\omega|}{|\boldsymbol{q}|})$ scales as $u(x) \sim \text{const.} + x^2$. The eigenvalues of the transverse modes, $e^R_{1,2}$, do not diverge near Γ or L, therefore the cutoff θ_0 has been set to zero.

In writing these asymptotic expressions, we have neglected the angular dependence in the momentum. The validity of this approximation has been numerically verified. For $|\omega| > \boldsymbol{q}^2$, the physical modes $i = 1, 2, 3$ lead to a dressed photon Green's function of the form

$$D^{\mu\nu} = \frac{P_1^{\mu\nu} + P_2^{\mu\nu}}{\frac{1}{g^2}(\boldsymbol{q}^2 c^2 - \omega^2) + \frac{1}{2\sqrt{3}\pi}(|\boldsymbol{q}| - i\,\text{sgn}(\omega)\frac{\omega^2}{|\boldsymbol{q}|})}$$
$$+ \frac{P_3^{\mu\nu}}{\frac{1}{g^2}(\boldsymbol{q}^2 c^2 - \omega^2) + \frac{1}{2\sqrt{3}\pi}(|\boldsymbol{q}|\ln\frac{|\boldsymbol{q}|}{|\omega|} + i\,\text{sgn}(\omega)|\boldsymbol{q}|)}. \tag{5.58}$$

Note that the imaginary parts have opposite signs and that the $P_3^{\mu\nu}$ term will contribute negatively to the specific heat. The photon "bare" velocity c and the coupling g come from integrating out the gapped spinon bands at higher energies. The "bare" velocity c should be comparable to the mean Dirac velocity of the nodal line spinons, $c \sim 1$, and we take $g \lesssim 1$ following Ref. [42]. Therefore, at small $\boldsymbol{q}$, we have $|\boldsymbol{q}| > \boldsymbol{q}^2 > \omega^2$, and we only keep $|\boldsymbol{q}|$ in the real part. The free energy can then be written as $F_{\text{sta}} = F^{1,2}_{\text{sta}} + F^3_{\text{sta}}$, where the contributions $F^{1,2}_{\text{sta}}$ and F^3_{sta} correspond to the eigenvalues $e^R_{1,2}$ and e^R_3, respectively:

$$F^{1,2}_{\text{sta}} = -2\int_0^\Lambda \frac{q^2 dq}{2\pi^2}\int_0^{|\boldsymbol{q}|}\frac{d\omega}{2\pi}\frac{1}{e^{\beta\omega}-1}2\tan^{-1}\frac{\omega^2}{\boldsymbol{q}^2}, \tag{5.59a}$$

$$F^3_{\text{sta}} = -2\int_0^\Lambda \frac{q^2 dq}{2\pi^2}\int_{\boldsymbol{q}^2}^{<|\boldsymbol{q}|}\frac{d\omega}{2\pi}\frac{1}{e^{\beta\omega}-1}\tan^{-1}\frac{1}{\ln\frac{|\omega|}{|\boldsymbol{q}|}}, \tag{5.59b}$$

where the dimensionless parameter Λ is the upper momentum cutoff at which the nodal

line approximation becomes invalid. Setting $x = \omega/|\boldsymbol{q}|$ in $F_{\text{sta}}^{1,2}$, we obtain

$$F_{\text{sta}}^{1,2} \sim -\int_0^\Lambda q^3 dq \int_0^1 dx \frac{x^2}{e^{\beta|\boldsymbol{q}|x} - 1} \sim -\int_0^\Lambda dq q^3 F\left(\frac{|\boldsymbol{q}|}{T}\right), \tag{5.60}$$

where $F(y) = \int_0^1 dx \frac{x^2}{e^{yx}-1}$. For $y \to 0$, we have $F(y) = \frac{1}{2y} + O(1)$, while for $y \to +\infty$, the upper limit can be extended to $+\infty$, and we have $F(y) \to 2\zeta(3)/y^3$. Therefore, at low temperatures, $T < \Lambda$, we have $F_{\text{sta}}^{1,2} \sim -2(\int_0^T dq q^3 \frac{T}{q} + \int_T^\Lambda dq q^3 \frac{T^3}{q^3}) \sim -\Lambda T^3 + O(T^4)$, and the leading contribution to free energy is $-\Lambda T^3$.

For the remaining contribution F_{sta}^3, we perform the following transformation:

$$F_{\text{sta}}^3 \xrightarrow{\omega \equiv q^{\alpha+1}} -2\int_0^\Lambda q^2 dq \int_1^{\alpha_0 > 0} \frac{q^{\alpha+1}}{\alpha(e^{\beta q^{\alpha+1}} - 1)} d\alpha$$

$$\xrightarrow{z \equiv \beta q^{\alpha+1}} 2\int_{\alpha_0 > 0}^1 \frac{d\alpha}{\alpha(\alpha+1)} T^{\frac{\alpha+4}{\alpha+1}} \int_0^{\frac{\Lambda^{\alpha+1}}{T}} \frac{z^{\frac{3}{\alpha+1}}}{e^z - 1} dz. \tag{5.61}$$

Numerics show that F_{sta}^3 is independent of α_0 whenever $\alpha_0 < 0.5$. Note also that, when $z \gg 1$, we can approximate $e^z - 1 \sim e^z$, meaning that, at large z, the integral will contribute to the free energy with an exponentially small term $e^{-\frac{1}{T}}$. Therefore, we can safely extend the upper limit to infinity, and the integral in z then gives

$$\int_0^\infty \frac{z^{\frac{3}{\alpha+1}}}{e^z - 1} dz = \Gamma\left(\frac{4+\alpha}{1+\alpha}\right) \text{Li}_{\frac{4+\alpha}{1+\alpha}}(1). \tag{5.62}$$

Since it is approximately true for $0.5 < \alpha < 1$ that

$$\frac{\Gamma\left(\frac{4+\alpha}{1+\alpha}\right) \text{Li}_{\frac{4+\alpha}{1+\alpha}}(1)}{\alpha(\alpha+1)} \sim \frac{0.84}{\alpha^2}, \tag{5.63}$$

the contribution F_{sta}^3 takes the leading-order form

$$F_{\text{sta}}^3 \sim \int_{\alpha_0}^1 \frac{1}{\alpha^2} T^{\frac{\alpha+4}{\alpha+1}} d\alpha \sim -\frac{T^{\frac{5}{2}}}{\ln T} + O\left(\frac{T^{\frac{5}{2}}}{\ln^2 T}\right). \tag{5.64}$$

From all the analysis above, we conclude that the contribution F_{sta}^3 dominates the

dressed photon free energy at low temperature. Note that this dominant term contributes negatively to the specific heat.

5.4.5 Final result for the specific heat

At the non-interacting level, the temperature scaling of the spinon free energy can be obtained from the spinon density of states by a simple power counting. The spinons near the nodal lines and the Γ point have densities of states $g(\epsilon) \propto \epsilon$ and $g(\epsilon) \propto \sqrt{\epsilon}$, and contribute to the specific heat as $c_v \propto T^2$ and $c_v \propto T^{\frac{3}{2}}$, respectively. The final result for specific heat is then

$$c_v \sim T^{\frac{3}{2}} + \frac{T^{\frac{3}{2}}}{\ln T} + \text{subleading terms.} \tag{5.65}$$

Compared to a U(1) QSL with gapped matter fields, the leading term in the specific heat has a lower power law exponent, $c_v \propto T^{3/2}$, while the subleading term has a negative contribution at low temperature. Since the Dirac velocity v is related to the pyrochlore spin exchange J by $v \sim Ja/\hbar$, the small value of J (typically a few meV) indicates that this $T^{3/2}$ scaling likely dominates at low temperature over non-magnetic contributions and may serve as strong evidence for the observation of a nodal star spin liquid.

5.5 Discussion and outlook

5.5.1 Summary

In this chapter, we obtain the complete classification of spin–orbit-coupled spin liquids with either $\mathbb{Z}_2$ or U(1) gauge structure on the pyrochlore lattice, within the PSG framework for Abrikosov fermions. We find that there are at most 18 U(1) and 28 $\mathbb{Z}_2$ PSG classes with full pyrochlore space group symmetry, and that the number of classes reduces to 16 for U(1) and increases to 48 for $\mathbb{Z}_2$ if time reversal symmetry is further imposed. We present the explicit form of the mean-field Hamiltonian for each PSG class upon gauge fixing. We also show that, in the U(1) case, several classes of mean-field ansätze possess robust spinon zero modes along high symmetry lines in the Brillouin zone and that these nodal lines are protected by the projective screw symmetry. A low energy effective theory for the nodal line spinons coupled to U(1) gauge fields is given. Finally, we calculate the spinon contribution to the photon self energy at one loop level and study the thermodynamics of the dressed photon within the RPA approximation. We find that the most dominant contributions to the specific heat are $T^{3/2}$ from the bare spinons and $T^{3/2}/\ln T$ from the dressed photons.

5.5.2 $\mathbb{Z}_2$ PSGs from fermionic and bosonic partons

We now discuss the relationship between the $\mathbb{Z}_2$ PSGs obtained from fermionic and bosonic partons. In a previous work [94], we employed Schwinger bosons to classfy

$\mathbb{Z}_2$ spin liquids on the pyrochlore lattice with full lattice and time reversal symmetries. There, we found 16 distinct PSG classes and labeled them by four $\mathbb{Z}_2$ parameters, n_1, n_{ST_1}, $n_{\overline{C}_6 S}$, and $n_{\overline{C}_6}$, that are the bosonic counterparts of the χ's in the current work. The other IGG parameters are all related to these four parameters, for example, we have $n_{S\overline{C}_6} = n_1 + n_{\overline{C}_6} + n_{ST_1}$, $n_{\mathcal{T}\overline{C}_6} = n_{\overline{C}_6}$, and $n_{\mathcal{T}S} = n_1 + n_{ST_1}$.

By comparing these bosonic quantum numbers with the fermionic ones, we see that each bosonic class corresponds to an appropriate class in the fermionic PSG with lattice and time reversal symmetries. In fact, the bosonic classes all have their counterparts already in the fermionic PSG with only pyrochlore space group symmetry through the corresponding $\mathbb{Z}_2$ quantum numbers ($\eta_{S\overline{C}_6} = \eta_1 \eta_{ST_1} \eta_{\overline{C}_6}$). The fermionic PSG, however, has a larger number of classes, some of which do not have bosonic counterparts. From Appendix A.7, it is seen that the additional fermionic classes exist due to the violation of the condition $\eta_{S\overline{C}_6} = \eta_1 \eta_{ST_1} \eta_{\overline{C}_6}$ or as a result of multiple solutions to the SU(2) equation (which are distinguished by an additional discrete parameter j). Upon imposing time reversal symmetry, the number of fermionic classes increases from 28 to 48, and the 16 bosonic classes still have 16 counterparts among them.

Physically, the bosonic and fermionic PSGs are supposed to describe fractionalized excitations with bosonic and fermionic statistics, respectively: the bosonic and fermionic spinons. This has been well understood for 2D $\mathbb{Z}_2$ QSLs with topological order. In the 2D case, the elementary (fractionalized) excitations are bosonic spinons, fermionic spinons, and visons. A fermionic spinon can be viewed as a bound state of a bosonic

spinon and a vison, which induces a corresponding product rule between the vison, boson, and fermion PSGs. It was argued in Ref. [98] on general grounds that the classes common in bosonic and fermionic PSGs realize gapped $\mathbb{Z}_2$ symmetric spin liquids, while the additional classes in the fermionic PSG realize symmetry protected gapless $\mathbb{Z}_2$ spin liquids. However, it is not clear whether the claim directly applies to our case. Concretely, one can compare the independent nonzero mean-field parameters at a given bond level between the corresponding bosonic and fermionic classes, and the numbers do not always match. The possible reasons are that (i) the required assumption of U(1) spin symmetry for the proof of Ref. [98] is absent in our case, and (ii) the dimensionality is different in our case. Indeed, the dimensional augmentation to 3D may fundamentally change the correspondence between the bosonic and fermionic PSGs since the visons are now line-like objects and do not straightforwardly relate bosonic and fermionic spinons to each other.

Understanding the relation between the fermionic and bosonic PSG classifications is an important goal. In addition to extracting the statistics of the fractionalized excitations discussed above, it can be used to map out the phases proximate to a QSL and the possible transition types. Indeed, the bosonic representation has the fundamental advantage that it can describe a transition to a magnetically ordered state via the condensation of bosonic spinons, while such a transition cannot be easily described in the fermionic representation. Therefore, we hope to establish a clearer understanding of this important relation in a future work.

5.5.3 $\mathbb{Z}_2$ and U(1) PSGs using fermionic partons

The $\mathbb{Z}_2$ mean-field ansätze have spinon pairing terms which manifestly break the U(1) symmetry down to its subgroup $\mathbb{Z}_2$. However, in special cases, when some of the mean-field parameters are switched off, the $\mathbb{Z}_2$ ansätze may possess an enlarged symmetry. If this enlarged symmetry is (or contains) U(1), the ansatz with parameters switched off belongs to some "root" U(1) PSG class and the $\mathbb{Z}_2$ PSG can be viewed as being derived from this U(1) PSG class by "gauge symmetry breaking" via the Higgs mechanism. The simplest way one can enlarge $\mathbb{Z}_2$ symmetry to U(1) is by switching off all the pairing parameters in a $\mathbb{Z}_2$ ansatz. If this can be consistently done without violating the PSG, we obtain an explicit U(1) ansatz with only hopping terms. For example, if we take the non-projective $\mathbb{Z}_2$ class (00)–(000) and naively switch off the pairings, we get exactly the U(1) non-projective mean-field state 0–(00)–(00).

However, the correspondence between a $\mathbb{Z}_2$ and a U(1) ansatz may not always be apparent and may be masked by the different gauge fixing conventions used for the $\mathbb{Z}_2$ and the U(1) ansätze. For example, a mean-field Hamiltonian with only singlet pairing terms (a_p and its equivalents at further neighbor bonds) also has a U(1) symmetry. This pairing U(1) symmetry can be converted to the usual hopping U(1) symmetry by an appropriate gauge transformation. For $\mathbb{Z}_2$ classes with time reversal and $(\chi_{\mathcal{T}\overline{C}_6}, \chi_{\mathcal{T}S}, k) = (0,0,3)$ (see Table 5.2), such a gauge transformation can be chosen as

$$W = e^{-i\frac{\pi}{4}\sigma^2},\tag{5.66}$$

which transforms the time reversal PSG according to $W_{\mathcal{T}}(\boldsymbol{r}_\mu) = i\sigma^3 \rightarrow WW_{\mathcal{T}}(\boldsymbol{r}_\mu)W^\dagger =$

$i\sigma^1$. The mean-field parameters therefore transform as

$$i(\mathrm{Re}a\sigma^1 + \mathrm{Im}b\sigma^2) \to i(-\mathrm{Re}a\sigma^3 + \mathrm{Im}b\sigma^2), \tag{5.67}$$

i.e., the real part of the pairing term is transformed into a hopping term, which is consistent with Eq. (5.12). In this case, keeping only the real part of the singlet pairing will recover a U(1) ansatz.

In closing this subsection, we point out that a general mapping between $\mathbb{Z}_2$ and U(1) pyrochlore PSG classes is still lacking. Understanding such a relation will be important in mapping out phase diagrams containing various spin liquids and magnetic orders.

5.5.4 The non-projective U(1) class: topological insulator

Let us examine the topological properties of the U(1) PSG class 0–(00)–(00): this is the "trivial" class in which symmetries are realized linearly (i.e., nonprojectively). This symmetry structure also applies to physical electrons instead of spinons: it can describe ordinary, non-fractionalized itinerant electrons on the pyrochlore lattice. Such systems have been intensely studied in the context of pyrochlore iridates [80, 52, 168]. There, the most striking prediction from theory is the existence of a topological insulator phase, which occupies a finite volume in the phase space spanned by spin–orbit couplings up to NNN [80, 52, 168].

The most complete of these prior works [80, 52, 168] is Ref. [168], which determined the general form of the Hamiltonian up to second neighbor hoppings. Here, we provide an explicit mapping between the parameters used there and those used in Table 5.3:

there are in total two real independent parameters (t_1, t_2) for the NN bonds and three real independent parameters (t'_1, t'_2, t'_3) for the NNN bonds [168], which are related to our PSG results by $(t_1, t_2, t'_1, t'_2, t'_3) = (\text{Im}a, \text{Im}c, \text{Im}A, \text{Im}B + \text{Im}D, \text{Im}B - \text{Im}D)$. This serves as a partial check of our classification and allows the results in Refs [80, 52, 168] to directly apply in the PSG context.

Given the existence of a topological insulator phase in the "trivial" U(1) PSG class, it is reasonable to believe that other classes may also support nontrivial topological phases. Among them, it would be of specific interest to identify those that are protected by the *projectiveness* of the symmetry and would appear only in systems with fractionalized degrees of freedom.

5.5.5 Future directions

The mean-field ansätze for the PSG classes listed in this work provide abundant ground state candidates for model spin Hamiltonians on the pyrochlore lattice. In the works reported so far, the monopole flux state [23] has the lowest energy as a variational mean-field ansatz for the pyrochlore Heisenberg model. The monopole flux state does not belong to our classification with the full pyrochlore lattice symmetry since it spontaneously breaks lattice inversion. An interesting question is then whether any of the fully symmetric states may be energetically favored by the Heisenberg model, and if not, what is the physical reason for the energy being lowered by spontaneous symmetry breaking. In this regard, it is interesting to study the PSG classification of chiral spin liquids on

the pyrochlore lattice, in which certain space group symmetries are replaced by them composed with time reversal symmetries. Furthermore, since rare-earth pyrochlore materials are intrinsically spin–orbit coupled, it is also natural to take our PSG ansätze as variational states for the full spin–orbit coupled pyrochlore exchange model [133]. These questions are addressed in an ongoing work that will be reported elsewhere.

One outcome of this work is the realization, in several PSG classes, of the nodal star U(1) spin liquid, which represents a new family of pyrochlore U(1) spin liquids beyond the known prototypes, whose low energy nodal structure is protected by the pyrochlore space group symmetries. We point out that the proof of the symmetry protected nature of the nodal lines also applies to several classes of chiral spin liquids, including the monopole flux state [23]. In the present work, our main focus has been on the spinon corrections to the gauge field. Subsequent questions – such as how the gauge field feeds back into the spinons and how the vertices receive corrections – have been outside the scope of this work and require a more involved calculation. These calculations may reveal additional contributions to the thermodynamic properties and will provide insights for another important observable, the spin susceptibility. Even at the non-interacting level, the nodal line spinons will lead to spectral features that should be observable in, e.g., neutron scattering experiments. For example, a broad low energy continuum should be seen along appropriate high-symmetry planes of the Brillouin zone. The observation of such signatures may serve as direct evidence for a pyrochlore spin liquid state. We leave the study of these aspects of the nodal star U(1) spin liquid to a future work.

There are also several more broad directions to be explored. The pyrochlore PSG may be studied from the perspective of symmetry protected crystalline insulators and symmetry enriched topological orders. Apart from the case of the non-projective U(1) ansätze mentioned in the preceding subsection, the topological aspects of the spinon bands have not been investigated in this work and deserve further study. Another future direction is the stability of the gapless states beyond the mean field approximation. While at the latter level, we have proven that the nodal line is symmetry protected, it is not clear if it remains robust against symmetry allowed spinon interactions. In this regard, it would be interesting to look for criteria that forbid a single gapped many-body ground state of the spinon Hamiltonian from appearing in the presence of spinon interactions and full pyrochlore symmetry, similar to the proposals of Ref. [98]. In the context of $\mathbb{Z}_2$ QSLs, a related theme would be to generalize the Lieb-Schultz-Mattis theorem to the pyrochlore lattice and other geometrically frustrated 3D lattice types. The screw symmetry, which is crucial to the nodal star spin liquids, is an instance of nonsymmorphic symmetry and, in this regard, it is compelling to connect our results with recent works, such as Refs. [164, 39] and especially Ref. [156] (considering that the classification result for the pyrochlore space group there is missing).

Appendix A

Pyrochlore PSG

A.1 Lattice and time reversal symmetries

In this subsection, we establish the convention and notation for this work and give a brief introduction to the symmetry properties of the pyrochlore lattice.

The pyrochlore lattice consists of four FCC-type sublattices which we label by $\mu = 0, 1, 2, 3$. The lattice vectors $\boldsymbol{e}_1$, $\boldsymbol{e}_2$, and $\boldsymbol{e}_3$ are defined as

$$\boldsymbol{e}_1 = \frac{a}{2}(\hat{\boldsymbol{y}} + \hat{\boldsymbol{z}}), \qquad \boldsymbol{e}_2 = \frac{a}{2}(\hat{\boldsymbol{z}} + \hat{\boldsymbol{x}}), \qquad \boldsymbol{e}_3 = \frac{a}{2}(\hat{\boldsymbol{x}} + \hat{\boldsymbol{y}}), \tag{A.1}$$

where a is the cubic lattice constant, the Cartesian coordinate has its basis $\hat{\boldsymbol{x}}$, $\hat{\boldsymbol{y}}$, and $\hat{\boldsymbol{z}}$ aligned with the cubic system of the pyrochlore lattice, and its origin sits on a $\mu = 0$ site. We define the following sublattice-dependent coordinate:

$$(r_1, r_2, r_3)_\mu \equiv \boldsymbol{r}_\mu \equiv r_1 \boldsymbol{e}_1 + r_2 \boldsymbol{e}_2 + r_3 \boldsymbol{e}_3 + \frac{1}{2}\boldsymbol{e}_\mu, \tag{A.2}$$

where it is implicitly understood that $\boldsymbol{e}_0 = 0$.

The space group of the pyrochlore lattice group is $Fd\bar{3}m$. It is generated by the following five symmetry operations:

$$T_1 \colon \boldsymbol{r}_\mu \to (r_1 + 1, r_2, r_3)_\mu, \tag{A.3a}$$
$$T_2 \colon \boldsymbol{r}_\mu \to (r_1, r_2 + 1, r_3)_\mu, \tag{A.3b}$$
$$T_3 \colon \boldsymbol{r}_\mu \to (r_1, r_2, r_3 + 1)_\mu, \tag{A.3c}$$
$$\overline{C}_6 \colon \boldsymbol{r}_\mu \to (-r_3 - \delta_{\mu,3}, -r_1 - \delta_{\mu,1}, -r_2 - \delta_{\mu,2})_{\overline{C}_6(\mu)}, \tag{A.3d}$$
$$S \colon \boldsymbol{r}_\mu \to (-r_1 - \delta_{\mu,1}, -r_2 - \delta_{\mu,2}, r_1 + r_2 + r_3 + 1 - \delta_{\mu,0})_{S(\mu)}, \tag{A.3e}$$

where T_1, T_2, and T_3 are translations along the lattice vectors $\boldsymbol{e}_1$, $\boldsymbol{e}_2$, and $\boldsymbol{e}_3$, respectively, $\overline{C}_6$ is a sixfold rotoinversion around the [111] axis, and S is a nonsymmorphic screw operation which is the composition of a twofold rotation around $\boldsymbol{e}_3$ and a translation by $\boldsymbol{e}_3/2$. In the above equations, we defined the symmetry action on the sublattice indices:

$\overline{C}_6(\mu) = 0, 2, 3, 1$ and $S(\mu) = 3, 1, 2, 0$ for $\mu = 0, 1, 2, 3$. By definition, the rotoinversion can be written as the composition of an inversion (with respect to the origin) and a threefold rotation around the [111] axis: $\overline{C}_6 = I \circ C_3$, with $I = \overline{C}_6^3$ and $C_3 = \overline{C}_6^4$. The The generators $\{I, C_3\}$ are therefore equivalent to the generator $\overline{C}_6$; we choose a single generator $\overline{C}_6$ to reduce the number of generators and group relations.

The point group of the pyrochlore lattice, formally defined as the quotient group of the space group and the group of pure translations, is the cubic group O_h. This group is minimally generated by $\overline{C}_6$ and S', where S' is a twofold rotation around $\hat{e}_3$, distinguished from the space-group generator S by the lack of a subsequent translation along $\hat{\epsilon}_3$. The detailed structure of the group O_h is given in App. A.2.

In addition to the pyrochlore space group symmetries, time-reversal operation $\mathcal{T}$ is an internal symmetry that commutes with all space-group operations and satisfies $\mathcal{T}^2 = -1$ when acting on a half-integer spin state. The pyrochlore symmetry group is then completely characterized by the following group relations:

$$T_i T_{i+1} T_i^{-1} T_{i+1}^{-1} = 1, \quad i = 1, 2, 3, \tag{A.4a}$$

$$\overline{C}_6^6 = 1, \tag{A.4b}$$

$$S^2 T_3^{-1} = 1, \tag{A.4c}$$

$$\overline{C}_6 T_i \overline{C}_6^{-1} T_{i+1} = 1, \quad i = 1, 2, 3, \tag{A.4d}$$

$$S T_i S^{-1} T_3^{-1} T_i = 1, \quad i = 1, 2, \tag{A.4e}$$

$$S T_3 S^{-1} T_3^{-1} = 1, \tag{A.4f}$$

$$(\overline{C}_6 S)^4 = 1, \tag{A.4g}$$

$$(\overline{C}_6^3 S)^2 = 1, \tag{A.4h}$$

$$\mathcal{T}^2 = -1, \tag{A.4i}$$

$$\mathcal{T} \mathcal{O} \mathcal{T}^{-1} \mathcal{O}^{-1} = 1, \quad \mathcal{O} \in \{T_1, T_2, T_3, \overline{C}_6, S\}, \tag{A.4j}$$

where it is implicitly understood that $i + 3 \equiv i$.

A.2 Point-group structure

The space group $Fd\overline{3}m$ belongs to the cubic crystal system with point group O_h. The point group O_h has order 48 and is the symmetry group of a pyrochlore primitive cell – a pair of corner sharing tetrahedra. It has a direct product structure $O_h \cong S_4 \times \mathbb{Z}_2$, which can be understood as following.

We label the seven vertices by $\mu^\pm$, where $\mu = 0, 1, 2, 3$ is the sublattice index and "+" ("−") denotes the upper (lower) tetrahedron (where $0^+ = 0^-$ is the shared corner), then the symmetry operations in O_h are permutations over two sets $\{0, 1, 2, 3\}$ and $\{+, -\}$. The generators include a threefold rotation $C_3 = (123)$, a screw operation (modding out translations) $S = (03)(+-)$ and an inversion $I = (+-)$, written in terms of the cycle

notation for permutations. We also define the operation $\Sigma = S \circ I = (03)$ for future convenience. (We can also define $\overline{C}_6 = C_3 \circ I$ to reduce the number of generators, since equivalently $C_3 = \overline{C}_6^4$ and $I = \overline{C}_6^3$.) The inversion I is the generator of the $\mathbb{Z}_2$ group, therefore we can write $O_{\mathrm{h}} \cong S_4 \cup (I \circ S_4)$, where $I \circ S_4$ is the coset of S_4 left-composed by I. The subgroup S_4 corresponds exactly to the tetrahedron group, T_{d}. The 24 elements of the group $S_4 \simeq T_{\mathrm{d}}$ are generated by Σ and C_3 as (where it is understood $4 \equiv 0$)

$$
\begin{aligned}
(1) &= C_3 \circ C_3 \circ C_3, \\
(12) &= \Sigma \circ C_3 \circ \Sigma \circ C_3^{-1} \circ \Sigma \circ C_3, \\
(13) &= \Sigma \circ C_3 \circ \Sigma \circ C_3^{-1} \circ \Sigma, \\
(14) &= \Sigma \circ C_3 \circ \Sigma \circ C_3^{-1} \circ \Sigma \circ C_3^{-1} \circ \Sigma \circ C_3 \circ \Sigma \circ C_3, \\
(23) &= \Sigma \circ C_3 \circ \Sigma \circ C_3^{-1} \circ \Sigma \circ C_3^{-1}, \\
(24) &= C_3 \circ \Sigma \circ C_3^{-1} \circ \Sigma \circ C_3^{-1} \circ \Sigma, \\
(34) &= \Sigma, \\
(123) &= C_3, \\
(132) &= C_3^{-1}, \\
(124) &= \Sigma \circ C_3 \circ \Sigma, \\
(142) &= \Sigma \circ C_3^{-1} \circ \Sigma, \\
(134) &= \Sigma \circ C_3 \circ \Sigma \circ C_3^{-1}, \\
(143) &= \Sigma \circ C_3 \circ \Sigma \circ C_3^{-1} \circ \Sigma \circ C_3 \circ \Sigma \circ C_3^{-1}, \\
(234) &= C_3^{-1} \circ \Sigma \circ C_3 \circ \Sigma \circ C_3^{-1} \circ \Sigma \circ C_3 \circ \Sigma, \\
(243) &= C_3^{-1} \circ \Sigma \circ C_3 \circ \Sigma, \\
(1243) &= \Sigma \circ C_3, \\
(14)(23) &= \Sigma \circ C_3 \circ \Sigma \circ C_3, \\
(1342) &= \Sigma \circ C_3 \circ \Sigma \circ C_3 \circ \Sigma \circ C_3, \\
(1234) &= C_3 \circ \Sigma, \\
(13)(24) &= C_3 \circ \Sigma \circ C_3 \circ \Sigma, \\
(1432) &= C_3 \circ \Sigma \circ C_3 \circ \Sigma \circ C_3 \circ \Sigma, \\
(1324) &= C_3 \circ \Sigma \circ C_3, \\
(12)(34) &= C_3 \circ \Sigma \circ C_3^{-1} \circ \Sigma \circ C_3, \\
(1423) &= C_3 \circ \Sigma \circ C_3^{-1} \circ \Sigma \circ C_3^{-1} \circ \Sigma \circ C_3.
\end{aligned}
\tag{A.5}
$$

Eqs. (A.5) will be useful in determining the mean field ansätze parameter constraints for the PSG classes.

For the on-site bond $\mathbf{0}_0 \to \mathbf{0}_0$, the 12 group elements that map the bond back are

$$(1),\ (12),\ (13),\ (23),\ (123),\ (13),\ (+-),\ (12)(+-),$$
$$(13)(+-),\ (23)(+-),\ (123)(+-),\ (13)(+-),$$

Consider the case for the NN bond $\mathbf{0}_0 \to \mathbf{0}_1$. The four group elements that map the bond back are

$$(1),\ (14),\ (23),\ (14)(23). \tag{A.6}$$

For the NNN bond $\mathbf{0}_1 \to \mathbf{0}_2 - \hat{e}_2$, it can be checked that only the identity (1) and the element $(12)(+-) = S \circ C_3 \circ S \circ C_3^{-1} \circ S \circ C_3$ map the bond back.

A.3 Basis for irreps of T_d and condensation results

We first give the representation analysis result for the spins $\mathbf{S}$ on a single tetrahedron, which can be equally applied to pyrochlore lattices with a Γ point order. The twelve-component spin $\mathbf{S}$ form a 12-dimensional representation of the tetrahedron group T_d. The group T_d has irreducible representation (irrep)A_1, A_2, E, T_1, T_2. $\mathbf{S}$ can be decomposed into irreps $A_2, E, T_{1,A}, T_{1,B}$ and T_2. The corresponding basis and orders are listed in Table. A.1. This is simply a reproduction of TABLE III in Ref. [172].

The basis are

$$\mathbf{S}_1 = \frac{1}{2\sqrt{3}}(1, 1, 1, 1, -1, -1, -1, 1, -1, -1, -1, 1),$$

$$\mathbf{S}_2 = \frac{1}{2\sqrt{6}}(-2, 1, 1, -2, -1, -1, 2, 1, -1, 2, -1, 1),$$

$$\mathbf{S}_3 = \frac{1}{2\sqrt{2}}(0, -1, 1, 0, 1, -1, 0, -1, -1, 0, 1, 1),$$

$$\mathbf{S}_4 = \frac{1}{2}(1, 0, 0, 1, 0, 0, 1, 0, 0, 1, 0, 0),$$

$$\mathbf{S}_5 = \frac{1}{2}(0, 1, 0, 0, 1, 0, 0, 1, 0, 0, 1, 0),$$

$$\mathbf{S}_6 = \frac{1}{2}(0, 0, 1, 0, 0, 1, 0, 0, 1, 0, 0, 1),$$

$$\mathbf{S}_7 = -\frac{1}{2\sqrt{2}}(0, 1, 1, 0, -1, -1, 0, -1, 1, 0, 1, -1),$$

$$\mathbf{S}_8 = -\frac{1}{2\sqrt{2}}(1, 0, 1, -1, 0, 1, -1, 0, -1, 1, 0, -1),$$

$$\mathbf{S}_9 = -\frac{1}{2\sqrt{2}}(1, 1, 0, -1, 1, 0, 1, -1, 0, -1, -1, 0),$$

Irrep	Basis	Orders
A_2	$\mathbf{S}_1$	all in-all out
E	$\mathbf{S}_2, \mathbf{S}_3$	Ψ_2 and Ψ_3
$T_{1,A}$	$\mathbf{S}_4, \mathbf{S}_5, \mathbf{S}_6$	collinear FM
$T_{1,B}$	$\mathbf{S}_7, \mathbf{S}_8, \mathbf{S}_9$	non-collinear FM
T_2	$\mathbf{S}_{10}, \mathbf{S}_{11}, \mathbf{S}_{12}$	Palmer-Chalker

Table A.1: Correspondence between orders, irreps and basis of irreps

$$\mathbf{S}_{10} = \frac{1}{2\sqrt{2}}(0, -1, 1, 0, 1, -1, 0, 1, 1, 0, -1, -1),$$

$$\mathbf{S}_{11} = \frac{1}{2\sqrt{2}}(1, 0, -1, -1, 0, -1, -1, 0, 1, 1, 0, 1),$$

$$\mathbf{S}_{12} = \frac{1}{2\sqrt{2}}(-1, 1, 0, 1, 1, 0, -1, -1, 0, 1, -1, 0). \tag{A.7a}$$

The three vectors $\mathbf{S}^r$, $\mathbf{S}^c$, and $\mathbf{S}^s$ for the paraphase 0-(100)Γ, mentioned in Eq. (4.32), are

$$\mathbf{S}^r = (0, 0, -1, 0, 0, 1, 0, 0, 1, 0, 0, -1), \tag{A.8a}$$
$$\mathbf{S}^c = (-1, 0, 0, -1, 0, 0, 1, 0, 0, 1, 0, 0), \tag{A.8b}$$
$$\mathbf{S}^s = (0, -1, 0, 0, 1, 0, 0, -1, 0, 0, 1, 0). \tag{A.8c}$$

The three vectors $\mathbf{S}^r$, $\mathbf{S}^c$, and $\mathbf{S}^s$ for the paraphase 0-(001)Γ, mentioned in Sec. 4.4.6, are

$$\mathbf{S}^r = (4, 4, 7, -8, -4, -1, -4, -8, -1, 0, 0, 9), \tag{A.9a}$$
$$\mathbf{S}^c = (1, -8, 4, 1, -4, 8, -7, 4, -4, 9, 0, 0), \tag{A.9b}$$
$$\mathbf{S}^s = (-8, 1, 4, 4, -7, -4, -4, 1, 8, 0, 9, 0). \tag{A.9c}$$

In writing down the Ginzburg–Landau theory for the paraphase 0-(010)Γ, the transfor-

mation rules of $\phi_1, \phi_2, \overline{\phi}_1, \overline{\phi}_2$ are

$$
\overline{C}_6 : \begin{pmatrix} \phi_1 \\ \phi_2 \\ \overline{\phi}_1 \\ \overline{\phi}_2 \end{pmatrix} \rightarrow
$$

$$
\begin{pmatrix}
\frac{\left(\frac{1}{6}-\frac{i}{6}\right)((1+2i)\delta+(1-i)\Delta)}{\delta} & \frac{\left(\frac{1}{6}+\frac{i}{6}\right)(\delta+\Delta)}{\delta} & -\frac{\left(\frac{1}{2}-\frac{i}{2}\right)\zeta}{\delta} & 0 \\
-\frac{\left(\frac{1}{6}-\frac{i}{6}\right)(\delta+\Delta)}{\delta} & \frac{\left(\frac{1}{6}+\frac{i}{6}\right)((1-2i)\delta+(1+i)\Delta)}{\delta} & 0 & -\frac{\left(\frac{1}{2}+\frac{i}{2}\right)\zeta}{\delta} \\
-\frac{\left(\frac{1}{2}+\frac{i}{2}\right)\zeta}{\delta} & 0 & \frac{\left(\frac{1}{6}+\frac{i}{6}\right)((1-2i)\delta+(1+i)\Delta)}{\delta} & \frac{\left(\frac{1}{6}-\frac{i}{6}\right)(\delta+\Delta)}{\delta} \\
0 & -\frac{\left(\frac{1}{2}-\frac{i}{2}\right)\zeta}{\delta} & -\frac{\left(\frac{1}{6}+\frac{i}{6}\right)(\delta+\Delta)}{\delta} & \frac{\left(\frac{1}{6}-\frac{i}{6}\right)((1+2i)\delta+(1-i)\Delta)}{\delta}
\end{pmatrix} \begin{pmatrix} \phi_1 \\ \phi_2 \\ \overline{\phi}_1 \\ \overline{\phi}_2 \end{pmatrix},
$$

$$
\text{(A.10)}
$$

$$
S : \begin{pmatrix} \phi_1 \\ \phi_2 \\ \overline{\phi}_1 \\ \overline{\phi}_2 \end{pmatrix} \rightarrow \begin{pmatrix}
\frac{1}{\sqrt{2}} & -\frac{1}{\sqrt{2}} & 0 & 0 \\
-\frac{1}{\sqrt{2}} & -\frac{1}{\sqrt{2}} & 0 & 0 \\
0 & 0 & \frac{1}{\sqrt{2}} & -\frac{1}{\sqrt{2}} \\
0 & 0 & -\frac{1}{\sqrt{2}} & -\frac{1}{\sqrt{2}}
\end{pmatrix} \begin{pmatrix} \phi_1 \\ \phi_2 \\ \overline{\phi}_1 \\ \overline{\phi}_2 \end{pmatrix}, \qquad \text{(A.11)}
$$

where the definition of δ, Δ and ζ has been given in Section 4.4.6. We see that in this case the fields transform to their complex conjugates under O_{h}.

The only quartic term invariant under O_{h} is

$$
\Phi = \left[4(|\phi_1|^2 + |\phi_2|^2) + \left((-1+i)\phi_1^2 - (1+i)\phi_2^2 - i\phi_1\phi_2 + c.c. \right) \right]^2. \qquad \text{(A.12)}
$$

In writing down the Ginzburg–Landau theory for the paraphase 0-(100)Γ, the transformation rules of $\phi_{1,2}$ under $\overline{C}_6$ and S are recorded by the following matrices:

$$
U^{(100)\Gamma}_{\overline{C}_6} = \frac{1}{2} \begin{pmatrix} 1-i & 1-i \\ -1-i & 1+i \end{pmatrix}, \quad U^{(100)\Gamma}_S = \frac{1}{\sqrt{2}} \begin{pmatrix} 0 & -1-i \\ 1-i & 0 \end{pmatrix}. \qquad \text{(A.13)}
$$

There are six quartic terms that are invariant under O_{h}. Three of them can be written as Φ_i^2, where

$$
\Phi_1 = |\phi_1|^2 + |\phi_2|^2,
$$
$$
\Phi_2 = \frac{1}{2}\left(|\phi_1|^2 - |\phi_2|^2 \right) + \left(\frac{1+3i}{4}\phi_1^2 + \frac{1-2i}{2}\phi_1\phi_2 + \frac{1-i}{2}\phi_1\phi_2^* + \frac{3-i}{4}\phi_2^2 + c.c. \right),
$$
$$
\Phi_3 = |\phi_1|^2 - |\phi_2|^2 + \left(\frac{\phi_1^2}{2} - \frac{1+i}{2}\phi_1\phi_2 + (1-i)\phi_1\phi_2^* - \frac{i}{2}\phi_2^2 + c.c \right).
$$

$$
\text{(A.14)}
$$

In writing down the Ginzburg–Landau theory for the paraphase 0-(101)Γ, the transformation rules of $\phi_{1,2}$ under $\overline{C}_6$ and S are recorded by the following matrices:

$$\widetilde{U}_{\overline{C}_6}^{(101)\Gamma} = iU_{\overline{C}_6}^{(100)\Gamma}, \quad \widetilde{U}_S^{(101)\Gamma} = U_S^{(100)\Gamma}. \tag{A.15}$$

the extra factor of i for $\overline{C}_6$ is due to $n_{\overline{C}_6} = 1$.

In writing down the Ginzburg–Landau theory for the paraphase 0-(110)Γ, the transformation rules of $\chi_{1,2}$ under $\overline{C}_6$ and S are recorded by the following matrices:

$$U_{\overline{C}_6}^{(110)\Gamma} = \begin{pmatrix} \frac{1}{2} & -\frac{\sqrt{3}}{2} \\ \frac{\sqrt{3}}{2} & \frac{1}{2} \end{pmatrix}, \quad U_S^{(110)\Gamma} = \begin{pmatrix} \frac{\sqrt{\frac{3}{2}}}{\sqrt{3}+3} & -\frac{\sqrt{6}+\frac{3}{\sqrt{2}}}{\sqrt{3}+3} \\ -\frac{\sqrt{6}+\frac{3}{\sqrt{2}}}{\sqrt{3}+3} & -\frac{\sqrt{\frac{3}{2}}}{\sqrt{3}+3} \end{pmatrix}. \tag{A.16}$$

the only quadratic and quartic order parameter are the trivial one: $(\chi_1^2 + \chi_2^2)^i$, $i = 1, 2$. At sextic order, there are two terms allowed:

$$(\chi_1^2 + \chi_2^2)^3, \quad \frac{1}{3}(\chi_1 - \chi_2)\chi_2(3\chi_1^2 - \chi_2^2)(\chi_1^2 + 4\chi_1\chi_2 + \chi_2^2). \tag{A.17}$$

In writing down the Ginzburg–Landau theory for the paraphase 0-(111)Γ, the transformation rules of $\phi_{1,2}$ under $\overline{C}_6$ and S are recorded by the following matrices:

$$\overline{U}_{\overline{C}_6}^{(111)\Gamma} = \frac{1}{2}\begin{pmatrix} 1-i & -1+i \\ -1-i & -1-i \end{pmatrix}, \quad \overline{U}_S^{(111)\Gamma} = \frac{1}{\sqrt{2}}\begin{pmatrix} 0 & -1-i \\ -1+i & 0 \end{pmatrix}. \tag{A.18}$$

A.4   PSG equations

The PSG equations are, by definition,

$$(G_{T_i}T_i)(G_{T_{i+1}}T_{i+1})(G_{T_i}T_i)^{-1}(G_{T_{i+1}}T_{i+1})^{-1} \in \text{IGG}, \tag{A.19a}$$
$$(G_{\overline{C}_6}\overline{C}_6)^6 \in \text{IGG}, \tag{A.19b}$$
$$(G_S S)^2 (G_{T_3}T_3)^{-1} \in \text{IGG}, \tag{A.19c}$$
$$(G_{\overline{C}_6}\overline{C}_6)(G_{T_i}T_i)(G_{\overline{C}_6}\overline{C}_6)^{-1}(G_{T_{i+1}}T_{i+1}) \in \text{IGG}, \tag{A.19d}$$
$$(G_S S)(G_{T_i}T_i)(G_S S)^{-1}(G_{T_3}T_3)^{-1}(G_{T_i}T_i) \in \text{IGG}, \tag{A.19e}$$
$$(G_S S)(G_{T_3}T_3)(G_S S)^{-1}(G_{T_3}T_3)^{-1} \in \text{IGG}, \tag{A.19f}$$
$$[(G_{\overline{C}_6}\overline{C}_6)(G_S S)]^4 \in \text{IGG}, \tag{A.19g}$$
$$[(G_{\overline{C}_6}\overline{C}_6)^3(G_S S)]^2 \in \text{IGG}. \tag{A.19h}$$

where IGG $= \mathbb{Z}_2$ or U(1).

For bosonic $\mathbb{Z}_2$ PSG, the corresponding phase equations are

$$\phi_{T_i}(\boldsymbol{r}_\mu) + \phi_{T_{i+1}}[T_i^{-1}(\boldsymbol{r}_\mu)] - \phi_{T_i}[T_{i+1}^{-1}(\boldsymbol{r}_\mu)] - \phi_{T_{i+1}}(\boldsymbol{r}_\mu) = n_i \pi, \qquad \text{(A.20a)}$$

$$\phi_{\overline{C}_6}(\boldsymbol{r}_\mu) + \phi_{\overline{C}_6}[\overline{C}_6^{-1}(\boldsymbol{r}_\mu)] + \phi_{\overline{C}_6}[\overline{C}_6^{-2}(\boldsymbol{r}_\mu)]$$
$$+\phi_{\overline{C}_6}[\overline{C}_6^{-3}(\boldsymbol{r}_\mu)] + \phi_{\overline{C}_6}[\overline{C}_6^{-4}(\boldsymbol{r}_\mu)] + \phi_{\overline{C}_6}[\overline{C}_6^{-5}(\boldsymbol{r}_\mu)] = n_{\overline{C}_6}\pi, \qquad \text{(A.20b)}$$

$$\phi_S(\boldsymbol{r}_\mu) + \phi_S[S^{-1}(\boldsymbol{r}_\mu)] - \phi_{T_3}(\boldsymbol{r}_\mu) = n_S \pi, \qquad \text{(A.20c)}$$

$$\phi_{\overline{C}_6}(\boldsymbol{r}_\mu) + \phi_{T_i}[\overline{C}_6^{-1}(\boldsymbol{r}_\mu)] - \phi_{\overline{C}_6}[T_{i+1}(\boldsymbol{r}_\mu)] + \phi_{T_{i+1}}[T_{i+1}(\boldsymbol{r}_\mu)] = n_{\overline{C}_6 T_i}\pi, \quad \text{(A.20d)}$$

$$\phi_S(\boldsymbol{r}_\mu) + \phi_{T_i}[S^{-1}(\boldsymbol{r}_\mu)] - \phi_S[T_3^{-1}T_i(\boldsymbol{r}_\mu)] - \phi_{T_3}[T_i(\boldsymbol{r}_\mu)] + \phi_{T_i}[T_i(\boldsymbol{r}_\mu)] = n_{ST_i}\pi, \quad \text{(A.20e)}$$

$$\phi_S(\boldsymbol{r}_\mu) + \phi_{T_3}[S^{-1}(\boldsymbol{r}_\mu)] - \phi_S[T_3^{-1}(\boldsymbol{r}_\mu)] - \phi_{T_3}(\boldsymbol{r}_\mu) = n_{ST_3}\pi, \qquad \text{(A.20f)}$$

$$\phi_{\overline{C}_6}(\boldsymbol{r}_\mu) + \phi_S[\overline{C}_6^{-1}(\boldsymbol{r}_\mu)] + \phi_{\overline{C}_6}[(\overline{C}_6 S)^{-1}(\boldsymbol{r}_\mu)] + \phi_S[(\overline{C}_6 S\overline{C}_6)^{-1}(\boldsymbol{r}_\mu)]$$
$$+\phi_{\overline{C}_6}[(\overline{C}_6 S\overline{C}_6 S)^{-1}(\boldsymbol{r}_\mu)] + \phi_S[(\overline{C}_6 S\overline{C}_6 S\overline{C}_6)^{-1}(\boldsymbol{r}_\mu)]$$
$$+\phi_{\overline{C}_6}[(\overline{C}_6 S\overline{C}_6 S\overline{C}_6 S)^{-1}(\boldsymbol{r}_\mu)] + \phi_S[(\overline{C}_6 S\overline{C}_6 S\overline{C}_6 S\overline{C}_6)^{-1}(\boldsymbol{r}_\mu)] = n_{\overline{C}_6 S}\pi, \quad \text{(A.20g)}$$

$$\phi_{\overline{C}_6}(\boldsymbol{r}_\mu) + \phi_{\overline{C}_6}[\overline{C}_6^{-1}(\boldsymbol{r}_\mu)] + \phi_{\overline{C}_6}[\overline{C}_6^{-2}(\boldsymbol{r}_\mu)] + \phi_S[\overline{C}_6^{-3}(\boldsymbol{r}_\mu)]$$
$$+\phi_{\overline{C}_6}[(\overline{C}_6^3 S)^{-1}(\boldsymbol{r}_\mu)] + \phi_{\overline{C}_6}[(\overline{C}_6^3 S\overline{C}_6)^{-1}(\boldsymbol{r}_\mu)]$$
$$+\phi_{\overline{C}_6}[(\overline{C}_6^3 S\overline{C}_6^2)^{-1}(\boldsymbol{r}_\mu)] + \phi_S[S(\boldsymbol{r}_\mu)] = n_{S\overline{C}_6}\pi \qquad \text{(A.20h)}$$

where both Eq. (A.20a) and Eq. (A.20d) stand for three equations $i = 1, 2, 3$, and Eq. (A.20e) stands for two equations $i = 1, 2$.

For fermionic PSG, the corresponding SU(2) equations are

$$W_{T_i}(\boldsymbol{r}_\mu)W_{T_{i+1}}[T_i^{-1}(\boldsymbol{r}_\mu)]W_{T_i}^{-1}[T_{i+1}^{-1}(\boldsymbol{r}_\mu)]W_{T_{i+1}}^{-1}(\boldsymbol{r}_\mu) = e^{i\sigma^3 \chi_i}, \qquad \text{(A.21a)}$$

$$W_{\overline{C}_6}(\boldsymbol{r}_\mu)W_{\overline{C}_6}[\overline{C}_6^{-1}(\boldsymbol{r}_\mu)]W_{\overline{C}_6}[\overline{C}_6^{-2}(\boldsymbol{r}_\mu)]W_{\overline{C}_6}[\overline{C}_6^{-3}(\boldsymbol{r}_\mu)]\cdot$$
$$W_{\overline{C}_6}[\overline{C}_6^{-4}(\boldsymbol{r}_\mu)]W_{\overline{C}_6}[\overline{C}_6^{-5}(\boldsymbol{r}_\mu)] = e^{i\sigma^3 \chi_{\overline{C}_6}} \qquad \text{(A.21b)}$$

$$W_S(\boldsymbol{r}_\mu)W_S[S^{-1}(\boldsymbol{r}_\mu)]W_{T_3}^{-1}(\boldsymbol{r}_\mu) = e^{i\sigma^3 \chi_S}, \qquad \text{(A.21c)}$$

$$W_{\overline{C}_6}(\boldsymbol{r}_\mu)W_{T_i}[\overline{C}_6^{-1}(\boldsymbol{r}_\mu)]W_{\overline{C}_6}^{-1}[T_{i+1}(\boldsymbol{r}_\mu)]W_{T_{i+1}}[T_{i+1}(\boldsymbol{r}_\mu)] = e^{i\sigma^3 \chi_{\overline{C}_6 T_i}}, \qquad \text{(A.21d)}$$

$$W_S(\boldsymbol{r}_\mu)W_{T_i}[S^{-1}(\boldsymbol{r}_\mu)]W_S^{-1}[T_3^{-1}T_i(\boldsymbol{r}_\mu)]W_{T_3}^{-1}[T_i(\boldsymbol{r}_\mu)]W_{T_i}[T_i(\boldsymbol{r}_\mu)] = e^{i\sigma^3 \chi_{ST_i}}, \qquad \text{(A.21e)}$$

$$W_S(\boldsymbol{r}_\mu)W_{T_3}[S^{-1}(\boldsymbol{r}_\mu)]W_S^{-1}[T_3^{-1}(\boldsymbol{r}_\mu)]W_{T_3}^{-1}(\boldsymbol{r}_\mu) = e^{i\sigma^3 \chi_{ST_3}}, \qquad \text{(A.21f)}$$

$$W_{\overline{C}_6}(\boldsymbol{r}_\mu)W_S[\overline{C}_6^{-1}(\boldsymbol{r}_\mu)]W_{\overline{C}_6}[(\overline{C}_6 S)^{-1}(\boldsymbol{r}_\mu)]\cdot$$
$$W_S[(\overline{C}_6 S\overline{C}_6)^{-1}(\boldsymbol{r}_\mu)]W_{\overline{C}_6}[(\overline{C}_6 S\overline{C}_6 S)^{-1}(\boldsymbol{r}_\mu)]\cdot$$
$$W_S[(\overline{C}_6 S\overline{C}_6 S\overline{C}_6)^{-1}(\boldsymbol{r}_\mu)]W_{\overline{C}_6}[(\overline{C}_6 S\overline{C}_6 S\overline{C}_6 S)^{-1}(\boldsymbol{r}_\mu)]\cdot$$
$$W_S[(\overline{C}_6 S\overline{C}_6 S\overline{C}_6 S\overline{C}_6)^{-1}(\boldsymbol{r}_\mu)] = e^{i\sigma^3 \chi_{\overline{C}_6 S}}, \qquad \text{(A.21g)}$$

$$W_{\overline{C}_6}[\overline{C}_6^{-2}(\boldsymbol{r}_\mu)]W_S[\overline{C}_6^{-3}(\boldsymbol{r}_\mu)]W_{\overline{C}_6}[(\overline{C}_6^3 S)^{-1}(\boldsymbol{r}_\mu)]\cdot$$
$$W_{\overline{C}_6}[(\overline{C}_6^3 S\overline{C}_6)^{-1}(\boldsymbol{r}_\mu)]W_{\overline{C}_6}[(\overline{C}_6^3 S\overline{C}_6^2)^{-1}(\boldsymbol{r}_\mu)]W_S[S(\boldsymbol{r}_\mu)] = e^{i\sigma^3 \chi_{S\overline{C}_6}}, \qquad \text{(A.21h)}$$

where all the $\chi \in [0, 2\pi)$ for U(1) IGG, and $\chi \in \{0, \pi\}$ for $\mathbb{Z}_2$ IGG.

A.5   Solving bosonic $\mathbb{Z}_2$ PSG equations

First we solve Eq. (A.20a). Due to gauge freedom of second type, we can use a gauge transformation to achieve $\phi_{T_1}(r_1, r_2, r_3)_\mu = \phi_{T_2}(0, r_2, r_3)_\mu = \phi_{T_3}(0, 0, r_3) = 0$. Then Eq. (A.20a) gives

$$\phi_{T_1}(\boldsymbol{r}_\mu) = 0, \quad \phi_{T_2}(\boldsymbol{r}_\mu) = n_1 \pi r_1, \quad \phi_{T_3}(\boldsymbol{r}_\mu) = n_3 \pi r_1 + n_2 \pi r_2 \quad (\mathrm{mod}\ 2\pi). \qquad (A.22)$$

Using Eq. (A.22) to solve Eq. (A.20d)

$$\phi_{\overline{C}_6}(r_1, r_2, r_3)_\mu - \phi_{\overline{C}_6}(r_1, r_2 + 1, r_3)_\mu + n_1 \pi r_1 = n_{\overline{C}_6 T_1} \pi, (A.23a)$$

$$\phi_{\overline{C}_6}(r_1, r_2, r_3)_\mu - n_1 \pi (r_2 + \delta_{\mu=2}) - \phi_{\overline{C}_6}(r_1, r_2, r_3 + 1)_\mu + n_3 \pi r_1 + n_2 \pi r_2 = n_{\overline{C}_6 T_2} \pi, (A.23b)$$

$$\phi_{\overline{C}_6}(r_1, r_2, r_3)_\mu - n_3 \pi (r_2 + \delta_{\mu=2}) - n_2 \pi (r_3 + \delta_{\mu=3}) - \phi_{\overline{C}_6}(r_1 + 1, r_2, r_3)_\mu = n_{\overline{C}_6 T_3} \pi \ (A.23c)$$

we get $n_1 = n_2 = n_3$, and

$$\phi_{\overline{C}_6}(\boldsymbol{r}_\mu) = \phi_{\overline{C}_6}(\boldsymbol{0}_\mu) + (n_{\overline{C}_6 T_3} + n_1 \delta_{\mu=2,3}) \pi r_1 + n_{\overline{C}_6 T_1} \pi r_2 \\ + (n_{\overline{C}_6 T_2} + n_1 \delta_{\mu=2}) \pi r_3 + n_1 \pi (r_1 r_2 + r_1 r_3). \qquad (A.24)$$

Then using Eq. (A.22) to solve Eq. (A.20e) and (A.20f), we get

$$\phi_S(\boldsymbol{r}_\mu) = \phi_S(\boldsymbol{0}_\mu) + (n_{ST_3} + n_1 \delta_{\mu=1,2} - n_{ST_1}) \pi r_1 + (n_{ST_3} + n_1 \delta_{\mu=2} - n_{ST_2}) \pi r_2 \\ + (n_{ST_3} + n_1 \delta_{\mu=1,2}) \pi r_3 - \frac{1}{2} n_1 \pi (r_1 + r_2)(r_1 + r_2 + 1). \qquad (A.25)$$

Using Eqs. (A.22), (A.24) and (A.25) to solve Eq. (A.20g) and Eq. (A.20h) we get

$$\sum_{\mu=0}^{3} \phi_{\overline{C}_6}(\boldsymbol{0}_\mu) + \phi_S(\boldsymbol{0}_\mu) = \left(n_{\overline{C}_6 S} + \sum_{i=1}^{3} n_{\overline{C}_6 T_i} \right) \pi, \qquad (A.26)$$

and

$$n_{ST_3} + \sum_{i=1}^{3} n_{\overline{C}_6 T_i} = 0, \qquad (A.27a)$$

$$3\phi_{\overline{C}_6}(\boldsymbol{0}_0) + \sum_{j=1}^{3} \phi_{\overline{C}_6}(\boldsymbol{0}_j) + \phi_S(\boldsymbol{0}_0) + \phi_S(\boldsymbol{0}_3) = \left(n_{S\overline{C}_6} + \sum_{j=2}^{3} n_{\overline{C}_6 T_j} \right) \pi, \qquad (A.27b)$$

$$2\phi_S(\mathbf{0}_i) + 2\sum_{j=1}^{3}\phi_{\overline{C}_6}(\mathbf{0}_j) = n_{S\overline{C}_6}\pi, \quad i = 1, 2. \tag{A.27c}$$

Then, from Eq. (A.20b) we get

$$6\phi_{\overline{C}_6}(\mathbf{0}_0) = n_{\overline{C}_6}\pi, \tag{A.28a}$$

$$2\sum_{j=1}^{3}\phi_{\overline{C}_6}(\mathbf{0}_j) + \sum_{i=1}^{3}n_{\overline{C}_6 T_i}\pi = n_{\overline{C}_6}\pi, \tag{A.28b}$$

and Eq. (A.20c) gives

$$n_{ST_3} = 0 \tag{A.29}$$

and

$$\phi_S(\mathbf{0}_0) + \phi_S(\mathbf{0}_3) = n_S\pi, \tag{A.30a}$$
$$2\phi_S(\mathbf{0}_1) + (n_1 + n_{ST_1})\pi = n_S\pi, \tag{A.30b}$$
$$2\phi_S(\mathbf{0}_2) + (n_1 + n_{ST_2})\pi = n_S\pi. \tag{A.30c}$$

Eqs. (A.27a) and (A.29) further imply that

$$n_{\overline{C}_6 T_1} + n_{\overline{C}_6 T_2} + n_{\overline{C}_6 T_3} = 0. \tag{A.31}$$

This completes solving the inter-unit cell part of the space group PSG equations. We can use some of the remaining gauge freedom to simplify results. In order to use the IGG freedom we notice that Eq. (A.19c), (A.19d) and (A.19e) have operators that appear odd number of times. According to our analysis in the main text, we can set $n_S = 0$, and two out of the three parameters $n_{\overline{C}T_i}$ to be zero, which together with Eq. (A.31) means that $n_{\overline{C}_6 T_1} = n_{\overline{C}_6 T_2} = n_{\overline{C}_6 T_3} = 0$. The independent $\mathbb{Z}_2$ parameters at this point are

$$n_1, \quad n_{\overline{C}_6}, \quad n_{ST_1}, \quad n_{ST_2}, \quad n_{\overline{C}_6 S}, \quad n_{S\overline{C}_6}. \tag{A.32}$$

Then we add time reversal operation. From

$$(G_{\mathcal{T}}\mathcal{T})(\mathcal{G}_{\mathcal{O}}\mathcal{O})(G_{\mathcal{T}}\mathcal{T})^{-1}(\mathcal{G}_{\mathcal{O}}\mathcal{O})^{-1} \in \mathbb{Z}_2 \tag{A.33}$$

where $\mathcal{O} \in \{T_1, T_2, T_3, \overline{C}_6, S\}$, we get

$$\phi_{\mathcal{T}}(\mathbf{r}_\mu) - \phi_{\mathcal{T}}[T_i^{-1}(\mathbf{r}_\mu)] - 2\phi_{T_i}(\mathbf{r}_\mu) = n_{\mathcal{T}T_i}\pi, \tag{A.34a}$$
$$\phi_{\mathcal{T}}(\mathbf{r}_\mu) - \phi_{\mathcal{T}}[\overline{C}_6^{-1}(\mathbf{r}_\mu)] - 2\phi_{\overline{C}_6}(\mathbf{r}_\mu) = n_{\mathcal{T}\overline{C}_6}\pi, \tag{A.34b}$$

$$\phi_{\mathcal{T}}(\boldsymbol{r}_\mu) - \phi_{\mathcal{T}}[S^{-1}(\boldsymbol{r}_\mu)] - 2\phi_S(\boldsymbol{r}_\mu) \;=\; n_{\mathcal{T}S}\pi. \tag{A.34c}$$

where Eq. (A.34a) stands for three equations $i = 1, 2, 3$. From Eq. (A.34a) we get

$$\phi_{\mathcal{T}}(\boldsymbol{r}_\mu) = \phi_{\mathcal{T}}(\boldsymbol{0}_\mu) + \pi \sum_{i=1}^{3} n_{\mathcal{T}T_i} r_i. \tag{A.35}$$

From Eq. (A.34b) we get $n_{\mathcal{T}T_1} = n_{\mathcal{T}T_2} = n_{\mathcal{T}T_3} \equiv n_{\mathcal{T}T}$, and

$$2\phi_{\overline{C}_6}(\boldsymbol{0}_0) \;=\; n_{\mathcal{T}\overline{C}_6}\pi, \tag{A.36a}$$
$$\phi_{\mathcal{T}}(\boldsymbol{0}_i) - \phi_{\mathcal{T}}(\boldsymbol{0}_{i-1}) + n_{\mathcal{T}T}\pi - 2\phi_{\overline{C}_6}(\boldsymbol{0}_i) \;=\; n_{\mathcal{T}\overline{C}_6}\pi, \quad i = 1, 2, 3, \tag{A.36b}$$

therefore $n_{\mathcal{T}\overline{C}_6} + n_{\mathcal{T}T} = n_{\overline{C}_6}$. Finally Eq. (A.34c) gives $n_{\mathcal{T}T} = 0$, $n_{ST_1} = n_{ST_2} = n_{\mathcal{T}S} - n_1$, and

$$\phi_{\mathcal{T}}(\boldsymbol{0}_0) - \phi_{\mathcal{T}}(\boldsymbol{0}_3) - 2\phi_S(\boldsymbol{0}_0) = (n_1 + n_{ST_1})\pi. \tag{A.37}$$

Lastly the equation $\mathcal{T}^2 = -1$ gives no constraint.

Now we have solved all the inter-unit cell part of the PSG equations. The intra-unit cell part gives

$$2\phi_{\overline{C}_6}(\boldsymbol{0}_0) \;=\; n_{\overline{C}_6}\pi, \tag{A.38a}$$

$$2\sum_{j=1}^{3}\phi_{\overline{C}_6}(\boldsymbol{0}_j) \;=\; n_{\overline{C}_6}\pi, \tag{A.38b}$$

$$\phi_S(\boldsymbol{0}_0) + \phi_S(\boldsymbol{0}_3) \;=\; 0, \tag{A.38c}$$
$$2\phi_S(\boldsymbol{0}_i) + (n_1 + n_{ST_1})\pi \;=\; 0, \quad i = 1, 2, \tag{A.38d}$$

$$\sum_{\mu=0}^{3}\phi_{\overline{C}_6}(\boldsymbol{0}_\mu) + \phi_S(\boldsymbol{0}_\mu) \;=\; n_{\overline{C}_6 S}\pi, \tag{A.38e}$$

$$3\phi_{\overline{C}_6}(\boldsymbol{0}_0) + \sum_{j=1}^{3}\phi_{\overline{C}_6}(\boldsymbol{0}_j) \;=\; n_{S\overline{C}_6}\pi, \tag{A.38f}$$

$$2\sum_{j=1}^{3}\phi_{\overline{C}_6}(\boldsymbol{0}_j) + 2\phi_S(\boldsymbol{0}_i) \;=\; n_{S\overline{C}_6}\pi, \quad i = 1, 2, \tag{A.38g}$$

$$\phi_{\mathcal{T}}(\boldsymbol{0}_i) - \phi_{\mathcal{T}}(\boldsymbol{0}_{i-1}) - 2\phi_{\overline{C}_6}(\boldsymbol{0}_i) \;=\; n_{\overline{C}_6}\pi, \quad i = 1, 2, 3, \tag{A.38h}$$
$$\phi_{\mathcal{T}}(\boldsymbol{0}_0) - \phi_{\mathcal{T}}(\boldsymbol{0}_3) - 2\phi_S(\boldsymbol{0}_0) \;=\; (n_1 + n_{ST_1})\pi. \tag{A.38i}$$

Then we use the gauge freedom of second type. Note under gauge transformation

$$\phi(\boldsymbol{r}_\mu) = \phi_\mu, \quad \mu = 0, 1, 2, 3, \tag{A.39}$$

we have $\phi_{\mathcal{O}}(\boldsymbol{r}_\mu) \to \phi_{\mathcal{O}}(\boldsymbol{r}_\mu) + \phi(\boldsymbol{r}_\mu) - \phi[\mathcal{O}^{-1}(\boldsymbol{r})_\mu]$, where ϕ is an artitrary $U(1)$ phase, we have $\phi_{\overline{C}_6}(\mathbf{0})_0 \to \phi_{\overline{C}_6}(\mathbf{0})_0$, $\phi_{\overline{C}_6}(\mathbf{0})_i \to \phi_{\overline{C}_6}(\mathbf{0})_i + \phi_i - \phi_{i+1}$, $\phi_S(\mathbf{0})_0 \to \phi_S(\mathbf{0})_0 + \phi_0 - \phi_3$, $\phi_S(\mathbf{0})_{1,2} \to \phi_S(\mathbf{0})_{1,2}$, $\phi_S(\mathbf{0})_3 \to \phi_S(\mathbf{0})_3 + \phi_3 - \phi_0$, and $\phi_{\mathcal{T}}(\mathbf{0})_\mu \to \phi_{\mathcal{T}}(\mathbf{0})_\mu + 2\phi_\mu$. Then, we can choose the value of ϕ_μ to fix

$$\phi_{\mathcal{T}}(\mathbf{0}_\mu) = 0, \tag{A.40}$$

and

$$\phi_{\overline{C}_6}(\mathbf{0}_\mu) = (\frac{n_{\overline{C}_6}}{2} + p_\mu)\pi, \tag{A.41a}$$

$$\phi_S(\mathbf{0}_0) = -\phi_S(\mathbf{0}_3) = (\frac{n_1 + n_{ST_1}}{2} + m_0)\pi, \tag{A.41b}$$

$$\phi_S(\mathbf{0}_{1,2}) = (-\frac{n_1 + n_{ST_1}}{2} + m_{1,2})\pi, \tag{A.41c}$$

where p_μ, m_0 and $m_{1,2}$ are all $\mathbb{Z}_2$ parameters.

Note we still have a discrete gauge freedom: we can choose a particular sublattice ν and define gauge transformation

$$\phi(\boldsymbol{r}_\mu) = \pi\delta_{\mu,\nu}, \tag{A.42}$$

then Eq. (A.40) is preserved but the relative phase of $\phi_{\overline{C}_6}$ can be changed. By choosing $\nu = 1, 2, 3$ we can use gauge (A.42) to fix $p_1 = p_2 = p_3 \equiv p$. Furthermore, we can use the global $\mathbb{Z}_2$ freedom for $\phi_{\overline{C}_6}(\boldsymbol{r}_\mu)$ and $\phi_S(\boldsymbol{r}_\mu)$ to fix $p_0 = 0$ and $m_1 = 0$. Then, let $\nu = 0, 3$, we can use gauge (A.42) to fix $m_0 = 0$. By checking Eqs. (A.38), we have $n_{S\overline{C}_6} = n_{\overline{C}_6} + n_1 + n_{ST_1}$, $p = n_1 + n_{ST_1}$ and $m_2 = n_{\overline{C}_6 S}$. The final solution is presented in Eq. (4.1).

A.6   Solving fermionic U(1) PSG equations

The general form for $W_{\mathcal{O}}(\boldsymbol{r})$ is $W_{\mathcal{O}}(\boldsymbol{r}) = (i\sigma^1)^{w_{\mathcal{O}}} e^{i\sigma^3 \phi_{\mathcal{O}}(\boldsymbol{r})}$, where $w_{\mathcal{O}} = 0$ or 1, $\mathcal{O} \in \{T_1, T_2, T_3, \overline{C}_6, S\}$. From Eq. (A.21e) we see we must have $w_{T_3} = 0$, further from Eq. (A.21d) we have $w_{T_1} = w_{T_2} = 0$. Therefore Eq. (A.21a) becomes a pure phase equation

$$\phi_{T_i}(\boldsymbol{r}_\mu) + \phi_{T_{i+1}}[T_i^{-1}(\boldsymbol{r}_\mu)] - \phi_{T_i}[T_{i+1}^{-1}(\boldsymbol{r}_\mu)] - \phi_{T_{i+1}}(\boldsymbol{r}_\mu) = \chi_i, \tag{A.43}$$

using gauge freedom to set $\phi_{T_1}(\boldsymbol{r}_\mu) = 0$, $\phi_{T_2}(r_1, 0, 0)_\mu = 0$, and $\phi_{T_3}(r_1, r_2, 0) = 0$, we have

$$\phi_{T_1}(\boldsymbol{r}_\mu) = 0, \quad \phi_{T_2}(\boldsymbol{r}_\mu) = -\chi_1 r_1, \quad \phi_{T_3}(\boldsymbol{r}_\mu) = \chi_3 r_1 - \chi_2 r_2. \tag{A.44}$$

Eq. (A.21d) gives

$$(-1)^{w_{\overline{C}_6}} \left(\phi_{\overline{C}_6}(\boldsymbol{r}_\mu) + \phi_{T_i}[\overline{C}_6^{-1}(\boldsymbol{r}_\mu)] - \phi_{\overline{C}_6}[T_{i+1}(\boldsymbol{r}_\mu)] \right) + \phi_{T_{i+1}}[T_{i+1}(\boldsymbol{r}_\mu)] = \chi_{\overline{C}_6 T_i}, \quad \text{(A.45)}$$

consistency condition

$$\Delta_i \phi_{\overline{C}_6}(\boldsymbol{r}_\mu) + \Delta_{i+1} \phi_{\overline{C}_6}[T_i^{-1}(\boldsymbol{r}_\mu)] = \Delta_{i+1} \phi_{\overline{C}_6}(\boldsymbol{r}_\mu) + \Delta_i \phi_{\overline{C}_6}[T_{i+1}^{-1}(\boldsymbol{r}_\mu)], \quad i = 1, 2, 3 \quad \text{(A.46)}$$

where we defined $\Delta_i \phi(\boldsymbol{r}_\mu) = \phi(\boldsymbol{r}_\mu) - \phi[T_i^{-1}(\boldsymbol{r}_\mu)]$, requires

$$(-1)^{w_{\overline{C}_6}} \chi_1 = \chi_3, \quad -\chi_1 + (-1)^{w_{\overline{C}_6}} \chi_2 = 0, \quad \chi_2 = (-1)^{w_{\overline{C}_6}} \chi_3, \quad \text{(A.47)}$$

which means that, if $w_{\overline{C}_6} = 0$, then $\chi_1 = \chi_2 = \chi_3$ and no quantization condition is imposed on $\chi_{1,2,3}$; if $w_{\overline{C}_6} = 1$, then $\chi_1 = \chi_2 = \chi_3 = 0$ or π. Combining the two cases we can write

$$\phi_{\overline{C}_6}(\boldsymbol{r}_\mu) = -r_1(r_2 - r_3)\chi_1 - (\delta_{\mu,2} - \delta_{\mu,3})\chi_1 r_1 + \delta_{\mu,2}\chi_1 r_3 \\ - (-1)^{w_{\overline{C}_6}}(\chi_{\overline{C}_6 T_3} r_1 + \chi_{\overline{C}_6 T_1} r_2 + \chi_{\overline{C}_6 T_2} r_3) + \rho_\mu, \quad \text{(A.48)}$$

where we abbreviated $\rho_\mu \equiv \phi_{\overline{C}_6}(0, 0, 0)_\mu$. Plug the expression (A.48) in Eq. (A.21b), we get the condition

• When $w_{\overline{C}_6} = 0$,

$$6\rho_0 = 2(\rho_1 + \rho_2 + \rho_3) + \chi_{\overline{C}_6 T_1} + \chi_{\overline{C}_6 T_2} + \chi_{\overline{C}_6 T_3} = \chi_{\overline{C}_6}; \quad \text{(A.49)}$$

• when $w_{\overline{C}_6} = 1$,

$$\chi_{\overline{C}_6} = \chi_{\overline{C}_6 T_1} + \chi_{\overline{C}_6 T_2} + \chi_{\overline{C}_6 T_3} = 0. \quad \text{(A.50)}$$

Plug the result (A.44) in Eqs. (A.21e) and Eq. (A.21f), we get

$$\Delta_1 \phi_S(\boldsymbol{r}_\mu) = \chi_1(r_1 - r_2 + \delta_{\mu,1} - \delta_{\mu,2}) + (-1)^{w_S}(-\chi_{ST_1} + \chi_{ST_3}), \quad \text{(A.51a)}$$
$$\Delta_2 \phi_S(\boldsymbol{r}_\mu) = \chi_1(2r_1 - (-1)^{w_S} r_1 - r_2 + 2\delta_{\mu,1} - \delta_{\mu,2}) + (-1)^{s_W}(-\chi_{ST_2} + \chi_{ST_3}), \quad \text{(A.51b)}$$
$$\Delta_3 \phi_S(\boldsymbol{r}_\mu) = \chi_1((1 + (-1)^{w_S})(r_1 - r_2) + \delta_{\mu,1} - \delta_{\mu,2}) + (-1)^{w_S} \chi_{ST_3}. \quad \text{(A.51c)}$$

Consistency conditions for ϕ_S similar to (A.46) give

$$(-2 + (-1)^{w_S})\chi_1 = \chi_1, \quad (1 + (-1)^{w_S})\chi_1 = 0, \quad 0 = -(1 + (-1)^{w_S})\chi_1, \quad \text{(A.52)}$$

therefore when $w_S = 0$, $\chi_1 = 0$ or π; when $w_S = 1$, $\chi_1 = 0$, $\frac{\pi}{2}$, π or $\frac{3\pi}{2}$. And

$$
\begin{aligned}
\phi_S(\boldsymbol{r}_\mu) = {} & \left(\frac{(r_1+1)r_1}{2} - \frac{(r_2+1)r_2}{2} - r_1 r_2 \right) \chi_1 \\
& + \left[(\delta_{\mu,1} - \delta_{\mu,2})\chi_1 + (-1)^{w_S}(\chi_{ST_3} - \chi_{ST_1}) \right] r_1 \\
& + \left[(2\delta_{\mu,1} - \delta_{\mu,2})\chi_1 + (-1)^{w_S}(\chi_{ST_3} - \chi_{ST_2}) \right] r_2 \\
& + \left[(\delta_{\mu,1} - \delta_{\mu,2})\chi_1 + (-1)^{w_S}\chi_{ST_3} \right] r_3 \\
& + \theta_\mu,
\end{aligned}
\tag{A.53}
$$

where we abbreviated $\theta_\mu = \phi_S(0,0,0)_\mu$. Plug the result (A.53) and (A.44) into Eq. (A.21c), we get

- When $w_S = 0$,

$$
\chi_{ST_3} = 0, \tag{A.54a}
$$
$$
\theta_0 + \theta_3 = 2\theta_1 - \chi_1 + \chi_{ST_1} = 2\theta_2 + \chi_1 + \chi_{ST_2} = \chi_S; \tag{A.54b}
$$

- When $w_S = 1$,

$$
2\chi_1 + 2\chi_{ST_1} - \chi_{ST_3} = 2\chi_1 - 2\chi_{ST_2} + \chi_{ST_3} = 0, \tag{A.55a}
$$
$$
-\theta_0 + \theta_3 + \chi_{ST_3} = -\chi_1 - \chi_{ST_1} + \chi_{ST_3} = \chi_1 - \chi_{ST_2} + \chi_{ST_3} = \theta_0 - \theta_3 = \chi_S. \tag{A.55b}
$$

At this point we are left with two equations, (A.21g) and (A.21h). Depending on the $\mathbb{Z}_2$ value of $w_{\overline{C}_6}$ and w_S we have the following four cases:

- $(w_{\overline{C}_6}, w_S) = (0,0)$: Eq. (A.21g) gives

$$
\chi_{\overline{C}_6 T_1} + \chi_{\overline{C}_6 T_2} + \chi_{\overline{C}_6 T_3} + \sum_{\mu=0}^{3} (\rho_\mu + \theta_\mu) = \chi_{\overline{C}_6 S}, \tag{A.56}
$$

and Eq. (A.21h) gives

$$
2\chi_{ST_1} - 3\chi_{\overline{C}_6 T_1} + 3\chi_{\overline{C}_6 T_2} - \chi_{\overline{C}_6 T_3} = 2\chi_{ST_2} - 3\chi_{\overline{C}_6 T_1} - \chi_{\overline{C}_6 T_2} + 3\chi_{\overline{C}_6 T_3} = 0, \tag{A.57a}
$$
$$
\begin{aligned}
\theta_0 + \theta_3 + 3\rho_0 + \rho_1 + \rho_2 + \rho_3 + \chi_{\overline{C}_6 T_2} + \chi_{\overline{C}_6 T_3} &= 2\theta_1 + 2(\rho_1 + \rho_2 + \rho_3) + 2\chi_{\overline{C}_6 T_1} + 2\chi_{\overline{C}_6 T_3} \\
&= 2\theta_2 + 2(\rho_1 + \rho_2 + \rho_3) + 2\chi_{\overline{C}_6 T_1} + 2\chi_{\overline{C}_6 T_2} \\
&= \chi_{S\overline{C}_6}.
\end{aligned} \tag{A.57b}
$$

- $(w_{\overline{C}_6}, w_S) = (0,1)$: Eq. (A.21g) gives

$$
-\theta_0 - \theta_1 + \theta_2 + \theta_3 + \rho_0 - \rho_1 + \rho_2 - \rho_3 + \chi_{\overline{C}_6 T_1} - \chi_{\overline{C}_6 T_2} - \chi_{\overline{C}_6 T_3} = \chi_{\overline{C}_6 S}, \tag{A.58a}
$$

240

$$\theta_0 + \theta_1 - \theta_2 - \theta_3 - \rho_0 + \rho_1 - \rho_2 + \rho_3$$
$$- 2(\chi_{ST_1} - \chi_{ST_2} + \chi_{ST_3}) + \chi_{\overline{C}_6 T_1} - \chi_{\overline{C}_6 T_2} - \chi_{\overline{C}_6 T_3} = \chi_{\overline{C}_6 S}, \tag{A.58b}$$
$$2(-\chi_{ST_1} + \chi_{ST_2} - \chi_{ST_3}) + 2(\chi_{\overline{C}_6 T_1} - \chi_{\overline{C}_6 T_2} - \chi_{\overline{C}_6 T_3}) = 0, \tag{A.58c}$$

where the second equation can be obtained from the first and the third. Eq. (A.21h) gives

$$- \chi_{ST_3} + \chi_{\overline{C}_6 T_1} - \chi_{\overline{C}_6 T_2} - \chi_{\overline{C}_6 T_3} = 0, \tag{A.59a}$$
$$- \theta_0 + \theta_3 + 3\rho_0 - \rho_1 - \rho_2 - \rho_3 - \chi_{\overline{C}_6 T_2} - \chi_{\overline{C}_6 T_3} = -\chi_{ST_3} + \chi_{\overline{C}_6 T_1} - \chi_{\overline{C}_6 T_2} - \chi_{\overline{C}_6 T_3}$$
$$= \theta_0 - \theta_3 - 3\rho_0 + \rho_1 + \rho_2 + \rho_3 + \chi_{\overline{C}_6 T_2} + \chi_{\overline{C}_6 T_3}$$
$$= \chi_{S\overline{C}_6}, \tag{A.59b}$$

- $(w_{\overline{C}_6}, w_S) = (1, 0)$: Eq. (A.21g) gives

$$2(\chi_{ST_1} - \chi_{ST_2} + \chi_{ST_3}) + 2(\chi_{\overline{C}_6 T_1} - \chi_{\overline{C}_6 T_2} - \chi_{\overline{C}_6 T_3}) = 0, \tag{A.60a}$$
$$- \theta_0 - \theta_1 + \theta_2 + \theta_3 - \rho_0 + \rho_1 - \rho_2 + \rho_3 + \chi_{\overline{C}_6 T_1} - \chi_{\overline{C}_6 T_2} - \chi_{\overline{C}_6 T_3}$$
$$= \theta_0 + \theta_1 - \theta_2 - \theta_3 + \rho_0 - \rho_1 + \rho_2 - \rho_3 - \chi_{\overline{C}_6 T_1} + \chi_{\overline{C}_6 T_2} + \chi_{\overline{C}_6 T_3}$$
$$= \chi_{\overline{C}_6 S}, \tag{A.60b}$$

this gives $2\chi_{\overline{C}_6 S} = 0$ so $\chi_{\overline{C}_6 S} = 0$ or π. Eq. (A.21h) gives

$$\chi_{ST_3} - \chi_{\overline{C}_6 T_1} - \chi_{\overline{C}_6 T_2} - \chi_{\overline{C}_6 T_3} = 0, \tag{A.61a}$$
$$- \theta_0 + \theta_3 - \rho_0 + \rho_1 - \rho_2 + \rho_3 - \chi_{\overline{C}_6 T_2} - \chi_{\overline{C}_6 T_3} = 0 = \chi_{S\overline{C}_6}. \tag{A.61b}$$

- $(w_{\overline{C}_6}, w_S) = (1, 1)$: Eq. (A.21g) gives

$$\sum_{\mu=0}^{3} (\theta_\mu - \rho_\mu) = \chi_{\overline{C}_6 S}, \tag{A.62}$$

and Eq. (A.21h) gives

$$- 2\chi_{ST_1} + \chi_{ST_3} = -2\chi_{ST_2} + \chi_{ST_3} = 0, \tag{A.63a}$$
$$\theta_0 + \theta_3 - \rho_0 - \rho_1 + \rho_2 - \rho_3 + \chi_{\overline{C}_6 T_2} + \chi_{\overline{C}_6 T_3} = 2\theta_1 - 2\rho_1 - 2\rho_2 + 2\rho_3 - 2\chi_{\overline{C}_6 T_2}$$
$$= 2\theta_2 + 2\rho_1 - 2\rho_2 - 2\rho_3 - 2\chi_{\overline{C}_6 T_3} = \chi_{S\overline{C}_6}. \tag{A.63b}$$

We now choose a gauge to fix some of the phases. This gauge applies to all four classes above. First, under gauge transformation $W(\boldsymbol{r}_\mu) = 1$ for $\mu = 0$, $W(\boldsymbol{r}_i) = e^{i\sigma^3 \psi_i r_i}$ for $i = 1, 2, 3$, where ψ_i is any constant phase, the values of $\chi_{\overline{C}_6 T_1}$, $\chi_{\overline{C}_6 T_2}$ and χ_{ST_2} change. This means they are ineffective in labeling the PSG classes, and by properly choosing ψ_i

we can set them to be

$$\chi_{\overline{C}_6 T_1} = 0, \quad \chi_{\overline{C}_6 T_2} = 0, \quad \chi_{ST_2} = 0. \tag{A.64}$$

Then, we can use the IGG freedom (the freedom of choosing a global U(1) phase) to set

$$\rho_0 = \theta_2 = 0 \quad \Rightarrow \quad \chi_{\overline{C}_6} = 0. \tag{A.65}$$

Finally, using the "sublattice" gauge transformation

$$W(\boldsymbol{r}_\mu) = e^{i\phi_\mu} \tag{A.66}$$

where ϕ_μ is any constant phase, $W_{\overline{C}_6}(\boldsymbol{r}_\mu)$ for $\mu = 1, 2$ and $W_S(\boldsymbol{r}_\mu)$ for $\mu = 0$ will transform as

$$
\begin{aligned}
(i\sigma^1)^{w_{\overline{C}_6}} e^{i\phi_{\overline{C}_6}(\boldsymbol{r}_1)\sigma^3} &\rightarrow e^{i\phi_1\sigma^3}(i\sigma_1)^{w_{\overline{C}_6}} e^{i\phi_{\overline{C}_6}(\boldsymbol{r}_2)\sigma^3} e^{-i\phi_3\sigma^3} \\
&= (i\sigma^1)^{w_{\overline{C}_6}} e^{i((-1)^{w_{\overline{C}_6}}\phi_1 + \phi_{\overline{C}_6}(\boldsymbol{r}_1) - \phi_3)\sigma^3},
\end{aligned} \tag{A.67a}
$$

$$
\begin{aligned}
(i\sigma^1)^{w_{\overline{C}_6}} e^{i\phi_{\overline{C}_6}(\boldsymbol{r}_1)\sigma^3} &\rightarrow e^{i\chi_1\sigma^3}(i\sigma^1)^{w_{\overline{C}_6}} e^{i\phi_{\overline{C}_6}(\boldsymbol{r}_2)\sigma^3} e^{-i\phi_1\sigma^3} \\
&= (i\sigma_1)^{w_{\overline{C}_6}} e^{i((-1)^{w_{\overline{C}_6}}\phi_2 + \phi_{\overline{C}_6}(\boldsymbol{r}_2) - \phi_1)\sigma^3},
\end{aligned} \tag{A.67b}
$$

$$
\begin{aligned}
(i\sigma_1)^{w_S} e^{i\phi_S(\boldsymbol{r}_0)\sigma^3} &\rightarrow e^{i\phi_0\sigma^3}(i\sigma^1)^{w_S} e^{i\phi_S(\boldsymbol{r}_0)\sigma^3} e^{-i\phi_3\sigma^3} \\
&= (i\sigma^1)^{w_S} e^{i((-1)^{w_S}\phi_0 + \phi_S(\boldsymbol{r}_0) - \phi_3)\sigma^3}.
\end{aligned} \tag{A.67c}
$$

Then, by properly choosing $\phi_{0,1,2,3}$ we are able to set

$$\rho_1 = \rho_2 = \theta_0 = 0. \tag{A.68}$$

Eqs. (A.64), (A.65) and (A.68) significantly simply Eqs. (A.56)–(A.63), and furthermore allow them to be solved without any ambiguity. The final result is presented in Table 5.1.

A.7 Solving fermionic $\mathbb{Z}_2$ PSG equations

In solving the $\mathbb{Z}_2$ PSG equations (A.21), all the $\chi \in \{0, \pi\}$, therefore we introduce a short hand notation

$$\eta = e^{i\sigma^3\chi} = \pm 1 \quad \text{for } \chi\text{'s in Eq. (A.21)} \tag{A.69}$$

The general form for $W_{\overline{C}_6}(\boldsymbol{r}_\mu)$ and $W_S(\boldsymbol{r}_\mu)$ is given in Eqs. (5.1b) and (5.1c). Here, in order to clearly distinguish different notations, we will rewrite the SU(2) matrices at the origin $W_{\mathcal{O},\mu}$ using a different symbol

$$g_{\mathcal{O},\mu} \equiv W_{\mathcal{O},\mu} \quad \text{for } \mathcal{O} = \overline{C}_6, S. \tag{A.70}$$

The solution is in complete parallel to the U(1) PSG case which we briefly review below.

First solve Eq. (A.21a): using gauge freedom as in the U(1) case, we get

$$W_{T_1}(\boldsymbol{r}_\mu) = 1, \quad W_{T_2}(\boldsymbol{r}_\mu) = \eta_1^{r_1}, \quad W_{T_3}(\boldsymbol{r}_\mu) = \eta_3^{r_1}\eta_2^{r_2}. \tag{A.71}$$

Then solve Eq. (A.21d): plugging in the solution (A.71), we have

$$W_{\overline{C}_6}(\boldsymbol{r}_\mu)W_{\overline{C}_6}^{-1}[T_2(\boldsymbol{r}_\mu)]\eta_1^{r_1} = \eta_{\overline{C}_6 T_1}, \tag{A.72a}$$

$$W_{\overline{C}_6}(\boldsymbol{r}_\mu)\eta_1^{-(r_2+\delta_{\mu,2})}W_{\overline{C}_6}^{-1}[T_3(\boldsymbol{r}_\mu)]\eta_3^{r_1}\eta_2^{r_2} = \eta_{\overline{C}_6 T_2}, \tag{A.72b}$$

$$W_{\overline{C}_6}(\boldsymbol{r}_\mu)\eta_3^{-(r_2+\delta_{\mu,2})}\eta_2^{-(r_3+\delta_{\mu,3})}W_{\overline{C}_6}^{-1}[T_1(\boldsymbol{r}_\mu)] = \eta_{\overline{C}_6 T_3}. \tag{A.72c}$$

Consistency condition requires $\eta_1 = \eta_2 = \eta_3$ and we get

$$W_{\overline{C}_6}(\boldsymbol{r}_\mu) = g_{\overline{C}_6,\mu}\eta_1^{r_1(r_2+r_3)} \cdot (\eta_{\overline{C}_6 T_3}\eta_1^{\delta_{\mu,2}+\delta_{\mu,3}})^{r_1}\eta_{\overline{C}_6 T_1}^{r_2}(\eta_{\overline{C}_6 T_2}\eta_1^{\delta_{\mu,2}})^{r_3}. \tag{A.73}$$

Then solve Eq. (A.21e) and Eq. (A.21f): plugging in the solution (A.71), we have

$$W_S(\boldsymbol{r}_\mu)W_S^{-1}[T_1 T_3^{-1}(\boldsymbol{r}_\mu)]\eta_1^{-(r_1+r_2+1)} = \eta_{ST_1}, \tag{A.74a}$$

$$W_S(\boldsymbol{r}_\mu)\eta_1^{-(r_1+\delta_{\mu,1})}W_S^{-1}[T_2 T_3^{-1}(\boldsymbol{r}_\mu)]\eta_1^{-(r_1+r_2+1)}\eta_1^{r_1} = \eta_{ST_2}, \tag{A.74b}$$

$$W_S(\boldsymbol{r}_\mu)\eta_1^{-(r_1+r_2+\delta_{\mu,1}+\delta_{\mu,2})}W_S^{-1}[T_3^{-1}(\boldsymbol{r}_\mu)]\eta_1^{-(r_1+r_2)} = \eta_{ST_3}. \tag{A.74c}$$

The consistency condition is always satisfied, and we have

$$W_S(\boldsymbol{r}_\mu) = g_{S,\mu}\eta_1^{\frac{(r_1+r_2)(r_1+r_2+1)}{2}}(\eta_{ST_1}\eta_{ST_3}\eta_1^{\delta_{\mu,1}+\delta_{\mu,2}})^{r_1}(\eta_{ST_2}\eta_{ST_3}\eta_1^{\delta_{\mu,2}})^{r_2}(\eta_{ST_3}\eta_1^{\delta_{\mu,1}+\delta_{\mu,2}})^{r_3}. \tag{A.75}$$

Now we are left with Eqs. (A.21b), (A.21c), (A.21g), and (A.21h). Plugging the solution for $W_{T_{1,2,3},\overline{C}_6,S}$ that we just obtained in these equations, we are led to the following constraints

$$\eta_{\overline{C}_6 T_1}\eta_{\overline{C}_6 T_2}\eta_{\overline{C}_6 T_3} = 1, \tag{A.76a}$$

$$\eta_{ST_3} = 1, \tag{A.76b}$$

and the following equations to solve

$$g_{\overline{C}_6,0}^6 = (g_{\overline{C}_6,1}g_{\overline{C}_6,3}g_{\overline{C}_6,2})^2 = \eta_{\overline{C}_6}, \tag{A.77a}$$

$$g_{S,1}^2\eta_{ST_1}\eta_1 = g_{S,2}^2\eta_{ST_2}\eta_1 = g_{S,3}g_{S,0} = \eta_S, \tag{A.77b}$$

$$g_{\overline{C}_6,0}g_{S,0}g_{\overline{C}_6,3}g_{S,2}g_{\overline{C}_6,2}g_{S,1}g_{\overline{C}_6,1}g_{S,3} = \eta_{\overline{C}_6 S}, \tag{A.77c}$$

$$\eta_{\overline{C}_6 T_1}g_{\overline{C}_6,0}^3g_{S,0}g_{\overline{C}_6,3}g_{\overline{C}_6,2}g_{\overline{C}_6,1}g_{S,3} = \eta_{S\overline{C}_6}, \tag{A.77d}$$

$$g_{\overline{C}_6,1}g_{\overline{C}_6,3}g_{\overline{C}_6,2}g_{S,1}g_{\overline{C}_6,1}g_{\overline{C}_6,3}g_{\overline{C}_6,2}g_{S,1} = \eta_{S\overline{C}_6}, \tag{A.77e}$$

$$g_{\overline{C}_6,2}g_{\overline{C}_6,1}g_{\overline{C}_6,3}g_{S,2}g_{\overline{C}_6,2}g_{\overline{C}_6,1}g_{\overline{C}_6,3}g_{S,2} = \eta_{S\overline{C}_6}, \tag{A.77f}$$

$$g_{\overline{C}_6,3}g_{\overline{C}_6,2}g_{\overline{C}_6,1}g_{S,3}g_{\overline{C}_6,0}^3 g_{S,0}\eta_{\overline{C}_6 T_1} = \eta_{S\overline{C}_6}. \tag{A.77g}$$

First let us use the IGG gauge freedom to simplify these equations. We can always set $\eta_S = \eta_{\overline{C}_6 T_1} = \eta_{\overline{C}_6 T_2} = 1$, and by Eq. (A.76a) we also have $\eta_{\overline{C}_6 T_3} = 1$. Then, under the "sublattice" gauge transformation (A.66), we can fix $g_{\overline{C}_6,1} = 1$, $g_{\overline{C}_6,2} = 1$, and $g_{S,0} = 1$. Note this also implies $g_{S,3} = 1$. To summarize, gauge fixing gives

$$g_{\overline{C}_6,1} = g_{\overline{C}_6,2} = g_{S,0} = g_{S,3} = 1. \tag{A.78}$$

Now Eq. (A.77) is simplified to

$$g_{\overline{C}_6,0}^6 = g_{\overline{C}_6,3}^2 = \eta_{\overline{C}_6}, \tag{A.79a}$$

$$g_{S,1}^2 \eta_{ST_1}\eta_1 = g_{S,2}^2 \eta_{ST_2}\eta_1 = 1, \tag{A.79b}$$

$$g_{\overline{C}_6,0}g_{\overline{C}_6,3}g_{S,2}g_{S,1} = \eta_{\overline{C}_6 S}, \tag{A.79c}$$

$$g_{\overline{C}_6,0}^3 g_{\overline{C}_6,3} = \eta_{S\overline{C}_6}, \tag{A.79d}$$

$$g_{\overline{C}_6,3}g_{S,1}g_{\overline{C}_6,3}g_{S,1} = \eta_{S\overline{C}_6}, \tag{A.79e}$$

$$g_{\overline{C}_6,3}g_{S,2}g_{\overline{C}_6,3}g_{S,2} = \eta_{S\overline{C}_6}. \tag{A.79f}$$

Next we claim that

$$\eta_{ST_1} = \eta_{ST_2}. \tag{A.80}$$

The proof proceeds as follows: If $\eta_{\overline{C}_6} = 1$ then Eq. (A.79a) gives $g_{\overline{C}_6,3} = \pm 1$, which together with Eqs. (A.79e) and (A.79f) proves (A.80) in Eq. (A.79b). If $\eta_{\overline{C}_6} = -1$, then $g_{\overline{C}_6,3} = i\boldsymbol{a}\cdot\boldsymbol{\sigma}$ for some unit vector $\boldsymbol{a}$, and we proceed to prove $\eta_{ST_1} = \eta_{ST_2}$ by contradiction: without loss of generality we assume $\eta_{ST_1}\eta_1 = 1 = -\eta_{ST_2}\eta_1$, then $g_{S,1} \equiv \eta_{S,1} = \pm 1$ and $g_{S,2} = i\boldsymbol{b}\cdot\boldsymbol{\sigma}$ for some unit vector $\boldsymbol{b}$. Therefore Eq. (A.79e) gives $\eta_{S\overline{C}_6} = -1$, and Eq. (A.79f) gives $[(i\boldsymbol{a}\cdot\boldsymbol{\sigma})(i\boldsymbol{b}\cdot\boldsymbol{\sigma})]^2 = -1$, which implies $\boldsymbol{a} \perp \boldsymbol{b}$ and that $g_{\overline{C}_6,3}g_{S,2} = -i\boldsymbol{c}\cdot\boldsymbol{\sigma}$ with $\boldsymbol{c} = \boldsymbol{b} \times \boldsymbol{a}$. Then from Eq. (A.79c) we get $g_{\overline{C}_6,0} = i\boldsymbol{c}\cdot\boldsymbol{\sigma}\eta_{S\overline{C}_6}\eta_{S,1}$, which contradicts Eq. (A.79d) given that $\boldsymbol{c} \perp \boldsymbol{a}$. Therefore Eq. (A.80) holds.

Next, depending on the value of $\eta_{S\overline{C}_6}$, $\eta_{\overline{C}_6}$, η_{ST_1} and η_1, we have the following cases:

- If $\eta_1\eta_{ST_1} = 1$, then $g_{S,1} = \pm 1$ and $g_{S,2} = \pm 1$, then we have

$$\eta_{S\overline{C}_6} = g_{\overline{C}_6,3}^2 = \eta_{\overline{C}_6}, \tag{A.81}$$

  meaning that Eq. (A.79c) to the cubic power gives $g_{\overline{C}_6,0}^3 = g_{\overline{C}_6,3}^{-3}\eta_{S\overline{C}_6}g_{S,2}g_{S,1}$; together with Eq. (A.81) we see that

$$g_{S,1}g_{S,2} = \eta_{\overline{C}_6 S}. \tag{A.82}$$

We have the following two cases after gauge fixing:

244

– When $\eta_{S\overline{C}_6} = \eta_{\overline{C}_6} = 1$,

$$(g_{\overline{C}_6,0}, g_{\overline{C}_6,3}, g_{S,1}, g_{S_2}) = (1, 1, 1, \eta_{\overline{C}_6 S}); \tag{A.83}$$

– When $\eta_{S\overline{C}_6} = \eta_{\overline{C}_6} = -1$,

$$(g_{\overline{C}_6,0}, g_{\overline{C}_6,3}, g_{S,1}, g_{S_2}) = (-i\sigma^k, i\sigma^k, 1, \eta_{\overline{C}_6 S}), \tag{A.84}$$

where σ^k can be any of the three Pauli matrices.

- If $\eta_1 \eta_{ST_1} = -1$, we have $g_{S,1} = i\boldsymbol{n}_1 \cdot \boldsymbol{\sigma}$ and $g_{S,2} = i\boldsymbol{n}_2 \cdot \boldsymbol{\sigma}$ for some unit vectors $\boldsymbol{n}_1$ and $\boldsymbol{n}_2$. We have:

  – If $\eta_{\overline{C}_6} = 1$, then $g_{\overline{C}_6,3} = \pm 1$ therefore $\eta_{S\overline{C}_6} = -1$. Combine (A.79c) and (A.79d) we get $(g_{S,2}g_{S,1})^{-3} = -\eta_{S\overline{C}_6}$, which gives $g_{S,2}g_{S,1} = e^{i\frac{\pi}{3}j\boldsymbol{n}\cdot\boldsymbol{\sigma}}$ for some unit vector $\boldsymbol{n}$, and $j = 1, 3$ for $\eta_{\overline{C}_6 S} = 1$ while $j = 0, 2$ for $\eta_{\overline{C}_6 S} = -1$. This then implies $\boldsymbol{n}_2 \cdot \boldsymbol{n}_1 + i(\boldsymbol{n}_2 \times \boldsymbol{n}_1) \cdot \boldsymbol{\sigma} = -e^{i\frac{\pi}{3}j\boldsymbol{n}\cdot\boldsymbol{\sigma}}$. After gauge fixing, we get

$$\begin{aligned}
&(g_{\overline{C}_6,0}, g_{\overline{C}_6,3}, g_{S,1}, g_{S,2}) \\
&= (-\sigma^k(\cos\frac{\pi j}{3}\sigma^k + \sin\frac{\pi j}{3}\sigma^{k+1}), 1, i\sigma^k, i(\cos\frac{\pi j}{3}\sigma^k + \sin\frac{\pi j}{3}\sigma^{k+1})),
\end{aligned} \tag{A.85}$$

  where σ^k can be any of the three Pauli matrices. This gives eight classes depending on the values of η_1, $\eta_{\overline{C}_6}$ and j.

  – if $\eta_{\overline{C}_6} = -1$, we have $g_{\overline{C}_6,3} = i\boldsymbol{n}_3 \cdot \boldsymbol{\sigma}$ for some $\boldsymbol{n}_3$, and $g_{\overline{C}_6,0}^3 = -i\boldsymbol{n}_3 \cdot \boldsymbol{\sigma}\eta_{S\overline{C}_6}$. Define $g_{\overline{C}_6,0} = e^{i\theta\boldsymbol{n}_0\cdot\boldsymbol{\sigma}}$, then we have $\cos 3\theta = 0$, $\theta = \frac{\pi(2j+1)}{6}$, which gives $g_{\overline{C}_6,0} = e^{-i\frac{\pi(2j+1)}{6}(-1)^j\eta_{S\overline{C}_6}\boldsymbol{n}_3\cdot\boldsymbol{\sigma}}$, with independent $j = 0, 1, 2$. Choose gauge fixing such that $g_{S,1} = i\sigma^k$ where σ^k is any of the three Pauli matrices (we denote the corresponding $\boldsymbol{n}_1$ as $\boldsymbol{x}_k$) and $g_{S,2} = e^{i\phi\sigma^{k-1}}i\sigma^k$ for some ϕ, then equation (A.79e) requires that $\boldsymbol{n}_3$ be either parallel (anti-parallel) or perpendicular to $\boldsymbol{x}_k$, depending on the value of $\eta_{S\overline{C}_6}$. After gauge fixing, we obtain the following form:

    * If $\eta_{S\overline{C}_6} = 1$, we have

$$(g_{\overline{C}_6,0}, g_{\overline{C}_6,3}, g_{S,1}, g_{S,2}) = (i\sigma^k, i\sigma^k, i\sigma^k, \eta_{\overline{C}_6 S}i\sigma^k), \tag{A.86}$$

    the parameters $\eta_{\overline{C}_6 S}$ and η_1 give four independent classes.
    * If $\eta_{S\overline{C}_6} = -1$, we have

$$\begin{aligned}
&(g_{\overline{C}_6,0}, g_{\overline{C}_6,3}, g_{S,1}, g_{S,2}) \\
&= (e^{i\frac{\pi(2j+1)}{6}(-1)^j\sigma^{k-1}}, i\sigma^{k-1}, i\sigma^k, -\eta_{\overline{C}_6 S}i\sigma^k e^{i(\frac{\pi}{2}+\frac{\pi(2j+1)}{6}(-1)^j)\sigma^{k-1}}),
\end{aligned} \tag{A.87}$$

245

where $j = 0, 1$ together with $\eta_{\overline{C}_6 S}$ and η_1 gives eight independent classes.

The final result is presented in Table 5.2.

A.8 Fermionic U(1) PSG: adding time reversal

There is one complication when considering time reversal $\mathcal{T}$. Acting on spins, it is the anti-unitary operator

$$\mathcal{T}\colon \hat{\boldsymbol{S}} \to i\sigma^y \mathcal{K} \hat{\boldsymbol{S}}(-i\sigma^y \mathcal{K}), \tag{A.88}$$

where $\mathcal{K}$ is the complex conjugation operator that complex conjugates everything on its right. This induces an action on Ψ as

$$\mathcal{T}\colon \Psi \to (i\sigma^y)\mathcal{K}\Psi. \tag{A.89}$$

Introducing a gauge field associated to $\mathcal{T}$, we have

$$G_{\mathcal{T}} \circ \mathcal{T}\colon \Psi(\boldsymbol{r}_\mu) \to (i\sigma^y)\mathcal{K}\Psi(\boldsymbol{r}_\mu)W_{\mathcal{T}}(\boldsymbol{r}_\mu). \tag{A.90}$$

Now we apply this to a mean-field bond:

$$
\begin{aligned}
G_{\mathcal{T}} \circ \mathcal{T}\colon H^{\alpha}_{\boldsymbol{r}_\mu,\boldsymbol{r}'_\nu} \to &\operatorname{Tr}\left[(\sigma^\alpha)^*(i\sigma^y)\mathcal{K}\Psi(\boldsymbol{r}_\mu)W_{\mathcal{T}}(\boldsymbol{r}_\mu)u^{\alpha}_{\boldsymbol{r}_\mu,\boldsymbol{r}'_\nu}W^{\dagger}_{\mathcal{T}}(\boldsymbol{r}'_\nu)\Psi^{\dagger}(\boldsymbol{r}'_\nu)(-i\sigma^y)\mathcal{K}\right] \\
= &\operatorname{Tr}\left[(\sigma^\alpha)^*\sigma^y\Psi(\boldsymbol{r}_\mu)W^*_{\mathcal{T}}(\boldsymbol{r}_\mu)\left(u^{\alpha}_{\boldsymbol{r}_\mu,\boldsymbol{r}'_\nu}\right)^*W^T_{\mathcal{T}}(\boldsymbol{r}'_\nu)\Psi^{\dagger}(\boldsymbol{r}'_\nu)\sigma^y\right],
\end{aligned} \tag{A.91}
$$

where we have noted that both the bond $u^{\alpha}_{\boldsymbol{r}_\mu,\boldsymbol{r}'_\nu}$ and σ^α are complex-conjugated by $\mathcal{K}$. However we can get rid of this complex conjugation by defining a new gauge field $\widetilde{W}_{\mathcal{T}}(\boldsymbol{r}_\mu)$ by

$$W_{\mathcal{T}}(\boldsymbol{r}_\mu) \equiv i\sigma^2 \widetilde{W}_{\mathcal{T}}(\boldsymbol{r}_\mu). \tag{A.92}$$

Using the identity $\sigma^2 u \sigma^2 = u^*$ for $u \in \mathrm{SU}(2)$, we have $W^*_{\mathcal{T}}(\boldsymbol{r}_\mu) = \widetilde{W}_{\mathcal{T}}(\boldsymbol{r}_\mu)i\sigma^2$ and

$$
\begin{aligned}
\sigma^2 \left(u^{0}_{\boldsymbol{r}_\mu,\boldsymbol{r}'_\nu}\right)^* \sigma^2 &= -u^{0}_{\boldsymbol{r}_\mu,\boldsymbol{r}'_\nu}, \\
\sigma^2 \left(u^{(i)}_{\boldsymbol{r}_\mu,\boldsymbol{r}'_\nu}\right)^* \sigma^2 &= u^{(i)}_{\boldsymbol{r}_\mu,\boldsymbol{r}'_\nu}, \quad i = x, y, z,
\end{aligned} \tag{A.93}
$$

and

$$
\begin{aligned}
\sigma^2(\sigma^0)^*\sigma^2 &= \sigma^0, \\
\sigma^2(\sigma^i)^*\sigma^2 &= -\sigma^i, \quad i = x, y, z,
\end{aligned} \tag{A.94}
$$

we see that the form (5.6) is specially designed so that

$$G_{\mathcal{T}} \circ \mathcal{T}: H^{\alpha}_{\boldsymbol{r}_{\mu},\boldsymbol{r}'_{\nu}} = \text{Tr}\left[\sigma^{\alpha}\Psi_{\boldsymbol{r}_{\mu}} u^{\alpha}_{\boldsymbol{r}_{\mu},\boldsymbol{r}'_{\nu}} \Psi^{\dagger}_{\boldsymbol{r}'_{\nu}}\right] \rightarrow -\text{Tr}\left[\sigma^{\alpha}\Psi_{\boldsymbol{r}_{\mu}} \widetilde{W}_{\mathcal{T}}(\boldsymbol{r}_{\mu}) u^{\alpha}_{\boldsymbol{r}_{\mu},\boldsymbol{r}'_{\nu}} \widetilde{W}^{\dagger}_{\mathcal{T}}(\boldsymbol{r}'_{\nu}) \Psi^{\dagger}_{\boldsymbol{r}'_{\nu}}\right].$$
$$(A.95)$$

Therefore, with the redefined gauge $\widetilde{W}_{\mathcal{T}}$, $\widetilde{\mathcal{T}} = G_{\mathcal{T}} \circ \mathcal{T}$ can be regarded as a unitary operation with an additional sign flip for the mean-field parameters (this sign flip keeps track of the anti-unitarity of $\mathcal{T}$).

For the rest of the appendices and in the main text, we will remove the "∼" in $\widetilde{W}_{\mathcal{T}}$ and call it $W_{\mathcal{T}}$ for simplicity. It is then easy to see that in a time reversal symmetric ansatz Eq. (A.95) leads to Eq. (5.9).

The SU(2) equations associated with Eqs. (A.4j) snd (A.4i) are

$$W_{\mathcal{T}}(\boldsymbol{r}_{\mu})W_{T_i}(\boldsymbol{r}_{\mu})W_{\mathcal{T}}^{-1}[T_i^{-1}(\boldsymbol{r}_{\mu})]W_{T_i}^{-1}(\boldsymbol{r}_{\mu}) = e^{i\sigma^3 \chi_{\mathcal{T}T_i}}, \tag{A.96a}$$

$$W_{\mathcal{T}}(\boldsymbol{r}_{\mu})W_{\overline{C}_6}(\boldsymbol{r}_{\mu})W_{\mathcal{T}}^{-1}[\overline{C}_6^{-1}(\boldsymbol{r}_{\mu})]W_{\overline{C}_6}^{-1}(\boldsymbol{r}_{\mu}) = e^{i\sigma^3 \chi_{\mathcal{T}\overline{C}_6}}, \tag{A.96b}$$

$$W_{\mathcal{T}}(\boldsymbol{r}_{\mu})W_S(\boldsymbol{r}_{\mu})W_{\mathcal{T}}^{-1}[S^{-1}(\boldsymbol{r}_{\mu})]W_S^{-1}(\boldsymbol{r}_{\mu}) = e^{i\sigma^3 \chi_{\mathcal{T}S}}, \tag{A.96c}$$

$$W_{\mathcal{T}}^2(\boldsymbol{r}_{\mu}) = e^{i\sigma^3 \chi_{\mathcal{T}}}, \tag{A.96d}$$

where all the $\chi \in [0, 2\pi)$ for U(1) IGG, and $\chi \in \{0, \pi\}$ for $\mathbb{Z}_2$ IGG.

The above analysis explains the general strategy of treating the projective time reversal operation. Below we specialize to case of a U(1) gauge group and solve the corresponding PSG equations (A.96). The general form of $W_{\mathcal{T}}$ is

$$W_{\mathcal{T}}(\boldsymbol{r}_{\mu}) = (i\sigma^1)^{w_{\mathcal{T}}} e^{i\phi_{\mathcal{T}}(\boldsymbol{r}_{\mu})\sigma^3}, \tag{A.97}$$

where $w_{\mathcal{T}} = 0$ or 1. We now discuss these two cases separately.

When $w_{\mathcal{T}} = 0$, Eq. (A.96a) gives

$$\phi_{\mathcal{T}}(\boldsymbol{r}_{\mu}) = \phi_{\mathcal{T}}(\boldsymbol{0}_{\mu}) + \sum_{i=1}^{3} \chi_{\mathcal{T}T_i} r_i. \tag{A.98}$$

Then look at Eq. (A.96d). We can use the IGG freedom to set $\chi_{\mathcal{T}} = 0$. This requires

$$2\phi_{\mathcal{T}}(\boldsymbol{0}_{\mu}) = 2\chi_{\mathcal{T}T_i} = 0, \quad \mu = 0, 1, 2, 3 \text{ and } i = 1, 2, 3. \tag{A.99}$$

Plug the form (A.98) in Eqs. (A.96b) and (A.96c), we get

$$(-1)^{w_{\overline{C}_6}}\chi_{\mathcal{T}T_3} + \chi_{\mathcal{T}T_1} = (-1)^{w_{\overline{C}_6}}\chi_{\mathcal{T}T_1} + \chi_{\mathcal{T}T_2} = (-1)^{w_{\overline{C}_6}}\chi_{\mathcal{T}T_2} + \chi_{\mathcal{T}T_3} = 0, \tag{A.100a}$$

$$\phi_{\mathcal{T}}(\boldsymbol{0}_0)((-1)^{w_{\overline{C}_6}} - 1) = (-1)^{w_{\overline{C}_6}}\phi_{\mathcal{T}}(\boldsymbol{0}_3) - \phi_{\mathcal{T}}(\boldsymbol{0}_1)$$

$$= (-1)^{w_{\overline{C}_6}}\phi_{\mathcal{T}}(\boldsymbol{0}_1) - \phi_{\mathcal{T}}(\boldsymbol{0}_2)$$

$$= (-1)^{w_{\overline{C}_6}}\phi_{\mathcal{T}}(\boldsymbol{0}_2) - \phi_{\mathcal{T}}(\boldsymbol{0}_3)$$

$$= -\chi_{\mathcal{T}\overline{C}_6}, \tag{A.100b}$$

247

$$-\chi_{\mathcal{T}T_1}((-1)^{w_S}+1)+(-1)^{w_S}\chi_{\mathcal{T}T_3}=-\chi_{\mathcal{T}T_2}((-1)^{w_S}+1)+(-1)^{w_S}\chi_{\mathcal{T}T_3}$$
$$=\chi_{\mathcal{T}T_3}((-1)^{w_S}-1)=0, \tag{A.100c}$$
$$\phi_{\mathcal{T}}(\mathbf{0}_3)(-1)^{w_S}-\phi_{\mathcal{T}}(\mathbf{0}_0)-\chi_{\mathcal{T}T_3}(-1)^{w_S}=\phi_{\mathcal{T}}(\mathbf{0}_1)((-1)^{w_S}-1)-\chi_{\mathcal{T}T_1}(-1)^{w_S}$$
$$=\phi_{\mathcal{T}}(\mathbf{0}_1)((-1)^{w_S}-1)-\chi_{\mathcal{T}T_1}(-1)^{w_S}$$
$$=\phi_{\mathcal{T}}(\mathbf{0}_0)(-1)^{w_S}-\phi_{\mathcal{T}}(\mathbf{0}_3)$$
$$=-\chi_{\mathcal{T}S}, \tag{A.100d}$$

Eqs. (A.100a) and (A.100c) only give zero solution $\chi_{\mathcal{T}T_1}=\chi_{\mathcal{T}T_2}=\chi_{\mathcal{T}T_3}=0$ for any combinations of $w_{\overline{C}_6}=0,1$ and $w_S=0,1$. Then, Eqs. (A.100b) and (A.100d) have the only solution $\phi_{\mathcal{T}}(\mathbf{0}_0)=\phi_{\mathcal{T}}(\mathbf{0}_1)=\phi_{\mathcal{T}}(\mathbf{0}_2)=\phi_{\mathcal{T}}(\mathbf{0}_3)$; and by further using the IGG freedom of time reversal we can set this phase to zero. Therefore the final solution for $w_{\mathcal{T}}=0$ is $W_{\mathcal{T}}(\boldsymbol{r}_\mu)=1$. However, this implies $u^\alpha_{\boldsymbol{r}_\mu,\boldsymbol{r}'_\nu}=-u^\alpha_{\boldsymbol{r}_\mu,\boldsymbol{r}'_\nu}$ according to Eq. (5.9), which gives vanishing mean-field ansätze. This indicates that $w_{\mathcal{T}}=0$ is not physical.

Next consider the case $w_{\mathcal{T}}=1$. We again solve Eq. (A.96a) first: consistency condition requires $-2\chi_1=0$, therefore $\chi_1=0$ or π, and we have

$$\phi_{\mathcal{T}}(\boldsymbol{r}_\mu)=\phi_{\mathcal{T}}(\mathbf{0}_\mu)-\sum_{i=1}^{3}\chi_{\mathcal{T}T_i}r_i. \tag{A.101}$$

Then we solve Eqs. (A.96b) and (A.96c). In all four cases given by $w_{\overline{C}_6}=0$ or 1 and $w_S=0$ or 1, we have $2\chi_{\overline{C}_6T_1}=2\chi_{\overline{C}_6T_2}=2\chi_{\overline{C}_6T_3}=2\chi_{ST_1}=2\chi_{ST_2}=2\chi_{ST_3}=0$. Then, since $\chi_1=0$ or π and $\chi_{ST_1}=0$ or $2\pi/3$ are the only possible values in the space group PSG solution, we see that

$$\chi_{\overline{C}_6T_1}=\chi_{\overline{C}_6T_2}=\chi_{\overline{C}_6T_3}=\chi_{ST_1}=\chi_{ST_2}=\chi_{ST_3}=0. \tag{A.102}$$

Furthermore, analogous to the $w_{\mathcal{T}}=0$ case, we obtain $\chi_{\mathcal{T}T_1}=\chi_{\mathcal{T}T_2}=\chi_{\mathcal{T}T_3}=0$ and $\phi_{\mathcal{T}}(\mathbf{0}_0)=\phi_{\mathcal{T}}(\mathbf{0}_1)=\phi_{\mathcal{T}}(\mathbf{0}_2)=\phi_{\mathcal{T}}(\mathbf{0}_3)$. Then we can always set this phase to zero using the IGG freedom of time reversal. This further implies

$$\chi_{\mathcal{T}\overline{C}_6}=\chi_{\mathcal{T}S}=0. \tag{A.103}$$

In conclusion, in the U(1) PSG case, adding time reversal symmetry does not introduce additional PSG parameters but further restricts $\chi_1=0$ or π, and $\chi_{ST_1}=0$. The time reversal gauge part has the form (in our choice of gauge fixing)

$$W_{\mathcal{T}}(\boldsymbol{r}_\mu)=i\sigma^1. \tag{A.104}$$

The final result is presented in Table 5.1.

A.9 Fermionic $\mathbb{Z}_2$ PSG: adding time reversal

In this subsection we assume that all the space group PSG equations have been solved (and gauge-fixed). We then add time reversal to the PSG and solve all the PSG equations containing time reversal: just as in the U(1) case, we are solving Eqs. (A.96), but now the right-hand sides of these equations are ± 1. From Eq. (A.96a) we get

$$W_{\mathcal{T}}(\boldsymbol{r}_\mu) = g_{\mathcal{T},\mu} \eta_{\mathcal{T}T_1}^{r_1} \eta_{\mathcal{T}T_2}^{r_2} \eta_{\mathcal{T}T_3}^{r_3}, \tag{A.105}$$

where we followed the notation in the last appendix: $g_{\mathcal{T},\mu} \equiv W_{\mathcal{T},\mu}$. Plug the form (A.105) in Eqs. (A.96b)–(A.96d), we obtain

$$\eta_{\mathcal{T}T_1} = \eta_{\mathcal{T}T_2} = \eta_{\mathcal{T}T_3} = 0 \tag{A.106}$$

and

$$g_{\mathcal{T},0} g_{\overline{C}_6,0} g_{\mathcal{T},0}^{-1} g_{\overline{C}_6,0}^{-1} = g_{\mathcal{T},1} g_{\overline{C}_6,1} g_{\mathcal{T},3}^{-1} g_{\overline{C}_6,1}^{-1}$$
$$= g_{\mathcal{T},2} g_{\overline{C}_6,2} g_{\mathcal{T},1}^{-1} g_{\overline{C}_6,2}^{-1} = g_{\mathcal{T},3} g_{\overline{C}_6,3} g_{\mathcal{T},2}^{-1} g_{\overline{C}_6,3}^{-1} = \eta_{\mathcal{T}\overline{C}_6}, \tag{A.107a}$$
$$g_{\mathcal{T},0} g_{S,0} g_{\mathcal{T},3}^{-1} g_{S,0}^{-1} = g_{\mathcal{T},1} g_{S,1} g_{\mathcal{T},1}^{-1} g_{S,1}^{-1}$$
$$= g_{\mathcal{T},2} g_{S,2} g_{\mathcal{T},2}^{-1} g_{S,2}^{-1} = g_{\mathcal{T},3} g_{S,3} g_{\mathcal{T},0}^{-1} g_{S,3}^{-1} = \eta_{\mathcal{T}S}, \tag{A.107b}$$
$$g_{\mathcal{T},\mu}^2 = \eta_{\mathcal{T}}. \tag{A.107c}$$

Eq. (A.106) means that $W_{\mathcal{T}}(\boldsymbol{r}_\mu) = g_{\mathcal{T},\mu}$, which only depends on the sublattice indices. We now claim that $\eta_{\mathcal{T}} = -1$. Otherwise $\eta_{\mathcal{T}} = 1$, then $g_{\mathcal{T},\mu}$ has the form of a sign factor $\eta_{\mathcal{T},\mu} = \pm 1$ times the identity matrix. Plugging this form in Eqs. (A.107a) and (A.107b) gives $1 = \eta_{\mathcal{T},1}\eta_{\mathcal{T},3} = \eta_{\mathcal{T},2}\eta_{\mathcal{T},1} = \eta_{\mathcal{T},3}\eta_{\mathcal{T},2} = \eta_{\mathcal{T}\overline{C}_6}$ and $\eta_{\mathcal{T},0}\eta_{\mathcal{T},3} = 1 = \eta_{\mathcal{T}S}$, meaning that all the sublattice signs $\eta_{\mathcal{T},\mu}$ must be the same. As was argued in Appendix A.8 this will lead to a vanishing mean-field ansätze. Therefore we must have $\eta_{\mathcal{T}} = -1$.

Recall that in classifying the space group PSG in Appendix A.7 gauge fixing already gives $g_{\overline{C}_6,1} = g_{\overline{C}_6,2} = g_{S,0} = g_{S,3} = 1$. Then Eqs. (A.107a) and (A.107b) enforce

$$g_{\mathcal{T},1} = \eta_{\mathcal{T}\overline{C}_6} \eta_{\mathcal{T}S} g_{\mathcal{T},0}, \quad g_{\mathcal{T},2} = \eta_{\mathcal{T}S} g_{\mathcal{T},0}, \quad g_{\mathcal{T},3} = \eta_{\mathcal{T}S} g_{\mathcal{T},0}, \tag{A.108}$$

and the two equations reduce to

$$g_{\mathcal{T},0} g_{\overline{C}_6,0} = \eta_{\mathcal{T}\overline{C}_6} g_{\overline{C}_6,0} g_{\mathcal{T},0}, \quad g_{\mathcal{T},0} g_{\overline{C}_6,3} = \eta_{\mathcal{T}\overline{C}_6} g_{\overline{C}_6,3} g_{\mathcal{T},0},$$
$$g_{\mathcal{T},0} g_{S,1} = \eta_{\mathcal{T}S} g_{S,1} g_{\mathcal{T},0}, \quad g_{\mathcal{T},0} g_{S,2} = \eta_{\mathcal{T}S} g_{S,2} g_{\mathcal{T},0}. \tag{A.109}$$

$g_{\mathcal{T},0}$ is then determined by $g_{\overline{C}_6,0}, g_{\overline{C}_6,3}, g_{S,1}, g_{S,2}$ and there are five cases listed below.

- In the case $(\eta_1 \eta_{ST_1}, \eta_{\overline{C}_6}, \eta_{S\overline{C}_6}) = (1,1,1)$, we have $(g_{\overline{C}_6,0}, g_{\overline{C}_6,3}, g_{S,1}, g_{S,2}) = (1,1,1,\eta_{\overline{C}_6 S})$, we see we must have $\eta_{\mathcal{T}\overline{C}_6} = \eta_{\mathcal{T}S} = 1$, and it is easy to use the remaining global SU(2) gauge freedom to set e.g. $g_{\mathcal{T},0} = i\sigma^k$, where σ^k can be any of the three Pauli matrices.

- In the case $(\eta_1\eta_{ST_1}, \eta_{\overline{C}_6}, \eta_{S\overline{C}_6}) = (1, -1, -1)$, we have $(g_{\overline{C}_6,0}, g_{\overline{C}_6,3}, g_{S,1}, g_{S,2}) = (-i\sigma^k, i\sigma^k, 1, \eta_{\overline{C}_6 S})$, it is easy to see from the expression of $g_{S,1}$ and $g_{S,2}$ that $\eta_{TS} = 1$. Then time reversal is either $g_{T,0} = i\sigma^k$ which gives $\eta_{T\overline{C}_6} = 1$, or $g_{T,0} = i\sigma^{k-1}$ which gives $\eta_{T\overline{C}_6} = -1$. Note we have used the gauge freedom (rotating along σ^k axis) to set $g_{T,0} = i\sigma^{k-1}$.

- In the case $(\eta_1\eta_{ST_1}, \eta_{\overline{C}_6}, \eta_{S\overline{C}_6}) = (-1, 1, -1)$, we have $(g_{\overline{C}_6,0}, g_{\overline{C}_6,3}, g_{S,1}, g_{S,2}) = (-\eta_{\overline{C}_6 S} e^{i\frac{\pi j}{3}\sigma^{k-1}}, 1, i\sigma^k, i\sigma^k e^{i\frac{\pi j}{3}\sigma^{k-1}})$. When $\eta_{\overline{C}_6 S} = 1$, we get $j = 1, 3$, and when $\eta_{\overline{C}_6 S} = -1$, we get $j = 0, 2$. We always have $\eta_{T\overline{C}_6} = 1$. If $j = 1$ or 2, then we must have $g_{T,0} = i\sigma^{k-1}$, and $\eta_{TS} = -1$; if $j = 0$ or 3, then we can have $g_{T,0} = i\sigma^k$ or $g_{T,0} = i\sigma^{k-1}$ (after gauge fixing), which gives $g_{TS} = 1$ or $g_{TS} = -1$, respectively.

- In the case $(\eta_1\eta_{ST_1}, \eta_{\overline{C}_6}, \eta_{S\overline{C}_6}) = (-, -, +)$, $g_{\overline{C}_6,0} = i\sigma^k$, $g_{\overline{C}_6,3} = i\sigma^k$, $g_{S,1} = i\sigma^k$, $g_{S,2} = \eta_{\overline{C}_6 S} i\sigma^k$. Two solutions exist: we can have either $g_{T,0} = i\sigma^k$ corresponding to $\eta_{T\overline{C}_6} = \eta_{TS} = 1$, or $g_{T,0} = i\sigma^{k-1}$ (after gauge fixing), corresponding to $\eta_{T\overline{C}_6} = \eta_{TS} = -1$.

- Lastly, in the case $(\eta_1\eta_{ST_1}, \eta_{\overline{C}_6}, \eta_{S\overline{C}_6}) = (-1, -1, -1)$, $g_{\overline{C}_6,0} = e^{i\frac{\pi(2j+1)}{6}(-1)^j\sigma^{k-1}}$, $g_{\overline{C}_6,3} = i\sigma^{k-1}$, $g_{S,1} = i\sigma^k$, $g_{S,2} = \eta_{\overline{C}_6 S} i\sigma^{k+1} e^{i\frac{\pi(2j+1)}{6}(-1)^j\sigma^{k-1}}$. When $j = 0$ we must have $\eta_{T\overline{C}_6} = 1$ and $g = i\sigma^{k-1}$, which gives $\eta_{TS} = -1$; when $j = 1$ three solutions exist: we can have $g = i\sigma^{k-1}$ corresponding to $(\eta_{T\overline{C}_6}, \eta_{TS}) = (1, -1)$, or $g = i\sigma^k$ corresponding to $(\eta_{T\overline{C}_6}, \eta_{TS}) = (-1, 1)$, or $g = i\sigma^{k+1}$ corresponding to $(\eta_{T\overline{C}_6}, \eta_{TS}) = (-1, -1)$.

The final result is presented in Table 5.2.

A.10 0-flux symmetry properties

In this Appendix we study the symmetry transformation of the Hamiltonian and operators in the 0-flux ansätze in more detail. Under an arbitrary symmetry operation $\mathcal{O}$, following Eq. (1.33) we have

$$G_{\mathcal{O}} \circ \mathcal{O}: \Psi_{\boldsymbol{r}_\mu} \to U_{\mathcal{O}}^\dagger \Psi_{\mathcal{O}(\boldsymbol{r}_\mu)} W_{\mathcal{O},\mu} e^{i\sigma^3 \phi_{\mathcal{O}}[\mathcal{O}(\boldsymbol{r}_\mu)]}, \tag{A.110}$$

In the case of U(1) PSG (with or without time reversal) and time reversal symmetric $\mathbb{Z}_2$ PSG in our chosen gauge, we can always write, with the help of the $\mathbb{Z}_2$ parameter $w_{\mathcal{O}}$, $W_{\mathcal{O},\mu} = (i\sigma^1)^{w_{\mathcal{O}}} e^{i\sigma^3 \phi^0_{\mathcal{O},\mu}}$, where $\phi^0_{\mathcal{O},\mu}$ is some phase that can be absorbed into the definition of $\phi_{\mathcal{O}}(\boldsymbol{r}_\mu)$, and we call $\bar{\phi}_{\mathcal{O}}(\boldsymbol{r}_\mu) = \phi_{\mathcal{O}}(\boldsymbol{r}_\mu) + \phi^0_{\mathcal{O},\mu}$. We have

$$G_{\mathcal{O}} \circ \mathcal{O}: \begin{pmatrix} f_{\boldsymbol{r}_\mu} \\ f^\dagger_{\boldsymbol{r}_\mu} \end{pmatrix} \to V_{\mathcal{O}, w_{\mathcal{O}}} e^{i\tau^3 \bar{\phi}_{\mathcal{O}}[\mathcal{O}(\boldsymbol{r}_\mu)]} \begin{pmatrix} f_{\mathcal{O}(\boldsymbol{r}_\mu)} \\ f^\dagger_{\mathcal{O}(\boldsymbol{r}_\mu)} \end{pmatrix}, \tag{A.111}$$

with

$$V_{\mathcal{O},w_{\mathcal{O}}} = \begin{pmatrix} U_{\mathcal{O}}^{\dagger} & \\ & U_{\mathcal{O}}^{T} \end{pmatrix} (-i\tau^2\sigma^2)^{w_{\mathcal{O}}}, \tag{A.112}$$

where we defined Pauli matrices $\tau^{1,2,3}$ to act on the subspace of $f_{\boldsymbol{r}_\mu}$ and $f_{\boldsymbol{r}_\mu}^{\dagger}$. Note that $f_{\boldsymbol{r}_\mu}^{\dagger}$ is understood as $(f_{\boldsymbol{r}_\mu}^{\dagger})^T = \left(f_{\boldsymbol{r}_\mu\uparrow}^{\dagger}, f_{\boldsymbol{r}_\mu\downarrow}^{\dagger} \right)^T$.

Then, Fourier transform gives

$$\begin{aligned}
\begin{pmatrix} f_{\mu,\boldsymbol{k}} \\ f_{\mu,-\boldsymbol{k}}^{\dagger} \end{pmatrix} &= \frac{1}{\sqrt{N}} \sum_{\boldsymbol{r}} e^{-i\boldsymbol{k}\cdot\boldsymbol{r}_\mu} \begin{pmatrix} f_{\boldsymbol{r}_\mu} \\ f_{\boldsymbol{r}_\mu}^{\dagger} \end{pmatrix} \\
&\xrightarrow{G_{\mathcal{O}}\circ\mathcal{O}} \frac{V_{\mathcal{O},w_{\mathcal{O}}}}{\sqrt{N}} \sum_{\boldsymbol{r}} e^{-i\boldsymbol{k}\cdot\boldsymbol{r}_\mu} e^{i\tau^3\bar{\phi}_{\mathcal{O}}[\mathcal{O}(\boldsymbol{r}_\mu)]} \begin{pmatrix} f_{\mathcal{O}(\boldsymbol{r}_\mu)} \\ f_{\mathcal{O}(\boldsymbol{r}_\mu)}^{\dagger} \end{pmatrix} \\
&= \frac{V_{\mathcal{O},w_{\mathcal{O}}}}{\sqrt{N}} \sum_{\boldsymbol{r}} e^{-i[\boldsymbol{k}\cdot\mathcal{O}^{-1}(\boldsymbol{r}_{\mathcal{O}(\mu)})-\tau^3\bar{\phi}_{\mathcal{O}}(\boldsymbol{r}_{\mathcal{O}(\mu)})]} \begin{pmatrix} f_{\boldsymbol{r}_{\mathcal{O}(\mu)}} \\ f_{\boldsymbol{r}_{\mathcal{O}(\mu)}}^{\dagger} \end{pmatrix},
\end{aligned} \tag{A.113}$$

Using the general structure

$$\bar{\phi}_{\overline{C}_6}(\boldsymbol{r}_\mu) = \phi_{\overline{C}_6 T_3} r_1 + \rho_\mu, \qquad \bar{\phi}_S(\boldsymbol{r}_\mu) = -\phi_{ST_1} r_1 + 3\phi_{ST_1} r_2 + \theta_\mu, \tag{A.114}$$

we have

$$\left[\boldsymbol{k}\cdot\mathcal{O}^{-1}(\boldsymbol{r}_{\mathcal{O}(\mu)}) - \tau^3\bar{\phi}_{\mathcal{O}}(\boldsymbol{r}_{\mathcal{O}(\mu)}) \right]\Big|_{\mathcal{O}=\overline{C}_6} = \left(\overline{C}_6(\boldsymbol{k}) - \tau^3\phi_{\overline{C}_6 T_3}\hat{\boldsymbol{b}}_1 \right)\cdot\boldsymbol{r} - \boldsymbol{k}\cdot\boldsymbol{e}_\mu - \tau^3\rho_{\overline{C}_6}, \tag{A.115a}$$

$$\left[\boldsymbol{k}\cdot\mathcal{O}^{-1}(\boldsymbol{r}_{\mathcal{O}(\mu)}) - \tau^3\bar{\phi}_{\mathcal{O}}(\boldsymbol{r}_{\mathcal{O}(\mu)}) \right]\Big|_{\mathcal{O}=S} = \left(S(\boldsymbol{k}) - \tau^3(-\phi_{ST_1}\hat{\boldsymbol{b}}_1 + 3\phi_{ST_1}\hat{\boldsymbol{b}}_2) \right)\cdot\boldsymbol{r} - \boldsymbol{k}\cdot\boldsymbol{e}_\mu - \tau^3\theta_{\overline{C}_6}, \tag{A.115b}$$

we have

$$G_{\overline{C}_6}\circ\overline{C}_6\colon \begin{pmatrix} f_{\mu,\boldsymbol{k}} \\ f_{\mu,-\boldsymbol{k}}^{\dagger} \end{pmatrix} \to V_{\overline{C}_6,w_{\overline{C}_6}} e^{i(\boldsymbol{k}\cdot\boldsymbol{e}_\mu+\rho_{\overline{C}_6(\mu)})} \begin{pmatrix} f_{\overline{C}_6(\mu),\overline{C}_6(\boldsymbol{k})-\phi_{\overline{C}_6 T_3}\hat{\boldsymbol{b}}_1} \\ f_{\overline{C}_6(\mu),\overline{C}_6(-\boldsymbol{k})-\phi_{\overline{C}_6 T_3}\hat{\boldsymbol{b}}_1}^{\dagger} \end{pmatrix}, \tag{A.116a}$$

$$G_S\circ S\colon \begin{pmatrix} f_{\mu,\boldsymbol{k}} \\ f_{\mu,-\boldsymbol{k}}^{\dagger} \end{pmatrix} \to V_{S,w_S} e^{i(\boldsymbol{k}\cdot\boldsymbol{e}_\mu+\theta_{S(\mu)})} \begin{pmatrix} f_{S(\mu),S(\boldsymbol{k})+\phi_{ST_1}(\hat{\boldsymbol{b}}_1-3\hat{\boldsymbol{b}}_2)} \\ f_{S(\mu),S(-\boldsymbol{k})+\phi_{ST_1}(\hat{\boldsymbol{b}}_1-3\hat{\boldsymbol{b}}_2)}^{\dagger} \end{pmatrix}. \tag{A.116b}$$

Appendix B

Gauge-field calculations

B.1 Gauge invariance at one-loop level

It is know that for a generic Hamiltonian couple to a U(1) gauge field, gauge invariance requires that 1) the photon self energy $\Pi(q)$ vanishes when the photon external momentum $\boldsymbol{q}$ vanishes and that 2) Ward identity holds. These statements holds perturbatively at each loop level. Here we explicitly proof these two statements for non-interacting fermions coupled to a U(1) gauge field at one-loop level. For a generic tight binding Hamiltonian

$$H_0 = \sum_{\boldsymbol{r}_\mu, \boldsymbol{r}'_\nu} c^\dagger_{\boldsymbol{r}_\mu} h_{\boldsymbol{r}_\mu, \boldsymbol{r}'_\nu} c_{\boldsymbol{r}'_\nu}, \tag{B.1}$$

the U(1) gauge coupling is introduced via the Peierl's substitution:

$$H[A] = \sum_{\boldsymbol{r}_\mu, \boldsymbol{r}'_\nu} c^\dagger_{\boldsymbol{r}_\mu} h_{\boldsymbol{r}_\mu, \boldsymbol{r}'_\nu} e^{iA_{\boldsymbol{r}_\mu, \boldsymbol{r}'_\nu}} c_{\boldsymbol{r}'_\nu} + \sum_{\boldsymbol{r}_\mu} A_{0,\boldsymbol{r}_\mu} n_{\boldsymbol{r}_\mu} \tag{B.2}$$

the spatial fluctuation of the gauge field is small at short distance, suggesting that we can expand the exponential for the gauge field. To quadratic order of A we obtain

$$
\begin{aligned}
H[A] = & H_0 + \sum_{\boldsymbol{k},\boldsymbol{q}} A^i(-q) c^\dagger_{\boldsymbol{k}+\boldsymbol{q}/2} \frac{\partial h(\boldsymbol{k})}{\partial k_i} c_{\boldsymbol{k}-\boldsymbol{q}/2} + \sum_{\boldsymbol{k},\boldsymbol{q}} i A^0(-q) c^\dagger_{\boldsymbol{k}+\boldsymbol{q}/2} c_{\boldsymbol{k}-\boldsymbol{q}/2} \\
& + \sum_{\boldsymbol{k},\boldsymbol{q}} A^i(q) A^j(q') c^\dagger_{\boldsymbol{k}+\boldsymbol{q}'} \frac{\partial^2 h(\boldsymbol{k})}{\partial k_j \partial k_i} c_{\boldsymbol{k}-\boldsymbol{q}} + O(A^3),
\end{aligned}
\tag{B.3}
$$

up to this order we have the usual minimal coupling vertex $Ac^\dagger c$ as well as a *diamagnetic* vertex $A^2 c^\dagger c$. These two vertices lead to the two diagrams at one-loop shown in Fig. 5.2: the usual vacuum polarization bubble (left) and the "tadpole" diagram (right). Note that the diamagnetic term vanishes for a Dirac Hamiltonian since it is linear in momentum. In

the following we show that the contribution of these two one-loop diagrams cancel each other at $q = 0$, and furthermore the sum of the them at finite momentum and frequency satisfies the Ward identity.

The vacuum polarization bubble diagram in Fig. 5.2 originates from the $Ac^\dagger c$ term. The vertex expression $\gamma_\mu(\boldsymbol{k}) = \delta_{\mu 0} + \delta_{\mu,i}\partial_{k_i}h$, i.e. the vertex is unity for the temporal component $\mu = 0$ and is $\partial_{k_i}h$ for the spatial component. The "tadpole" diagram originates from the $A^2 c^\dagger c$ term. The vertex expression is $\gamma_{\mu\nu}(\boldsymbol{k}) = \delta_{\mu,i}\delta_{\nu,j}\partial_{k_i}\partial_{k_j}h$, i.e. the vertex only exists for μ, ν both being spatial indices, with vertex expression $\partial_{k_i}\partial_{k_j}h$. The two diagrams have the following expression

$$
\begin{aligned}
\Pi^{(1)}_{1,\mu\nu}(q) &= \int \frac{d^4k}{(2\pi)^4} \mathrm{Tr}[\gamma_\mu(\boldsymbol{k})G_0(k+q/2)\gamma_\nu(\boldsymbol{k})G_0(k-q/2)], \\
\Pi^{(1)}_{2,\mu\nu}(q) &= \int \frac{d^4k}{(2\pi)^4} \mathrm{Tr}[\gamma_{\mu\nu}(\boldsymbol{k})G_0(k-q)].
\end{aligned}
\tag{B.4}
$$

We now show that $\Pi^{(1)}_{1,\mu\nu}(q = 0) + \Pi^{(1)}_{2,\mu\nu}(q = 0) = 0$. First of all, when one of the μ, ν is a temporal component, say $\nu = 0$, then $\Pi^{(1)}_{2,\mu\nu} = 0$ and we are only left with $\Pi^{(1)}_{1,\mu 0}(\boldsymbol{q} = 0)$: in the following we write $k_0 = \omega$. We have

$$
\begin{aligned}
\Pi^{(1)}_{1,\mu 0}(q = 0) &= \int \frac{d^4k}{(2\pi)^4} \mathrm{Tr}[\gamma_\mu(\boldsymbol{k})G_0^2(\boldsymbol{k})] = \int \frac{d^4k}{(2\pi)^4} \mathrm{Tr}\left[\gamma_\mu(\boldsymbol{k})\left(\frac{1}{\omega - h(\boldsymbol{k})}\right)^2\right] \\
&= -\int \frac{d^4k}{(2\pi)^4} \mathrm{Tr}\left[\gamma_\mu(\boldsymbol{k})\frac{\partial}{\partial\omega}\left(\frac{1}{\omega - h(\boldsymbol{k})}\right)\right] \\
&= -\int \frac{d^3\boldsymbol{k}}{(2\pi)^4} \mathrm{Tr}\left[\gamma_\mu(\boldsymbol{k})\frac{1}{\omega - h(\boldsymbol{k})}\right]\Bigg|_{\omega=-\infty}^{\omega=+\infty} = 0,
\end{aligned}
\tag{B.5}
$$

where we have used the fact that if h is diagonalized as $h = U^\dagger \Lambda U$, then $\frac{1}{(\omega - h)^2} = U^\dagger \frac{1}{(\omega - \Lambda)^2} U = U^\dagger \left(-\frac{\partial}{\partial\omega}\left(\frac{1}{\omega - \Lambda}\right)\right) U = -\frac{\partial}{\partial\omega}\left(\frac{1}{\omega - h}\right)$. We therefore see that $\Pi^{(1)}_{1,\mu 0}(\boldsymbol{q} = 0) = 0$ for any μ. This means that $\Pi^{(1)}_{1,0\nu}(q = 0) = 0$ for any ν. Then, we look at spatial

components (note we have suppressed the arguments $\boldsymbol{k}$ below):

$$
\begin{aligned}
\Pi^{(1)}_{1,ij}(q=0) &+ \Pi^{(1)}_{2,ij}(q=0) \\
&= \int \frac{d^4k}{(2\pi)^4}\mathrm{Tr}\left[\partial_{k_i}h\frac{1}{\omega-h}\partial_{k_j}h\frac{1}{\omega-h}\right] + \int \frac{d^4k}{(2\pi)^4}\mathrm{Tr}\left[\partial_{k_i}\partial_{k_j}h\frac{1}{\omega-h}\right] \\
&= \int \frac{d^4k}{(2\pi)^4}\mathrm{Tr}\left[\partial_{k_i}h\frac{1}{\omega-h}\partial_{k_j}h\frac{1}{\omega-h}\right] - \int \frac{d^4k}{(2\pi)^4}\mathrm{Tr}\left[\partial_{k_j}h\partial_{k_i}\left(\frac{1}{\omega-h}\right)\right] \\
&= \int \frac{d^4k}{(2\pi)^4}\mathrm{Tr}\left[\partial_{k_i}h\frac{1}{\omega-h}\partial_{k_j}h\frac{1}{\omega-h}\right] - \int \frac{d^4k}{(2\pi)^4}\mathrm{Tr}\left[\partial_{k_j}h\frac{1}{\omega-h}\partial_{k_i}h\frac{1}{\omega-h}\right] \\
&= 0,
\end{aligned} \tag{B.6}
$$

where we have used the fact that $\partial(K^{-1}) = -K^{-1}(\partial K)K^{-1}$ for any (non-singular) matrix K. Therefore we have proved that the photon self-energy vanishes at one-loop level when photon external momentum is zero.

Next we show that Ward identity holds at one-loop level $q_\mu\left(\Pi^{(1)}_{1,\mu i}(q) - \Pi^{(1)}_{2,\mu i}(q)\right) = 0$. First, only the vacuum polarization diagram contributes to the $\mu 0$ component:

$$
q_\mu\Pi^{(1)}_{1,\mu 0}(q) = \int \frac{d^4k}{(2\pi)^4}\mathrm{Tr}\left[\frac{-q_0 + q_i\partial_{k_i}h(\boldsymbol{k})}{(k_0+q_0/2-h(\boldsymbol{k}+\boldsymbol{q}/2))(k_0-q_0/2-h(\boldsymbol{k}-\boldsymbol{q}/2))}\right], \tag{B.7}
$$

note that

$$
(k_0+q_0/2-h(\boldsymbol{k}+\boldsymbol{q}/2)) - (k_0-q_0/2-h(\boldsymbol{k}-\boldsymbol{q}/2)) = q_0 - q_i\partial_{k_i}h(\boldsymbol{k}) + o(q), \tag{B.8}
$$

this means that

$$
q_\mu\Pi^{(1)}_{1,\mu 0}(q) = \int \frac{d^4k}{(2\pi)^4}\mathrm{Tr}\left[\frac{1}{k_0+q_0/2-h(\boldsymbol{k}+\boldsymbol{q}/2)} - \frac{1}{k_0-q_0/2-h(\boldsymbol{k}-\boldsymbol{q}/2)}\right], \tag{B.9}
$$

which gives zero since the two terms only differ by a shift. Similarly, we have

$$
q_\mu\Pi^{(1)}_{1,\mu i} = \int \frac{d^4k}{(2\pi)^4}\mathrm{Tr}\left[(-q_0 + q_j\partial_{k_j}h(\boldsymbol{k}))\frac{1}{k_0+q_0/2-h(\boldsymbol{k}+\boldsymbol{q}/2)}\partial_{k_i}h(\boldsymbol{k})\frac{1}{k_0-q_0/2-h(\boldsymbol{k}-\boldsymbol{q}/2)}\right],
$$
$$
\tag{B.10}
$$

and similar to the $\mu 0$ component case, we get

$$q_\mu \Pi_{1,\mu i}^{(1)} = \int \frac{d^4 k}{(2\pi)^4} \mathrm{Tr}\left[\partial_{k_i} h(\boldsymbol{k})\left(\frac{1}{k_0 + q_0/2 - h(\boldsymbol{k}+\boldsymbol{q}/2)} - \frac{1}{k_0 - q_0/2 - h(\boldsymbol{k}-\boldsymbol{q}/2)}\right)\right],$$
(B.11)

on the other hand we have $\frac{1}{2} q_i \partial_{k_i} \partial_{k_j} h(\boldsymbol{k}) = \partial_{k_j} h(\boldsymbol{k}+\boldsymbol{q}/2) - \partial_{k_j} h(\boldsymbol{k}) + o(q) = \partial_{k_j} h(\boldsymbol{k}) - \partial_{k_j} h(\boldsymbol{k}-\boldsymbol{q}/2) + o(q)$, and

$$
\begin{aligned}
q_j \Pi_{2,ji}^{(1)} &= \int \frac{d^4 k}{(2\pi)^4} \mathrm{Tr}\left[\frac{q_j \partial_{k_j} \partial_{k_i} h(\boldsymbol{k})}{k_0 - q_0 - h(\boldsymbol{k}-\boldsymbol{q})}\right] \\
&= \int \frac{d^4 k}{(2\pi)^4} \mathrm{Tr}\left[\frac{\partial_{k_j} h(\boldsymbol{k}-\boldsymbol{q}/2) - \partial_{k_j} h(\boldsymbol{k}-\boldsymbol{q}) + \partial_{k_j} h(\boldsymbol{k}-\boldsymbol{q}) - \partial_{k_j} h(\boldsymbol{k}-3\boldsymbol{q}/2)}{k_0 - q_0 - h(\boldsymbol{k}-\boldsymbol{q})}\right] \\
&= \int \frac{d^4 k}{(2\pi)^4} \mathrm{Tr}\left[\frac{\partial_{k_j} h(\boldsymbol{k}) - \partial_{k_j} h(\boldsymbol{k}-\boldsymbol{q}/2)}{k_0 - q_0/2 - h(\boldsymbol{k}-\boldsymbol{q}/2)}\right] + \int \frac{d^4 k}{(2\pi)^4} \mathrm{Tr}\left[\frac{\partial_{k_j} h(\boldsymbol{k}+\boldsymbol{q}/2) - \partial_{k_j} h(\boldsymbol{k})}{k_0 + q_0/2 - h(\boldsymbol{k}+\boldsymbol{q}/2)}\right],
\end{aligned}
$$
(B.12)

where we have shifted the integral variables. Therefore we see that (denote $\Pi_{2,0\mu}^{(1)} = 0$)

$$q_\mu \left(\Pi_{1,\mu i}^{(1)}(q) - \Pi_{2,\mu i}^{(1)}(q)\right) = \int \frac{d^4 k}{(2\pi)^4} \mathrm{Tr}\left[\frac{\partial_{k_i} h(\boldsymbol{k}+\boldsymbol{q}/2)}{k_0 + q_0/2 - h(\boldsymbol{k}+\boldsymbol{q}/2)} - \frac{\partial_{k_i} h(\boldsymbol{k}-\boldsymbol{q}/2)}{k_0 - q_0/2 - h(\boldsymbol{k}-\boldsymbol{q}/2)}\right],$$
(B.13)

which gives zero on the Brillouin zone. Therefore Ward identity holds at one-loop level.

B.2 Deriving the photon vacuum bubble: scaling analysis

We study the 00 component of the vacuum polarization diagram: after completing the frequency integral, we have (again in imaginary time)

$$D(q) \equiv \Pi_{1,00}^{(1)}(q) = -\pi \mathrm{Re}\left[\int \frac{d^3 \boldsymbol{k}}{(2\pi)^3} \frac{1 - \hat{\boldsymbol{d}}_{\boldsymbol{k}+\boldsymbol{q}/2} \cdot \hat{\boldsymbol{d}}_{\boldsymbol{k}-\boldsymbol{q}/2}}{|\boldsymbol{d}_{\boldsymbol{k}+\boldsymbol{q}/2}| + |\boldsymbol{d}_{\boldsymbol{k}-\boldsymbol{q}/2}| + iq_0}\right],$$
(B.14)

with $\hat{\boldsymbol{d}} = \boldsymbol{d}/|\boldsymbol{d}|$. To separate the contribution along the nodal line and that in the vicinity of the Γ point, we use the identity $1 = \frac{x}{a+x} + \frac{a}{a+x}$, where we set $a = c\boldsymbol{q}^2$ and $x = |\boldsymbol{d}_{\boldsymbol{k}+\boldsymbol{q}/2}| + |\boldsymbol{d}_{\boldsymbol{k}-\boldsymbol{q}/2}| + iq_0$, so that

$$D(q) = D_1(q) + D_2(q),$$
(B.15)

with

$$D_1(q) = -\pi \mathrm{Re}\left[\int \frac{d^3\boldsymbol{k}}{(2\pi)^3} \frac{1 - \hat{\boldsymbol{d}}_{\boldsymbol{k}+\boldsymbol{q}/2} \cdot \hat{\boldsymbol{d}}_{\boldsymbol{k}-\boldsymbol{q}/2}}{|\boldsymbol{d}_{\boldsymbol{k}+\boldsymbol{q}/2}| + |\boldsymbol{d}_{\boldsymbol{k}-\boldsymbol{q}/2}| + iq_0 + c\boldsymbol{q}^2}\right], \tag{B.16a}$$

$$D_2(q) = -\pi \mathrm{Re}\left[\int \frac{d^3\boldsymbol{k}}{(2\pi)^3} \frac{c\boldsymbol{q}^2(1 - \hat{\boldsymbol{d}}_{\boldsymbol{k}+\boldsymbol{q}/2} \cdot \hat{\boldsymbol{d}}_{\boldsymbol{k}-\boldsymbol{q}/2})}{(|\boldsymbol{d}_{\boldsymbol{k}+\boldsymbol{q}/2}| + |\boldsymbol{d}_{\boldsymbol{k}-\boldsymbol{q}/2}| + iq_0)(|\boldsymbol{d}_{\boldsymbol{k}+\boldsymbol{q}/2}| + |\boldsymbol{d}_{\boldsymbol{k}-\boldsymbol{q}/2}| + iq_0 + c\boldsymbol{q}^2)}\right], \tag{B.16b}$$

the choice of $a = c\boldsymbol{q}^2$ is made to agree with the scaling $\boldsymbol{d}_{\boldsymbol{k}} \propto \boldsymbol{q}^2$ near the Γ point (see Eq. (5.35)) and guarantees that D_2 extracts the contribution in vicinity of the Γ point. Having in mind that at small $\boldsymbol{q}$ the leading order $\boldsymbol{q}$ result is isotropic in $\boldsymbol{q}$. Therefore we choose a specific direction for $\boldsymbol{q}$: $\boldsymbol{q} = q_z\hat{\boldsymbol{z}}$.

We first look at $D_2(q)$: since $D_2(q)$ is supported in vicinity of the Γ point, we expand $\boldsymbol{d}_{\boldsymbol{k}}$ as in Eq. (5.35). Rescaling $\boldsymbol{k} = \boldsymbol{x}q_z$ and $\boldsymbol{d}_{\boldsymbol{k}} = q_z^2\boldsymbol{\epsilon}_{\boldsymbol{k}}$, we have

$$D_2(q) \sim -c\pi|q_z|\mathrm{Re}\left[\int \frac{d^3\boldsymbol{x}}{(2\pi)^3} \frac{1 - \hat{\boldsymbol{\epsilon}}_{\boldsymbol{x}+\hat{\boldsymbol{z}}/2} \cdot \hat{\boldsymbol{\epsilon}}_{\boldsymbol{x}-\hat{\boldsymbol{z}}/2}}{(|\boldsymbol{\epsilon}_{\boldsymbol{x}+\hat{\boldsymbol{z}}/2}| + |\boldsymbol{\epsilon}_{\boldsymbol{x}-\hat{\boldsymbol{z}}/2}| + iq_0/\boldsymbol{q}^2)(|\boldsymbol{\epsilon}_{\boldsymbol{x}+\hat{\boldsymbol{z}}/2}| + |\boldsymbol{\epsilon}_{\boldsymbol{x}-\hat{\boldsymbol{z}}/2}| + iq_0/|\boldsymbol{q}| + c)}\right] + O(q^2), \tag{B.17}$$

First look at the case of $q_0 = 0$. In this case, the integral in $D_2(q)$ is well behaved, which can be easily seen in the original expression (B.16b): the only singularity comes from $|\boldsymbol{d}_{\boldsymbol{k}+\boldsymbol{q}/2}| + |\boldsymbol{d}_{\boldsymbol{k}+\boldsymbol{q}/2}| = 0$, or $|\boldsymbol{\epsilon}_{\boldsymbol{k}+\boldsymbol{q}/2}||\boldsymbol{\epsilon}_{\boldsymbol{k}-\boldsymbol{q}/2}| = 0$, which gives isolated points $(x_1, x_2, x_3) = (\pm 1/2, \pm 1/2, 0)$. Expand around these points: $x_1 = \pm 1/2 + \eta\xi_1$, $x_2 = \pm 1/2 + \eta\xi_2$, and $x_3 = \eta\xi_3$, we see that $|\boldsymbol{\epsilon}_{\boldsymbol{k}+\boldsymbol{q}/2}||\boldsymbol{\epsilon}_{\boldsymbol{k}-\boldsymbol{q}/2}| \sim \eta f(\xi_1, \xi_2, \xi_3)$ where the function f is well behaved; therefore these singularities are integrable. We can also relax the integral for $\boldsymbol{x}$ to the infinite plane and still get finite results. Therefore the integral in $D_2(q)$ is well behaved, and $D_2(\boldsymbol{q}, q_0 = 0)$ scales linearly with $|\boldsymbol{q}|$.

Next, we need to extract the scaling behavior at finite frequency; analytic continuation $iq_0 \to \omega + i\delta$ is needed. First, the real part of $D_2(q)$ is of the form $D_2(q) = |\boldsymbol{q}|f(\omega/\boldsymbol{q}^2)$, where f is a well-behaved function whose value is always finite (according to the $q_0 = 0$ analysis above). However it might be useful to see how the actual scaling looks like. What we care is when $w = \omega/\boldsymbol{q}^2 \ll 1$ since this is the regime that $D_2(q)$ has both real and imaginary parts. In this regime, $1 - \hat{\boldsymbol{\epsilon}}_{\boldsymbol{x}+\hat{\boldsymbol{z}}/2} \cdot \hat{\boldsymbol{\epsilon}}_{\boldsymbol{x}-\hat{\boldsymbol{z}}/2}$ is finite (numerically verified), therefore the scaling is determined simply by $\int \frac{d^3\boldsymbol{x}}{(2\pi)^3} \frac{1}{(|\boldsymbol{\epsilon}_{\boldsymbol{x}+\hat{\boldsymbol{z}}/2}| + |\boldsymbol{\epsilon}_{\boldsymbol{x}-\hat{\boldsymbol{z}}/2}| \pm (w+i\delta))}$. The result is $\sim \int \frac{r^2 dr}{r \pm (w+i\delta)} \sim (\mp wr + r^2/2 + w^2 \ln(\pm w + r))|_0^R + i\pi w^2\mathrm{sgn}(w)$, we see that we have scaling $w^2 \ln|w| + i\pi w^2\mathrm{sgn}(w)$. Note that the real part $w^2 \ln|w|$ is in addition to other contributions in $f(w)$. Therefore in the limit $\omega \to 0$, we recover the scaling $D_2(q) \sim |q_z|$.

Next we deal with $D_1(q)$. The numerator can be simplified: notice that $\boldsymbol{d}_{\boldsymbol{k}+\boldsymbol{q}/2}^2 + \boldsymbol{d}_{\boldsymbol{k}-\boldsymbol{q}/2}^2 - 2|\boldsymbol{d}_{\boldsymbol{k}+\boldsymbol{q}/2}||\boldsymbol{d}_{\boldsymbol{k}-\boldsymbol{q}/2}| = (|\boldsymbol{d}_{\boldsymbol{k}+\boldsymbol{q}/2}| - |\boldsymbol{d}_{\boldsymbol{k}-\boldsymbol{q}/2}|)^2 \sim (\sin q \sin k)^2$, and $(\boldsymbol{d}_{\boldsymbol{k}+\boldsymbol{q}/2} - \boldsymbol{d}_{\boldsymbol{k}-\boldsymbol{q}/2})^2 =$

$8\sin^2 k_z \sin^2 \frac{q_z}{2}$, therefore we can substitute

$$1 - \hat{\boldsymbol{d}}_{\boldsymbol{k}+\boldsymbol{q}/2} \cdot \hat{\boldsymbol{d}}_{\boldsymbol{k}-\boldsymbol{q}/2} = \frac{-(|\boldsymbol{d}_{\boldsymbol{k}+\boldsymbol{q}/2}| - |\boldsymbol{d}_{\boldsymbol{k}-\boldsymbol{q}/2}|)^2 + (\boldsymbol{d}_{\boldsymbol{k}+\boldsymbol{q}/2} - \boldsymbol{d}_{\boldsymbol{k}-\boldsymbol{q}/2})^2}{2|\boldsymbol{d}_{\boldsymbol{k}+\boldsymbol{q}/2}||\boldsymbol{d}_{\boldsymbol{k}-\boldsymbol{q}/2}|} \sim \frac{\sin^2 q \sin^2 k}{2|\boldsymbol{d}_{\boldsymbol{k}+\boldsymbol{q}/2}||\boldsymbol{d}_{\boldsymbol{k}-\boldsymbol{q}/2}|}. \tag{B.18}$$

since $D_1(q)$ receives contribution mainly along the line, we can make the rescaling $k_1 = k_3 + qx_1$, $k_2 = k_3 + qx_2$ and the approximation $|d_{\boldsymbol{k}\pm\boldsymbol{q}/2}| = |\boldsymbol{q}||\sin k_3| f_\pm(x_1, x_2) + O(q^3)$, where $f_\pm(x_1, x_2) = \sqrt{(1 \mp 2(x_1 + x_2) + 4x_1^2 + 4x_2^2 - 4x_1 x_2)/2}$, we further have

$$1 - \hat{\boldsymbol{d}}_{\boldsymbol{k}+\boldsymbol{q}/2} \cdot \hat{\boldsymbol{d}}_{\boldsymbol{k}-\boldsymbol{q}/2} \sim \frac{1}{f_+(\boldsymbol{x}) f_-(\boldsymbol{x})}. \tag{B.19}$$

Then after analytic continuation to real frequency we have

$$D_1(q\hat{\boldsymbol{z}}, \omega) = -\frac{|\boldsymbol{q}|}{2\pi^2} \int d^2\boldsymbol{x} \frac{1}{f_+(\boldsymbol{x}) f_-(\boldsymbol{x})} \times$$
$$\int_0^\pi dk_3 \left(\frac{1}{|\sin k_3|(f_+ + f_-) + \frac{\omega}{|\boldsymbol{q}|} + c|\boldsymbol{q}| + i\delta} + \frac{1}{|\sin k_3|(f_+ + f_-) - \frac{\omega}{|\boldsymbol{q}|} + c|\boldsymbol{q}| - i\delta} \right), \tag{B.20}$$

the first integral gives (here we only consider $\omega \ll q \ll 1$)

$$D_1^{(1)} = -\frac{|\boldsymbol{q}|}{\pi^2} \ln\left(\frac{1}{|\frac{\omega}{|\boldsymbol{q}|} + c|\boldsymbol{q}||} \right) C_0 - i\frac{|\boldsymbol{q}|}{2\pi^2} \int d^2\boldsymbol{x} \frac{\Theta(0 < -\frac{\omega}{|\boldsymbol{q}|} - c|\boldsymbol{q}| < f_+ + f_-)}{f_+(\boldsymbol{x}) f_-(\boldsymbol{x}) \sqrt{(f_+(\boldsymbol{x}) + f_-(\boldsymbol{x}))^2 - (\frac{\omega}{|\boldsymbol{q}|} + c|\boldsymbol{q}|)^2}}, \tag{B.21}$$

where we defined

$$C_0 = \int d^2\boldsymbol{x} \frac{1}{f_+(\boldsymbol{x}) f_-(\boldsymbol{x})(f_+(\boldsymbol{x}) + f_-(\boldsymbol{x}))}. \tag{B.22}$$

the imaginary part vanishes for $|\omega| \ll \boldsymbol{q}^2$ since in this regime the Heaviside function has zero support. When $|\boldsymbol{q}| \gg \omega \gg \boldsymbol{q}^2$, we can ignore the $c|\boldsymbol{q}|^2$ term, and we have

$$D_1(q\hat{\boldsymbol{z}}, \omega) = -|\boldsymbol{q}| \ln\left(\frac{1}{|c^2\boldsymbol{q}^2 - \frac{\omega^2}{q^2}|} \right) C_0 - i|\boldsymbol{q}|\mathrm{sgn}(\omega) \left[g\left(\frac{\omega}{|\boldsymbol{q}|} \right) \Theta(|\boldsymbol{q}| \gg |\omega| > c\boldsymbol{q}^2) + \frac{\omega^2}{\boldsymbol{q}^4} \Theta(|\omega| \ll \boldsymbol{q}^2) \right], \tag{B.23}$$

where $g(x)$ is a function of $x = \omega/g$. We verify numerically that $g(\frac{\omega}{|\boldsymbol{q}|}) = C_0 + \frac{1}{2}(\frac{\omega}{|\boldsymbol{q}|})^2$. As we will show in the next appendix, a pure nodal line approximation can recover the calculation here by introducing a cutoff θ_0 for integrals along the nodal line at the Γ point of the form $\theta_0 \sim \boldsymbol{q}$.

To summarize, the 00 component $D(q) = \Pi^{00}(q)$ receives contribution of $D_2(q) \sim$

$|\boldsymbol{q}|f(\omega/q^2)$ near the Γ point and receives contribution $D_1 = -|\boldsymbol{q}|\ln\left(\frac{1}{|c^2|\boldsymbol{q}|^2-\omega^2/q^2|}\right) - i|\boldsymbol{q}|g(\omega/q)\Theta(|\boldsymbol{q}| \gg |\omega| > c\boldsymbol{q}^2)$ along the nodal lines. At small frequency $\omega \ll q^2$, $D(q)$ is real and is dominated by the nodal line ($q\ln(1/q)$ vs q).

The $0i$ and ij components can be analyzed in the same way. We have

$$\Pi^{(1)}_{1,0i}(q) = -i\pi\mathrm{Re}\left[\int \frac{d^3\boldsymbol{k}}{(2\pi)^3} \frac{\frac{|\boldsymbol{d}_{\boldsymbol{k}+\boldsymbol{q}/2}|-|\boldsymbol{d}_{\boldsymbol{k}-\boldsymbol{q}/2}|}{|\boldsymbol{d}_{\boldsymbol{k}-\boldsymbol{q}/2}|+|\boldsymbol{d}_{\boldsymbol{k}+\boldsymbol{q}/2}|}\frac{C_i(\boldsymbol{k},\boldsymbol{q})}{|\boldsymbol{d}_{\boldsymbol{k}-\boldsymbol{q}/2}||\boldsymbol{d}_{\boldsymbol{k}+\boldsymbol{q}/2}|} - \frac{D_i(\boldsymbol{k},\boldsymbol{q})}{|\boldsymbol{d}_{\boldsymbol{k}-\boldsymbol{q}/2}||\boldsymbol{d}_{\boldsymbol{k}+\boldsymbol{q}/2}|}}{|\boldsymbol{d}_{\boldsymbol{k}+\boldsymbol{q}/2}| + |\boldsymbol{d}_{\boldsymbol{k}-\boldsymbol{q}/2}| + iq_0}\right] q_0\sin k_i,$$
$$\text{(B.24a)}$$

$$\Pi^{(1)}_{1,ii}(q) = -2\pi\mathrm{Re}\left[\int \frac{d^3\boldsymbol{k}}{(2\pi)^3}\frac{1-\hat{B}_i(\boldsymbol{k},\boldsymbol{q})}{|\boldsymbol{d}_{\boldsymbol{k}+\boldsymbol{q}/2}|+|\boldsymbol{d}_{\boldsymbol{k}-\boldsymbol{q}/2}|+iq_0}\right]\sin^2 k_i, \tag{B.24b}$$

$$\Pi^{(1)}_{1,ij}(q) = \pi\mathrm{Re}\left[\int \frac{d^3\boldsymbol{k}}{(2\pi)^3}\frac{1-2\hat{B}_i(\boldsymbol{k},\boldsymbol{q})-2\hat{B}_j(\boldsymbol{k},\boldsymbol{q})}{|\boldsymbol{d}_{\boldsymbol{k}+\boldsymbol{q}/2}|+|\boldsymbol{d}_{\boldsymbol{k}-\boldsymbol{q}/2}|+iq_0}\right]\sin k_i\sin k_j, \tag{B.24c}$$

where (it is understood $i+3 \equiv i$)

$$\hat{B}_i = \hat{\boldsymbol{d}}_{\boldsymbol{k}-\boldsymbol{q}/2}\cdot\hat{\boldsymbol{d}}_{\boldsymbol{k}+\boldsymbol{q}/2} - 3\hat{d}^i_{\boldsymbol{k}-\boldsymbol{q}/2}\hat{d}^i_{\boldsymbol{k}+\boldsymbol{q}/2}, \tag{B.25a}$$

$$C_i = \frac{1}{2}[(d^{i+2}_{\boldsymbol{k}-\boldsymbol{q}/2} + d^{i+2}_{\boldsymbol{k}+\boldsymbol{q}/2}) - (d^{i+1}_{\boldsymbol{k}-\boldsymbol{q}/2} + d^{i+1}_{\boldsymbol{k}+\boldsymbol{q}/2})], \tag{B.25b}$$

$$D_i = \frac{1}{2}[(d^{i+2}_{\boldsymbol{k}-\boldsymbol{q}/2} - d^{i+2}_{\boldsymbol{k}+\boldsymbol{q}/2}) - (d^{i+1}_{\boldsymbol{k}-\boldsymbol{q}/2} - d^{i+1}_{\boldsymbol{k}+\boldsymbol{q}/2})], \tag{B.25c}$$

Due to the appearance of $\sin k_i$ coming from the vertex expressions, the Γ point will contribute at a much higher order: $\Pi^{(1)}_{1,0i} \sim q^2$, and $\Pi^{(1)}_{1,ij} \sim q^3$. Furthermore, the nodal line contribution becomes

$$\Pi^{(1)}_{1,0i} = -iq_0\frac{1}{2\pi^2}\int d^2\boldsymbol{x}\frac{c_{0i}(\boldsymbol{x})}{f_+(\boldsymbol{x})f_-(\boldsymbol{x})}\times$$
$$\int_0^\pi dk_3\left(\frac{1}{|\sin k_3|(f_+ + f_-) + \frac{\omega}{|\boldsymbol{q}|} + c|\boldsymbol{q}| + i\delta} + \frac{1}{|\sin k_3|(f_+ + f_-) - \frac{\omega}{|\boldsymbol{q}|} + c|\boldsymbol{q}| - i\delta}\right)$$
$$\text{(B.26)}$$

Note that the numerator of Eq. (B.24a) gives

$$\sim \frac{\sin q\sin k}{|\boldsymbol{d}_{\boldsymbol{k}+\boldsymbol{q}/2}||\boldsymbol{d}_{\boldsymbol{k}-\boldsymbol{q}/2}|} \tag{B.27}$$

(c.f. Eq. (B.18)), therefore it requires an extra $|\boldsymbol{q}|$ and an extra $\sin k_i$ to cancel the

$|\boldsymbol{q}|^2 \sin^2 k_3$ coming from $|\boldsymbol{d}_{\boldsymbol{k}+\boldsymbol{q}/2}||\boldsymbol{d}_{\boldsymbol{k}-\boldsymbol{q}/2}|$ in Eq. (B.27). Then, for the ij components

$$\Pi^{(1)}_{1,ij} = -\frac{|\boldsymbol{q}|}{2\pi^2} \int d^2\boldsymbol{x} \frac{c_{ij}(\boldsymbol{x})}{f_+(\boldsymbol{x})f_-(\boldsymbol{x})} \times$$

$$\int_0^\pi dk_3 \left(\frac{\sin^2 k_3}{|\sin k_3|(f_+ + f_-) + \frac{\omega}{|\boldsymbol{q}|} + c|\boldsymbol{q}| + i\delta} + \frac{\sin^2 k_3}{|\sin k_3|(f_+ + f_-) - \frac{\omega}{|\boldsymbol{q}|} + c|\boldsymbol{q}| - i\delta} \right)$$

$$(\text{B}.28)$$

which gives

$$\begin{aligned}
\Pi^{(1)}_{1,0i} &\sim \omega n_{0i}(\hat{\boldsymbol{q}}) \ln(1/|w|^2) + i\omega g(w), \\
\Pi^{(1)}_{1,ij} &\sim |\boldsymbol{q}| \left(n_{ij}(\hat{\boldsymbol{q}})(2 - \pi w) + m_{ij}(\hat{\boldsymbol{q}})w^2 \ln(1/w) \right) - i|\boldsymbol{q}|w^2 g(w),
\end{aligned} \tag{B.29}$$

where $w = \omega/|\boldsymbol{q}| \ll 1$ and $|\boldsymbol{q}| \gg |\omega| \gg c\boldsymbol{q}^2$ (The discrete poles when $|\omega| \ll \boldsymbol{q}^2$ are not included here). We see that the nodal line contribution also dominates in these components. Note the above expressions hold only in the scaling sense; for example, the $|\boldsymbol{q}|$ factor in $\Pi^{(1)}_{1,ij}$ must have a component dependent form in order for Ward identity to hold. On the other hand, these expressions already have the right scaling for Ward identity to hold. The detailed form of these scaling functions can be found in the next section.

Therefore in photon thermodynamics we just have to concentrate on the nodal line and not the Γ region. This validates the QED calculation in the next section.

Finally, we mention that the momentum dependent part of $\Pi_{2,ij}$ starts to contribute at quadratic order in q^2: this is because due to the special form of $h(\boldsymbol{k})$ we have

$$\begin{aligned}
\Pi^{(1)}_{2,ij} &= \int \frac{d^4k}{(2\pi)^4} \text{Tr} \left[\frac{\partial_{k_i}\partial_{k_j}h(\boldsymbol{k})}{k_0 - q_0 - h(\boldsymbol{k}-\boldsymbol{q})} \right] = \int \frac{d^4k}{(2\pi)^4} \text{Tr} \left[\frac{\partial_{k_i}\partial_{k_j}h(\boldsymbol{k}+\boldsymbol{q}))}{k_0 - h(\boldsymbol{k})} \right] \\
&= \delta_{ij} \int \frac{d^4k}{(2\pi)^4} \text{Tr} \left[\frac{\partial^2_{k_i}h(\boldsymbol{k}+\boldsymbol{q})}{k_0 - h(\boldsymbol{k})} \right],
\end{aligned} \tag{B.30}$$

since $h(-\boldsymbol{k}) = h(\boldsymbol{k})$, if we expand $\partial^2_{k_i}h(\boldsymbol{k}+\boldsymbol{q})$, the term linear in $\boldsymbol{q}$ is odd in $\boldsymbol{k}$ vanishes after the integral over $\boldsymbol{k}$, leaving the leading order contribution quadratic in $\boldsymbol{q}$.

B.3 Deriving the photon vacuum bubble: nodal line approximation

We concluded in the last Appendix that the calculation of photon self-energy at one-loop level amounts to calculating the momentum dependent part of the vacuum polarization bubble. This is the diagram resulted from the minimal coupling term $A_i(-\boldsymbol{q})\partial_{k_i}\mathcal{H}(\boldsymbol{k})\psi^\dagger_{\boldsymbol{k}+\boldsymbol{q}/2}\psi_{\boldsymbol{k}-\boldsymbol{q}/2}$. The expressions for this diagram and the vertex have been given in Eqs. (5.41) and (5.42).

The bare Green's function for the spinons has the explicit form

$$
\begin{aligned}
G_0(k) &= \frac{1}{ik_0 - \mathcal{H}} = \frac{ik_0 + \mathcal{H}}{-k_0^2 - E^2} \\
&= -\frac{ik_0 + \cos k_1(\sigma^2 - \sigma^3) + \cos k_2(\sigma^3 - \sigma^1) + \cos k_3(\sigma^1 - \sigma^2)}{k_0^2 + (\cos k_1 - \cos k_2)^2 + (\cos k_2 - \cos k_3)^2 + (\cos k_3 - \cos k_1)^2}.
\end{aligned}
$$ (B.31)

To evaluate the vacuum polarization bubble near the nodal star region, we first need to write the momentum in local coordinates. Denote the nodal line by $(\varsigma_1, \varsigma_2, \varsigma_3)$, where $\varsigma_{1,2,3} = \pm 1$ labels different nodal lines. For each nodal line, we denote

$$
\varepsilon_3 = \frac{1}{\sqrt{3}}(\varsigma_1 \hat{x} + \varsigma_2 \hat{y} + \varsigma_3 \hat{z}), \quad \varepsilon_1 = \frac{1}{\sqrt{2}}(\varsigma_1 \hat{x} - \varsigma_2 \hat{y}), \quad \varepsilon_2 = \frac{1}{\sqrt{6}}(\varsigma_1 \hat{x} + \varsigma_2 \hat{y} - 2\varsigma_3 \hat{z}), \quad \text{(B.32)}
$$

any momentum will be expanded in these coordinates: denote $\boldsymbol{k} = k_1 \hat{x} + k_2 \hat{y} + k_3 \hat{z} = c\varepsilon_3 + a(\varepsilon_1 \cos\theta + \varepsilon_2 \sin\theta) + b(-\varepsilon_1 \sin\theta + \varepsilon_2 \cos\theta)$, then we have

$$
k_1 = \varsigma_1 \left(\frac{c}{\sqrt{3}} + \eta \left(\frac{a}{\sqrt{2}} + \frac{b}{\sqrt{6}} \right) \cos\theta + \eta \left(\frac{a}{\sqrt{6}} - \frac{b}{\sqrt{2}} \right) \sin\theta \right), \tag{B.33a}
$$

$$
k_2 = \varsigma_2 \left(\frac{c}{\sqrt{3}} + \eta \left(-\frac{a}{\sqrt{2}} + \frac{b}{\sqrt{6}} \right) \cos\theta + \eta \left(\frac{a}{\sqrt{6}} + \frac{b}{\sqrt{2}} \right) \sin\theta \right), \tag{B.33b}
$$

$$
k_3 = \varsigma_3 \left(\frac{c}{\sqrt{3}} - \eta \frac{2b}{\sqrt{6}} \cos\theta - \eta \frac{2a}{\sqrt{6}} \sin\theta \right). \tag{B.33c}
$$

First, expand the Hamiltonian (5.34a) to first order of η and then set $\eta = 1$, we obtain

$$
\mathcal{H} = \sin\frac{c}{\sqrt{3}} \left(\frac{(-a + \sqrt{3}b)\cos\theta + (\sqrt{3}a + b)\sin\theta}{\sqrt{2}} \sigma^1 - \frac{(a + \sqrt{3}b)\cos\theta + (\sqrt{3}a - b)\sin\theta}{\sqrt{2}} \sigma^2 \right.
$$
$$
\left. + \sqrt{2}(a\cos\theta - b\sin\theta)\sigma^3 \right),
$$ (B.34)

with the energy $E^2(\boldsymbol{k}) = 3\sin^2\frac{c}{\sqrt{3}}(a^2 + b^2) = v^2(a^2 + b^2)$ where we defined $v \equiv \sqrt{3}\sin\frac{c}{\sqrt{3}}$. From now on, for any $\boldsymbol{k}$ dependent function $f = f(\boldsymbol{k})$, we will introduce the notation $f_\pm \equiv f(\boldsymbol{k} \pm \boldsymbol{q}/2)$.

Using the Feynman parameterization we have

$$
\Pi^{\mu\nu}(q) = \int \frac{d^4k}{(2\pi)^4} \int_0^1 du \frac{Z^{\mu\nu}(k, q)}{\left[u(k_{0+}^2 + v_+^2(a_+^2 + b_+^2)) + (1 - u)(k_{0-}^2 + v_-^2(a_-^2 + b_-^2)) \right]^2},
$$
(B.35)

where we defined

$$Z^{\mu\nu} = \text{Tr}[\Gamma^\mu(\boldsymbol{k})(i(k_0 + q_0/2) + H(\boldsymbol{k} + \boldsymbol{q}/2))\Gamma^\nu(\boldsymbol{k})(i(k_0 - q_0/2) + H(\boldsymbol{k} - \boldsymbol{q}/2))]. \quad \text{(B.36)}$$

In local coordinates, $\Pi^{\mu\nu}(q)$ then can be written as

$$\Pi^{\mu\nu}(q) = \frac{\varsigma_1\varsigma_2\varsigma_3}{(2\pi)^4} \int d\kappa_0 \int \frac{d^2\boldsymbol{\kappa}_\perp}{g} \int d\kappa_\parallel \int_0^1 du \frac{Z^{\mu\nu}(k, q)}{(\kappa_0^2 + \boldsymbol{\kappa}_\perp^2 + \Delta)^2}, \quad \text{(B.37)}$$

where we defined

$$\kappa_0 = k_0 + (u - 1/2)q_0, \quad \boldsymbol{\kappa}_\perp = \sqrt{g}\left(\boldsymbol{k}_\perp + \frac{1}{2}f\boldsymbol{q}_\perp\right), \quad \kappa_\parallel = \frac{c}{\sqrt{3}}, \quad \text{(B.38)}$$

with

$$g = uv_+^2 + (1 - u)v_-^2, \qquad h = uv_+^2 - (1 - u)v_-^2,$$

$$f = \frac{h}{g} = \frac{uv_+^2 - (1 - u)v_-^2}{uv_+^2 + (1 - u)v_-^2}, \qquad \Delta = u(1 - u)q_0^2 + \frac{1}{4}(1 - f^2)gq_\perp^2. \quad \text{(B.39)}$$

The denominator has spherical symmetry with respect to $(\kappa_0, \boldsymbol{\kappa}_\perp)$. If we set $v_+ = v_- \equiv v$ then the isotropic (i.e. relativistic) limit is recovered: $\boldsymbol{\kappa}_\perp = \boldsymbol{k}_\perp + (u - 1/2)\boldsymbol{q}_\perp$ which agrees with $\kappa_0 = k_0 + (u - 1/2)q_0$; and $\frac{1}{4}g(1 - f^2)q_\perp^2 \to u(1 - u)q_\perp^2$ which agrees with $u(1 - u)q_0^2$.

Now we simplify the numerator $Z^{\mu\nu}$. The vertex Γ^μ in principle needs expansion according to powers of η, however for our purpose it suffices to keep the zeroth order, i.e. $\Gamma^1(\boldsymbol{k}) = \sin k_1(\sigma^2 - \sigma^3) \sim \varsigma_1 \sin\frac{c}{\sqrt{3}}(\sigma^2 - \sigma^3)$, and similarly $\Gamma^2(\boldsymbol{k}) \sim \varsigma_2 \sin\frac{c}{\sqrt{3}}(\sigma^3 - \sigma^1)$, and $\Gamma^3(\boldsymbol{k}) \sim \varsigma_3 \sin\frac{c}{\sqrt{3}}(\sigma^1 - \sigma^2)$. For later convenience we further define $\varsigma_0 \equiv 1$. This way in $Z^{\mu\nu}$ there will be prefactors of

$$\varsigma_\mu\varsigma_\nu\left(\sin\frac{c}{\sqrt{3}}\right)^{\delta_{\mu\neq 0}+\delta_{\nu\neq 0}} = \varsigma_\mu\varsigma_\nu\left(\frac{v}{\sqrt{3}}\right)^{\delta_{\mu\neq 0}+\delta_{\nu\neq 0}}.$$

We then apply Eq. (B.38) and $Z^{\mu\nu}$ will be written as polynomials of κ, up to quadratic order. Then only the constant terms in κ and the squared terms in κ needs to be kept since the other terms integrate to zero. The integral over $d^3\kappa = d\kappa_0 d^2\boldsymbol{\kappa}_\perp$ can then be evaluated. Using dimensional regularization

$$\int d^3\kappa \frac{\{\kappa^2, 1\}}{(\kappa^2 + \Delta)^2} = 4\pi \int d\kappa \frac{\{\kappa^4, \kappa^2\}}{(\kappa^2 + \Delta)^2} = \pi^2\{-3\Delta^{1/2}, \frac{1}{\Delta^{1/2}}\} \quad \text{(B.40)}$$

where the divergent part of the first term has been subtracted (this part is independent of the external momentum $\boldsymbol{q}$ and will cancel the divergence from the "tadpole" diagram).

We then have

$$\Pi^{\mu\nu}(q) = \frac{\varsigma_1\varsigma_2\varsigma_3}{(2\pi)^4}\int d\kappa_\| \varsigma_\mu\varsigma_\nu \left(\frac{v}{\sqrt{3}}\right)^{\delta_{\mu\neq0}+\delta_{\nu\neq0}}\int_0^1 du I^{\mu\nu}(\kappa_\|,q), \qquad (B.41)$$

where (note we have put back in $I^{\mu\nu}$ the extra $\frac{1}{g}$ in Eq. (B.37) resulted from the change of integral variables)

$$I^{00} = 4\pi^2\left(-I_1 q_0^2 + I_2 q_0^2 v_- v_+ - \frac{1}{6}I_2 Q^2 v_-^2 v_+^2 + \frac{1}{2}I_3 Q^2 v_-^3 v_+^3\right), \qquad (B.42a)$$

$$I^{0i} = -4\pi^2 q_0 Q_i v_- v_+ \frac{v_- + v_+}{2\sqrt{3}}I_2, \qquad\qquad i\in\{1,2,3\}, \qquad (B.42b)$$

$$I^{ii} = 4\pi^2\left(2I_1 q_0^2 + \frac{1}{3}I_2 Q^2 v_-^2 v_+^2 - \frac{1}{3}I_3 Q_{ii}^2 v_-^3 v_+^3\right), \qquad\qquad i\in\{1,2,3\}, \qquad (B.42c)$$

$$I^{ij} = -4\pi^2\left(I_1 q_0^2 + \frac{1}{6}I_2 Q^2 v_-^2 v_+^2 + \frac{1}{3}I_3 Q_{kk}^2 v_-^3 v_+^3\right), \qquad \{i,j,k\}=\{1,2,3\}, \qquad (B.42d)$$

where the definitions of Q, Q_i and Q_{ii} are in Eqs. (5.51), and we defined

$$I_1 = \frac{(1-u)u}{\sqrt{\Delta}g}, \qquad I_2 = \frac{(1-u)u}{\sqrt{\Delta}g^2}, \qquad I_3 = \frac{(1-u)u}{\sqrt{\Delta}g^3}. \qquad (B.43)$$

We note that the integrals $\int_0^1 I_{1,2,3}du$ for general $v_+\neq v_-$ can be evaluated, and the result is written in terms of the Elliptic functions. However we are allowed to set $v_+ = v_- = v$ in $I_{1,2,3}$ since the $\boldsymbol{q}$ dependence in $v_\pm$ does not affect the leading order of the photon self energy Π_1 which is linear in $\boldsymbol{q}$. Then we have

$$\int_0^1 I_1 du = \frac{\pi}{8v^2\sqrt{q_0^2 + \frac{Q^2}{3}v^2}}, \qquad \int_0^1 I_2 du = \frac{\pi}{8v^4\sqrt{q_0^2 + \frac{Q^2}{3}v^2}}, \qquad \int_0^1 I_3 du = \frac{\pi}{8v^6\sqrt{q_0^2 + \frac{Q^2}{3}v^2}},$$
$$(B.44)$$

This allows us to write

$$\int_0^1 I^{\mu\nu}du = \frac{\pi^3}{2\sqrt{q_0^2 + \frac{Q^2}{3}v^2}}\times$$
$$\begin{pmatrix} \frac{1}{3}Q^2 & -\frac{q_0 Q_1}{\sqrt{3}v} & -\frac{q_0 Q_2}{\sqrt{3}v} & -\frac{q_0 Q_3}{\sqrt{3}v} \\ -\frac{q_0 Q_1}{\sqrt{3}v} & 2\frac{q_0^2}{v^2} + \frac{1}{3}Q^2 - \frac{1}{3}Q_{11}^2 & -\frac{q_0^2}{v^2} - \frac{1}{6}Q^2 - \frac{1}{3}Q_{33}^2 & -\frac{q_0^2}{v^2} - \frac{1}{6}Q^2 - \frac{1}{3}Q_{22}^2 \\ -\frac{q_0 Q_2}{\sqrt{3}v} & -\frac{q_0^2}{v^2} - \frac{1}{6}Q^2 - \frac{1}{3}Q_{33}^2 & 2\frac{q_0^2}{v^2} + \frac{1}{3}Q^2 - \frac{1}{3}Q_{22}^2 & -\frac{q_0^2}{v^2} - \frac{1}{6}Q^2 - \frac{1}{3}Q_{11}^2 \\ -\frac{q_0 Q_3}{\sqrt{3}v} & -\frac{q_0^2}{v^2} - \frac{1}{6}Q^2 - \frac{1}{3}Q_{22}^2 & -\frac{q_0^2}{v^2} - \frac{1}{6}Q^2 - \frac{1}{3}Q_{11}^2 & 2\frac{q_0^2}{v^2} + \frac{1}{3}Q^2 - \frac{1}{3}Q_{33}^2 \end{pmatrix}.$$
$$(B.45)$$

The matrix on the right has two zero eigenvalues and two nonzero eigenvalues, $\frac{3\pi^3}{2v^2}\sqrt{q_0^2 + \frac{Q^2}{3}v^2}$ and $\frac{3\pi^3}{2v^2}\frac{q_0^2 + \frac{1}{9}Q^2 v^2}{\sqrt{q_0^2 + \frac{Q^2}{3}v^2}}$. And we have

$$\Pi^{\mu\nu}(q) = \frac{\varsigma_1\varsigma_2\varsigma_3}{(2\pi)^4}\int d\kappa_\| \frac{\pi^3}{2\sqrt{q_0^2 + \frac{Q^2}{3}v^2}}\times$$

$$\begin{pmatrix}
\frac{1}{3}Q^2 & -\varsigma_1\frac{q_0 Q_1}{3} & -\varsigma_2\frac{q_0 Q_2}{3} & -\varsigma_3\frac{q_0 Q_3}{3} \\
-\varsigma_1\frac{q_0 Q_1}{3} & \frac{2}{3}q_0^2 + \frac{v^2}{9}(Q^2 - Q_{11}^2) & -\varsigma_1\varsigma_2\left[\frac{q_0^2}{3} + \frac{v^2}{18}(Q^2 + 2Q_{33}^2)\right] & -\varsigma_1\varsigma_3\left[\frac{q_0^2}{3} - \frac{v^2}{18}(Q^2 + 2Q_{22}^2)\right] \\
-\varsigma_2\frac{q_0 Q_2}{3} & -\varsigma_1\varsigma_2\left[\frac{q_0^2}{3} + \frac{v^2}{18}(Q^2 + 2Q_{33}^2)\right] & \frac{2}{3}q_0^2 + \frac{v^2}{9}(Q^2 - Q_{22}^2) & -\varsigma_2\varsigma_3\left[\frac{q_0^2}{3} + \frac{v^2}{18}(Q^2 + 2Q_{11}^2)\right] \\
-\varsigma_3\frac{q_0 Q_3}{3} & -\varsigma_1\varsigma_3\left[\frac{q_0^2}{3} + \frac{v^2}{18}(Q^2 + 2Q_{22}^2)\right] & -\varsigma_1\varsigma_2\left[\frac{q_0^2}{3} + \frac{v^2}{18}(Q^2 + 2Q_{11}^2)\right] & \frac{2}{3}q_0^2 + \frac{v^2}{9}(Q^2 - Q_{33}^2)
\end{pmatrix}.$$

$$(B.46)$$

The matrix now has two zero eigenvalues and two nonzero eigenvalues $\frac{\pi^3(q_0^2 + \frac{1}{3}Q^2)}{2\sqrt{q_0^2 + \frac{Q^2}{3}v^2}}$ and

$\frac{\pi^3}{2}\sqrt{q_0^2 + \frac{Q^2}{3}v^2}$.

The final integral is over $\kappa_\|$. To do this, cutoff must be imposed in the vicinity of Γ and L points where the Dirac velocity vanishes:

$$\int_{\theta_0}^{\pi - \theta_0} d\kappa_\| \frac{1}{\sqrt{A + \sin^2\kappa_\|}} = \frac{F(\pi - \theta_0, -\frac{1}{A}) - F(\theta_0, -\frac{1}{A})}{\sqrt{A}}, \tag{B.47a}$$

$$\int_{\theta_0}^{\pi - \theta_0} d\kappa_\| \frac{\sin^2\kappa_\|}{\sqrt{A + \sin^2\kappa_\|}} = \sqrt{A}\left(E(\pi - \theta_0, -\frac{1}{A}) - E(\theta_0, -\frac{1}{A}) - F(\pi - \theta_0, -\frac{1}{A}) + F(\theta_0, -\frac{1}{A})\right),$$

$$(B.47b)$$

with $A = \frac{q_0^2}{Q^2}$. Note that we can safely set $\theta_0 = 0$ in the second integral.

Bibliography

[1] P. W. Anderson. Ordering and antiferromagnetism in ferrites. *Phys. Rev.*, 102:1008–1013, May 1956.

[2] Philip W Anderson. Resonating valence bonds: A new kind of insulator? *Materials Research Bulletin*, 8(2):153–160, 1973.

[3] M. Baenitz, Ph. Schlender, J. Sichelschmidt, Y. A. Onykiienko, Z. Zangeneh, K. M. Ranjith, R. Sarkar, L. Hozoi, H. C. Walker, J.-C. Orain, H. Yasuoka, J. van den Brink, H. H. Klauss, D. S. Inosov, and Th. Doert. NaYbS$_2$: A planar spin-$\frac{1}{2}$ triangular-lattice magnet and putative spin liquid. *Phys. Rev. B*, 98:220409, Dec 2018.

[4] X. Bai, J. A. M. Paddison, E. Kapit, S. M. Koohpayeh, J.-J. Wen, S. E. Dutton, A. T. Savici, A. I. Kolesnikov, G. E. Granroth, C. L. Broholm, J. T. Chalker, and M. Mourigal. Magnetic excitations of the classical spin liquid MgCr$_2$O$_4$. *Phys. Rev. Lett.*, 122:097201, Mar 2019.

[5] Leon Balents. Spin liquids in frustrated magnets. *Nature*, 464(7286):199–208, 2010.

[6] Leon Balents, Lorenz Bartosch, Anton Burkov, Subir Sachdev, and Krishnendu Sengupta. Putting competing orders in their place near the mott transition. *Phys. Rev. B*, 71:144508, Apr 2005.

[7] Leon Balents, Lorenz Bartosch, Anton Burkov, Subir Sachdev, and Krishnendu Sengupta. Putting competing orders in their place near the mott transition. ii. the doped quantum dimer model. *Phys. Rev. B*, 71:144509, Apr 2005.

[8] A. Banerjee, C. A. Bridges, J. Q. Yan, A. A. Aczel, L. Li, M. B. Stone, G. E. Granroth, M. D. Lumsden, Y. Yiu, J. Knolle, S. Bhattacharjee, D. L. Kovrizhin, R. Moessner, D. A. Tennant, D. G. Mandrus, and S. E. Nagler. Proximate Kitaev quantum spin liquid behaviour in a honeycomb magnet. *Nature Materials*, 15(7):733–740, July 2016.

[9] Aron J. Beekman, Louk Rademaker, and Jasper van Wezel. An Introduction to Spontaneous Symmetry Breaking. *SciPost Phys. Lect. Notes*, page 11, 2019.

[10] Doron Bergman, Jason Alicea, Emanuel Gull, Simon Trebst, and Leon Balents. Order-by-disorder and spiral spin-liquid in frustrated diamond-lattice antiferromagnets. *Nature Physics*, 3(7):487–491, 2007.

[11] Doron L. Bergman, Gregory A. Fiete, and Leon Balents. Ordering in a frustrated pyrochlore antiferromagnet proximate to a spin liquid. *Phys. Rev. B*, 73:134402, Apr 2006.

[12] Jean-Sébastien Bernier, Michael J. Lawler, and Yong Baek Kim. Quantum order by disorder in frustrated diamond lattice antiferromagnets. *Phys. Rev. Lett.*, 101:047201, Jul 2008.

[13] Matthew S. Block, D. N. Sheng, Olexei I. Motrunich, and Matthew P. A. Fisher. Spin bose-metal and valence bond solid phases in a spin-1/2 model with ring exchanges on a four-leg triangular ladder. *Phys. Rev. Lett.*, 106:157202, Apr 2011.

[14] Mitchell M Bordelon, Eric Kenney, Chunxiao Liu, Tom Hogan, Lorenzo Posthuma, Marzieh Kavand, Yuanqi Lyu, Mark Sherwin, Nicholas P Butch, Craig Brown, et al. Field-tunable quantum disordered ground state in the triangular-lattice antiferromagnet $NaYbO_2$. *Nature Physics*, 15(10):1058–1064, 2019.

[15] Mitchell M. Bordelon, Chunxiao Liu, Lorenzo Posthuma, Eric Kenney, M. J. Graf, N. P. Butch, Arnab Banerjee, Stuart Calder, Leon Balents, and Stephen D. Wilson. Frustrated heisenberg $J_1 - J_2$ model within the stretched diamond lattice of $LiYbO_2$. *Phys. Rev. B*, 103:014420, Jan 2021.

[16] Mitchell M. Bordelon, Chunxiao Liu, Lorenzo Posthuma, P. M. Sarte, N. P. Butch, Daniel M. Pajerowski, Arnab Banerjee, Leon Balents, and Stephen D. Wilson. Spin excitations in the frustrated triangular lattice antiferromagnet $NaYbO_2$. *Phys. Rev. B*, 101:224427, Jun 2020.

[17] DF Bowman, E Cemal, T Lehner, AR Wildes, L Mangin-Thro, GJ Nilsen, MJ Gutmann, DJ Voneshen, D Prabhakaran, AT Boothroyd, et al. Role of defects in determining the magnetic ground state of ytterbium titanate. *Nature communications*, 10, 2019.

[18] S. T. Bramwell, M. J. Harris, B. C. den Hertog, M. J. P. Gingras, J. S. Gardner, D. F. McMorrow, A. R. Wildes, A. L. Cornelius, J. D. M. Champion, R. G. Melko, and T. Fennell. Spin correlations in $Ho_2Ti_2O_7$: A dipolar spin ice system. *Phys. Rev. Lett.*, 87:047205, Jul 2001.

[19] ST Bramwell and MJ Harris. Frustration in ising-type spin models on the pyrochlore lattice. *Journal of Physics: Condensed Matter*, 10(14):L215, 1998.

[20] Steven T Bramwell and Michel JP Gingras. Spin ice state in frustrated magnetic pyrochlore materials. *Science*, 294(5546):1495–1501, 2001.

[21] C Broholm, RJ Cava, SA Kivelson, DG Nocera, MR Norman, and T Senthil. Quantum spin liquids. *Science*, 367(6475), 2020.

[22] Finn Lasse Buessen, Max Hering, Johannes Reuther, and Simon Trebst. Quantum spin liquids in frustrated spin-1 diamond antiferromagnets. *Phys. Rev. Lett.*, 120:057201, Jan 2018.

[23] F. J. Burnell, Shoibal Chakravarty, and S. L. Sondhi. Monopole flux state on the pyrochlore lattice. *Phys. Rev. B*, 79:144432, Apr 2009.

[24] Y. Q. Cai, Q. Cui, X. Li, Z. L. Dun, J. Ma, C. dela Cruz, Y. Y. Jiao, J. Liao, P. J. Sun, Y. Q. Li, J. S. Zhou, J. B. Goodenough, H. D. Zhou, and J.-G. Cheng. High-pressure synthesis and characterization of the effective pseudospin $S = 1/2$ XY pyrochlores $R_2Pt_2O_7$ ($R =$ Er, Yb). *Phys. Rev. B*, 93:014443, Jan 2016.

[25] B. Canals and C. Lacroix. Pyrochlore antiferromagnet: A three-dimensional quantum spin liquid. *Phys. Rev. Lett.*, 80:2933–2936, Mar 1998.

[26] JR Chamorro, L Ge, J Flynn, MA Subramanian, M Mourigal, and TM McQueen. Frustrated spin one on a diamond lattice in $NiRh_2O_4$. *Phys. Rev. Materials*, 2(3):034404, 2018.

[27] J. D. M. Champion, A. S. Wills, T. Fennell, S. T. Bramwell, J. S. Gardner, and M. A. Green. Order in the heisenberg pyrochlore: The magnetic structure of $Gd_2Ti_2O_7$. *Phys. Rev. B*, 64:140407, Sep 2001.

[28] Lieh-Jeng Chang, DJ Huang, WH Li, Sang-Wook Cheong, W Ratcliff, and JW Lynn. Crossover from incommensurate to commensurate magnetic orderings in $CoCr_2O_4$. *Journal of Physics: Condensed matter*, 21(45):456008, 2009.

[29] Gang Chen. "magnetic monopole" condensation of the pyrochlore ice u(1) quantum spin liquid: Application to $Pr_2Ir_2O_7$ and $Yb_2Ti_2O_7$. *Phys. Rev. B*, 94:205107, Nov 2016.

[30] Gang Chen. Quantum paramagnet and frustrated quantum criticality in a spin-one diamond lattice antiferromagnet. *Phys. Rev. B*, 96:020412, Jul 2017.

[31] Lei Chen, Dai-Wei Qu, Han Li, Bin-Bin Chen, Shou-Shu Gong, Jan von Delft, Andreas Weichselbaum, and Wei Li. Two-temperature scales in the triangular-lattice heisenberg antiferromagnet. *Phys. Rev. B*, 99:140404, Apr 2019.

[32] Xuliang Chen, Zhaorong Yang, Yuanmiao Xie, Zhonghao Huang, Langsheng Ling, Shile Zhang, Li Pi, Yuping Sun, and Yuheng Zhang. Coexistence of incommensurate and commensurate spiral orders and pressure effect on polycrystalline $CoCr_2O_4$. *Journal of Applied Physics*, 113(17):17E129, 2013.

[33] Li Ern Chern and Yong Baek Kim. Magnetic order with fractionalized excitations in pyrochlore magnets with strong spin-orbit coupling. *Scientific reports*, 9(1):1–10, 2019.

[34] Ting-Pong Choy and Yong Baek Kim. Classification of quantum phases for the star-lattice antiferromagnet via a projective symmetry group analysis. *Phys. Rev. B*, 80:064404, Aug 2009.

[35] A V Chubukov and D I Golosov. Quantum theory of an antiferromagnet on a triangular lattice in a magnetic field. *Journal of Physics: Condensed Matter*, 3(1):69–82, jan 1991.

[36] Y. Cui, J. Dai, P. Zhou, P. S. Wang, T. R. Li, W. H. Song, J. C. Wang, L. Ma, Z. Zhang, S. Y. Li, G. M. Luke, B. Normand, T. Xiang, and W. Yu. Mermin-wagner physics, (h, t) phase diagram, and candidate quantum spin-liquid phase in the spin-$\frac{1}{2}$ triangular-lattice antiferromagnet $Ba_8CoNb_6O_{24}$. *Phys. Rev. Materials*, 2:044403, Apr 2018.

[37] Peng-Ling Dai, Gaoning Zhang, Yaofeng Xie, Chunruo Duan, Yonghao Gao, Zihao Zhu, Erxi Feng, Zhen Tao, Chien-Lung Huang, Huibo Cao, Andrey Podlesnyak, Garrett E. Granroth, Michelle S. Everett, Joerg C. Neuefeind, David Voneshen, Shun Wang, Guotai Tan, Emilia Morosan, Xia Wang, Hai-Qing Lin, Lei Shu, Gang Chen, Yanfeng Guo, Xingye Lu, and Pengcheng Dai. Spinon fermi surface spin liquid in a triangular lattice antiferromagnet $NaYbSe_2$. *Phys. Rev. X*, 11:021044, May 2021.

[38] Lei Ding, Pascal Manuel, Sebastian Bachus, Franziska Grußler, Philipp Gegenwart, John Singleton, Roger D. Johnson, Helen C. Walker, Devashibhai T. Adroja, Adrian D. Hillier, and Alexander A. Tsirlin. Gapless spin-liquid state in the structurally disorder-free triangular antiferromagnet $NaYbO_2$. *Phys. Rev. B*, 100:144432, Oct 2019.

[39] Dominic V. Else and Ryan Thorngren. Topological theory of lieb-schultz-mattis theorems in quantum spin systems. *Phys. Rev. B*, 101:224437, Jun 2020.

[40] N. Elstner and A. P. Young. Spin-1/2 heisenberg antiferromagnet on the kagome´ lattice: High-temperature expansion and exact-diagonalization studies. *Phys. Rev. B*, 50:6871–6876, Sep 1994.

[41] Patrik Fazekas. *Lecture notes on electron correlation and magnetism*, volume 5. World scientific, 1999.

[42] Junwu Gan and Eugene Wong. Non-fermi-liquid behavior in quantum critical systems. *Phys. Rev. Lett.*, 71:4226–4229, Dec 1993.

[43] Bin Gao, Tong Chen, David W. Tam, Chien-Lung Huang, Kalyan Sasmal, Devashibhai T. Adroja, Feng Ye, Huibo Cao, Gabriele Sala, Matthew B. Stone, Christopher Baines, Joel A. T. Verezhak, Haoyu Hu, Jae-Ho Chung, Xianghan Xu, Sang-Wook Cheong, Manivannan Nallaiyan, Stefano Spagna, M. Brian Maple, Andriy H. Nevidomskyy, Emilia Morosan, Gang Chen, and Pengcheng Dai. Experimental signatures of a three-dimensional quantum spin liquid in effective spin-1/2 $Ce_2Zr_2O_7$ pyrochlore. *Nature Physics*, 15(10):1052–1057, July 2019.

[44] Shang Gao, Oksana Zaharko, Vladimir Tsurkan, Yixi Su, Jonathan S White, Gregory S Tucker, Bertrand Roessli, Frederic Bourdarot, Romain Sibille, Dmitry Chernyshov, et al. Spiral spin-liquid and the emergence of a vortex-like state in $MnSc_2S_4$. *Nature Physics*, 13(2):157–161, 2017.

[45] Jason S Gardner, Michel JP Gingras, and John E Greedan. Magnetic pyrochlore oxides. *Reviews of Modern Physics*, 82(1):53, 2010.

[46] V. Ovidiu Garlea, Liurukara D. Sanjeewa, Michael A. McGuire, Cristian D. Batista, Anjana M. Samarakoon, David Graf, Barry Winn, Feng Ye, Christina Hoffmann, and Joseph W. Kolis. Exotic magnetic field-induced spin-superstructures in a mixed honeycomb-triangular lattice system. *Phys. Rev. X*, 9:011038, Feb 2019.

[47] J. Gaudet, D. D. Maharaj, G. Sala, E. Kermarrec, K. A. Ross, H. A. Dabkowska, A. I. Kolesnikov, G. E. Granroth, and B. D. Gaulin. Neutron spectroscopic study of crystalline electric field excitations in stoichiometric and lightly stuffed $Yb_2Ti_2O_7$. *Phys. Rev. B*, 92:134420, Oct 2015.

[48] J. Gaudet, K. A. Ross, E. Kermarrec, N. P. Butch, G. Ehlers, H. A. Dabkowska, and B. D. Gaulin. Gapless quantum excitations from an icelike splayed ferromagnetic ground state in stoichiometric $Yb_2Ti_2O_7$. *Phys. Rev. B*, 93:064406, Feb 2016.

[49] J. Gaudet, E. M. Smith, J. Dudemaine, J. Beare, C. R. C. Buhariwalla, N. P. Butch, M. B. Stone, A. I. Kolesnikov, Guangyong Xu, D. R. Yahne, K. A. Ross, C. A. Marjerrison, J. D. Garrett, G. M. Luke, A. D. Bianchi, and B. D. Gaulin. Quantum spin ice dynamics in the dipole-octupole pyrochlore magnet $Ce_2Zr_2O_7$. *Phys. Rev. Lett.*, 122:187201, May 2019.

[50] L Ge, J Flynn, Joseph AM Paddison, Matthew B Stone, S Calder, MA Subramanian, AP Ramirez, and M Mourigal. Spin order and dynamics in the diamond-lattice heisenberg antiferromagnets $CuRh_2O_4$ and $CoRh_2O_4$. *Phys. Rev. B*, 96(6):064413, 2017.

[51] M J P Gingras and P A McClarty. Quantum spin ice: a search for gapless quantum spin liquids in pyrochlore magnets. *Reports on Progress in Physics*, 77(5):056501, may 2014.

[52] H.-M. Guo and M. Franz. Three-dimensional topological insulators on the pyrochlore lattice. *Phys. Rev. Lett.*, 103:206805, Nov 2009.

[53] A. M. Hallas, J. Gaudet, N. P. Butch, M. Tachibana, R. S. Freitas, G. M. Luke, C. R. Wiebe, and B. D. Gaulin. Universal dynamic magnetism in Yb pyrochlores with disparate ground states. *Phys. Rev. B*, 93:100403, Mar 2016.

[54] A. M. Hallas, J. Gaudet, M. N. Wilson, T. J. Munsie, A. A. Aczel, M. B. Stone, R. S. Freitas, A. M. Arevalo-Lopez, J. P. Attfield, M. Tachibana, C. R. Wiebe, G. M. Luke, and B. D. Gaulin. Xy antiferromagnetic ground state in the effective $S = \frac{1}{2}$ pyrochlore $Yb_2Ge_2O_7$. *Phys. Rev. B*, 93:104405, Mar 2016.

[55] Alannah M. Hallas, Jonathan Gaudet, and Bruce D. Gaulin. Experimental insights into ground-state selection of quantum XY pyrochlores. *Annual Review of Condensed Matter Physics*, 9(1):105–124, 2018.

[56] M. J. Harris, S. T. Bramwell, P. C. W. Holdsworth, and J. D. M. Champion. Liquid-gas critical behavior in a frustrated pyrochlore ferromagnet. *Phys. Rev. Lett.*, 81:4496–4499, Nov 1998.

[57] MJ Harris and MP Zinkin. Frustration in the pyrochlore antiferromagnets. *Modern Physics Letters B*, 10(10):417–438, 1996.

[58] J. W. Harter, Z. Y. Zhao, J.-Q. Yan, D. G. Mandrus, and D. Hsieh. A parity-breaking electronic nematic phase transition in the spin-orbit coupled metal $Cd_2Re_2O_7$. *Science*, 356(6335):295–299, 2017.

[59] Yuta Hashimoto, Makoto Wakeshima, and Yukio Hinatsu. Magnetic properties of ternary sodium oxides $NaLnO_2$ (Ln=rare earths). *Journal of Solid State Chemistry*, 176(1):266–272, 2003.

[60] J. S. Helton, K. Matan, M. P. Shores, E. A. Nytko, B. M. Bartlett, Y. Yoshida, Y. Takano, A. Suslov, Y. Qiu, J.-H. Chung, D. G. Nocera, and Y. S. Lee. Spin dynamics of the spin-1/2 kagome lattice antiferromagnet $ZnCu_3(OH)_6Cl_2$. *Phys. Rev. Lett.*, 98:107204, Mar 2007.

[61] Christopher L. Henley. Ordering due to disorder in a frustrated vector antiferromagnet. *Phys. Rev. Lett.*, 62:2056–2059, Apr 1989.

[62] M. Hermanns, I. Kimchi, and J. Knolle. Physics of the kitaev model: Fractionalization, dynamic correlations, and material connections. *Annual Review of Condensed Matter Physics*, 9(1):17–33, 2018.

[63] Michael Hermele, Matthew P. A. Fisher, and Leon Balents. Pyrochlore photons: The $U(1)$ spin liquid in a $S = \frac{1}{2}$ three-dimensional frustrated magnet. *Phys. Rev. B*, 69:064404, Feb 2004.

[64] Max Hirschberger, Peter Czajka, SM Koohpayeh, Wudi Wang, and N Phuan Ong. Enhanced thermal hall conductivity below 1 kelvin in the pyrochlore magnet $Yb_2Ti_2O_7$. *arXiv preprint arXiv:1903.00595*, 2019.

[65] Max Hirschberger, Jason W. Krizan, R. J. Cava, and N. P. Ong. Large thermal hall conductivity of neutral spin excitations in a frustrated quantum magnet. *Science*, 348(6230):106–109, 2015.

[66] Biao Huang, Wonjune Choi, Yong Baek Kim, and Yuan-Ming Lu. Classification and properties of quantum spin liquids on the hyperhoneycomb lattice. *Phys. Rev. B*, 97:195141, May 2018.

[67] Biao Huang, Yong Baek Kim, and Yuan-Ming Lu. Interplay of nonsymmorphic symmetry and spin-orbit coupling in hyperkagome spin liquids: Applications to $Na_4Ir_3O_8$. *Phys. Rev. B*, 95:054404, Feb 2017.

[68] Kyusung Hwang, Tyler Dodds, Subhro Bhattacharjee, and Yong Baek Kim. Three-dimensional nematic spin liquid in a stacked triangular lattice $6H$-B structure. *Phys. Rev. B*, 87:235103, Jun 2013.

[69] Jason Iaconis, Chunxiao Liu, Gábor B. Halász, and Leon Balents. Spin Liquid versus Spin Orbit Coupling on the Triangular Lattice. *SciPost Phys.*, 4:003, 2018.

[70] Sean Injac, Alexander KL Yuen, Maxim Avdeev, Fabio Orlandi, and Brendan J Kennedy. Structural and magnetic studies of koso4, a 5d1 quantum magnet oxide. *Physical Chemistry Chemical Physics*, 21(14):7261–7264, 2019.

[71] Yasir Iqbal, Tobias Müller, Harald O. Jeschke, Ronny Thomale, and Johannes Reuther. Stability of the spiral spin liquid in $MnSc_2S_4$. *Phys. Rev. B*, 98:064427, Aug 2018.

[72] Makoto Isoda, Hiroki Nakano, and Tôru Sakai. Specific heat and magnetic susceptibility of ising-like anisotropic heisenberg model on kagome lattice. *Journal of the Physical Society of Japan*, 80(8):084704, 2011.

[73] Behnam Javanparast, Alexandre G. R. Day, Zhihao Hao, and Michel J. P. Gingras. Order-by-disorder near criticality in xy pyrochlore magnets. *Phys. Rev. B*, 91:174424, May 2015.

[74] Behnam Javanparast, Zhihao Hao, Matthew Enjalran, and Michel J. P. Gingras. Fluctuation-driven selection at criticality in a frustrated magnetic system: The case of multiple-**k** partial order on the pyrochlore lattice. *Phys. Rev. Lett.*, 114:130601, Apr 2015.

[75] D. G. Karraker. Magnetic susceptibility of Yb^{3+} in an octahedral environment. *The Journal of Chemical Physics*, 55(3):1084–1086, 1971.

[76] Itamar Kimchi, Adam Nahum, and T. Senthil. Valence bonds in random quantum magnets: Theory and application to YbMgGaO$_4$. *Phys. Rev. X*, 8:031028, Jul 2018.

[77] K. Kimura, S. Nakatsuji, and T. Kimura. Experimental realization of a quantum breathing pyrochlore antiferromagnet. *Phys. Rev. B*, 90:060414, Aug 2014.

[78] Alexei Kitaev. Anyons in an exactly solved model and beyond. *Ann. Phys.*, 321(1):2, 2006. January Special Issue.

[79] A. Krimmel, M. Mücksch, V. Tsurkan, M. M. Koza, H. Mutka, C. Ritter, D. V. Sheptyakov, S. Horn, and A. Loidl. Magnetic ordering and spin excitations in the frustrated magnet MnSc$_2$S$_4$. *Phys. Rev. B*, 73:014413, Jan 2006.

[80] Moyuru Kurita, Youhei Yamaji, and Masatoshi Imada. Topological insulators from spontaneous symmetry breaking induced by electron correlation on pyrochlore lattices. *Journal of the Physical Society of Japan*, 80(4):044708, 2011.

[81] G Lawes, B Melot, K Page, C Ederer, MA Hayward, Th Proffen, and R Seshadri. Dielectric anomalies and spiral magnetic order in CoCr$_2$O$_4$. *Phys. Rev. B*, 74(2):024413, 2006.

[82] Michael J. Lawler, Arun Paramekanti, Yong Baek Kim, and Leon Balents. Gapless spin liquids on the three-dimensional hyperkagome lattice of Na$_4$Ir$_3$O$_8$. *Phys. Rev. Lett.*, 101:197202, Nov 2008.

[83] Patrick A Lee. An end to the drought of quantum spin liquids. *Science*, 321(5894):1306–1307, 2008.

[84] SungBin Lee and Leon Balents. Theory of the ordered phase in a-site antiferromagnetic spinels. *Phys. Rev. B*, 78:144417, Oct 2008.

[85] M. Léger, E. Lhotel, M. Ciomaga Hatnean, J. Ollivier, A. R. Wildes, S. Raymond, E. Ressouche, G. Balakrishnan, and S. Petit. Spin dynamics and unconventional coulomb phase in Nd$_2$Zr$_2$O$_7$. *Phys. Rev. Lett.*, 126:247201, Jun 2021.

[86] E. Lhotel, S. Petit, S. Guitteny, O. Florea, M. Ciomaga Hatnean, C. Colin, E. Ressouche, M. R. Lees, and G. Balakrishnan. Fluctuations and all-in˘all-out ordering in dipole-octupole Nd$_2$Zr$_2$O$_7$. *Phys. Rev. Lett.*, 115:197202, Nov 2015.

[87] Yao-Dong Li and Gang Chen. Symmetry enriched u(1) topological orders for dipole-octupole doublets on a pyrochlore lattice. *Phys. Rev. B*, 95:041106, Jan 2017.

[88] Yao-Dong Li, Yao Shen, Yuesheng Li, Jun Zhao, and Gang Chen. Effect of spin-orbit coupling on the effective-spin correlation in YbMgGaO$_4$. *Phys. Rev. B*, 97:125105, Mar 2018.

[89] Yao-Dong Li, Xiaoqun Wang, and Gang Chen. Anisotropic spin model of strong spin-orbit-coupled triangular antiferromagnets. *Phys. Rev. B*, 94:035107, Jul 2016.

[90] Yuesheng Li, Devashibhai Adroja, Robert I. Bewley, David Voneshen, Alexander A. Tsirlin, Philipp Gegenwart, and Qingming Zhang. Crystalline electric-field randomness in the triangular lattice spin-liquid YbMgGaO$_4$. *Phys. Rev. Lett.*, 118:107202, Mar 2017.

[91] Yuesheng Li, Devashibhai Adroja, Pabitra K. Biswas, Peter J. Baker, Qian Zhang, Juanjuan Liu, Alexander A. Tsirlin, Philipp Gegenwart, and Qingming Zhang. Muon spin relaxation evidence for the u(1) quantum spin-liquid ground state in the triangular antiferromagnet YbMgGaO$_4$. *Phys. Rev. Lett.*, 117:097201, Aug 2016.

[92] Yuesheng Li, Gang Chen, Wei Tong, Li Pi, Juanjuan Liu, Zhaorong Yang, Xiaoqun Wang, and Qingming Zhang. Rare-earth triangular lattice spin liquid: A single-crystal study of YbMgGaO$_4$. *Phys. Rev. Lett.*, 115:167203, Oct 2015.

[93] Yuesheng Li, Haijun Liao, Zhen Zhang, Shiyan Li, Feng Jin, Langsheng Ling, Lei Zhang, Youming Zou, Li Pi, Zhaorong Yang, et al. Gapless quantum spin liquid ground state in the two-dimensional spin-1/2 triangular antiferromagnet ybmggao 4. *Scientific reports*, 5(1):1–8, 2015.

[94] Chunxiao Liu, Gábor B. Halász, and Leon Balents. Competing orders in pyrochlore magnets from a $\mathbb{Z}_2$ spin liquid perspective. *Phys. Rev. B*, 100:075125, Aug 2019.

[95] Chunxiao Liu, Gábor B Halász, and Leon Balents. Symmetric U(1) and $\mathbb{Z}_2$ spin liquids on the pyrochlore lattice. *Phys. Rev. B*, 104(5):054401, 2021.

[96] Weiwei Liu, Zheng Zhang, Jianting Ji, Yixuan Liu, Jianshu Li, Xiaoqun Wang, Hechang Lei, Gang Chen, and Qingming Zhang. Rare-earth chalcogenides: A large family of triangular lattice spin liquid candidates. *Chinese Physics Letters*, 35(11):117501, 2018.

[97] Yuan-Ming Lu. Symmetric Z_2 spin liquids and their neighboring phases on triangular lattice. *Phys. Rev. B*, 93:165113, Apr 2016.

[98] Yuan-Ming Lu. Symmetry-protected gapless $\mathbb{Z}_2$ spin liquids. *Phys. Rev. B*, 97:094422, Mar 2018.

[99] Yuan-Ming Lu, Ying Ran, and Patrick A. Lee. $\mathbb{Z}_2$ spin liquids in the $S = \frac{1}{2}$ heisenberg model on the kagome lattice: A projective symmetry-group study of schwinger fermion mean-field states. *Phys. Rev. B*, 83:224413, Jun 2011.

[100] Qiang Luo, Shijie Hu, Bin Xi, Jize Zhao, and Xiaoqun Wang. Ground-state phase diagram of an anisotropic spin-$\frac{1}{2}$ model on the triangular lattice. *Phys. Rev. B*, 95:165110, Apr 2017.

[101] Zhen Ma, Jinghui Wang, Zhao-Yang Dong, Jun Zhang, Shichao Li, Shu-Han Zheng, Yunjie Yu, Wei Wang, Liqiang Che, Kejing Ran, Song Bao, Zhengwei Cai, P. Čermák, A. Schneidewind, S. Yano, J. S. Gardner, Xin Lu, Shun-Li Yu, Jun-Ming Liu, Shiyan Li, Jian-Xin Li, and Jinsheng Wen. Spin-glass ground state in a triangular-lattice compound $YbZnGaO_4$. *Phys. Rev. Lett.*, 120:087201, Feb 2018.

[102] Gregory J MacDougall, Delphine Gout, Jerel L Zarestky, Georg Ehlers, Andrey Podlesnyak, Michael A McGuire, David Mandrus, and Stephen E Nagler. Kinetically inhibited order in a diamond-lattice antiferromagnet. *Proceedings of the National Academy of Sciences*, 108(38):15693–15698, 2011.

[103] Saptarshi Mandal and Naveen Surendran. Exactly solvable kitaev model in three dimensions. *Phys. Rev. B*, 79:024426, Jan 2009.

[104] Casey A Marjerrison, Cole Mauws, Arzoo Z Sharma, Christopher R Wiebe, Shahab Derakhshan, Chad Boyer, Bruce D Gaulin, and John E Greedan. Structure and magnetic properties of $KRuO_4$. *Inorganic Chemistry*, 55(24):12897–12903, 2016.

[105] V. S. Maryasin and M. E. Zhitomirsky. Triangular antiferromagnet with nonmagnetic impurities. *Phys. Rev. Lett.*, 111:247201, Dec 2013.

[106] Laura Messio, Claire Lhuillier, and Grégoire Misguich. Time reversal symmetry breaking chiral spin liquids: Projective symmetry group approach of bosonic mean-field theories. *Phys. Rev. B*, 87:125127, Mar 2013.

[107] Ryan V. Mishmash, James R. Garrison, Samuel Bieri, and Cenke Xu. Theory of a competitive spin liquid state for weak mott insulators on the triangular lattice. *Phys. Rev. Lett.*, 111:157203, Oct 2013.

[108] Seiji Miyashita. Magnetic properties of ising-like heisenberg antiferromagnets on the triangular lattice. *Journal of the Physical Society of Japan*, 55(10):3605–3617, 1986.

[109] R. Moessner and J. T. Chalker. Properties of a classical spin liquid: The heisenberg pyrochlore antiferromagnet. *Phys. Rev. Lett.*, 80:2929–2932, Mar 1998.

[110] Olexei I. Motrunich. Variational study of triangular lattice spin-1/2 model with ring exchanges and spin liquid state in $\kappa-(ET)_2cu_2(CN)_3$. *Phys. Rev. B*, 72:045105, Jul 2005.

[111] Yusuke Nambu, Satoru Nakatsuji, and Yoshiteru Maeno. Coherent behavior and nonmagnetic impurity effects of spin disordered state in $NiGa_2S_4$. *Journal of the Physical Society of Japan*, 75(4):043711, 2006.

[112] W. M. H. Natori, E. C. Andrade, E. Miranda, and R. G. Pereira. Chiral spin-orbital liquids with nodal lines. *Phys. Rev. Lett.*, 117:017204, Jul 2016.

273

[113] Shang-Qiang Ning, Liujun Zou, and Meng Cheng. Fractionalization and anomalies in symmetry-enriched U(1) gauge theories. *Phys. Rev. Research*, 2:043043, Oct 2020.

[114] Zohar Nussinov and Jeroen van den Brink. Compass models: Theory and physical motivations. *Rev. Mod. Phys.*, 87:1–59, Jan 2015.

[115] J. Oitmaa, R. R. P. Singh, B. Javanparast, A. G. R. Day, B. V. Bagheri, and M. J. P. Gingras. Phase transition and thermal order-by-disorder in the pyrochlore antiferromagnet $Er_2Ti_2O_7$: A high-temperature series expansion study. *Phys. Rev. B*, 88:220404, Dec 2013.

[116] Yoshihiko Okamoto, Gøran J. Nilsen, J. Paul Attfield, and Zenji Hiroi. Breathing pyrochlore lattice realized in *a*-site ordered spinel oxides $LiGaCr_4O_8$ and $LiInCr_4O_8$. *Phys. Rev. Lett.*, 110:097203, Feb 2013.

[117] T Ono, H Tanaka, O Kolomiyets, H Mitamura, T Goto, K Nakajima, A Oosawa, Y Koike, K Kakurai, J Klenke, P Smeibidle, and M Meißner. Magnetization plateaux of the S = 1/2 two-dimensional frustrated antiferromagnet Cs_2CuBr_4. *Journal of Physics: Condensed Matter*, 16(11):S773–S778, mar 2004.

[118] Joseph A. M. Paddison, Marcus Daum, Zhiling Dun, Georg Ehlers, Yaohua Liu, Matthew B. Stone, Haidong Zhou, and Martin Mourigal. Continuous excitations of the triangular-lattice quantum spin liquid $YbMgGaO_4$. *Nat. Phys.*, 13(2):117–122, 02 2017.

[119] Siddharth A Parameswaran, Ari M Turner, Daniel P Arovas, and Ashvin Vishwanath. Topological order and absence of band insulators at integer filling in non-symmorphic crystals. *Nature Physics*, 9(5):299–303, 2013.

[120] Michael Peskin. *An introduction to quantum field theory*. CRC press, 2018.

[121] A.M. Polyakov. Quark confinement and topology of gauge theories. *Nuclear Physics B*, 120(3):429 – 458, 1977.

[122] Arthur P Ramirez, A Hayashi, Robert Joseph Cava, R Siddharthan, and BS Shastry. Zero-point entropy in 'spin ice'. *Nature*, 399(6734):333–335, 1999.

[123] Ying Ran, Michael Hermele, Patrick A. Lee, and Xiao-Gang Wen. Projected-wave-function study of the spin-1/2 heisenberg model on the kagomé lattice. *Phys. Rev. Lett.*, 98:117205, Mar 2007.

[124] K. M. Ranjith, D. Dmytriieva, S. Khim, J. Sichelschmidt, S. Luther, D. Ehlers, H. Yasuoka, J. Wosnitza, A. A. Tsirlin, H. Kühne, and M. Baenitz. Field-induced instability of the quantum spin liquid ground state in the $J_{\text{eff}} = \frac{1}{2}$ triangular-lattice compound $NaYbO_2$. *Phys. Rev. B*, 99:180401, May 2019.

[125] E Rastelli and A Tassi. The rhombohedral heisenberg antiferromagnet: infinite degeneracy of the ground state and magnetic properties of solid oxygen. *Journal of Physics C: Solid State Physics*, 19(19):L423, 1986.

[126] J. G. Rau, L. S. Wu, A. F. May, L. Poudel, B. Winn, V. O. Garlea, A. Huq, P. Whitfield, A. E. Taylor, M. D. Lumsden, M. J. P. Gingras, and A. D. Christianson. Anisotropic exchange within decoupled tetrahedra in the quantum breathing pyrochlore $Ba_3Yb_2Zn_5O_{11}$. *Phys. Rev. Lett.*, 116:257204, Jun 2016.

[127] Jeffrey G. Rau, Eric Kin-Ho Lee, and Hae-Young Kee. Spin-orbit physics giving rise to novel phases in correlated systems: Iridates and related materials. *Annual Review of Condensed Matter Physics*, 7(1):195–221, 2016.

[128] Jeffrey G. Rau, Sylvain Petit, and Michel J. P. Gingras. Order by virtual crystal field fluctuations in pyrochlore xy antiferromagnets. *Phys. Rev. B*, 93:184408, May 2016.

[129] R. Rawl, L. Ge, H. Agrawal, Y. Kamiya, C. R. Dela Cruz, N. P. Butch, X. F. Sun, M. Lee, E. S. Choi, J. Oitmaa, C. D. Batista, M. Mourigal, H. D. Zhou, and J. Ma. $Ba_8CoNb_6O_{24}$: A spin-$\frac{1}{2}$ triangular-lattice heisenberg antiferromagnet in the two-dimensional limit. *Phys. Rev. B*, 95:060412, Feb 2017.

[130] Johannes Reuther, Shu-Ping Lee, and Jason Alicea. Classification of spin liquids on the square lattice with strong spin-orbit coupling. *Phys. Rev. B*, 90:174417, Nov 2014.

[131] Paul Romatschke. Fractional degrees of freedom at infinite coupling in large N_f qed in $2 + 1$ dimensions. *Phys. Rev. Lett.*, 123:241602, Dec 2019.

[132] Paul Romatschke and Matias Säppi. Thermal free energy of large N_f qed in $2 + 1$ dimensions from weak to strong coupling. *Phys. Rev. D*, 100:073009, Oct 2019.

[133] Kate A. Ross, Lucile Savary, Bruce D. Gaulin, and Leon Balents. Quantum excitations in quantum spin ice. *Phys. Rev. X*, 1:021002, Oct 2011.

[134] B. Roy, Abhishek Pandey, Q. Zhang, T. W. Heitmann, D. Vaknin, D. C. Johnston, and Y. Furukawa. Experimental evidence of a collinear antiferromagnetic ordering in the frustrated $CoAl_2O_4$ spinel. *Phys. Rev. B*, 88:174415, Nov 2013.

[135] Subir Sachdev. Kagome´- and triangular-lattice heisenberg antiferromagnets: Ordering from quantum fluctuations and quantum-disordered ground states with unconfined bosonic spinons. *Phys. Rev. B*, 45:12377–12396, Jun 1992.

[136] Sambuddha Sanyal, Kusum Dhochak, and Subhro Bhattacharjee. Interplay of uniform $U(1)$ quantum spin liquid and magnetic phases in rare-earth pyrochlore magnets: A fermionic parton approach. *Phys. Rev. B*, 99:134425, Apr 2019.

[137] Lucile Savary and Leon Balents. Coulombic quantum liquids in spin-1/2 pyrochlores. *Phys. Rev. Lett.*, 108:037202, Jan 2012.

[138] Lucile Savary and Leon Balents. Quantum spin liquids: a review. *Reports on Progress in Physics*, 80(1):016502, nov 2016.

[139] Lucile Savary, Emanuel Gull, Simon Trebst, Jason Alicea, Doron Bergman, and Leon Balents. Impurity effects in highly frustrated diamond-lattice antiferromagnets. *Phys. Rev. B*, 84:064438, Aug 2011.

[140] Lucile Savary, Kate A. Ross, Bruce D. Gaulin, Jacob P. C. Ruff, and Leon Balents. Order by quantum disorder in $Er_2Ti_2O_7$. *Phys. Rev. Lett.*, 109:167201, Oct 2012.

[141] Lucile Savary and T Senthil. Probing hidden orders with resonant inelastic x-ray scattering. *arXiv preprint arXiv:1506.04752*, 2015.

[142] Lucile Savary, Xiaoqun Wang, Hae-Young Kee, Yong Baek Kim, Yue Yu, and Gang Chen. Quantum spin ice on the breathing pyrochlore lattice. *Phys. Rev. B*, 94:075146, Aug 2016.

[143] A. Scheie, J. Kindervater, S. Säubert, C. Duvinage, C. Pfleiderer, H. J. Changlani, S. Zhang, L. Harriger, K. Arpino, S. M. Koohpayeh, O. Tchernyshyov, and C. Broholm. Reentrant phase diagram of $Yb_2Ti_2O_7$ in a <111> magnetic field. *Phys. Rev. Lett.*, 119:127201, Sep 2017.

[144] Rolph LE Schwarzenberger. *N-dimensional crystallography*, volume 41. Pitman Advanced Pub. Program, 1980.

[145] T. Senthil, Matthias Vojta, and Subir Sachdev. Weak magnetism and non-fermi liquids near heavy-fermion critical points. *Phys. Rev. B*, 69:035111, Jan 2004.

[146] Yao Shen, Yao-Dong Li, Hongliang Wo, Yuesheng Li, Shoudong Shen, Bingying Pan, Qisi Wang, HC Walker, Paul Steffens, Martin Boehm, et al. Evidence for a spinon fermi surface in a triangular-lattice quantum-spin-liquid candidate. *Nature*, 540(7634):559–562, 2016.

[147] Romain Sibille, Nicolas Gauthier, Han Yan, Monica Ciomaga Hatnean, Jacques Ollivier, Barry Winn, Uwe Filges, Geetha Balakrishnan, Michel Kenzelmann, Nic Shannon, and Tom Fennell. Experimental signatures of emergent quantum electrodynamics in $Pr_2Hf_2O_7$. *Nature Physics*, 2018.

[148] Romain Sibille, Elsa Lhotel, Monica Ciomaga Hatnean, Gøran J. Nilsen, Georg Ehlers, Antonio Cervellino, Eric Ressouche, Matthias Frontzek, Oksana Zaharko, Vladimir Pomjakushin, Uwe Stuhr, Helen C. Walker, Devashibhai T. Adroja, Hubertus Luetkens, Chris Baines, Alex Amato, Geetha Balakrishnan, Tom Fennell, and Michel Kenzelmann. Coulomb spin liquid in anion-disordered pyrochlore $Tb_2Hf_2O_7$. *Nature Communications*, 8:892, October 2017.

[149] Romain Sibille, Elsa Lhotel, Monica Ciomaga Hatnean, Geetha Balakrishnan, Björn Fåk, Nicolas Gauthier, Tom Fennell, and Michel Kenzelmann. Candidate quantum spin ice in the pyrochlore $Pr_2Hf_2O_7$. *Phys. Rev. B*, 94:024436, Jul 2016.

[150] Romain Sibille, Elsa Lhotel, Vladimir Pomjakushin, Chris Baines, Tom Fennell, and Michel Kenzelmann. Candidate quantum spin liquid in the Ce^{3+} pyrochlore stannate $Ce_2Sn_2O_7$. *Phys. Rev. Lett.*, 115:097202, Aug 2015.

[151] R. R. P. Singh and J. Oitmaa. High-temperature series expansion study of the heisenberg antiferromagnet on the hyperkagome lattice: Comparison with $na_4ir_3o_8$. *Phys. Rev. B*, 85:104406, Mar 2012.

[152] Yogesh Singh and P. Gegenwart. Antiferromagnetic mott insulating state in single crystals of the honeycomb lattice material Na_2IrO_3. *Phys. Rev. B*, 82:064412, Aug 2010.

[153] Young-Joon Song, Kyo-Hoon Ahn, Kwan-Woo Lee, and Warren E Pickett. Unquenched eg1 orbital moment in the mott-insulating antiferromagnet $KOsO_4$. *Phys. Rev. B*, 90(24):245117, 2014.

[154] Oleg A Starykh. Unusual ordered phases of highly frustrated magnets: a review. *Reports on Progress in Physics*, 78(5):052502, apr 2015.

[155] J. D. Thompson, P. A. McClarty, D. Prabhakaran, I. Cabrera, T. Guidi, and R. Coldea. Quasiparticle breakdown and spin hamiltonian of the frustrated quantum pyrochlore $Yb_2Ti_2O_7$ in a magnetic field. *Phys. Rev. Lett.*, 119:057203, Aug 2017.

[156] Ryan Thorngren and Dominic V. Else. Gauging spatial symmetries and the classification of topological crystalline phases. *Phys. Rev. X*, 8:011040, Mar 2018.

[157] Yoshifumi Tokiwa, Takuya Yamashita, Daiki Terazawa, Kenta Kimura, Yuichi Kasahara, Takafumi Onishi, Yasuyuki Kato, Mario Halim, Philipp Gegenwart, Takasada Shibauchi, Satoru Nakatsuji, Eun-Gook Moon, and Yuji Matsuda. Discovery of emergent photon and monopoles in a quantum spin liquid. *Journal of the Physical Society of Japan*, 87(6):064702, 2018.

[158] K. Tomiyasu, H. Suzuki, M. Toki, S. Itoh, M. Matsuura, N. Aso, and K. Yamada. Molecular spin resonance in the geometrically frustrated magnet $MgCr_2\mathbf{O}_4$ by inelastic neutron scattering. *Phys. Rev. Lett.*, 101:177401, Oct 2008.

[159] Chong Wang and T. Senthil. Time-reversal symmetric $U(1)$ quantum spin liquids. *Phys. Rev. X*, 6:011034, Mar 2016.

[160] Fa Wang. Schwinger boson mean field theories of spin liquid states on a honeycomb lattice: Projective symmetry group analysis and critical field theory. *Phys. Rev. B*, 82:024419, Jul 2010.

[161] Fa Wang and Ashvin Vishwanath. Spin-liquid states on the triangular and kagomé lattices: A projective-symmetry-group analysis of schwinger boson states. *Phys. Rev. B*, 74:174423, Nov 2006.

[162] Y. R. Wang. Specific heat of quantum heisenberg model on a triangular lattice with two exchange parameters and its application to ^{3}He adsorbed on graphite. *Phys. Rev. B*, 45:12608–12611, Jun 1992.

[163] Haruki Watanabe. Counting rules of nambu–goldstone modes. *Annual Review of Condensed Matter Physics*, 11(1):169–187, 2020.

[164] Haruki Watanabe, Hoi Chun Po, Ashvin Vishwanath, and Michael Zaletel. Filling constraints for spin-orbit coupled insulators in symmorphic and nonsymmorphic crystals. *Proceedings of the National Academy of Science*, 112(47):14551–14556, November 2015.

[165] Xiao-Gang Wen. Quantum orders and symmetric spin liquids. *Phys. Rev. B*, 65:165113, Apr 2002.

[166] Steven R. White and A. L. Chernyshev. Neél order in square and triangular lattice heisenberg models. *Phys. Rev. Lett.*, 99:127004, Sep 2007.

[167] William Witczak-Krempa, Gang Chen, Yong Baek Kim, and Leon Balents. Correlated quantum phenomena in the strong spin-orbit regime. *Annual Review of Condensed Matter Physics*, 5(1):57–82, 2014.

[168] William Witczak-Krempa, Ara Go, and Yong Baek Kim. Pyrochlore electrons under pressure, heat, and field: Shedding light on the iridates. *Phys. Rev. B*, 87:155101, Apr 2013.

[169] Cenke Xu, Fa Wang, Yang Qi, Leon Balents, and Matthew P. A. Fisher. Spin liquid phases for spin-1 systems on the triangular lattice. *Phys. Rev. Lett.*, 108:087204, Feb 2012.

[170] Y. Xu, J. Zhang, Y. S. Li, Y. J. Yu, X. C. Hong, Q. M. Zhang, and S. Y. Li. Absence of magnetic thermal conductivity in the quantum spin-liquid candidate YbMgGaO$_4$. *Phys. Rev. Lett.*, 117:267202, Dec 2016.

[171] Han Yan, Owen Benton, L. D. C. Jaubert, and Nic Shannon. Rank–2 $U(1)$ spin liquid on the breathing pyrochlore lattice. *Phys. Rev. Lett.*, 124:127203, Mar 2020.

[172] Han Yan, Owen Benton, Ludovic Jaubert, and Nic Shannon. Theory of multiple-phase competition in pyrochlore magnets with anisotropic exchange with application to Yb$_2$Ti$_2$O$_7$, Er$_2$Ti$_2$O$_7$, and Er$_2$Sn$_2$O$_7$. *Phys. Rev. B*, 95:094422, Mar 2017.

[173] Simeng Yan, David A. Huse, and Steven R. White. Spin-liquid ground state of the s = 1/2 kagome heisenberg antiferromagnet. *Science*, 332(6034):1173–1176, 2011.

[174] Xu Yang and Fa Wang. Schwinger boson spin-liquid states on square lattice. *Phys. Rev. B*, 94:035160, Jul 2016.

[175] Xu-Ping Yao, Yao-Dong Li, and Gang Chen. Pyrochlore U(1) spin liquid of mixed-symmetry enrichments in magnetic fields. *Phys. Rev. Research*, 2:013334, Mar 2020.

[176] A. Yaouanc, P. Dalmas de Réotier, P. Bonville, J. A. Hodges, V. Glazkov, L. Keller, V. Sikolenko, M. Bartkowiak, A. Amato, C. Baines, P. J. C. King, P. C. M. Gubbens, and A. Forget. Dynamical splayed ferromagnetic ground state in the quantum spin ice $Yb_2Sn_2O_7$. *Phys. Rev. Lett.*, 110:127207, Mar 2013.

[177] Yi-Zhuang You, Itamar Kimchi, and Ashvin Vishwanath. Doping a spin-orbit mott insulator: Topological superconductivity from the kitaev-heisenberg model and possible application to $(Na_2/Li_2)IrO_3$. *Phys. Rev. B*, 86:085145, Aug 2012.

[178] O Zaharko, Niels Bech Christensen, A Cervellino, Vladimir Tsurkan, A Maljuk, U Stuhr, C Niedermayer, F Yokaichiya, DN Argyriou, M Boehm, et al. Spin liquid in a single crystal of the frustrated diamond lattice antiferromagnet $CoAl_2O_4$. *Phys. Rev. B*, 84(9):094403, 2011.

[179] Vivien Zapf, Marcelo Jaime, and C. D. Batista. Bose-einstein condensation in quantum magnets. *Rev. Mod. Phys.*, 86:563–614, May 2014.

[180] Chen Zeng and Veit Elser. Numerical studies of antiferromagnetism on a kagomé net. *Phys. Rev. B*, 42:8436–8444, Nov 1990.

[181] Yahui Zhang and T. Senthil. Three Dimensional U(1) Nodal Line Spin Liquid. In *APS March Meeting Abstracts*, volume 2017 of *APS Meeting Abstracts*, page V48.001, March 2017.

[182] Weihong Zheng, John O. Fjærestad, Rajiv R. P. Singh, Ross H. McKenzie, and Radu Coldea. Excitation spectra of the spin-$\frac{1}{2}$ triangular-lattice heisenberg antiferromagnet. *Phys. Rev. B*, 74:224420, Dec 2006.

[183] M. E. Zhitomirsky. Magnetic phase diagram of a partially frustrated triangular antiferromagnet: The row model. *Phys. Rev. B*, 54(1):353–353, 1996.

[184] Yi Zhou, Kazushi Kanoda, and Tai-Kai Ng. Quantum spin liquid states. *Rev. Mod. Phys.*, 89:025003, Apr 2017.

[185] Zhenyue Zhu, P. A. Maksimov, Steven R. White, and A. L. Chernyshev. Disorder-induced mimicry of a spin liquid in $YbMgGaO_4$. *Phys. Rev. Lett.*, 119:157201, Oct 2017.

[186] Zhenyue Zhu, P. A. Maksimov, Steven R. White, and A. L. Chernyshev. Topography of spin liquids on a triangular lattice. *Phys. Rev. Lett.*, 120:207203, May 2018.

[187] Liujun Zou, Chong Wang, and T. Senthil. Symmetry enriched U(1) quantum spin liquids. *Phys. Rev. B*, 97:195126, May 2018.